A Fast Plasma Analyser For The Study Of The Solar Wind Interaction With Mars

Adrian Martin James

Mullard Space Science Laboratory
Department of Space and Climate Physics
University College London

Submitted to the University of London
for the degree of Doctor of Philosophy

January 1998

ProQuest LLC
789 East Eisenhower Parkway
P.O. Box 1346
Ann Arbor, MI 48106-1346

Abstract

This thesis describes the design and development of the FONEMA instrument to be flown aboard the Russian mission to Mars in 1996. Many probes have flown to Mars yet despite this many mysteries still remain, among them the nature of the interaction of the solar wind with the planetary obstacle. In this thesis I will present some of the results from earlier spacecraft and the models of the interaction that they suggest paying particular attention to the contribution of ion analysers. From these results it will become clear that a fast ion sensor is needed to resolve many of the questions about the magnetosphere of Mars. The FONEMA instrument was designed for this job making use of a novel electrostatic mirror and particle collimator combined with parallel magnetic and electrostatic fields to resolve the ions into mass and energy bins. Development and production of the individual elements is discussed in detail.

"...Our planet is a cradle of
intelligence, but one cannot remain
in the cradle for ever."
Konstantin Tsiolkovsky

List of Figures

List of Tables

1. Introduction

1.1 Missions to Mars

This introduction chapter discusses current theories being put forward for the structure and origins of the Martian magnetosphere. It is biased toward those theories and models which have a sound base in direct observation. In this light the chapter gives a brief history of spacecraft which have been to Mars and the results they obtained, and outlines some of the areas which still have to be studied in more detail if a clear picture of Mars and its environment is to be formed.

1.1.1 A brief history of exploration

The exploration of Mars began in 1960 when, on October 10th, the Soviet spacecraft Mars was launched. This spacecraft, and its sister craft launched four days later, both failed to achieve Earth orbit and were lost. It was not until 1962 that the Russians made a second attempt to reach Mars. At the end of that year three more Mars spacecraft were launched. Of these attempts only the craft launched on November 1st headed to the red planet, the other two failed to leave Earth orbit. Mars-1, as the successful spacecraft was designated, continued toward Mars until contact was lost early the following year when it had reached a distance of 105 million kilometres from Earth. This was before the mid-course correction and consequently Mars-1 passed by Mars at a distance of 193000 km. The Americans came into the race to reach Mars on November 5th 1964 with the launch of Mariner-3 from Cape Kennedy atop an Atlas-Agena D. Unfortunately the second stage failed to achieve the correct speed for Earth orbit and Mariner-3 went into solar orbit. It was Mariner-4 launched on November 25th that achieved the first successful fly-by of Mars. Arriving in July 1965, the Mariner-4 craft took 21 pictures of Mars, coming to within 9789 km of the surface. Only two days after the launch of Mariner-4, Zond-2 was launched from the USSR. This craft is believed to have been carrying a lander, however contact was lost with Zond-2 before encounter so the lander may not have separated. Although contact was lost Zond-2 would have passed within 1500 km of Mars.

No more launches took place until 1969 when Mariner-6 and Mariner-7 were launched on the 24th February and 27th March respectively. Both of these were successful fly-by missions returning pictures of the surface and other scientific data. Mariner-6 approached to 3392 km returning 75 pictures and Mariner-7 to within 3504 km returning 126 pictures. On the launch day of Mariner-7 another Soviet Mars probe was launched but it failed to reach Earth orbit.

The first two attempts of 1971 were launch failures, the Mariner-8 fly-by and the Kosmos-419 orbiter/lander. 1971 also saw three spacecraft go into orbit around Mars at about the same time. The two Russian orbiters Mars-2 and Mars-3 were both carrying landers: the Mars-2 lander carried a Soviet flag, but the Mars-3 lander carrying experiments failed after 20 seconds on the surface. The American Mariner-9 launched on May 30th arrived in November and went into an elliptical orbit taking 7329 pictures during eleven months of operation. It was from Mariner-9 photographs that landing sites were chosen for the Viking missions that followed in 1976.

No more American probes would go to Mars until the Viking landers in 1976. The Russians however launched four more probes in the interim period, all in 1974. Only Mars-5 is of importance to magnetospheric physics as it was one of the few Mars spacecraft to carry experiments to study the plasma environment of the planet. The only US craft carrying plasma instrumentation was the Mariner-4 fly-by probe. Unfortunately, Mars-5 only completed 20 orbits before contact was lost. Of the other Soviet launches that year, Mars-4 missed Mars by over 2000 km so failed to achieve orbit, returning only fly-by data; Mars-6 was a fly-by mission with a lander that only returned 120 seconds of descent data; and Mars-7, the sister craft to Mars-6 dropped a lander that missed the planet by 1280 km.

In 1976 the Americans successfully deployed two landers on the surface of Mars. The Viking-1 orbiter/lander was launched in August 1975 followed by Viking-2 a month later. Viking-1 reached Mars on June 19th 1976 and one month later on July 20th the Viking-1 lander touched down in Chryse (+22°, 47°). Viking-2 landed in Utopia (+48°, 226°) on September 3rd . Between the two landers 3000 photographs of the Martian surface were taken. The orbiters were responsible for over 50000 pictures of Mars.

The most recent excursions to Mars by the Russians were the two Phobos spacecraft, launched in 1988. This mission was designed to study the two moons of Mars, Phobos being the primary target, and Mars itself. A command fault meant that contact with Phobos-1 was lost before insertion into Mars orbit. Phobos-2 made 5 elliptical orbits with a closest approach of 850km and more than 100 circular orbits before contact was lost after only 57 days of operation. Although the mission ended prematurely Phobos-2 returned important data from the experiments it carried designed to study the magnetosphere of Mars. In 1994 the US launched the Mars Observer spacecraft, contact was lost, however, as it approached the planet.

Following the Phobos Missions the Soviets planned to launch Mars 94 in October 1994. This mission consisted of 2 Phobos type spacecraft including 2 orbiters, landers, penetrators, balloons and a Mars rover. Due to political upheaval in the USSR this mission slipped to a 1996 launch with only one spacecraft. It was hoped to fly the balloon and rover on a later mission. Unfortunately the Mars 96 spacecraft failed to leave earth orbit after its launch on November 16th 1996 and returned to earth early the following day. The Americans continue their study of Mars with the Mars Global Surveyor, an orbiter which will achieve its operational Mars orbit in early 1998 and Mars Pathfinder, a lander carrying a surface rover which landed in July 1997, returning new images of the Martian surface from the Ares Vallis region of Mars. Table 1-1 shows a summary of missions. It should be noted that many Russian spacecraft were not named until successfully launched and these have been called 'Mars' in the table.

Name	Country	Launch	Comment
MARS	USSR	10/10/60	Failed to achieve Earth Orbit
MARS	USSR	14/10/60	Failed to achieve Earth Orbit
MARS	USSR	24/10/62	Failed to leave Earth Orbit
MARS 1	USSR	1/11/62	Failed before mid-course correction
MARS	USSR	4/11/62	Failed to leave Earth Orbit
MARINER 3	USA	5/11/64	Failed to achieve Earth Orbit
MARINER 4	USA	28/11/64	First successful fly-by, 21 pictures returned
ZOND 2	USSR	30/11/64	Passed within 1500km but failed before encounter
MARINER 6	USA	24/2/69	Flyby probe returning 75 pictures and other data
MARINER 7	USA	27/3/69	Flyby probe returning 126 pictures and other data
MARS	USSR	27/3/69	Failed to achieve Earth Orbit
MARINER 8	USA	8/5/71	Failed to achieve Earth Orbit
COSMOS 419	USSR	10/5/71	Failed to leave Earth Orbit
MARS 2	USSR	19/5/71	Returned data from orbiter but not lander
MARS 3	USSR	28/5/71	Returned data from orbiter, lander failed on surface
MARINER 9	USA	30/5/71	Mars orbiter, returned 7000 pictures
MARS 4	USSR	21/7/73	Failed to achieve orbit, returned fly-by data
MARS 5	USSR	25/7/73	Returned some data from Mars orbit
MARS 6	USSR	5/8/73	Mars fly-by, lander returned 150s of data from descent
MARS 7	USSR	9/8/73	Mars fly-by, lander failed to enter Martian atmosphere
VIKING 1	USA	20/8/75	Mars orbiter returned pictures and data, first successful Mars lander returned pictures and data
VIKING 2	USA	9/9/75	Both orbiter and lander returned pictures and data
PHOBOS 1	USSR	7/7/88	Failed to achieve Mars orbit
PHOBOS 2	USSR	12/7/88	Failed on 18th April 1989 after 57 days in orbit
MARS OBSERVER	USA	25/9/92	Failed just prior to insertion orbit
MARS G. S.	USA	6/11/96	Reached Mars in September 1997
MARS 96	RUSSIA	16/11/96	Failed to leave Earth orbit
MARS PATHFINDER	USA	2/12/96	Reached the Martian surface on 4th July 1997

Table 1-1. Summary of missions to Mars.

1.2 The Martian Magnetosphere

Despite the number of spacecraft that have been to Mars, relatively little is known about the interaction of the planet with the solar wind. Many good reviews of the situation at Mars do exist however (*Intriligator and Smith*, 1979, *Russell*, 1980, *Schunk and Nagy*, 1980, *Vaisberg and Smirnov*, 1986, *Hunten et al.*, 1986, *Luhmann and Brace*, 1991, *Slavin et al.*, 1991, *Vaisberg*, 1992a, *Vaisberg*, 1992b). If Mars has a small intrinsic magnetic field, it is possible that the interaction is similar to that found at Earth and Mercury, where an almost impenetrable magnetospheric boundary deflects the solar wind around the planet. The other possibility is a Venus-like scenario, where a well developed ionosphere acts as the obstacle to the solar wind flow. Whatever the interaction, the size of the planet and lack of substantial atmosphere will mean that it will show major differences to magnetospheric interactions elsewhere in the solar system. The study of the interaction of Mars with the solar wind is not only of scientific importance in itself but also sheds light on other areas of planetology. Firstly, properties of the Martian atmosphere as measured by Viking, and its evolution are affected by the Mars-solar wind interaction (*Perez-De-Tejada*, 1992, *Luhmann and Bauer*, 1992). A study of any magnetic field present at Mars has implications for the likelihood of an intrinsic magnetic field and hence the existence of a liquid core (*Intriligator and Smith*, 1979, *Russell*, 1980). Mars is expected to have a core size comparable to Mercury and a field strength between that of Mercury and Earth would be expected if a dynamo persisted.

In this chapter the present theories for the solar wind interaction at Mars are compared in light of the spacecraft data available, especially from the recent Phobos missions. This will then highlight the importance of the plasma package of instruments aboard the Soviet Mars96 mission, and also the importance of the orbit, enabling measurements to be made below 1000km at the subsolar point. Before presenting the experimental data from previous missions the theoretical nature of the interaction will be discussed.

1.2.1 The solar wind at Mars

The solar wind is a stream of energetic charged particles, mainly protons and electrons, being ejected from the sun into the interplanetary medium. The expansion is near radial and reaches speeds up to 900kms^{-1} at 1 AU although the average solar wind speed at this distance is ~400 kms^{-1}. The Sun's magnetic field is also transported into the interplanetary medium becoming the interplanetary magnetic field or IMF. Due to flux-freezing the magnetic field is wound into a spiral so that when it interacts with an obstacle it is a predominantly E-W field arriving at the 'hosepipe' angle for that radius. This angle is dependent on the solar wind velocity but in average solar wind conditions at 1 AU the field varies from about 1-30nT with

B at about 50° to the Earth-Sun line (*Parks*, 1991). As the distance to the obstacle increases from the Sun the angle gets closer to 90° to the sun direction. The geometry of the solar wind at Mars is shown in Figure 1-1. The solar wind parameters, as predicted by a simple model of the quiet solar wind, for Venus , Earth and Mars are shown in Table 1-2 (*Schunk and Nagy*,1980).

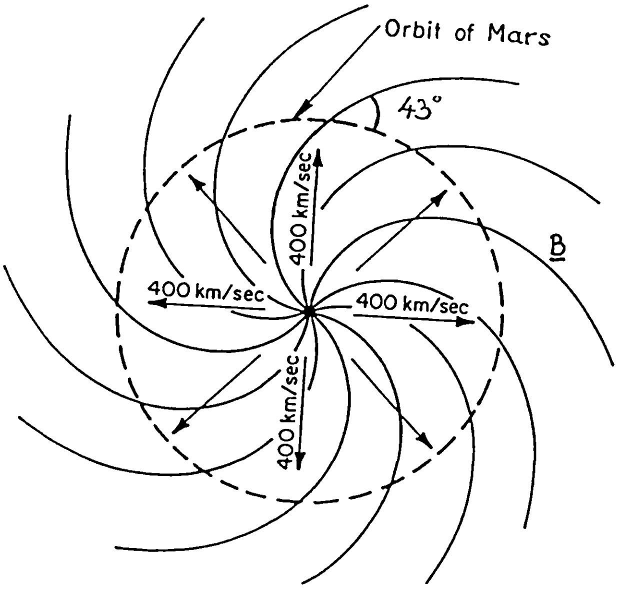

Figure 1-1. Diagram of the Parker Spiral showing the incident angle of the IMF at Mars (adapted from *Kiveson and Russell*, 1995).

	Venus	Earth	Mars
Distance, AU	0.72	1.00	1.52 (average)
Distance, r/Solar radii	155	215	327
Solar Wind speed, V, km s^{-1}	281	287	294
Electron density, n_e, cm^{-3}	19.4	9.88	4.2
Electron temperature, T_e, °K	1.6×10^5	1.3×10^5	9.7×10^4
Proton temperature, T_p, °K	4.0×10^4	3.3×10^4	2.4×10^4
Interplanetary magnetic field, B, nT	8.26	5.00	3.12
Ion acoustic speed, V_S, km s^{-1}	52.5	46.9	40.6
Alfven speed, V_A, km s^{-1}	40.9	34.7	33.3
Magnetosonic speed, V_{MS}, km s^{-1}	66.6	58.3	52.5
Mach no., M_S	5.35	6.12	7.24
Alfven mach no., M_A	6.87	8.27	8.83
Magnetosonic mach no., M_{MS}	4.22	4.92	5.60
Ratio of thermal to magnetic pressure, β	1.98	2.19	1.79

Table 1-2. Comparison of solar wind details for the terrestrial planets.

As the solar wind moves away from the Sun the temperature decreases and the density decreases as the gas expands adiabatically. This is shown in Table 1-2 by the reduction in both electron and proton temperatures at Mars, and the drop in electron density.

1.2.2 The Martian obstacle

It is apparent that even for quiet solar wind conditions the solar wind is a supersonic flow at all of the planets in Table 1-2, the solar wind speed being greater than the ion acoustic, Alfvenic and magnetosonic wave speeds. Since the terrestrial planets represent hard obstacles to the supersonic flow, a strong detached bow shock is required to deflect the bulk of the incident flow around the planet. Across the bow shock the solar wind is decelerated to subsonic speeds, and heated as the energy of the directed motion is converted into thermal energy. For Venus the interaction with the solar wind flow is ionospheric. At Earth the interaction is magnetospheric in nature, the intrinsic magnetic field acting as an obstacle within the flow. Three types of theoretical obstacles encountered by the solar wind, a non-conducting obstacle, conducting obstacle and a partially conducting obstacle are considered in the following section. Planetary bodies are likely to have a conductance between the two extremes.

1.2.3 Non-conducting obstacle

A magnetic field diffuses through an object with a timescale τ_d given by:

$$\tau_d \sim \mu_0 \sigma L^2$$

where L is the size, σ the electrical conductivity of the obstacle and μ_0 is the permeability of free space. If this diffusive timescale is much less than the timescale for changes in the ambient magnetic field then the field will pass through the body unperturbed. For a field frozen in to a plasma with speed V the object sees the field change over a convective timescale $\tau_c \sim L/V$. So for a body with a low magnetic Reynolds number, i.e. $R_m = \tau_d/\tau_c << 1$, the magnetic interaction is weak. If, as in the solar wind, the flow is supersonic, although the magnetic field can easily diffuse through the body the plasma particles cannot and are absorbed. Due to this absorbtion on the upstream surface a cavity is formed behind the object and a downstream wake appears as the surrounding plasma flows into the low pressure region. This interaction is shown in Figure 1-2, a).

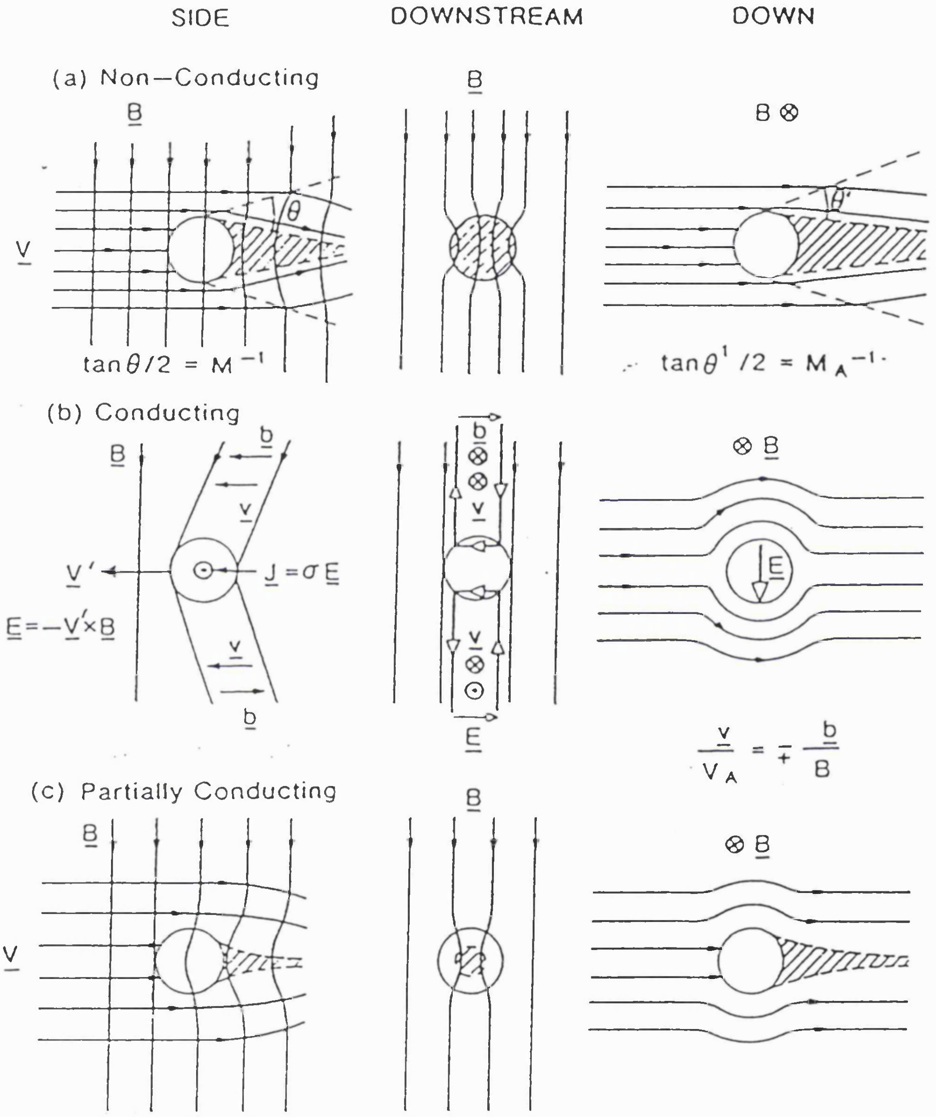

Figure 1-2. The interaction of the solar wind with a) a perfectly non-conducting; b) perfectly conducting; c) partially conducting object (*Bagenal*, 1985).

1.2.4 Perfectly conducting obstacle

When a relative motion V′ exists between a conducting body and a magnetized plasma the Lorentz electric field $\mathbf{E} = -\mathbf{V}'\times\mathbf{B}$ drives a current $\mathbf{J} = \sigma\mathbf{E}$ in the object, Figure 1-2, b). This current then perturbs the background magnetic field. Since the magnetized plasma is highly anisotropic, the parallel conductivity being much larger than the perpendicular conductivity, the current is carried away from the sides of the object along the magnetic field. In the MHD regime the plasma is also perturbed by the obstacle and in the case of a perfect conductor ($R_m >> 1$) the resulting motion of the plasma is such that there is essentially no downstream wake.

1.2.5 Partially conducting obstacle

The interaction for a partially conducting object is shown in Figure 1-2, c). In this case, some of the magnetized plasma is absorbed by the object because, unlike the perfect conductor, the background magnetic field is not deflected enough to allow all the plasma to flow around it. Hence, some of the plasma is absorbed and will be dissipated in the obstacle as Joule heating. The finite resistivity of the partial conductor means that the plasma flow, and the associated magnetic field, will be decelerated near the object. Further from the object, however, the plasma continues unperturbed, causing the magnetic field lines to become “draped” over the obstacle and forming a magnetic tail downstream.

1.2.6 Origin of obstacle

In the solar system there are two distinct types of obstacles which have being observed and studied in detail. The first, characteristic of Earth and Jupiter, is where the solar wind is held off by the intrinsic magnetic field of the planet. At the other extreme is Venus where the obstacle is formed by the atmosphere or ionosphere of the planet, and the pressure of this alone can hold off the solar wind. It is a combination of these two effects that appears to be at work on Mars. In the following section these two well studied cases will be discussed to show how each holds off the solar wind and to see if the conditions necessary appear at Mars.

1.2.7 Object with an atmosphere

On the dayside of an object having an atmosphere, ultraviolet light from the Sun will be able to photo-ionise neutrals in the upper atmosphere. The amount of ionisation taking place determines the conductivity of the upper layers of the atmosphere (ionosphere) and thus the type of interaction with the solar wind plasma flow that occurs. Where a dense ionosphere is present and the conductivity is very high the solar wind magnetic field will be excluded and the flow diverted around the object. The boundary between the solar wind and ionosphere is known as the ionopause and is situated where the combined magnetic and ram pressure of the solar wind is balanced by the particle pressure inside the boundary (see Figure 1-3).

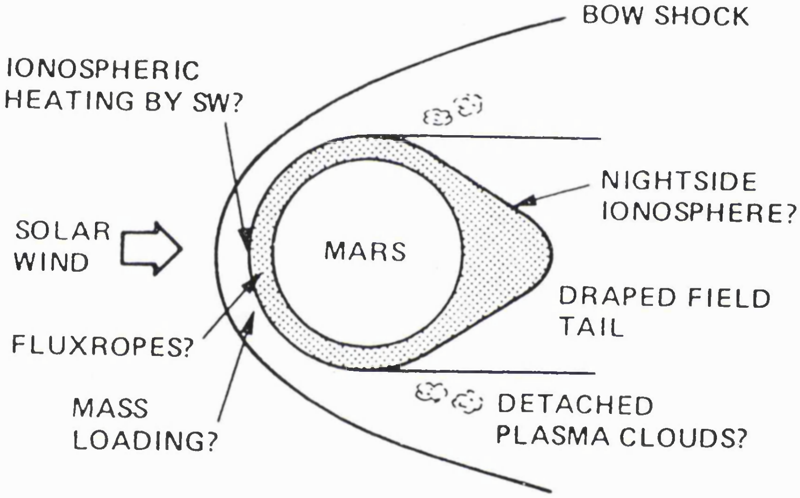

Figure 1-3. A purely ionospheric interaction with the Solar wind (*Hunten et al.*, 1986)

When the ionisation is low and the conductivity tends to zero the magnetic field and plasma are dragged through the resistive ionosphere producing a large downstream wake. Due to the relative motion to the plasma flow, any neutrals leaving the atmosphere and then being ionised will experience the Lorentz electric field. Thus, they will be accelerated up to the ambient flow rate, gaining momentum at the expense of the solar wind flow which is consequently slowed down. This process is called 'mass loading' and contributes to the draping of the magnetic field over an obstacle with a substantial atmosphere, e.g. at Venus, Titan and comets (*Bagenal*, 1985).

1.2.8 Magnetized object

In a magnetized object, the solar wind plasma is held off to a distance where the ram pressure of the external flow is matched by the Maxwell stress of the magnetic field. First proposed by *Chapman and Ferraro* (1931) the form of this interaction is given by:

$$\rho_{sw}V_{sw}^2 = \frac{B_0^2}{2\mu_0}\left(\frac{R_p}{R_{cf}}\right)^6$$

where B_0 is the magnetic dipole strength, R_p is the planets equatorial radius, R_{cf} is the standoff position, ρ_{sw} is the solar wind density and V_{sw} the solar wind velocity. Rearranging to find the ratio of standoff position to planetary radius gives:

$$\frac{R_{cf}}{R_p} = \left(\frac{B_0^2}{2\mu_0\rho_{sw}V_{sw}^2}\right)^{\frac{1}{6}}$$

This assumes that the IMF is much less than the planetary magnetic field at the standoff location (which is reasonable) and that the particle pressure inside the magnetospheric boundary is negligible which is valid for a large magnetosphere where the standoff location is well above the ionosphere e.g. at Earth. This is only a good first approximation and ignores the physical processes which may occur at a magnetospheric boundary such as electric currents formed due to reconnection processes. Actual values of the standoff distance have been found to be 1 or 2 times larger than that given by the equation above. However, to a first approximation, the magnetic field of the object deflects the plasma around it, producing a cavity in the solar wind. Generally some of the planetary magnetic field is pulled out by the solar wind into a long cylindrical magnetotail, extending far downstream of the planet. A diagram of this interaction is shown in Figure 1-4.

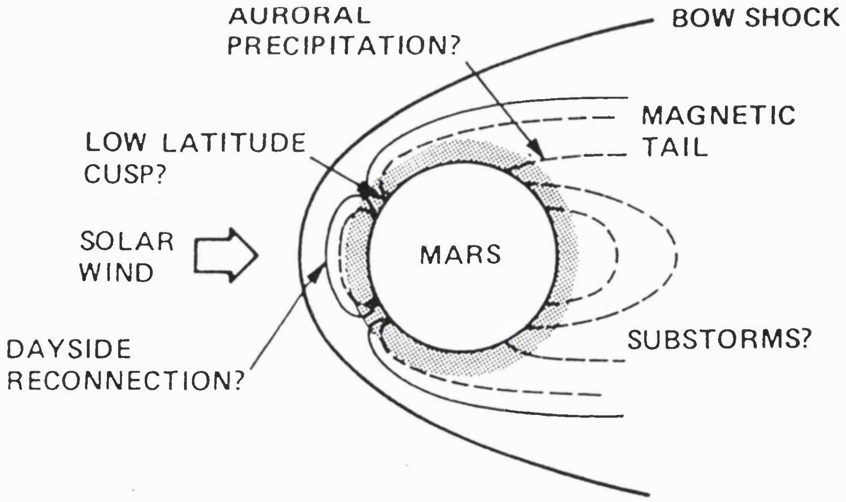

Figure 1-4. Solar wind interaction with a planet that has a significant intrinsic magnetic field (*Hunten et al.*, 1986)

1.3 Spacecraft observations of near Mars space

Having looked at the possible theoretical nature of the Martian interaction with the solar wind flow, the experimental evidence will now be considered. Out of all the attempts to study Mars so far only 13 missions have, in anyway, being successful. More surprisingly though, out of those 13 only 5 spacecraft contained any instrumentation for detailed study of the Martian plasma environment. These five are listed below in Table 1-3 showing the plasma detectors on board. The Interplanetary Plasma experiment (*Rosenthal*, 1981) and Faraday Cup experiment (*Anderson*, 1965) from Mariner 4 are not shown as they failed en route to Mars.

Spacecraft	Instrument name	Description
Mariner 4	Magnetometer	Helium Vector magnetometer (3 axis)
	LEP detectors	3 Geiger-Mueller tubes: 40keV-150keV electrons 670keV-3.1MeV protons 1 Solid State surface barrier detector: 0.5-11MeV protons
	Cosmic Ray Telescope	>40eV electrons >1MeV protons
Mars 2	Magnetometer	3 axis fluxgate, ±60nT range, 1nT resolution
	Ion Spectrometer	3° FOV(FWHM), 30eV-140eV, oriented Sunward
	Faraday cup	Electrons, ±40° FOV(FWHM), 0-400eV, antisunward
Mars 3	Magnetometer	3 axis fluxgate, ±60nT range, 1nT resolution
	Ion Spectrometer	3° FOV(FWHM), 30eV-10keV, oriented Sunward
	Faraday cup	Electrons, ±40° FOV(FWHM), 0-400eV, antisunward
Mars 5	Magnetometer	3 axis fluxgate, ±60nT range, 1nT resolution
	Ion Spectrometer	3° FOV(FWHM), 300eV-20keV, oriented Sunward
	Faraday cup	Electrons, ±40° FOV(FWHM), 0-300eV, antisunward
	Faraday cup	Ions, ±45° FOV(FWHM), 40eV-4.1keV, sunward
Phobos 2	MAGMA	3 axis fluxgate magnetometer, ±100nT, 0.05nT resolution
	FGMM	3 axis fluxgate magnetometer, ±100nT, 0.05nT resolution
	APV-F	Plasma Wave System: dipole antenna and Langmuir probe
	ASPERA	Plasma composition experiment (on a scanning platform): electrons: 1eV-50keV, 4π FOV ions: 0.5eV q^{-1}-24keV q^{-1}, 4π FOV
	TAUS	Ion spectrometer, H^+, He^{2+} and heavies, 30eV q^{-1}- 6keV q^{-1}, 40° x 40° FOV Sunward, 10° x 10° resolution
	HARP	Differential electrostatic analyser: ions and electrons: 0.2eV q^{-1}-800eV q^{-1}, 8x(10°x20°) bins facing antisunward
	SLED	Twin telescope particle-detector system: 2 solid state silicon surface barrier detectors, 30keV-3.4MeV, 40° x 40° FOV centred in the ecliptic at 55° to the west of sunward.
Mars Global Surveyor	MAG/ER	Two Triaxial Fluxgate Magnetometers: 16nT to 65526nT Electron Reflectometer: Symmetrical Quadspherical Electrostatic Analyser, FOV = 360 x 14°, 1eV to 10keV, dE/E of 0.25

Table 1-3. Summary of plasma detectors, showing selected parameters, used to study near Mars space.

As Table 1-3 shows few plasma experiments have been to Mars and little detailed data existed before the Phobos 2 mission in 1989. Unfortunately, even the amount of data from those instruments listed above is limited due to short mission spans, given in Table 1-4. Besides the data from the experiments shown in Table 1-3 other relevant data on the subject of the plasma environment of Mars has been obtained from radio occultation data from Mariners 4,6,7 and 9, Mars 2,3,4 and 5 and Viking 1 and 2 (*Kliore et al.*, 1992, and references therein), and electron density measurements during the planetary descent of the Viking landers (*Hanson et al.*, 1977, *Johnson and Hanson*, 1992).

Mission	Orbital Parameters	Closest Approach
Mariner 4	Flyby	13200km (areocentric), 3.9R_m Periapsis = 9850km
Mars 2	Apoapsides = 8R_M Period = 18hours Inclination = 48°	Periapsis = 1100km
Mars 3	Apoapsides = 62R_M Period = 12.5days Inclination = 62°	Periapsis = 1100km
Mars 5	Elliptic orbits (20) Apoapsides = 10R_M Period = 24hours 50min Inclination = 32°	Periapsis = 1170km (first orbit) Periapsis = 2000km (last orbit)
Phobos 2	Elliptic orbits (4) Apoapsides = 20R_M Period = 77hours Inclination = 0.86°	Periapsis = 866.9 to 841.3km (elliptical)
	Circular Orbits (114) Inclination = 1.26° Period = 8.01hours	Periapsis = 6144.8km (circular)

R_M = 3397km

Table 1-4. Orbital passes of Mars for spacecraft carrying plasma instrumentation.

Many of the early investigations look at the evidence for bowshock crossings in the magnetic field data and electron spectra returned by the spacecraft that have visited Mars. The position of the bowshock at Mars allows the height of the obstacle above the planet to be estimated, based on models of what has been observed at Earth, and later Venus, Mercury and comets. An estimate of obstacle height at the sub solar point (stagnation point) and a knowledge of the local solar wind conditions then give an estimate of the pressure from within the obstacle as described earlier. Where an additional magnetic pressure is required to support the ionospheric pressure, the question is then whether this is an intrinsic magnetic field on Mars, an induced field in the ionosphere or an enhancement of the interplanetary magnetic field.

1.3.1 Mariner 4

The first data on the plasma environment of Mars came from Mariner 4 and was published in *Science* in 1965. Two of these papers, *O'Gallagher and Simpson* (1965) and *Van Allen et al.* (1965), present data from the two charged particle detectors, the Cosmic Ray Telescope from the University of Chicago and the Low Energy Particle package from the University of Iowa respectively. Both of these detector systems were hoping to detect stably trapped particles in radiation belts similar to those at Earth. Both, however, found none; they also found no bursts of electron flux associated with a bowshock. Based on the fly-by distance (9850km from the planetary surface) and assuming an Earth like signature for the plasma environment, they came to the same conclusion that the magnetic moment of Mars is at most 0.1% that of the Earth ($M_E = 8 \times 10^{15}$ T m^{-3}) i.e. an equatorial magnetic field of less than 200nT at the surface. In the same journal the data from the magnetometer is also presented. *Smith et al.* (1965) report a 5nT jump in the field and a doubling of the amplitude of fluctuations possibly associated with a weak bow shock at Mars. They then assume that the interaction of the solar wind with a significant Martian dipole would produce effects geometrically similar to those seen near Earth. Therefore, scaling from the Earth parameters then gives a maximum magnetic dipole at Mars, M_M, of 3×10^{-4} M_E (2.4×10^{12} T m^3 or an equatorial field of 67nT) based on the bowshock position. Results from the plasma detector reported by *Lazarus et al.* (1967) show a broader than average energy spectrum from about 100 to 300eV when the spacecraft was inside the proposed bow shock, but, due to failure of the high voltage making the data unreliable, this data was considered indecisive for confirmation of the shock wave.

A similar model to that used by Van Allen is used by *Dryer and Heckman* (1967) and predicts that $M_M = 2.1\times10^{-4}$ M_E. *Clouthier et al.* (1970) go further and propose a simple gas-dynamic model that assumes a negligible magnetic field (less than 50nT) and a purely ionospheric interaction at Mars. *Spreiter et al.* (1970) extend their hydromagnetic theory of solar wind flow past the Earth to include nonmagnetic planets such as Venus and Mars that have a sufficient ionosphere to deflect the solar plasma around the planet. Their theory combined with available data indicates an ionospheric boundary for Mars at an altitude of between 155 and 175km. This compares well with the 130km given as the height of the peak electron density from the radio occultation data (*Kliore*, 1965). For this paper the Mariner 4 trajectory was at all times assumed to be outside any bowshock. A revised model (*Spreiter and Rizzi*, 1972), assuming that the magnetometer data did record a weak bowshock, claims a purely ionospheric model without the need to postulate a planetary magnetic field. They accept the Dryer and Heckman value for the dipole as an upper limit but state that the actual existence of such a field should not be inferred from Mariner 4 observations.

1.3.2 Mars 2 and 3

With the arrival of the Soviet Mars 2 and Mars 3 spacecraft at the red planet in December of 1971 it was hoped that the controversy of whether a planetary magnetic field exists or not would be resolved. Initial analysis of the magnetic field data from Mars 2 and Mars 3 was performed by *Dolginov et al.* (1973). They interpreted the data as showing a bowshock with a shock front at double the height inferred by *Spreiter et al.* (1970) and *Spreiter and Rizzi* (1972): this gives an obstacle height of 990km as opposed to the 170km obtained with a purely ionospheric model of the interaction. Dolginov *et al.* state that all the observations can be accounted for by an intrinsic Martian field deformed and controlled by the solar wind. They give the magnitude of this field as $2.4 \times 10^{24}\mathrm{Tm}^{-3}$ and an equatorial surface field intensity of 60nT, assuming that such a small dipole is either the remnant of a past dynamo field or that the field at Mars is undergoing a period of polarity reversal. *Gringauz et al.* (1973) used two months (4 orbits) of data from the Mars 3 Faraday cup detector, and a few orbits from the same instrument on Mars 2, to analyse electrons up to 400eV in energy. By comparison with the electron flux increase at the terrestrial bow shock they are able to confirm a shock crossing of both spacecraft, flux enhancements occurring almost simultaneously with the magnetic fluctuations. Similar analysis to that used by Dolginov *et al.* gives the same estimate for the stagnation point of the shock wave at an altitude of 2000km at the subsolar point. This indicates an obstacle height of 1000km and an equatorial field of 50-60nT. *Russell et al.* (1984) simulate the results from the Mars 3 magnetometer using a gas dynamic model without the need to invoke an intrinsic magnetic field for Mars. *Wallis* (1974) also questions the validity of the data and suggests that the observed field enhancement reported by *Dolginov et al.* could be due to local induced currents or currents shorting out polarisation fields.

1.3.3 Mars 5

It was a Soviet spacecraft that provided the next data, as the Mars 5 spacecraft arrived at Mars in early 1974. Unfortunately Mars 5 failed after insertion into its final working orbit so only 2 weeks of data from the four transitional orbits are available. *Gringauz et al.* (1976) studied data from the ion and electron retarding potential analysers and found the characteristic signature of a crossing of the bowshock into the transition region, a change of the charged particle spectra as the ions are thermalised. From values of the areocentric distance, the Sun-Mars-satellite angle when the spacecraft crossed the bowshock and gas dynamic calculations the obstacle height was estimated to be a minimum of 500km. The same author then used bowshock crossing data from all 3 Soviet Mars spacecraft to give an obstacle height of 1200 ± 800km, and cautions that the available data is not sufficient for unambiguous definition of the obstacle. Data from the tri-axial flux gate magnetometer on Mars 5 is shown for 13th February 1974 in Figure 1-5 (*Dolginov et al.*, 1976a). Mars 5 itself only made a few measurements of IMF but the sign of the field compares favourably with the conditions predicted from the conditions at earth. Dolginov *et al.* then go on to show that the direction of the measured field near Mars is independent of this predicted IMF and is therefore of magnetospheric origin. They also show that the magnetic field is dependent on the solar wind activity. Finally their new prediction for the magnetic moment of the Martian dipole is 2.4×10^{22} G cm^3, and the equatorial surface field as 64nT.

Both Gringauz and Dolginov interpret the data from Mars 2, Mars 3 and Mars 5 as suggesting an interaction between the solar wind and an intrinsic Martian magnetic field (*Dolginov et al.*, 1976b). However, two other models exist that are inconsistent with this view. In the first the field is of interplanetary origin and is compressed and strengthened behind the bow shock as seen at Venus (*Dolginov et al.*, 1968, *Bridge et al.*, 1967, *Ness et al.*, 1974). The second model (*Dessler*, 1968 and *Johnson*, 1969) suggests that the observed field is induced in the ionosphere by the electric field of the solar wind $\mathbf{E}= -(\mathbf{V}\cdot\mathbf{B})$, where $\mathbf{V}$ is the solar wind velocity and $\mathbf{B}$ is the interplanetary magnetic field. The first model was rejected by *Dolginov et al.* (1976a) after further examination of the Mars 3 data. This model would expect field enhancements to be pronounced immediately behind the bow shock, but although the bow shock crossings were clearly defined the greatest enhancements were always found at pericentre during each orbit.

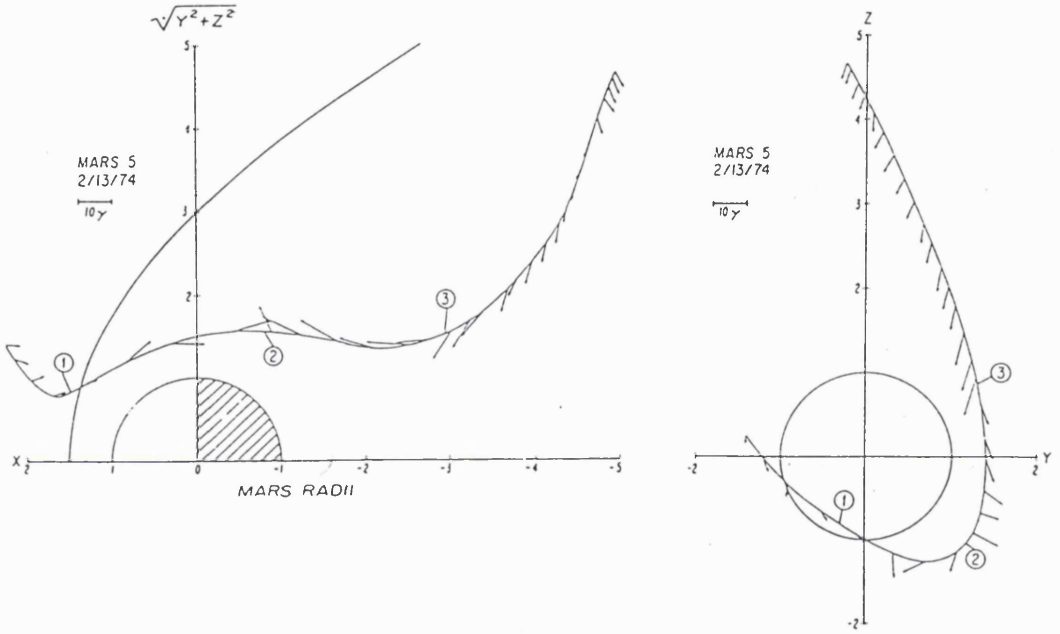

Figure 1-5. Magnetic field vector projections in solar cylindrical co-ordinates along the Mars 5 orbit on February 13, 1974.

1.3.4 Viking 1 and 2

The two Viking lander descents of 1976 provided electron density data from the upper atmosphere of Mars (*Hanson et al.*, 1977). A theoretical model of the Martian ionosphere was constructed on the basis of these measurements by *Chen et al.* (1978). *Intriligator and Smith* (1979) used this model to obtain estimates of the ion and electron number densities and temperatures in the upper ionosphere of Mars. From these they estimate the total pressure available from the ionosphere and show that it is only 0.4 of that needed to hold off the solar wind pressure at Mars. They conclude that Mars has neither a Venus-like or Earth-like interaction with the solar wind but is an intermediate case needing a magnetic field of some form to provide the additional pressure needed. The bow shock modeling method and the gas dynamic model were reviewed for all the terrestrial planets by *Slavin and Holzer* (1981), *Slavin et al.* (1983) and *Slavin et al.* (1984), confirming the assertions of *Intriligator and Smith.* Up to this point in time, however, there had been only a few bowshock crossings at Mars, especially in the downstream region, and with far from adequate sampling times. *Vaisberg and Smirnov* (1986) re-iterate this point and also introduce the idea that atmospheric neutrals may play an important part in the Martian/solar wind interaction through mass loading of the interplanetary plasma. They cite *Levine et al.* (1974) when suggesting helium, produced by radiogenic decay, may be the most important constituent of the upper atmosphere when considering a cometary type interaction. *Shingawa and Cravens* (1989) present a new one dimensional multispecies magnetohydrodynamic model of the dayside ionosphere of Mars. They conclude, tentatively, that their results show that the solar wind-Mars interaction is analogous to the solar wind-Venus ionospheric interaction under highly magnetized conditions and that the intrinsic field is very small ($B \leq 30nT$) and does not play a major role. It should be noted here that data from the radio occultation observations of the Martian ionosphere do not show any evidence of the variability that would be expected if there were a direct solar wind interaction with the ionosphere (*Schunck and Nagy*, 1980).

1.3.5 Phobos 2

No spacecraft were to go to Mars for thirteen years after the launch of Viking until the Soviet Union launched Phobos 1 and 2 on the 7th and 12th of July 1988. Unfortunately contact with Phobos 1 was lost after just a few weeks during the trip to Mars and Phobos 2 was left to carry out the scientific programme. Unfortunately, although successfully reaching Mars and completing several manoeuvres to bring the spacecraft close to the largest satellite of the planet, Phobos, the spacecraft was lost as it attempted to change orientation to image the Martian moon. Before contact was lost on 27th March Phobos 2 had completed five 80 hour elliptical orbits and over a hundred circular orbits at the altitude of Phobos, 6145km (*Sagdeev and Zakharov*, 1989). Phobos 2 was a well equipped spacecraft for studying all aspects of Mars, Phobos and their space environment, so despite the mission ending prematurely a wealth of new data was produced by the package of eight plasma instruments outlined in Table 1-3.

Initial results from the magnetometer data (*Riedler et al.*, 1989) confirmed the bowshock position at the lower end of the range of previous predictions, putting the height of the planetopause at 400km above the Martian surface. The elliptical orbits of Phobos 2 around Mars placed the spacecraft directly behind the planet in the tail and here it was found that the magnetic field, as at Venus, was controlled by the IMF (*Yeroshenko et al.*, 1990, *Zhang et al.*, 1991). Later, *Riedler et al.* (1991) clarify that the IMF dependence of the tail lobes at 2.8 R_M, where the measurements were taken, suggests an induced character of the tail field outside that distance. They do concede, however, that there are certain features in the magnetic field data which could be interpreted as traces of an intrinsic field. This is a reference to the work by *Mohlmann et al.* (1991) who use time series analysis to identify 8, 12, and 24 hour peaks in the FGMM and MAGMA data, suggesting a co-rotating component to the field. The assumption is that the main periodicity is of 24 hour with harmonics at 12 and 8 hours, however, the fact that the amplitudes of the harmonics are larger than the basic period questions this assumption. *Russell et al.* (1992) explain these periodicities by showing that a 24 hour peak can be produced in an idealized time series containing obvious features of the solar wind interaction but no intrinsic field effects and that the 8 hour periodicity is expected from the orbit.

Grard et al. (1989) report on the first electric field measurements made at Mars by the plasma-wave system on board Phobos 2. Both the Langmuir probe data and the wave data identified shock foot crossings consistent with a model summarising earlier measurements of the bowshock at Mars. This data also showed that the plasma density was variable on a daily basis and on the third orbit a density, comparable to the Viking retarding potential analyser measurements (taken at 300-350km), was measured at periapsis (860km).

Particle data from the Phobos 2 mission was provided by four instruments: ASPERA, TAUS, HARP, and SLED. Data from ASPERA (*Lundin et al.*, 1989) shows ionospheric plasma escape for the first time, although some heavy ion outflow is suggested for differences in ion spectra measurements on Mars 5 (*Vaisberg et al.*, 1976). It is found that the composition of the ionic outflow is consistent with the cold-plasma composition in the topside ionosphere as measured by Viking, and that oxygen ions, accelerated to several keV, dominate. These high speed tailward flows, discovered deep inside the tail, a region not preciously investigated, were also seen by the TAUS instrument (*Rosenbauer et al.*, 1989). Lundin *et al.* and Rosenbauer *et al.* both believe that these auroral ion beams are responsible for an oxygen loss of approximately 3×10^{25} ions s^{-1}. This corresponds to an evacuation of the present total atmospheric oxygen content of Mars, bound in CO_2 and O_2, in less than 100 million years. Figure 1-6, taken from *Verigin et al.* (1991) shows heavy ion spectra as the spacecraft passed through the tail region on one of the circular orbits.

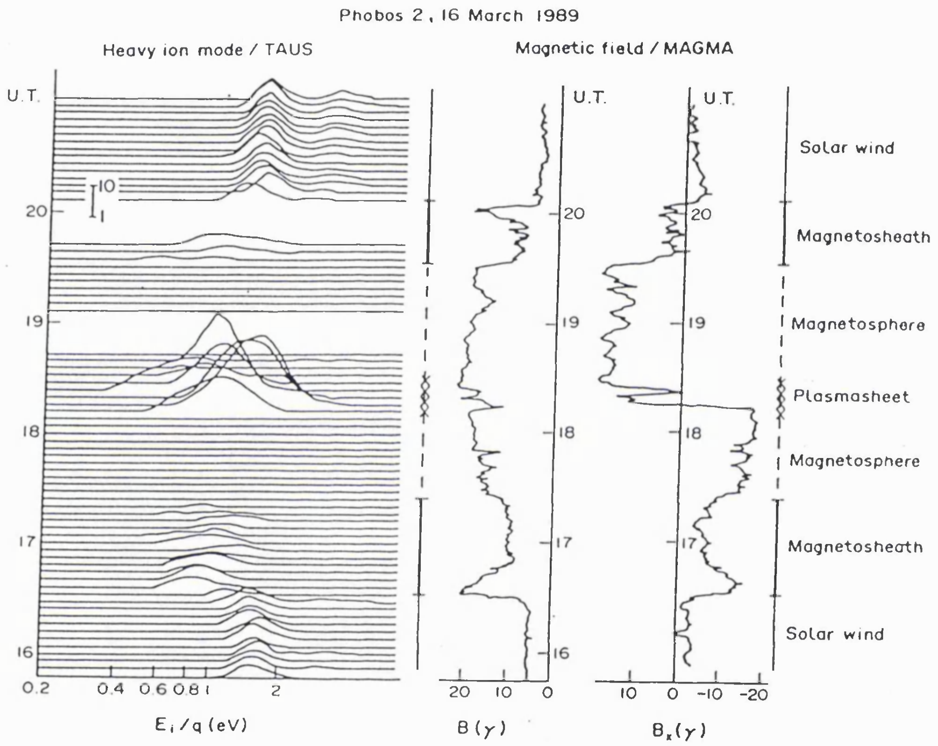

Figure 1-6. Four minute averages of energy spectra on 16 March 1989 from the TAUS instrument. The different space regions are labelled alongside the magnetometer data from the same period.

ASPERA proton measurements are also used by *Dolginov and Zhuzgov* (1991) to identify what they interpret as the Martian magnetosphere boundary. Figure 1-7 shows a plasmagram from February 8 1989; a shock front crossing can easily be identified and as the spacecraft moves closer to the planet the particle density decreases slowly before dropping to the counting limit of the instrument. This effect is consistent with magnetospheric boundary crossings at Earth.

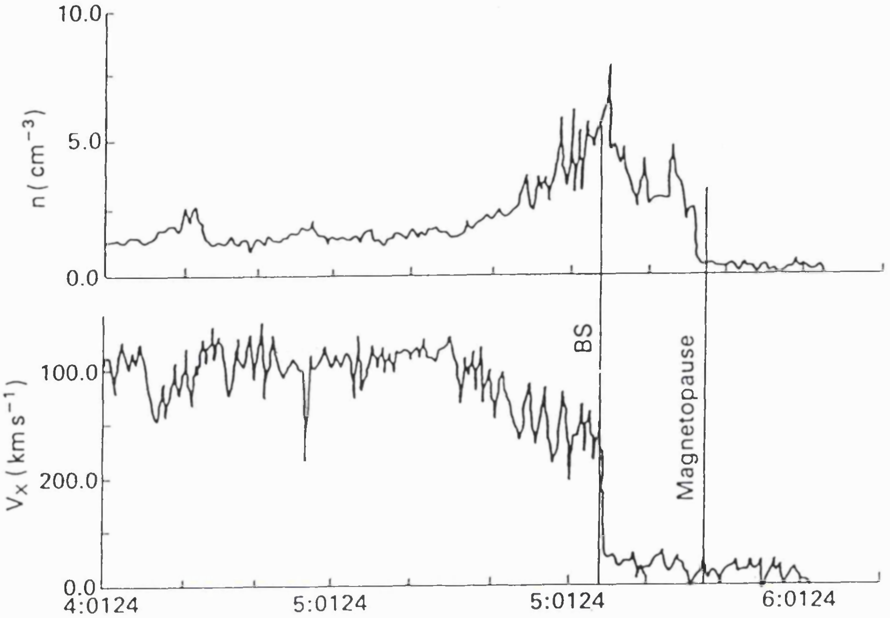

Figure 1-7. Plasmagram of changing density (n) and radial velocity (V_x) of protons measured aboard PHOBOS-2 with the ASPERA instrument on February 8 1989 (from *Dolginov and Zhuzgov*, 1991)

The importance of a mass discriminating ion analyser for plasma studies is again demonstrated by *Barabash and Norberg* (1994) and *Barabash et al.* (1995) who use the ASPERA data to show the existence of a Martian Helium corona.

Another first for Phobos 2 was the discovery of the plasma sheet with accelerated electrons in the inner magnetotail measured by the HARP instrument (*Shutte et al.*, 1989). Similar electron spectra were also detected in the magnetosheath indicating that the plasma processes involved are probably similar in nature. Telescope 1 of the SLED instrument found evidence for a zone of enhanced radiation inside the Martian environment, at an altitude of less than 900km (*Afonin et al.*, 1989). If Mars has an intrinsic magnetic field and a true magnetosphere these observed enhancements could represent a trapped ion population (30-350keV) similar to the inner Van Allen belt at Earth.

Finally, *Trotignon et al.* (1996), from measurements made by the TAUS, PWS and ASPERA instruments, conclude that Mars does not seem to possess any consistent intrinsic magnetic field and the magnetic moment of a possible dipole field is not believed to exceed 2.2 T m^3, that is to say about 1000 times less than at Earth. This is within 10% of the original estimates from *Van Allen et al.* (1965) and *O'Gallagher and Simpson* (1965). Although the estimates for the Martian dipole field may have remained the same, PHOBOS has given a clue to the complexity of the Mars - Solar wind interaction.

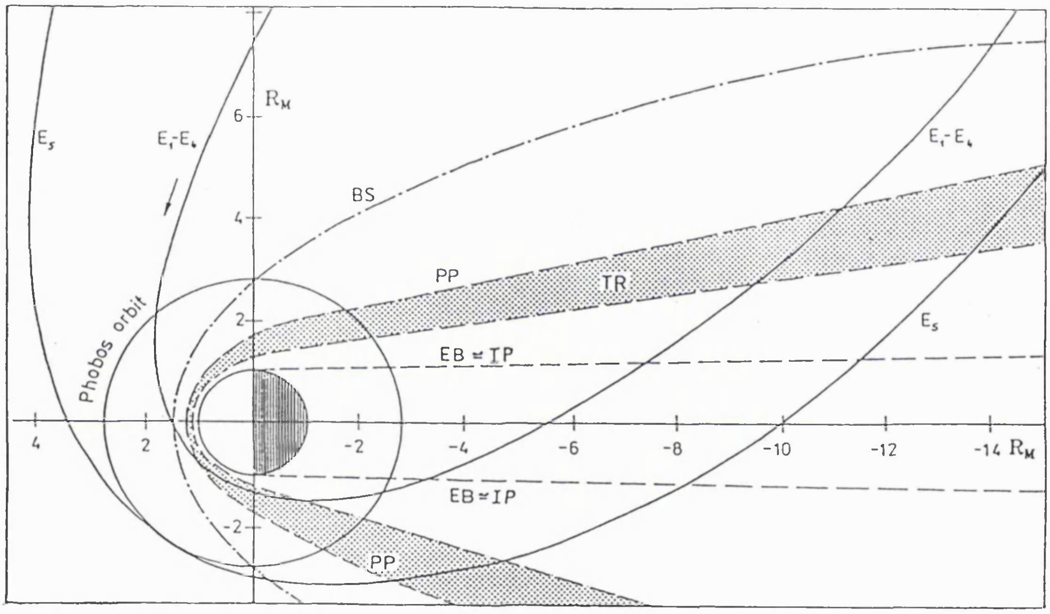

Figure 1-8. PHOBOS spacecraft trajectories projected onto the x-y Martian orbital plane. The plasma boundaries and layers, bow shock (BS), planetopause (PP), transition region (TR), eclipse boundary (EB), and orbit of Phobos are shown (from *Sauer et al.*, 1992).

1.3.6 Mars Global Surveyor

Although no data have yet been published a press release from NASA reports that a stronger than expected magnetic field of planetary origin was collected on 15th September 1997 (*Acuna*, 1997). This was seen at periapsis which was 150km above the surface of the planet for this highly elliptic orbit. Mars Global Surveyor will continue aerobraking until it attains a circular orbit just 378km above the Martian surface in early 1998.

1.4 The Mars96 Mission

Mars96 is part of Russia's long-term space programme dedicated to the study of the planet Mars. The primary objectives of the mission are to investigate the evolution and present-day geophysical, chemical, geological and atmospheric states of the planet and its interaction with the interplanetary environment. The payload of the Mars96 spacecraft includes 23 scientific instruments on an orbiter, 2 penetrators and 2 small stations. The launch of Mars96 took place in November 1996 but ended in disaster when the second stage failed to boost Mars 96 out of Earth orbit. Less than 4 hours after launch the spacecraft re-entered the atmosphere and landed in the Pacific ocean off the coast of Chile. The mission plan, however, was that after the 11 month transit the spacecraft would perform an elliptical transfer orbit before settling into the final Mars working orbit (*Zakharov*, 1994). The working orbit was planned to have had a period of 43 hours, an inclination of 106.13° and a pericentre of approximately 300km taking the Mars 96 spacecraft close enough to the planet to pass through the solar wind obstacle.

The FONEMA (Fast Omni-directional Non-scanning Energy Mass Analyser) instrument was one of a package of plasma instruments included on the orbiter payload to study the solar wind interaction with Mars (*Vaisberg et al.*, 1990). Mullard Space Science Laboratory (MSSL) was the Principal Investigator institute for the FONEMA instrument which was constructed in collaboration with the Institute of Space Science (IKI) in Russia, the Faculty of Mathematics and Physics, Charles University (MFFUK) in the Czech Republic, Centre d'Etude Spatiale des Rayonnements (CESR) in France, Spacecraft Technology (Ireland) Ltd (STIL) and the Special Design Bureau of the Soviet Academy of Sciences (OKB) in Bishkek, Kirghizia. FONEMA was to study the structure, dynamics and origin of the plasma population of near-Mars space by measurements of three dimensional distribution functions of hot ions with a high time resolution in the energy range from 20eV to

8keV. The accommodation of the FONEMA instrument on the extreme end of one of the solar panels of the Mars96 spacecraft is shown in Figure 1-9.

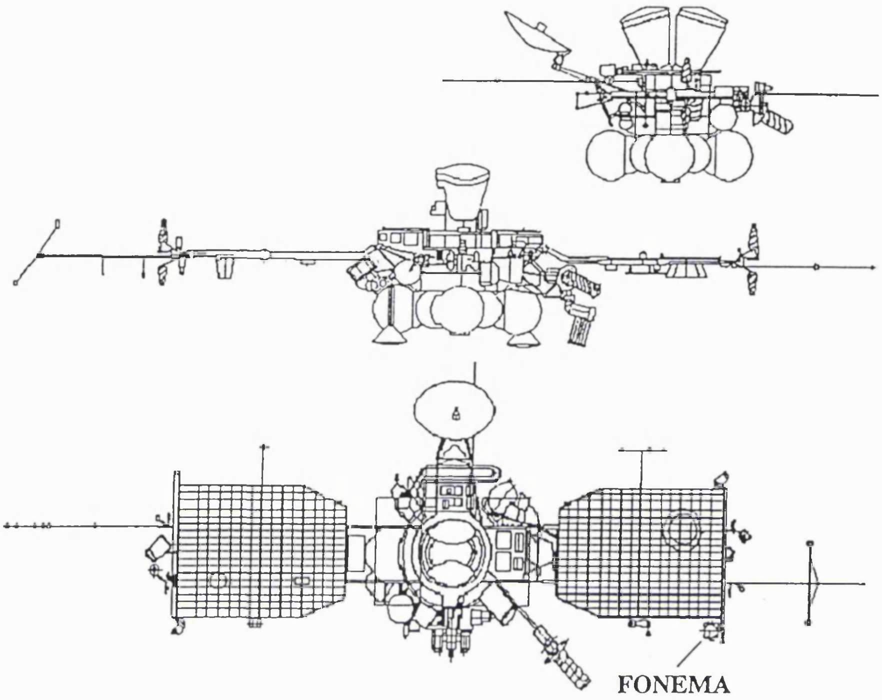

Figure 1-9. Mars 96 spacecraft showing accommodation of FONEMA

1.5 Why FONEMA?

The measurement of the ion velocity distribution function, with mass selection, requires four-dimensional measurements. Existing 3D plasma analysers have to scan sequentially in at least two of these dimensions, leading to relatively long sampling times and the time-aliasing of measurements. We have developed a new approach in which the ion spectrometer consists of a compact array of 36 energy mass analysers, based on the Thomson parabola analyser with **E** parallel to **B**, each one operating within a specific solid angle and together giving a total angular coverage of almost 4π steradians. Each analyser produces a two dimensional image of approximately energy versus mass. The instrument is able to make truly simultaneous measurements of the complete 3D distribution functions of several ions in the energy range from 20eV to 8keV. These distributions are obtained with a sensitivity large enough to provide temporal resolution as short as 125ms and to separate the major mass species. This sampling rate is a factor of 16 faster than any current 3D plasma analyser and becoming comparable with the sampling rate used by magnetometers. Since the instrument is designed to operate on a 3-axis stabilised spacecraft it is decoupled from the spinning motion.

With the proposed spacecraft orbit, FONEMA would have been able to detect the main known plasma populations, i.e. The solar wind, including alphas and oxygen, shocked solar wind, hot plasma "cushion", boundary layer, mass-loaded ions, tail fluxes and pick-up ions from the Martian exosphere and the interstellar gas. It will also be able to detect any significant new populations which may be encountered in the regions so far unexplored. More precisely FONEMA is anticipated to provide with the following results:

The origin of the Martian magnetosphere:

Velocity distribution functions of each ion species from FONEMA would have allowed the plasma sources to be identified, those in regions controlled by an intrinsic magnetic field or by mass loading should be easily identified. In conjunction with the magnetic field data and the electron component it would have allowed study of the structure, dynamics and origin of the magnetosphere.

The solar wind - Mars interactions:

FONEMA would have been able to detect the bowshock and the major boundaries within the Martian plasma environment. The bowshock crossing is easily distinguished by a sharp decrease in the radial velocity and a peak in the proton number density from plasmagrams shown in Figure 1-7 (*Dolginov and Zhuzgov*, 1991). As mentioned previously this also shows the decrease in density and sharp drop associated with the spacecraft passing through the transition region and then crossing the magnetopause.

Upstream region:

Solar wind deceleration upstream of the Martian terminator bow shock was recorded by the TAUS instrument on PHOBOS (*Verigin et al.*, 1991, *Zhang et al.*, 1997). These data were observed during all of the elliptical orbits and most of the circular orbits. The deceleration has been attributed to the mass loading by the ions originating from the hot oxygen/hydrogen corona of Mars and protons specularly reflected from the bow shock. A detailed investigation of the underlying microphysical processes is described by *Szego et al.* (1997). FONEMA's fast temporal resolution, combined with mass analysis, would have provided diagnostics of processes in the bowshock and of the possible importance of atmospheric ions in its formation, especially the effects of mass loading by oxygen/hydrogen ions of Martian origin. Mars 96 orbits were planned to allow bowshock crossings over a wide range of positions, especially on the dayside, allowing measurement of the importance of these effects at different latitudes and local time. High energy particles and accompanying wave activities are frequently found in the upstream region of planets. It is unclear whether these are due to Fermi acceleration at the bowshock or due to magnetospheric processes. Mars, with a weak magnetic field, provides an interesting environment in which to study these processes and hopefully improve current understanding of the acceleration process.

Magnetosheath:

Dubinin et al. (1997) have described the magnetosheath as a region characterised by strong coupling between solar wind protons and planetary ions. On the basis of measurements from the ASPERA instrument they have identified two transition boundaries in addition to the bowshock. The outer transition, called the 'heavy ion discontinuity' (HID), occurs when the mass density of the solar wind protons is matched by the mass density of the planetary ions, the discontinuity arising as a result of differential streaming of the two populations. The inner transition, or 'ion composition boundary' (ICB), occurs when the density of O^+ ions is approximately equal to the number of protons and separates the proton magnetosheath and the boundary layer populated mainly by planetary plasma. Inside the magnetopause boundary *Lundin et al.* (1990b, 1991) found that the density ratio O^+/H^+ exceeds unity. However, measurements at below 400eV using the HARP instrument on PHOBOS 2 did not indicate additional sharp boundaries (*Shutte et al.*, 1997). *Dubinin et al.* (1996) proposed a more structured transition layer with 'shock-like' structures. They go on to say that the 'striated shape of the surface indicates that the complicated structure of the sampling time of ion composition scans was not enough to resolve the structure of the transition'. The full 4π coverage of FONEMA combined with the fast time resolution would have allowed further investigation into these poorly understood regions.

The evolution of the Martian atmosphere:

The supply of matter from the solar wind, either as ions or fast neutrals, and the removal of atmospheric gases due to atmospheric heating by external sources and other solar wind induced processes, can be important in the evolution of the planetary atmosphere. These processes may provide important clues to atmospheric origins and evolution on all planets. The ASPERA instrument on PHOBOS found oxygen ions escaping from two main regions, as pick-up ions in the boundary layer and through the plasma sheet in the tail (*Lundin et al.*, 1990a, 1991). Oxygen flows from both regions were also seen in the TAUS data (*Verigin et al.*, 1991). As mentioned in a previous section ASPERA measurements also revealed the presence of planetary helium ions at Mars (*Barabash et al.*, 1995). Again, these observations are limited to three elliptical orbits and many circular orbits at the height of Phobos. Mars 96 orbits would have allowed extensive coverage of the tail region at different positions.

Exosphere of Mars:

The variation of flux of pick-up ions along an orbit reveals the height distribution of the neutral gas. This data used in conjunction with a model of the exosphere can help determine the density and temperature data at the base of the exosphere. Predictions of a hot oxygen corona at Mars from such a model were decribed by *Ip* (1988). The relative importance of solar activity to the exosphere can be determined by studying temporal variation in these parameters.

Hydrodynamic and kinetic instabilities:

These instabilities are important aspects of the physics of the bowshock, pick-up processes, anomalous ionisation processes and the transport of plasma near the magnetopause. FONEMA would have allowed simultaneous measurements on a large section of distribution functions of different ion species and so determine the specific parts of the velocity distribution functions that interact with the observed waves.

Plasma transport:

How is the transport of mass and energy controlled within the Martian environment? What is the role of field aligned currents, plasma convection, ionospheric outflow and does the conductivity of the Martin ionosphere affect the dynamics of the outer magnetosphere? These subjects have been studied using the limited PHOBOS data but more measurements from the Mars 96 spacecraft would have proved invaluable in determining the nature of these processes.

Cruise phase measurements:

In the cruise phase, about a month after launch, the Mars 96 spacecraft would have passed through the Earth's magnetic tail at a downstream distance of approximately 1000 Earth radii. This would have been the first time that plasma instruments had been able to observe the tail at such a large distance and would have given new insights into the way that the tail is modified at these distances. FONEMA would have also made measurements in the solar wind on a regular basis during the flight to Mars. These measurements would have looked for high frequency fluctuations in the solar wind parameters.

In summary, there are many interesting questions to be answered about the interaction between Mars and solar wind. From trying to find the answer to these problems a great deal can be learnt about the solar wind, the ionospheric/magnetospheric interaction and plasma processes in general. In order to solve these problems a suite of plasma instruments such as proposed for the Mars 96 mission is needed, and FONEMA forms an integral part of any such package.

2. The FONEMA instrument

2.1 Introduction

In the early exploration of space, measurements of the plasma environment within the inner solar system were limited to looking at high energy electrons, ions (with no mass discrimination) and the magnetic field topology. The earliest particle measurements were made at energies in excess of 1MeV for electrons and 30MeV for ions using detectors originally developed for the measurement of cosmic rays. With the discovery of the solar wind in 1962 it became clear that lower energy particles play a major role in the origin, transport, acceleration and loss processes of plasma populations, which led to the development of lower energy instruments. The recognition that heavy ions often have a similar abundance to protons in planetary plasma environments and that observation of different masses could provide clues to the source of the plasma populations led to the development of mass spectrometers.

In the plasma regions studied in space the shortest characteristic length is the Debye length, which, within the outer magnetosphere and plasma sheet is of the order of 10 meters. The largest plasma instruments flown are only of the order of 10cm, hence, the length scale of the instruments is much shorter than any characteristic length scale of the plasma, so the plasma will appear as merely an assemblage of non-interacting charged particles, without the collective behaviour generally assumed of a plasma (*Vasyliunas*, 1971). In this sense then plasma instruments flown aboard spacecraft can be viewed as conventional charged particle beam detectors. In this chapter the major types of plasma detectors are presented and their respective advantages and disadvantages discussed. This introduction draws from the many good reviews of the field of space plasma measurement which have appeared in the literature: *Vasyliunas* (1971), *Steckelmacher* (1973), *Balsiger* (1982), *Wilken* (1984), *Bame et al.* (1986), *Young* (1989) and *Gloeckler* (1990). Finally the FONEMA instrument will be introduced and the operation and major components highlighted.

2.2 Plasma measurement techniques

There are three main types of particle detector: those employing electrostatic and/or magnetic fields (E/B), time-of-flight (TOF) detectors and solid state detectors (SS). Generally, type I detectors (E/B) are only sensitive to ionic particle parameters such as energy/Q or mass/Q, with Q denoting ionic charge. Type II (SS and TOF) can measure charge Z and atomic number, therefore a combination of both detection principles is required to fully characterize an ion. 25 years ago there was a gap in the measurable energy range between the solid state detectors that could only see energies in excess of about 500keV/Q and deflection type spectrometers with an upper limit of approximately 20keV. Recent developments in solid state detectors have reduced this gap. The energy range of FONEMA is chosen so that solar wind protons and alphas can be recorded over a wide range of solar wind conditions and that lower energy ionospheric ions can be seen as they are accelerated up to the solar wind velocity. The following discussion will include only those detectors that operate in a similar energy range to FONEMA, i.e. 20eV up to 8keV.

2.3 Field based analysers

To a large extent space borne plasma analysers of all kinds have developed to make use of advances in the final detection device or electronics. It was only with the development of Channel Electron Multipliers (CEM) that individual particles could be counted. Even then no-one was particularly interested in developing non-scanning analysers outside the laboratory because of the problems in producing a space qualified one dimensional spatially resolving detector although some instruments used arrays of individual CEMs e.g. the AMPTE IRM plasma instrument (*Paschmann et al.*, 1985). Similarly it was only the development of suitable two dimensional MCP based detectors that allowed the development of instruments offering simultaneous measurements of two parameters. Currently, individual CEMs or MCPs make up almost all of the detecting systems used in ion detectors operating at energies less than 20keV. The exception to this is the Faraday cup detector which measures ion current directly.

2.3.1 Electrostatic only

2.3.1.1 Retarding Potential Analyser (RPA) and oscillating field RPA

The first observations of extraterrestrial plasma were carried out by *Gringauz et al.* (1961) using a very simple probe. Basically a collector plate is placed behind a grid which has a retarding potential applied to it. Ions whose energy per unit charge exceeded the potential on the retarding grid would reach the collector and a measurement of the current between the two grids then indicated the flux. This current measurement, however, is not possible when the instrument faces toward the sun. In this situation a photoelectric current of the order of 10^{-8}Acm^{-2} is emitted from the collector grid. Although this photocurrent is easily suppressed by placing another grid in front of the collector and biasing it a few volts negative with respect to the collector, there remains a reverse photocurrent produced by light reflected from the collector onto this suppressor grid. This current can be up to one tenth the direct current and would invalidate all but the highest current densities produced by solar wind particles. Despite this drawback these instruments were used extensively for ionospheric research (*Knudsen*, 1966). *Bridge et al.* (1960) overcame this difficult by modulating the plasma current, using an alternating electric field without modulating the photocurrent at the same time. The basic form of this instrument is shown in Figure 2-1. *Hanson et al.* (1977) successfully used oscillating RPAs on the descent of the VIKING landers to measure the ion concentration through the ionosphere of Mars.

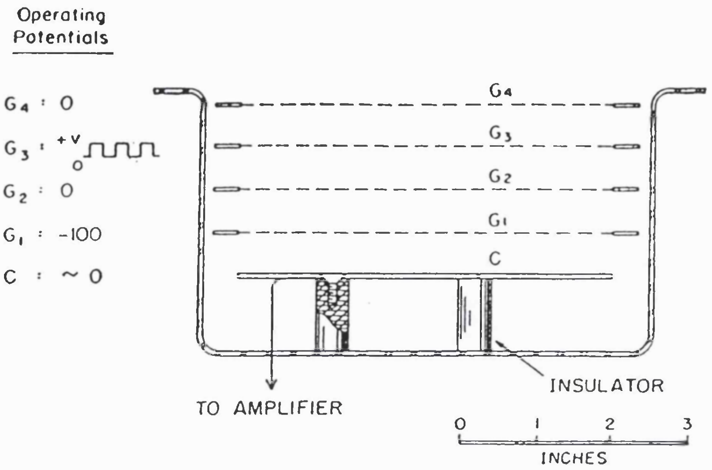

Figure 2-1. Schematic diagram of the modulated-potential Faraday cup (from *Bridge et al.*, 1960)

Normal retarding potential analysers were improved upon by *Hays and Sharp* (1973) with their hyperbolic analyser of the retarding potential type (HARP). This instrument is gridless and uses three electrodes to produce a rotationally symmetric quadropole field. This is arranged so that for a fixed potential only particles of an appropriate value of energy, position and direction will reach the detector (normally a CEM). The details of its operation are explained by *Shyn et al.* (1976). A number of these instruments in a fan arrangement were used on the HARP instrument flown on the Phobos mission (*Szucs et al.*, 1990), see Table 1-3 in Chapter 1. The integration period at each energy step was approximately 1s and a full distribution would take 75s to acquire. More recently a variation on the retarding plate analyser with very good energy resolution has been developed at MSSL (*Papatheodorou et al.*, 1996). The drawback of all forms of retarding potential analysers is that they require the full volts equivalent of the energies that they are to detect.

2.3.1.2 Curved plate analyser

The curved plate analyser forms the basis of most energy/charge stages of modern ion spectrographs. An early example of a space-borne instrument of this type is described by *Bader* (1962). *Neugebauer and Snyder* (1966) used such a device on Mariner 2 for the first detection of the solar wind flow. The nested analyser plates are sections of either cylindrical or spherical geometry. A field is applied between the plates such that the deflection of an ion of the correct energy/charge moves in a trajectory matched to the geometry of the plates. A suitable collector is placed at the output of the analyser. The advantage of the curved plate analyser over the simple retarding plate analysers is that the deflection voltage needed is only a fraction of the particle energy being detected. More recently the Giotto 3-dimensional positive ion analyser used curved plate analysers in two different ways (*Johnstone et al.*, 1986). Firstly the Johnstone Plasma Analyser uses a hemispherical electrostatic analyser followed by a quadrispherical angular dispersion sector to measure ions in the energy range from 0.01-20 keV/q over a 5° by 160° field of view. The aperture is arranged so that a full spacecraft spin in 4s allows almost full sky coverage. Secondly the Implanted Ion Sensor combines spherical electrostatic plates with TOF detectors in five separate analysers. This instrument measures the energy per charge distribution from 90eV/q to 90keV/q with discrimination of five mass groups. The time for a complete distribution is, however, 32 rotations of the spacecraft.

2.3.1.3 Bessel Box

The Bessel box is basically a cylinder with a central beam stop and an aperture at each end. A potential is applied to the beam stop and only ions in a narrow band of energy/charge can pass through the device. A miniaturised version of the Bessel box has recently been discussed by *Stalder et al.* (1993). The compact ion detector (CID) as flown on the STRV-1a spacecraft uses a similar approach to these devices (*Papatheodorou et al.*, 1996).

2.3.1.4 Oscillating field

The most common type of this instrument is the conventional quadrupole mass analyser. *Medley* (1977) used such a device for early studies of the ionosphere. Basically the resonant motion of a charged particle within an oscillating electric field is used to determine the ion parameters. Instruments based on this principle have been used successfully on the Atmospheric Explorer spacecraft C to E (*Pelz et al.*, 1973) and the Dynamics Explorer 2 spacecraft. More recently a quadrupole analyser has been flown on the Phobos spacecraft and was on the Mars96 orbiter. The MAK instrument was designed to measure neutral atoms and ion composition in the upper atmosphere of Mars. This instrument takes 10 seconds to provide one mass spectrum and provides no energy information.

Using a different concept is the 'path analyser' instrument by *Rosenbauer et al.* (1981) where both mass/charge (M/Q) and the particle velocity (v) are determined simultaneously. Ions are allowed to pass through an electric field oscillating with a sinusoidal time variation. The multitude of solutions to the equations of motion within the field are reduced to one by the introduction of a narrow channel whose shape matches the required trajectory. The period and amplitude of oscillation defined by the channel are then used to determine the (M/Q, v) couplet for the selected instrument parameters. Figure 2-2 shows the basic design for the Rosenbauer instrument (from *Wilken*, 1984).

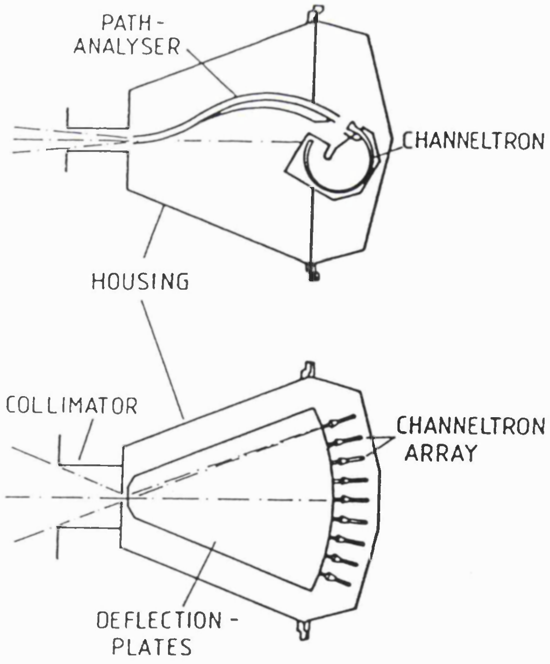

Figure 2-2. Cross-sectional and top view of the path analyser as flown on HELIOS.

Although this design allows for a light compact instrument, it exhibits an inherently poor sensitivity compared to similar instruments. This design is interesting in that it is the only device requiring only electric fields that can determine both mass and energy information. In the study of planetary magnetospheres where the density of ions of planetary origin can become significant and play a major role in the dynamics of the plasma it is important to be able to determine the ion mass. This lead to the development of two types of instruments: those employing time of flight techniques and those using magnetic fields to determine the mass of ions.

2.3.2 ExB

2.3.2.1 Wien Filter

In the Wien filter the electrostatic and magnetic fields are chosen so that for a given ion velocity the forces from both fields are equal. Pinholes placed at either end of the field region then only allow passage for a small range of values about the chosen velocity. As a velocity selector it can be used with another type of detector, for example a curved plate electrostatic analyser to determine the energy/charge, velocity and hence mass/charge of an incident ion. Instruments of this type have been flown aboard the GEOS spacecraft (*Balsiger et al.*, 1976) and AMPTE (*Shelley et al.*, 1985).

2.3.2.2 Electrostatic sector / Magnetic sector

This type of instrument is probably the most complex of ion spectrometers with a large number of variations. Basically they all consist of an electrostatic analyser to select energy followed by a magnetic sector of some form used as a mass spectrograph. Either of these analyser sections can be replaced by an $E \times B$ analyser used to select for velocity instead. One such instrument is the Ion Composition Experiment (ICE) by *Balsiger et al.* (1976) flown aboard GEOS. Here an electrostatic analyser is followed by a curved velocity selector using crossed electric and magnetic fields. The final detection device is a 20 stage discrete dynode electron multiplier. Primarily chosen for its large detection area (compared to a CEM) it also allows the experimenters to make use of the different secondary electron emissions of different species resulting in different output gains. This instrument possesses good mass and energy resolution over a large range. The disadvantage of this instrument is its small unidirectional field of view.

Many modern versions of these instruments make use of the new imaging techniques available with Microchannel Plates (MCPs) and possess a rotational symmetry allowing mass and angular information to be imaged. The Toroidal Imaging Mass-Angle Spectrograph (TIMAS) flown on the POLAR spacecraft is one such instrument. This was also one of the first plasma instruments to use an MCP with an imaging anode (*Shelley et al.*, 1995, *Walton et al.*, 1996). Previously, though, another ion spectrometer, HERS, flown on GIOTTO, used a novel discrete anode design by *Liptak et al.* (1984) to give both angular and mass information from the impact position on an MCP (*Balsiger et al.*,1986). The design of TIMAS is shown in Figure 2-3 as a cross-section, this is rotated through 360° about the y axis. Basically it consists of a toroidal electrostatic curved analyser followed by a ring of magnets used to select mass/charge. The detector consists of a chevron pair of MCPs and a wedge and strip anode system so that the radial position measures the mass/charge and the azimuthal position provides the input angle. Again, this instrument has the disadvantage of being dependent on spacecraft spin for full angular coverage and having to scan voltages to select for energy.

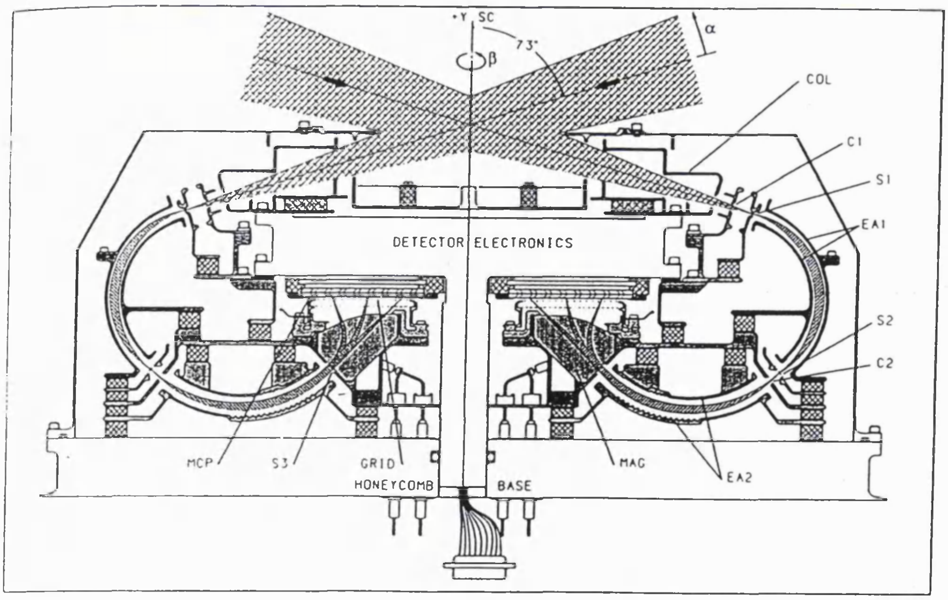

Figure 2-3. Cross-sectional view of the TIMAS instrument (from *Shelley et al.*, 1995).

A recent instrument by *Hirahara and Mukai* (1993) uses a spherical electrostatic analyser followed by a segmented magnet mass spectrometer. The mass resolution of this instrument is superior to that of the TIMAS instrument but is achieved at the expense of having five individual imaging detectors and a much reduced angular range and resolution. The ASPERA-S instrument on Mars 96 and also flown on PHOBOS is similar in design to TIMAS but with only a 90° spherical analyser followed by a ring of magnets used as part of a crossed field velocity selector (*Lundin et al.*, 1989). The imaging system on ASPERA-S uses discrete anodes (32 × 32) providing 32 mass bins by 32 angular bins. At present this is the most advanced energy mass analyser to have taken measurements at Mars. Although ASPERA has a 360° field of view it required a ±90° scanning platform to achieve full 4π coverage. Unfortunately during the short operational time of the PHOBOS spacecraft the scan facility was used only a few times.

2.3.2.3 Mattauch-Herzog

Mattauch type analysers use a combination of magnetostatic deflection (giving momentum/Q) and electrostatic deflection (giving E/Q) to determine the mass per charge ratio of ions. Arbitary field geometries produce different focussing for velocity and directional information. Choice of suitable field geometries can, however, remove this velocity dispersion. In 1934 Mattauch and Herzog described such a double-focussing device allowing simultaneous analysis of all masses within a limited range with high resolution and sensitivity (*Wilken*, 1984). A more recent space-borne version of this type is that by *Moore* (1977). This instrument shows good energy and mass resolution but again requires scanning of the electrostatic field and has a small field of view, approximately 4° × 6°. This instrument is of a flat geometry, although *Coplan et al.* (1984) has produced a cylindrical version and *Ghielmetti and Young* (1987) a toroidal version.

2.3.2.4 E parallel B

The only instrument to fit into this group is the Thomson parabola which has been used mainly within plasma laboratories and in nuclear fusion studies. Because it requires a two dimensional imaging system it has not until now been used for space instruments. There are two main designs in use. Firstly, those that use a large magnetic field to produce a deflection between 90° and 180°: *Roquemore and Medley* (1986), *Foote et al.* (1986), *Bartiromo et al.* (1987), *Armentout* (1990) and *Kusama et al.* (1990). Secondly, there are instruments that use a small deflection in both the electrostatic and magnetic field, *Kuswa et al.* (1973), *Slater* (1978), *Sakabe et al.* (1980), *Herold et al.* (1981), *Rhee* (1984), *Weber et al.* (1986), *Sato* (1987), *Yoneda et al.* (1988), *Yamamoto et al.* (1990), *Funsten et al.* (1997) and *Lu et al.* (1997). FONEMA is of the second kind and would have been the first space-borne Thomson parabola analyser. The basics of the Thomson parabola design are discussed in a later section in this chapter.

2.3.3 Time of flight analysers

Time of flight (TOF) analysers are commonly used as a mass discriminating element after ions are first E/Q selected in a conventional electrostatic analyser. The basic principle is that an incoming ion is pre-accelerated before passing through an entrance foil producing a secondary electron which is used to start a timer. The ion then passes through a second foil or impacts a solid-state detector producing another secondary electron which triggers a stop signal to stop the timer. With a known path length the time of the flight through the system will give the velocity. Because the energy/charge is already known the mass/charge can be easily deduced. The clock triggering signals are usually obtained by the signal produced from the secondary electrons when collected by an electron multiplier, i.e. a channel electron multiplier or a microchannel plate. If a solid state detector is used as the stop signal the ions are usually pre-accelerated to >20keV thereby accelerating the ions to energies above the solid state detector thresholds. An example of a curved plate analyser followed by a TOF detector is the Solar Wind Composition Spectrometer (SWICS) (*Gloeckler et al.*, 1990). A new approach to TOF analysis is described by *McComas and Nordholt* (1990) where in order to achieve higher mass resolution the ions are timed as they are reflected in a retarding linear electric field. The restoring force that an ion experiences is proportional to the depth that it travels into the field region. This instrument is part of the payload for the CASSINI spacecraft. One problem with TOF analysis is the amount of on-board data handling and associated electronics that is often required; this tends to make these instruments heavier than comparable mass spectrometers using magnetic fields for mass discrimination.

2.4 The FONEMA instrument

Most of the instruments in the previous section are designed for operation on spin stabilised spacecraft which will produce an inherent lower limit on the accumulation time of a complete distribution. Most of them, however, also require scanning and hence have a time resolution that is dependent on the field sweep frequency. This means that the only way to increase time resolution is to have less energy steps reducing energy resolution or shorter accumulation times at each energy reducing sensitivity.

FONEMA was designed and developed at MSSL and IKI for the Russian mission to the planet Mars (*Vaisberg et al.*, 1990, *Johnstone et al.*, 1988, *James et al.*, 1996). The design of this instrument was carried out with three specific objectives in mind:

- To measure 3D velocity distributions of ions of several mass groups simultaneously in the energy range from 20eV to 8keV.

- To measure these distributions on a 3 axis stabilised spacecraft.

- To measure complete distributions with a time resolution more than an order of magnitude faster than previously flown analysers i.e. 125ms.

The design arrived at is based on a combination of three main components that complement each other. Firstly, to allow for measurements of 3D distributions, a hyperbolic section electrostatic mirror was developed to focus ions arriving from anywhere within a full hemisphere of space onto 36 focus positions with a narrow convergence angle. Two such mirrors placed back to back allow for full 4π steradian coverage of space. The details of the mirror system, developed by *Fedorov et al.* (1996) at the Institute for Space Research (IKI), Moscow, are given in Chapter 3.

Secondly, to allow for fast velocity distributions an analyser system with no scanning of voltages was required. A compact Thomson Parabola analyser, designed and developed at MSSL, is described below and the performance and development of individual components of the analyser are explained in Chapters 3 through 5. Finally, to make use of the full capabilities of the Thomson Parabola analyser a 2D imaging system was needed. Development and operational characteristics of a wedge and strip anode encoding system mounted behind a microchannel plate chevron pair is discussed in Chapter 6.

The combination of these new techniques have meant that with FONEMA it is theoretically possible to have a dynamic range of 20 in energy for 4 mass groups without the need to scan voltages. The time resolution is then limited only by the speed of the electronics, at present 125ms. All of this is achieved whilst maintaining full 4π angular coverage and acceptable angular resolution.

2.5 The Thomson Parabola

The FONEMA instrument is based around the Thomson Parabola analyser (*Thomson*, 1911) which uses parallel electric and magnetic fields to determine the mass/charge and energy/charge of incident ions simultaneously. This concept is shown in Figure 2-4 in an exploded view of one of the FONEMA Thomson analysers. An ion entering the aperture is reflected by an electrostatic mirror through the focusing particle collimator into the main body of the analyser. Here it passes through an aperture in the magnetic field return plate, through the magnetic field region and the electrostatic field region before striking the image plane of the MCP / Wedge Strip anode detector system. The magnetic field deflects the ion in the +y direction by an amount inversely proportional to its momentum/charge. The electric field deflects in the x direction by an amount inversely proportional to energy/charge. Figure 2-5 shows details of one of the individual analysers used in FONEMA.

FONEMA Analyser

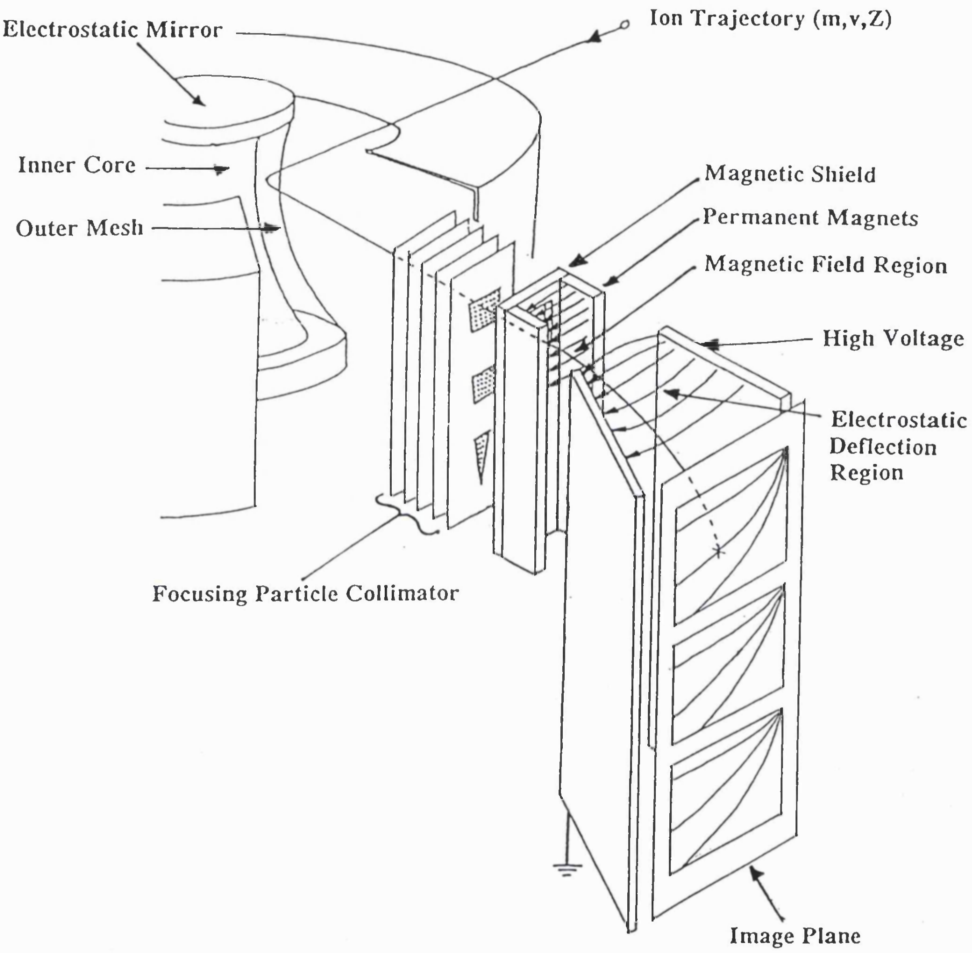

Figure 2-4. Basic Thomson Parabola analyser operation.

Each analyser unit contains 3 Thomson analysers sharing a common electrostatic field region, magnetic field region and detector system, that in combination with the electrostatic mirror covers a polar range of 90° and azimuthal range of 60°. There are six of these analyser units equally spaced around the central mirror to give coverage over a complete hemisphere. By placing 2 of these subsystems back to back, as shown in Figure 2-6, full sky coverage is achieved allowing simultaneous measurements of ion parameters on a 3 axis stabilised spacecraft.

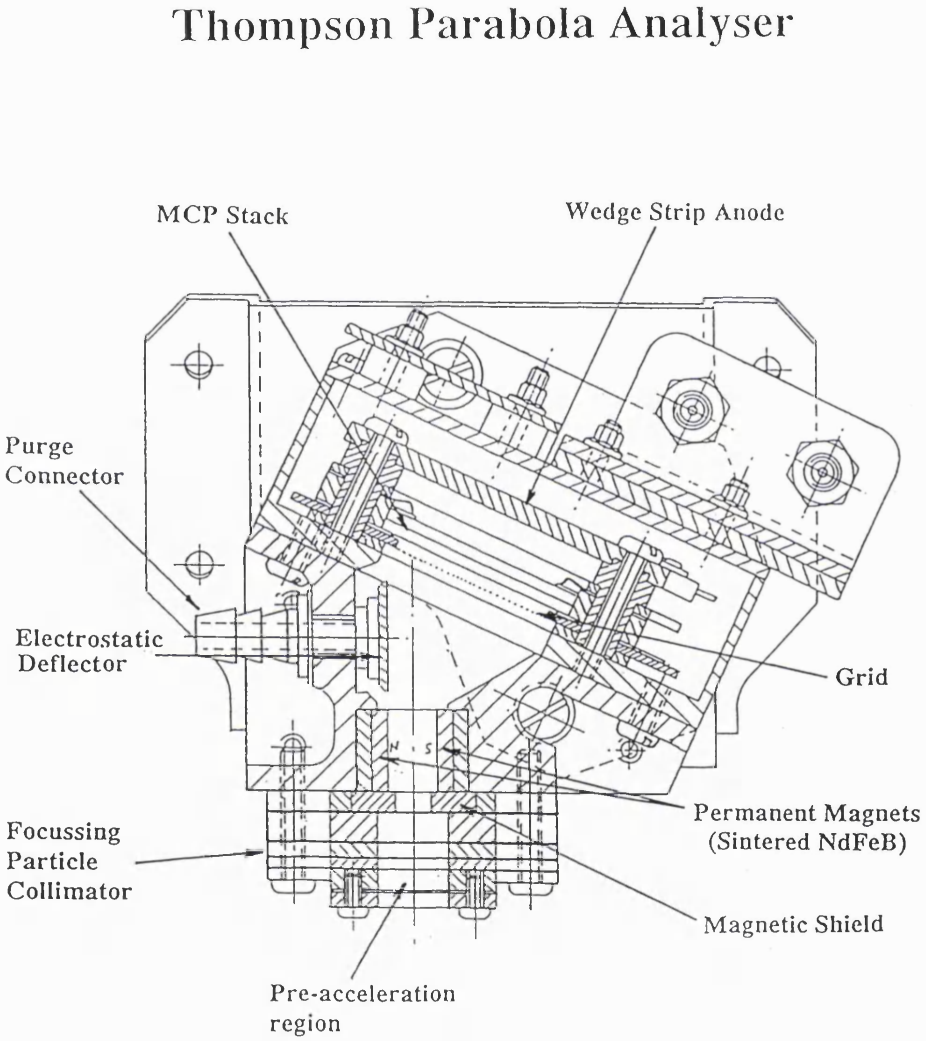

Figure 2-5. Mechanical drawing of a slice through one of the FONEMA analysers showing all of the major components.

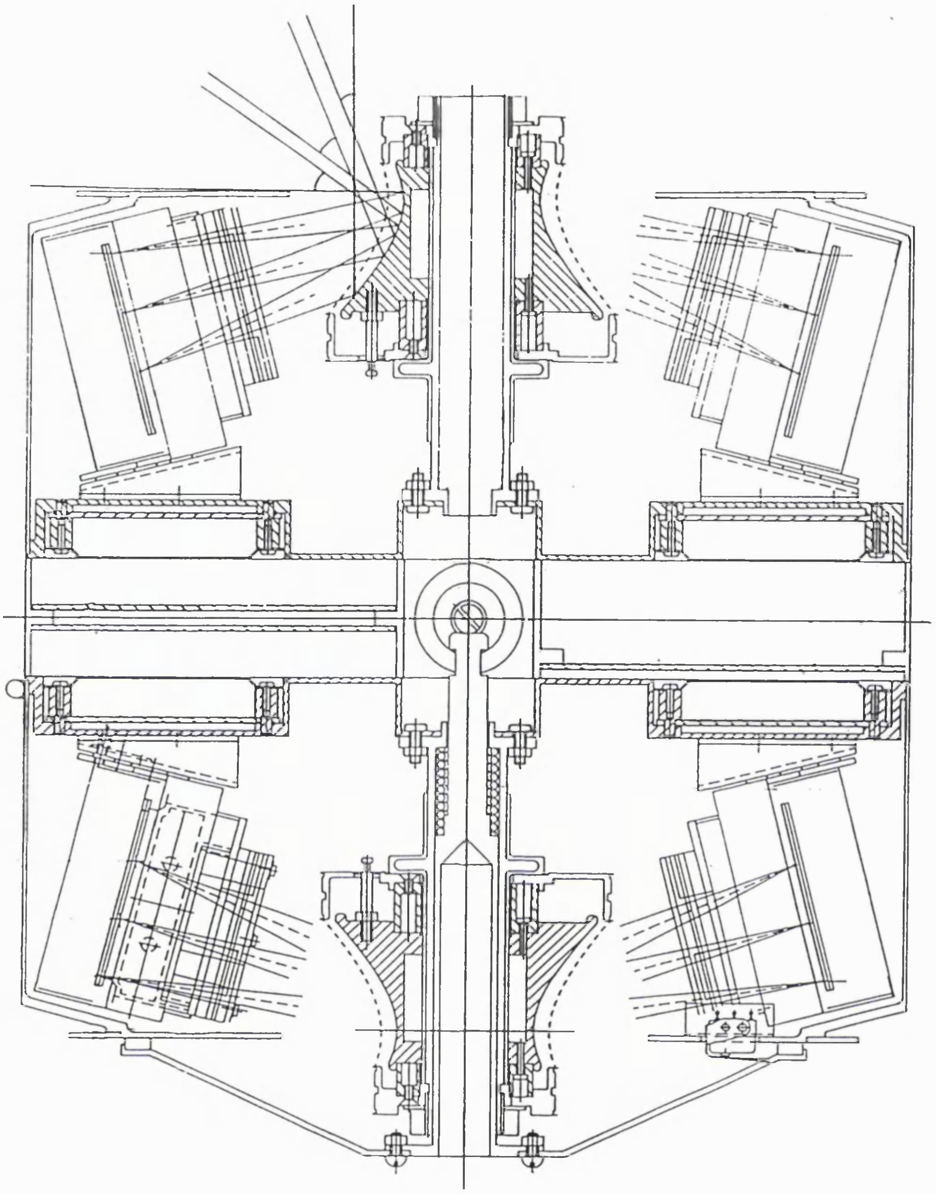

Figure 2-6. Mechanical detail of complete instrument showing the two hemispheres back to back allowing full 4π coverage.

2.6 Basic operation of Thomson parabola analyser

The principle of the Thomson parabola analyser as used in FONEMA is shown in Figure 2-4. Its design and performance are discussed in the remainder of this thesis. Firstly, however, the theoretical operation of an ideal Thomson parabola analyser will be discussed. Figure 2-7 shows an ideal analyser with parallel magnetic and electrostatic field sharing the same volume and ions undergoing only a small deflection angle to reach the image plane. Thomson analysers of this type have being described in the literature by *Sakabe et al.* (1980), *Rhee* (1984), *Weber et al.* (1986) and *Lu et al.* (1997), however, much of the following discussion on the Thomson parabola is based on a study by *Walton* (1987) used for the original instrument proposal (*Johnstone et al.*, 1988). If it is assumed that the electric field is E between the pole pieces and zero elsewhere the deflection in x is described by the equation:

$$x = \frac{q}{mv^2} E d^2 \tag{2.1}$$

and,

$$d^2 = l\left(\frac{l}{2} + L\right) \tag{2.2}$$

These equations are in SI units, where $q = Ze$ (Z is the charge number, e is the charge on an electron) and $m = Am_p$ (A is atomic mass number, m_p is the mass of a proton). l is the length of the field in the z direction and L is the length of the trajectory in the z direction outside the deflection region. Similarly the deflection in y due to the magnetic field, B, is given by:

$$y = \frac{q}{mv} B d^2 \tag{2.3}$$

Combining equations 2.1 and 2.3 by eliminating v yields the expression:

$$x = \frac{Em}{qB^2 d^2} y^2 \tag{2.4}$$

This produces the characteristic parabolic trace on the image plane. There is a unique parabola for ions of a fixed A/Z. From equations 2.1 and 2.3 an expression for v can be derived:

$$v = \frac{yE}{xB} \tag{2.5}$$

This is a straight line passing through the origin in the x-y plane corresponding to an iso-velocity line.

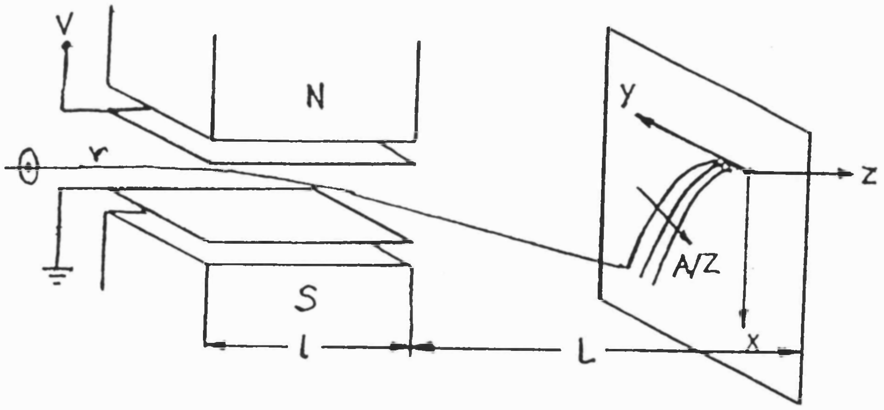

Figure 2-7. Principle of the Thomson parabola ion analyser (adapted from *Sakabe et al.*, 1980).

2.6.1 Energy resolution

If the energy resolution of the Thomson parabola is determined by the position resolution of the imaging system, then it can be determined from 2.1. Firstly equation 2.1 is restated in terms of the ions kinetic energy T.

$$x = \frac{q}{2T} E d^2 \qquad (2.6)$$

Differentiating with respect to x gives,

$$\frac{dx}{dT} = -\frac{qEd^2}{2T^2} \qquad (2.7)$$

Rearranging and dividing through by T

$$\frac{\Delta T}{T} = -\frac{2T\Delta x}{qEd^2} \qquad (2.8)$$

where Δx is the position resolution of the imaging system.

This equation shows that the energy resolution of the Thomson parabola is a strong function of the energy of the incident ion. For low energy ions $\Delta T/T$ is small i.e. good energy resolution is achieved but for high energies becomes increasingly larger. Figure 2-8 shows both the energy resolution and the deflection in the x axis for a typical Thomson parabola. At large deflections where the energy is low the resolution is 0.004 but rises to nearly 0.05 for higher energies.

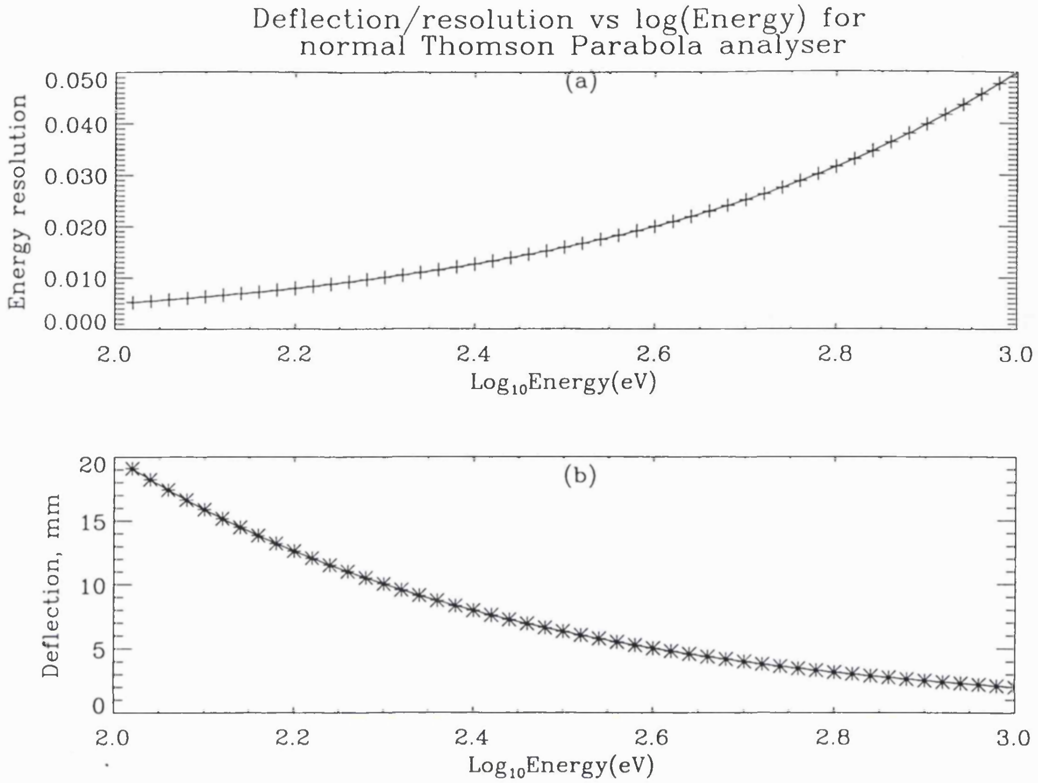

Figure 2-8. a) Energy resolution, $\Delta T/T$, for the normal Thomson Parabola plotted against $\log_{10}$(Energy) showing poor resolution at high energies. b) x deflection due to the electric field for this analyser: B = 2mT, E = 400Vm^{-1}, l = 10mm, L = 50mm and the detector resolution, Δx is assumed to be 100μm.

2.6.2 Pre-accelerated Thomson Parabola analyser

In an ideal spectrograph the energy resolution would be constant across the full range of energies, i.e. $x \propto log(T)$ using the notation above. It is not possible to achieve this in a Thomson Parabola analyser but an improvement can be made by accelerating the ions through a potential K before they enter the deflection region. Now the energy within the Thomson Parabola is given by $T + K$ and equation 2.6 becomes:

$$x = \frac{q}{2(T+K)} E d^2 \tag{2.9}$$

Therefore,

$$\frac{\Delta T}{T} = -\frac{2(T+K)^2 \Delta x}{qTEd^2} \tag{2.10}$$

The energy resolution can then be optimised by choosing the pre-acceleration voltage so that $\Delta T/T$ is the same at both ends of the energy range. Defining the energy range to be from T_1 to T_2 then requires that:

$$(\Delta T/T)_{T_1} = (\Delta T/T)_{T_2} \tag{2.11}$$

From equation 2.10 therefore

$$\frac{(T_1 + K)^2}{T_1} = \frac{(T_2 + K)^2}{T_2} \tag{2.12}$$

and rearranging to find K gives

$$K = \sqrt{T_1 T_2} \tag{2.13}$$

Referring to the example Thomson parabola as described in the caption of Figure 2-8, with an energy range of 100 to 1000eV, the pre-acceleration energy K = 316eV. In order to keep the maximum deflection the same the electric field is increased to 1664Vm^{-1} but all other parameters are kept the same. Figure 2-9 shows the energy resolution and deflection for this Thomson parabola. Note how the energy resolution is now optimised across the energy range. It can be shown that the resolution curve in Figure 2-9 (b) is perfectly symmetric, with the minimum at energy $T = K$. In Figure 2-9 (b) it can also be seen that the minimum deflection is now increased, i.e. the range of deflection values is reduced. This allows for a mask to be place over this region of the image plane (<5mm) so that the focus point of the collimator is no longer on the image plane and the maximum energy transmitted by the electrostatic mirror is just in the detected region. This mask can be used as a light trap to stop any UV solar photons that get through the collimator from being detected. Alternatively the electric field can be increased further to maintain the same overall deflection and the image plane can simply be shifted in the x direction. In this case the energy resolution is decreased further.

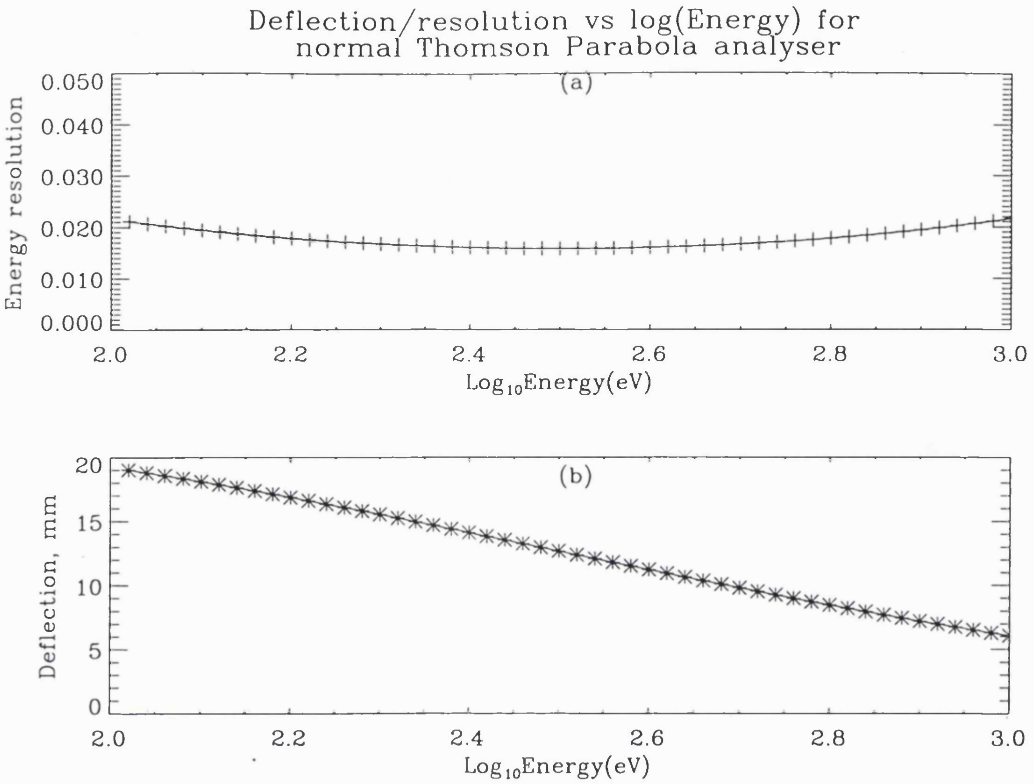

Figure 2-9. a) Energy resolution versus $\log_{10}$(Energy) for the pre-accelerated Thomson analyser showing the minimum resolution as 0.016 rising to 0.022 at the edges. b) x deflection versus energy for the pre-accelerated Thomson parabola.

Producing a more constant energy resolution is just one advantage of the pre-accelerated Thomson parabola. The energy range that the analyser has to deal with is also reduced by pre-accelerating. For the normal Thomson parabola this range, *R*, is defined as

$$R = T_2/T_1 \qquad (2.14)$$

but for the pre-accelerated Thomson parabola the range is

$$\frac{(T_2 + K)}{(T_1 + K)} = \sqrt{R} \qquad (2.15)$$

This makes the design of the optics much less critical. For the normal Thomson parabola described previously the range of energies, *R*, was equal to 10. For the pre-accelerated Thomson parabola in the example this range is reduced to just 3.16. Besides making the optics design less critical it could be used to extend the energy range of the instrument. Pre-acceleration also allows the possibility of tuning the best energy resolution to a particular energy. It can be shown that the best energy resolution always occurs at $T=K$, whatever the value of K.

2.6.3 Mass resolution

Mass resolution of the Thomson parabola is also improved by compressing the energy range as shown in Figure 2-10. Here the separation of the H^+ and He^+ at 1keV, i.e. minimum deflection in x for both analysers, is better by a factor of nearly 2. In fact it can be shown from equation 2.3 that the ratio of $\Delta m/m$ between the normal and pre-accelerated analysers for any energy T is given by:

$$\frac{(\Delta m/m)_{Normal}}{(\Delta m/m)_{Pre-acc}} = \sqrt{\frac{T+K}{T(1+\sqrt{R})}} \qquad (2.16)$$

where R and K are as previously defined. This expression holds true only when both the electrostatic field and magnetic field have being adjusted to give the same maximum deflection. In the simple Thomson parabola Δm/m varies by a factor of $\sqrt{R}$ in going from T_1 to T_2, but for the pre-accelerated version this is reduced to $\sqrt[4]{R}$.

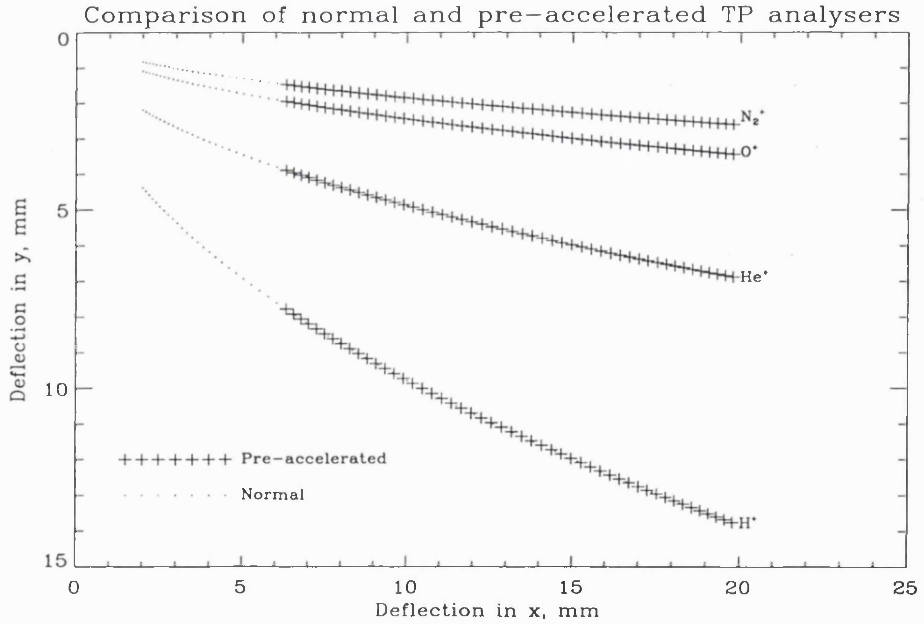

Figure 2-10. Parabolic tracks on the normal and pre-accelerated Thomson parabola analysers for the energy range 100 to 1000eV.

2.6.4 Disadvantages of pre-acceleration

Once the ions have been accelerated in order to get the same deflection it is necessary to increase both the electrostatic and the magnetic field. For the electrostatic field, in order to attain the same range of deflection, this increase can be shown to be:

$$\frac{\left(\sqrt{R}+1\right)^2}{\sqrt{R}} \qquad (2.17)$$

To simply keep the same maximum deflection as in Figure 2-10 the increase in going from the normal to the pre-accelerated Thomson parabola is:

$$\sqrt{R}+1 \qquad (2.18)$$

For the example Thomson parabola these two factors are 5.48 and 4.16 respectively.

In going from the normal Thomson parabola to the accelerated version, whilst maintaining the same maximum deflection in y, the magnetic field must increase by a factor:

$$\sqrt{\left(1+\sqrt{R}\right)} \qquad (2.19)$$

This is a factor of 2.04 for the example analyser.

Another disadvantage of pre-acceleration is the effect of focusing. In FONEMA a focusing electrostatic mirror is used to divert the ions from space into the Thomson parabola. If a planar pre-acceleration is used an energy dependent aberration occurs in the focus position, see Figure 2-11. This is because the electrostatic field of the pre-acceleration is not parallel to the converging ion trajectories. Therefore energy dependent deflection of the ions occurs in this region, lower energies being deflected most. If the optics are designed such that at $T = K$ the converging beam is focused at the image plane, then ions with $T > K$ are over-focused and those with $T < K$ are under-focused. Where the incoming particle trajectories are defined by a collimator system this effect will produce an energy dependent transmission factor in the collimator. This is discussed in Chapter 3. There are two solutions to this problem, either the pre-acceleration region must be curved such that all trajectories are parallel to the field or pre-acceleration must occur before the mirror. The latter solution would produce an energy dependent geometric factor.

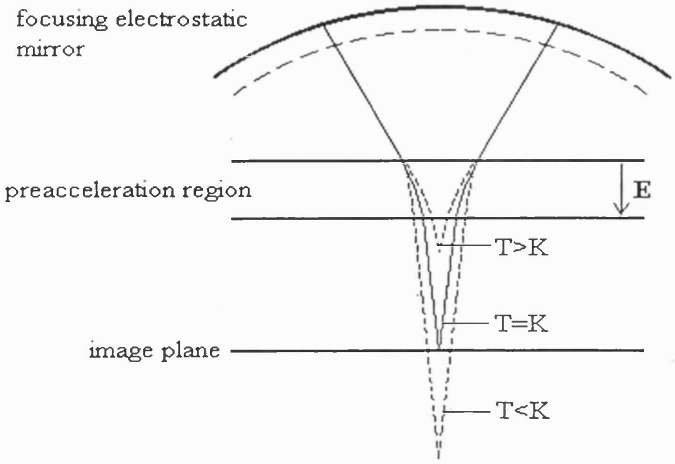

Figure 2-11. Effect of a planar pre-acceleration region between a focusing electrostatic mirror and image plane.

2.7 FONEMA Thomson parabola

For FONEMA the final images would be digitised uniformly across their area so it was important that the energy resolution was as uniform as possible. For this reason a pre-acceleration field was used. A further method of reducing the variation in energy resolution was to angle the image plane by 25°. This is seen clearly in Figure 2-5. Because the deflection angles in FONEMA would be relatively large, the lower energy ions followed a longer path length, this resulted in much better resolution for these ions. Unfortunately, to get the large deflection ions on the imaging area available would mean reducing the deflection voltage and hence the higher energy ions would be deflected less and resolution would be worse at those energies. By angling the image plane the variation in path length would be reduced and the final deflection on the image plane reduced for the lower energies. This approach had the added advantage that the angle of incidence of the ions to the MCP surface would be normalised resulting in less variation in angular dependent detector efficiency and gain.

Because the magnetic field is fixed if the deflection in y due to the magnetic field is fixed at the maximum 15mm for the lowest energy in mode 1, i.e. 20eV, for the higher energy modes the deflection will be less (see Table 8-1 in Chapter 8 for a definition of the modes). This of course will reduce the mass resolution for these modes. Because the most common modes to be used in flight will be mode 2 and mode 3 the magnetic field is designed to give a full deflection of 15mm in y for a 400eV proton in mode 1. This occurs when the x deflection is approximately 3mm at this point. Protons of a lower energy than this that enter detector 1 or detector 2 in an analyser will impact the image plane of detector 2 and detector 3 respectively. However, it should be possible to distinguish these events using information from the diagnostic images. Choosing a magnetic field that meets these requirements gives the highest possible resolution in the two most common operating modes.

The rest of this thesis deals with the development of the individual components within the Thomson parabola analysers and the operation of the final design.

3. The Collimator

3.1 Basic Principle

The collimator on FONEMA selects the directions from which particles enter into the Thomson Parabola Analysers after they are reflected off the electrostatic mirror. Each analyser has three collimators as its front component, each of these only allowing particles coming from a specific region of the mirror to pass through them. These regions are chosen so that the incident particles on the mirror within these areas cover a specific range of polar and azimuthal angles. In effect then the collimators allow passage to particles arriving from specific directions in space. The collimators are designed to allow full sky coverage without over-sampling ions from any particular region. Inevitably, due to the basic mirror structure and the relative geometry of the two subsystems some compromise has to be made.

As a consequence of its primary objective the collimator is the smallest aperture and hence dictates the geometric factor for the whole instrument in terms of open area. It should be noted, however, that there are other governing parameters to the detection efficiency from the mirror system such as the transmission factor, both spatially and in terms of energy. There is also a finite upper limit placed on the obtainable geometric factor by the physical dimensions of the mirror.

The collimator is made of a number of channels through which the particles pass into the detector. The dimensions of these channels define the spot size and hence the energy and mass resolution of the instrument as the whole.

3.2 Theoretical Design

3.2.1 Making a collimator

The ideal particle collimator would be one produced by line boring techniques, e.g. spark erosion, producing an array of channels through which the particles could pass. There are, however, drawbacks with this approach. Firstly, in order to increase the dynamic range in terms of energy it is a requirement that the ions are pre-accelerated before entering the analyser and the only place where this can sensibly take place is within the collimator itself. Secondly these techniques are difficult to perfect and therefore prove to be expensive. Finally, the mass of the collimators will be large which is not desirable for any space application.

A better approach would be to use a multi-plate collimator, i.e. a series of plates with a pattern of holes etched through each plate through which the particles can pass. A number of these plates would then define slices through the theoretical channels down which the particles travel. By appropriate spacing of these plates, and careful alignment, it was anticipated that an optimum design could be reached employing the lowest possible number of plates whilst still constraining the particles to only one theoretical channel. The design of the hole pattern would be determined by the design considerations outlined in the following sections.

3.2.2 Defining the limits from the mirror

The electrostatic mirror is made up of a solid central electrode and a mesh held at a lower potential placed around this, the difference in potential being the theoretical energy window for the mirror. Both the solid electrode and the mesh are of a hyperbolic cone design, the shape of the central electrode given by:

$$\frac{X^2}{(A-F)^2}-\frac{Z^2}{(C-L)^2}=1 \qquad (3.1)$$

and of the mesh is given by:

$$\frac{X^2}{(A+F)^2}-\frac{Z^2}{(C+L)^2}=1 \qquad (3.2)$$

where:

$A = 18.80\text{mm}, F = 3.50\text{mm}$

$C = 20.40\text{mm}, L = 2.86\text{mm}$

X and Z in these expressions are in millimetres and define the shape in the XZ plane, the full volume is constructed by rotation of this hyperbola about the Z axis (instrument axis). The central electrode is made of aluminium and could be machined to take on any profile; the mesh, however, is made of hundreds of straight wires held between endpoints at different azimuthal positions on two parallel disks. This method of construction results in a pure hyperbolic curve.

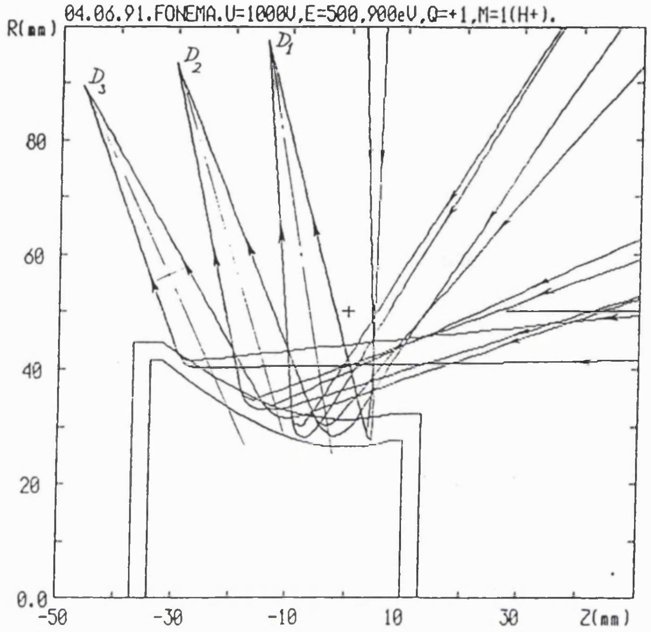

Figure 3-1. Ion trajectories through the mirror simulation showing limiting trajectories for 2 values of ion energy/mirror voltage for the 3 detectors.

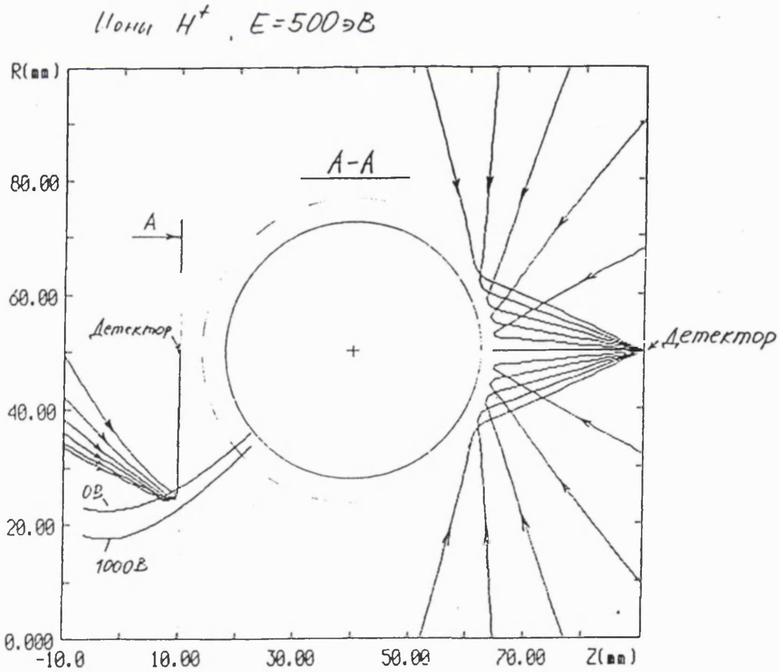

Figure 3-2. Mirror simulation results used to define the limiting azimuthal trajectories.

Figure 3-1 and Figure 3-2 show ion trajectories in polar and azimuthal views of the mirror simulation. By mapping these trajectories back to the focus point of each detector in the analysers the limiting trajectories for each collimator can be defined. Both these plots are taken from the simulation of the mirror performed at IKI, Moscow by Andrey Fedorov and Andrey Kozhuhovsky. The mirror axis defines the instrument axis and each analyser will have a field of view of ~90° in polar and ~60° in azimuth relative to this axis. As discussed in the last chapter each analyser comprises three detectors; detector 1 covers 0-20°, detector 2 covers 20-50°and detector 3 covers 50-90° in polar angle. All three detectors cover the full 60° in azimuth. These polar ranges reflect the limited geometry available with such a mirror construction. To achieve this with co-linear focal points for all three detectors, the focal plane has to be placed at 14° to the instrument axis.

In Figure 3-1 two input ion energies are used. The higher energy ion trajectory is seen to make a closer approach to the core of the mirror and although incident at a different polar angle reaches the same focus. This clearly shows that the polar angular range will vary with input energy, and this is also true for the azimuthal angular response. One reason for this energy dependence is that the spatial separation at the mesh of incoming and outgoing trajectories is larger for higher energy ions. For a planar mirror this is not a problem, however; for the geometry of the FONEMA mirrors this means that the ions travel through a different field regime at different energies. This effect is then intrinsic in the electrostatic mirror design.

Another variation in reflection angle is caused by scatter near the grounded mesh. At energies that are low relative to the mirror voltage the projection of the ion into the field region of the mirror is small. The electric field in the region near the mesh varies at the spatial frequency of the mesh. Reflection of ions of equal energy then becomes dependent on the actual incident position at the mirror. Figure 3-3 shows the trajectories for three different energies incident at different positions along a planar mesh. For the lower energy ions the angular dispersion at the grid is clearly evident and even for higher energy ions that pass close to a mesh wire the reflection angle can be altered significantly.

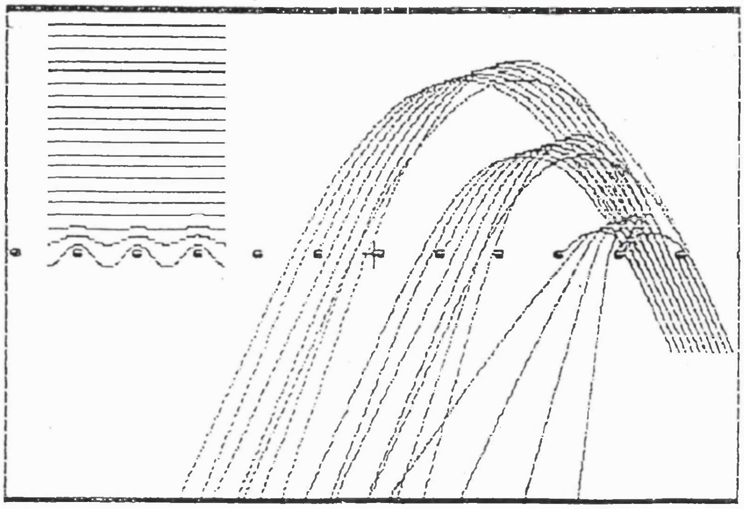

Figure 3-3. Operation of a planar electrostatic mirror, the mesh (seen edge on) is grounded whilst the bottom of the box is held at a positive potential. Trajectories of 3 energies are shown at 10 different start positions for the same angle of incidence. This plot shows how angular dispersion occurs at the grid as well as an energy dependent linear displacement.

So that absolute detection efficiencies for each species can be estimated it is important that the transmission values for the mirrors are mapped. Figure 3-4 shows experimental results from the mapping of the Flight Model (upper) mirror. Ions are emitted with a divergent beam from the Detector 2 focus position, reflected by the electrostatic mirror and measured with a large area position sensitive detector. In these experiments, carried out at IKI, the ion energy (E) is kept constant and the mirror voltage (U) varied. At small values of E/U, i.e. the left-hand plots, the angular coverage is fairly stable. The lighter regions represent higher counts. When E/U approaches unity the angular spread increases significantly. Events are also still recorded when E/U goes above 1, although the recorded numbers are very low compared with the input. This effect is much worse for detector 3 where the ion trajectories become more parallel to the mirror surfaces. In the detector 1 experiment, where ion trajectories are closer to the normal of the mirror surfaces, almost no events were recorded when the ion energy was greater than the mirror voltage. Figure 3-5 shows the mirror transmission results from Figure 3-4 summed in azimuthal angle to show the polar boundaries more clearly.

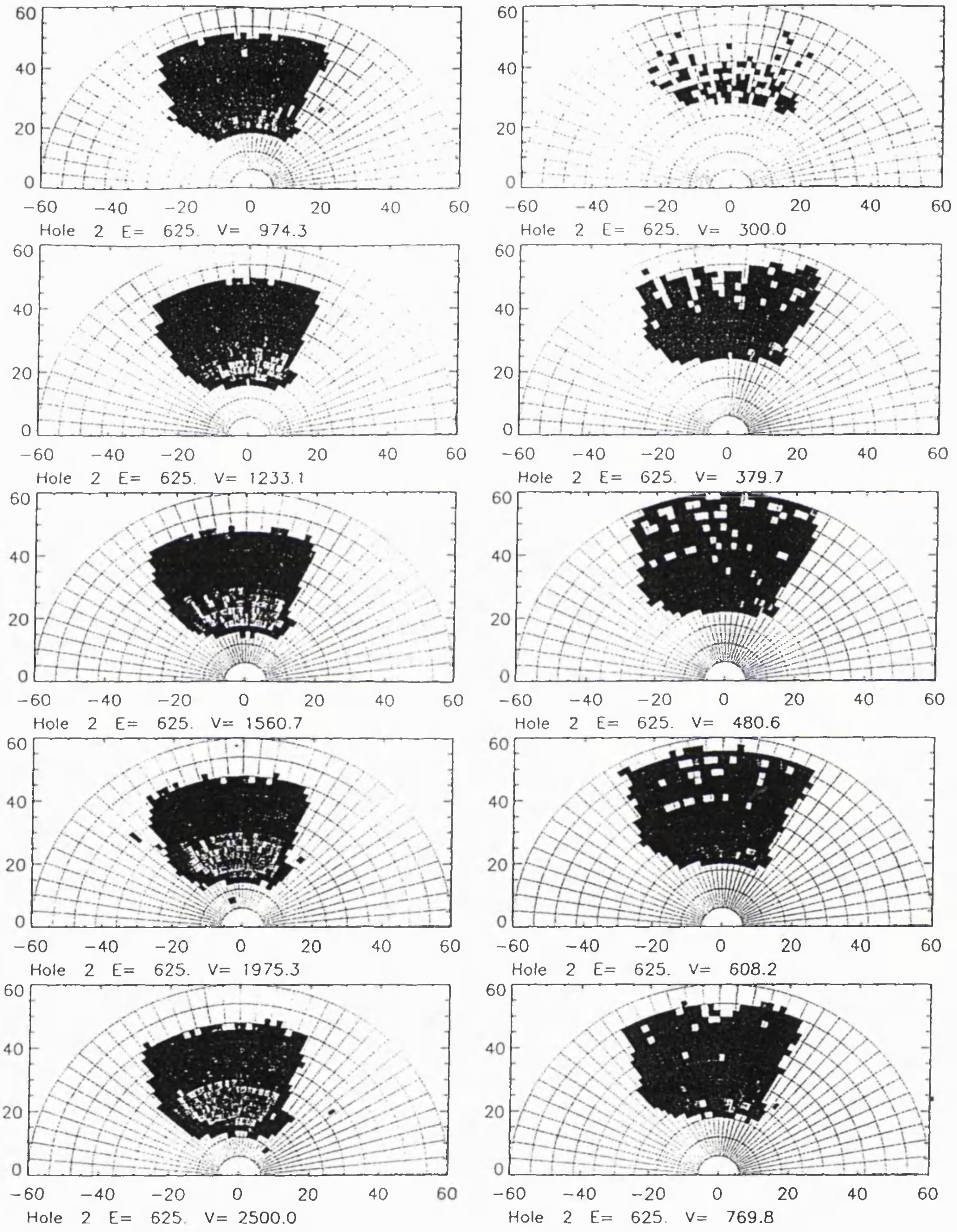

Figure 3-4. Set of detector 2 collimator responses for different E/U ratios. Lighter pixels represent higher counts, black is a count of 1.

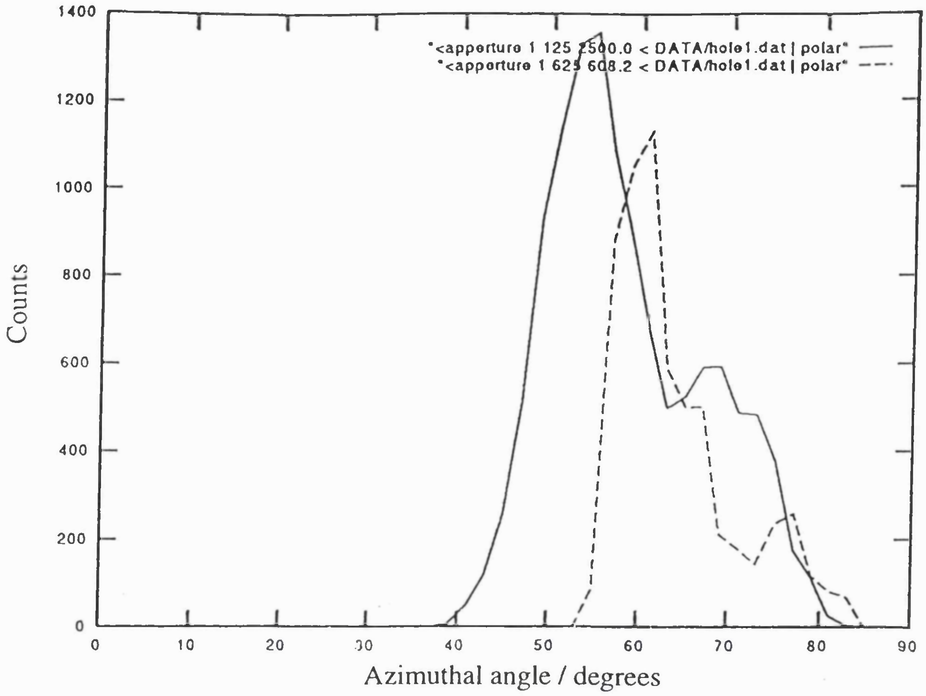

Figure 3-5. Mirror transmission for detector 2 summed over azimuthal angles. The solid line shows E/U = 20 and the dashed line shows E/U = 1.

The trajectories for the mean value of ion energy/mirror voltage are used to define the limits for the 3 collimator patterns. This is shown in more detail in Figure 3-6 and Table 3-1 which lists these limiting angles. Although this results in over-sampling at detector boundaries, to define the limits at higher energies would result in under-sampling, i.e. some portion of the plasma population would avoid detection altogether. It can be seen in Table 3-1 that for the detector 3 pattern that *ax1* is 0°, so the limits define a triangle for this detector. A hole at the apex of the triangle would allow ions from the 0° and 180° polar angle to enter the instrument and would be the same for all 6 analysers in either of the hemispheres. To combat this the hole in the collimator at this point is moved slightly so that the limiting trajectory through the hole occurs at the apex angles for ions of mean energy. Testing of the mirror, however, has shown that there will still be some energy dependent over-sampling in this region.

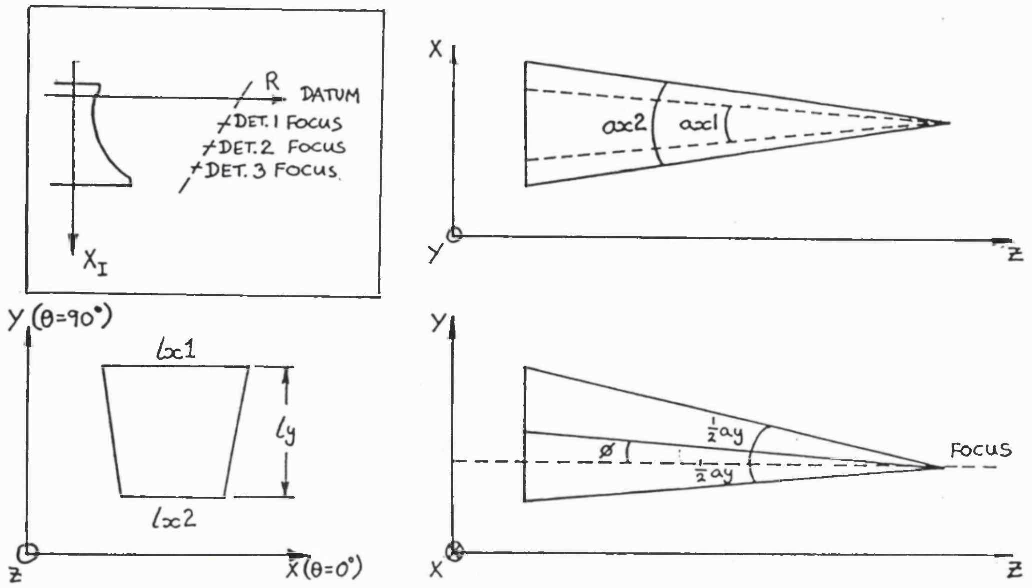

Figure 3-6. Views showing limiting rays through collimator and definition of values in Table 3-1. *lx1*, *lx2* and *ly* are all defined for the rear plate. The insert shows the focus positions of the 3 detectors relative to the mirror.

Detector	θ	ϕ	R	X_I	ax1	ax2	ay	lx1	lx2	ly
1	270°	5.14°	97.6	14.4	5.9°	6.4°	6.2°	2.71	2.91	2.84
2	90°	2.16°	93.6	30.4	4.4°	6.1°	7.2°	2.00	2.78	3.28
3	90°	10.26°	89.6	46.4	0.0°	4.4°	8.5°	0.00	2.06	4.00

Table 3-1. Collimator parameters derived from the electrostatic mirror simulation, see Figure 3-6 for definition of terms (all linear dimensions in mm). R is the radial distance from the instrument axis to the focus position, X_I is the distance below the datum (taken as the z=0 plane in the hyperbola calculation, equation 1.1 and 1.2).

3.2.3 Defining the spot size

In the FONEMA instrument the energy and mass resolution depend on the resolution of the parabolas formed on the image plane, which is defined by the inherent resolution of the imaging device and the spot size incident on the image plane. It is important for most applications to keep the spot size as small as possible and this is also true for FONEMA. The size of the spot produced on the image plane,

a, is dependent on the distance from the front collimator plate to the image plane, D_{fp}, size of hole in the collimator, d, and the length of the collimator, l_c, and is defined by the equation:

$$a = \frac{2dD_{fp}}{l_c} - d \qquad (3.3)$$

From equation 3.3 it can be seen that the spot size is directly proportional to the hole diameter and the distance of the collimator from the image plane but inversely proportional to the length of the collimator. However, the distance from the detector plane is limited by the overall geometry of the instrument and the hole size cannot be made too small if it is to retain its theoretical function as a hole in an infinitely thin shim. Mechanical requirements have the minimum thickness of this shim fixed at 50μm so as the hole diameter approaches this size and the hole turns into a tube more and more off-axis trajectories are lost. This then only leaves the option of increasing the length of collimator to reduce the spot size. Unfortunately, if the hole size is retained and the collimator length is increased the converging channels means that the ratio of hole to metal in the back collimator plate increases. If this becomes much greater than about 20% the collimator will need more 5 plates. Additionally, any increase in collimator dimension within the analyser reduces the distance available for the electrostatic and magnetic deflection fields. Also, the length of the collimator not only defines the spot size but also influences the overall geometric factor of the instrument.

3.2.4 Geometric Factor

The geometric factor of the instrument is the detected flux relative to the flux incident at the aperture as defined by the detector's geometry. This should not be confused with detection efficiency which will include losses due to other mechanisms within the instrument, e.g. quantum efficiency of the MCPs, deadtime etc.. As mentioned earlier, in FONEMA this is determined by the geometry of the mirror and collimator. The mirror is a fixed entity and only within the limits of what can be done with the collimator is the geometric factor adjustable. One of the design criteria for FONEMA was to be able to make fast measurements of plasma phenomena. To do this accurately, however, you need good statistics that only come about from a reasonable number of counts, so it is essential that the geometric factor is kept as high as possible. For the FONEMA instrument the highest particle flux rates will be from the solar wind direction possibly reaching rates of $10^9 cm^{-2}s^{-1}$ during periods of high solar activity. This value multiplied by the geometric factor will give the count rate for the detector. The electronics aboard FONEMA will only be able to cope with a count rate of $10^5 s^{-1}$, this means the maximum value that the geometric factor can take, over the angular range of the highest flux, is $10^{-4} cm^2 sr$.

The total geometric factor for the instrument is found by finding the geometric factor of one theoretical channel through the collimator system and multiplying by the total number of these channels. For a single channel through the collimator, assuming square holes, the geometric factor (*gf*) is defined as the open area of the exit aperture (*A*) multiplied by the solid angle (*SA*) which it can see:

$$gf = A \times SA \qquad (3.4)$$

The area, *A*, is simply the square of the length of the side of a hole and the solid angle, *SA*, applying the small angle rule, is the same area over the square of the plate separation. Therefore,

$$gf = \frac{d^4}{l_c^2} \qquad (3.5)$$

where d = length of side of the square collimator holes and l_c = length of the collimator. All of the preliminary calculations for the instrument proposal were carried out assuming circular holes. However, the use of square holes has no detrimental effect on the operation of the collimator and increases the available hole area in the final plate by 27.3% and the geometric factor by 62.1%.

Here it can be seen that if the geometric factor is to be kept high then the value of l_c must be kept down. Hence, there is a compromise between reducing the spot size by increasing l_c and increasing the geometric factor by reducing l_c. The requirement for a greater geometric factor meant that the final solution was for a collimator length of 8mm using square holes of 136μm giving a spot size of 1.02mm. From equation 3.2 this gives the geometric factor for a single channel perpendicular to the image plane as 5.345×10^{-8} cm^{2}sr. For non perpendicular channels, as the angle to the normal increases, the finite thickness of the individual shims means that the open area of each hole decreases and hence so does the geometric factor. A discussion of the relative importance of this effect is given in a later section in this chapter. The total geometric factor for the collimators is shown in Table 3-2.

Of course, the geometric factor could be increased further by placing more holes in each plate, but as the plate area is fixed, this only means a greater hole density. This will require more plates within the collimator design if suppression of strays is to be maintained. Preliminary computer models of a simple 7 hole collimator showed that a five plate collimator with a hole density of no greater than approximately 20% was the best compromise. It is possible to keep the hole size the same on the rear plate, maintaining the optimum density, and increase the size of the holes in the front plates of the collimator, making the area of holes proportional to the distance between the plate and the image plane. This will increase the geometric factor, but again only at the expense of the spot size. But this method would also require more plates to be added to the collimator.

3.2.5 Pattern Design

It is important in designing the pattern that the hole density is kept as constant as possible. If it is not then the 4π sampling of the instrument would not be uniform. The best way to do this is to use holes arranged in a 6 fold symmetry arrangement, i.e. at the centre and vertices of a hexagon. However this has problems when trying to fit this arrangement in the shapes defined by the limiting rays. For this reason it was decided to use equidistant rows with a suitable number of holes in each row to maintain a density balance. Figure 3-7 shows the final pattern for the collimator. This is the plate closest to the electrostatic mirror, which is 34mm from the image plane, the length of the side of each hole is 0.136mm.

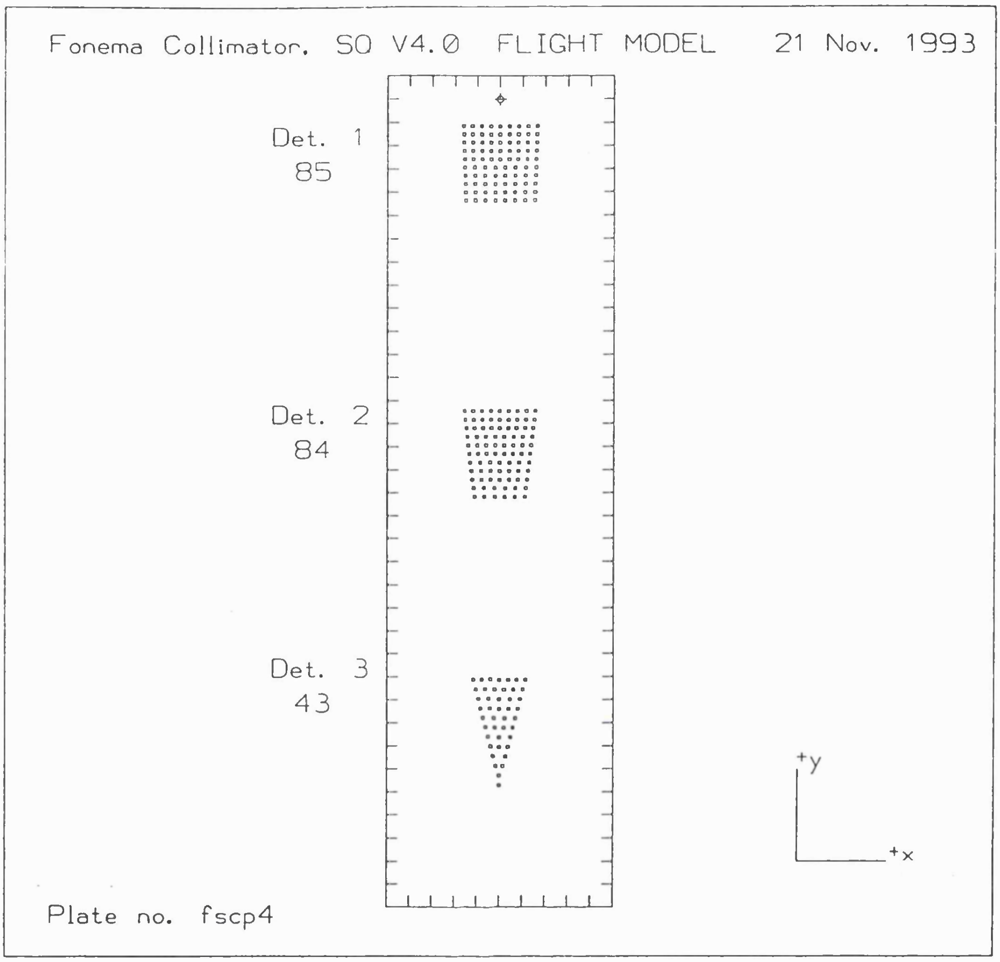

Figure 3-7. Hole pattern for the flight collimators showing number of holes for each of the 3 detectors.

Detector	s, mm^2	hole density, %	No. of holes	GF / cm^{2}sr
1	7.973	19.7	85	4.124×10^{-6}
2	7.835	19.8	84	4.237×10^{-6}
3	4.118	19.3	43	1.869×10^{-6}

Table 3-2. Exit area, s, hole density, number of holes and geometric factor for the 3 detectors within a single FONEMA collimator block. The geometric factors are the total of the individual channel values calculated in the next section.

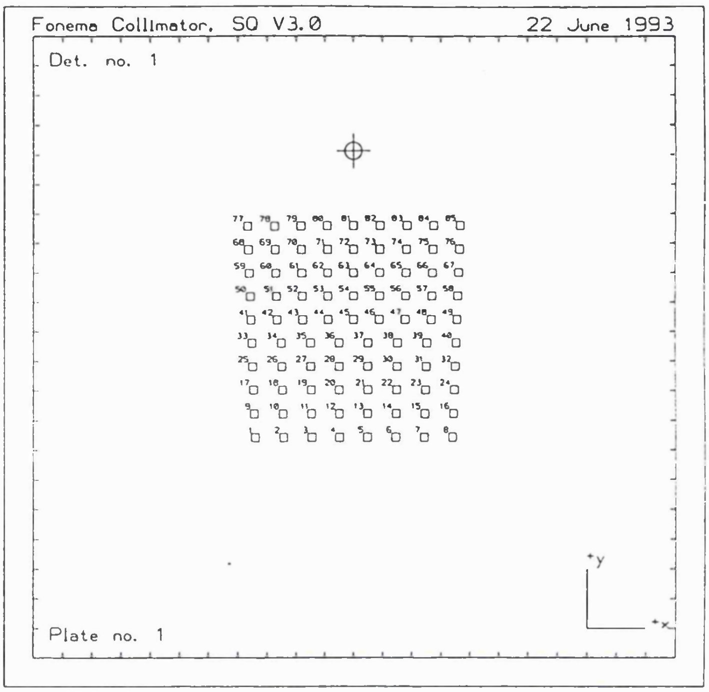

Figure 3-8. Hole pattern for Detector 1.

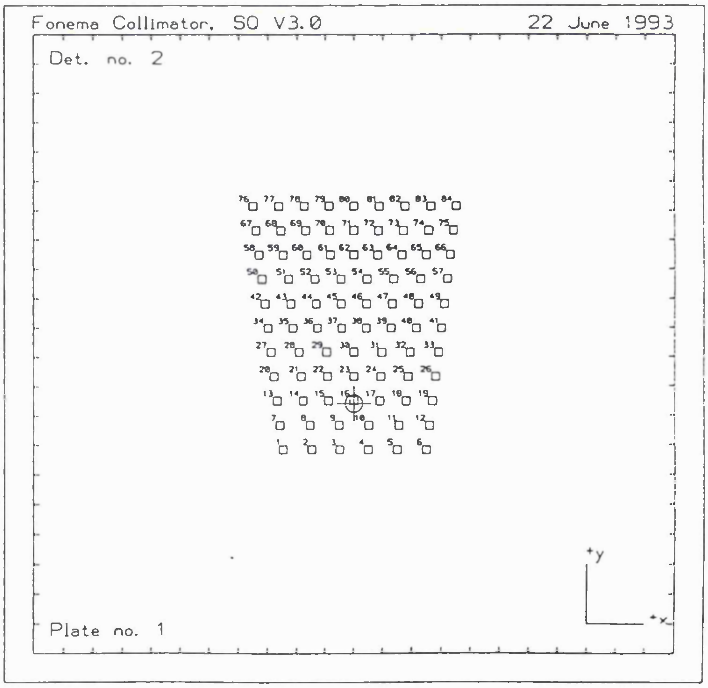

Figure 3-9. Hole pattern for Detector 2.

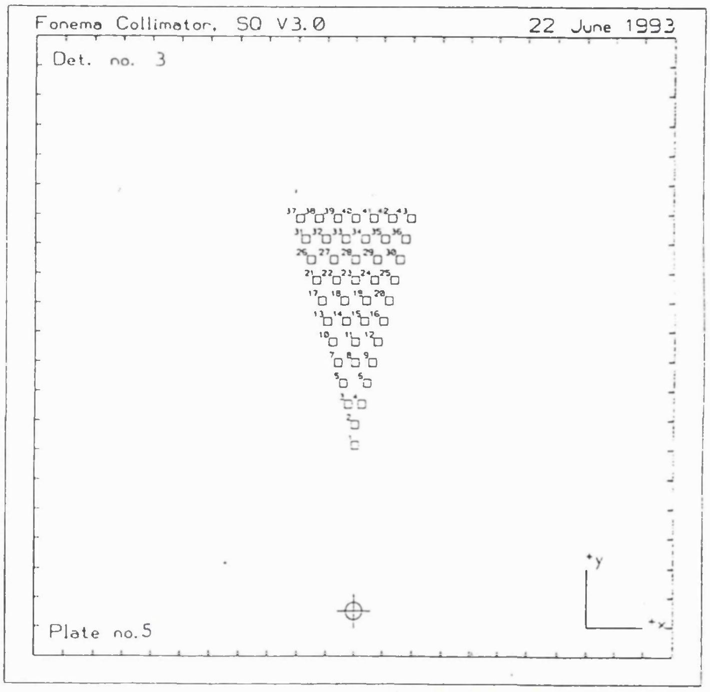

Figure 3-10. Hole pattern for Detector 3.

3.2.6 Variation of Geometric factor across pattern

The geometric factor for a pair of holes in parallel plates of negligible thickness whose centres lie on a normal is given by equation 3.5. If the centres are such that the channel produced through the collimator is no longer normal then an additional factor is needed to account for the angle, θ, from the normal:

$$gf = \frac{d^4}{l_c^2}\cos^2\theta \qquad (3.6)$$

If the finite thickness of the shim material is included in the calculation it can be shown that the geometric factor is best described by the expression:

$$gf = \frac{\cos^3\theta}{l_c^2}\left[d^2 - dt\sin\theta\left(|\cos\phi| + |\sin\phi|\right) + t^2\sin^2\theta\left(|\sin\phi\cos\phi|\right)\right]^2 \qquad (3.7)$$

where ϕ is the azimuthal angle, defined as that angle between the side of the hole and the projection of the line joining the centres onto the plane that contains the hole. A plot of the geometric factor versus ϕ for several values of θ is shown in Figure 3-11. This plot is for an 8mm long collimator with 136μm square holes, the thickness of the individual plates is 50μm.

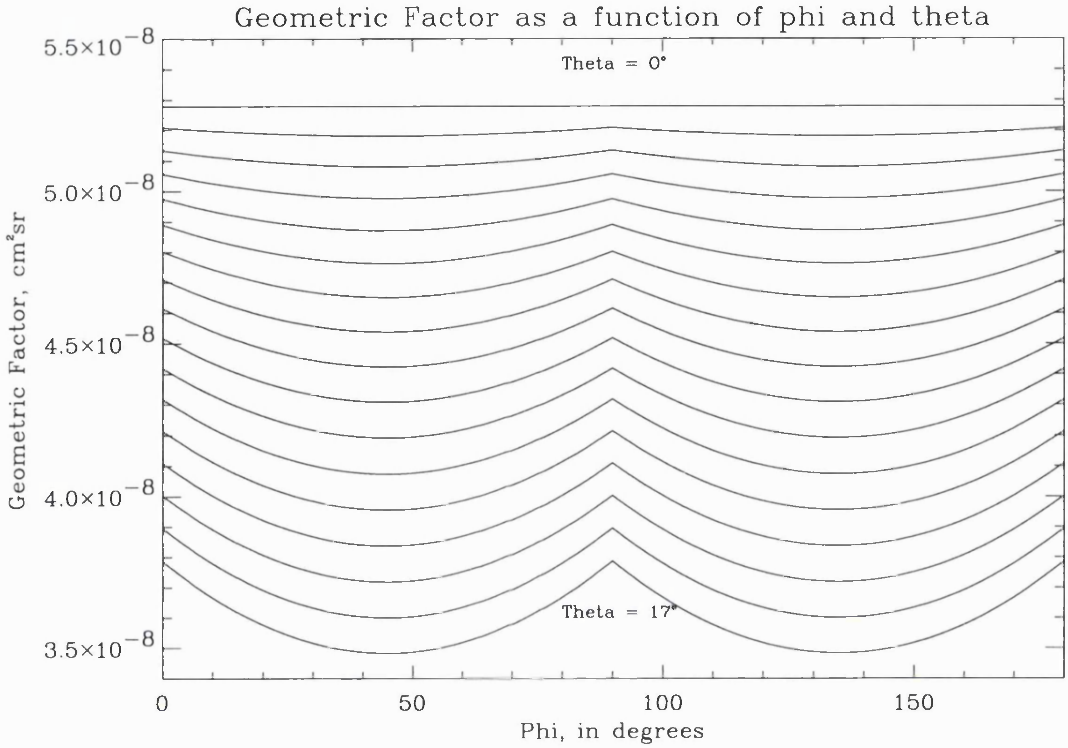

Figure 3-11. The geometric factor as a function of ϕ for values of θ ranging from 0° to 17°. The collimator is 8mm long, with 50μm shims and 136μm squares, hence the 90° repeat pattern in ϕ.

By calculating the θ and ϕ angles for the individual holes the geometric factor of each individual channel can be estimated. Figure 3-12 shows the geometric factor plotted against hole number, as shown in Figure 3-8 to Figure 3-10, for the 3 detectors. The geometric factor given in Table 3-2 is the sum of these individual geometric factors, taken over each detector.

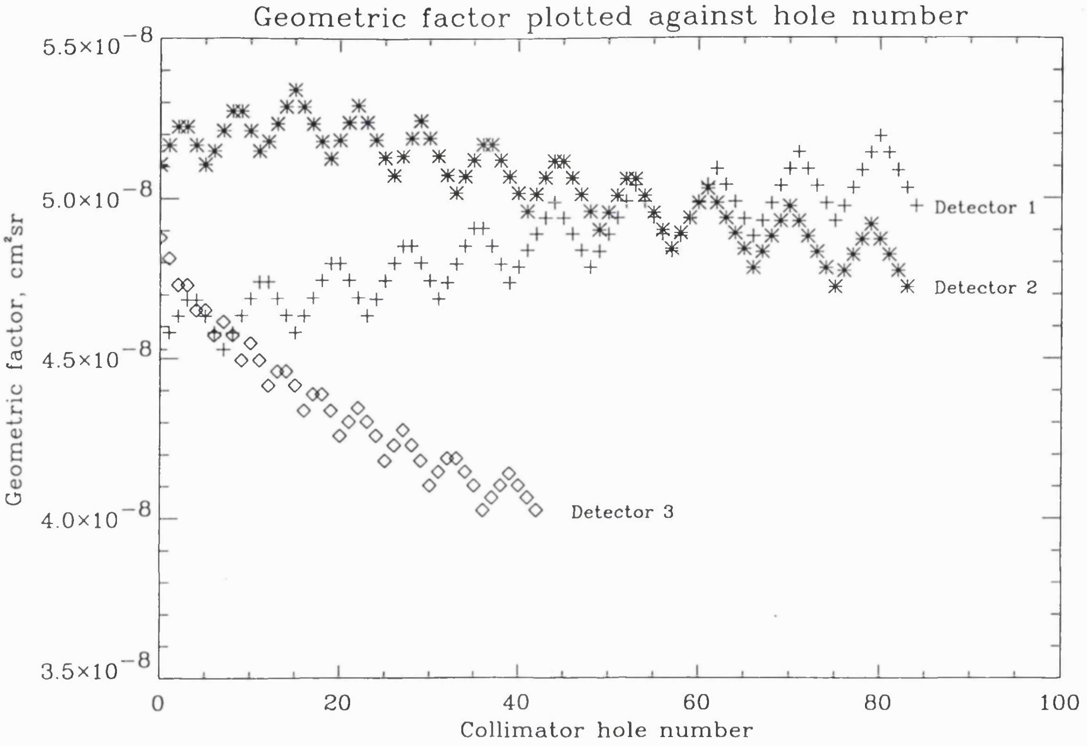

Figure 3-12. Calculated geometric factors for individual holes in the FONEMA collimator.

3.2.7 Theoretical model

After deciding on the positions of the holes on the two fixed plates at the front and the rear of the collimator the remaining plates must be positioned. The front plate refers to that plate closest to the electrostatic mirror and furthest from the image plane of the detector. Figure 3-13 shows the front plate, rear plate and an intermediate plate. If a particle is not to stray and create noise on the image it is important that if it passes at the extreme angle through the first 2 plates it will still not reach the next hole along in the following plate. It can be seen from the diagram the finite thickness of the shims used in the manufacture of the collimators is not considered, allowing for considerable simplification. Symmetry meant that the model could be reduced to a simple 2D model, even where square holes are considered rather than circular holes (initially circular holes were preferred because of ease of construction but this simply wasted the aperture area available; a square spot also matched up with the inherent square pixelation of the imaging detector).

Let s be the minimum distance between 2 holes in the collimator (see Figure 3-13) and a the length of the side of one of the square holes. If the intermediate plate is placed at l_n such that the limiting maximum angular range allows no stray holes then the plate position is simply given by:

$$l_n = \frac{a l_{n-1}}{a+s} \qquad (3.8)$$

where l_{n-1} is the position of rear plate (for each pair considered).

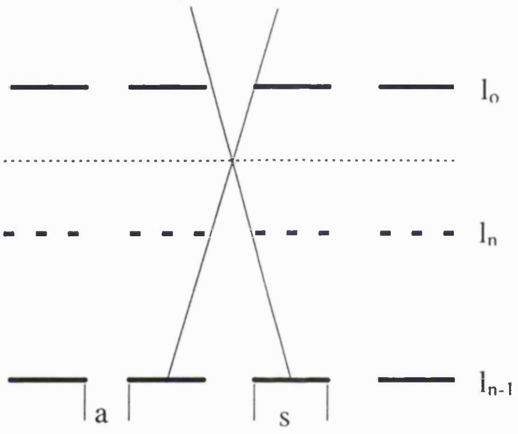

Figure 3-13. Simple 2D collimator with plate thickness assumed as negligible.

This tells us that by placing the second plate in this position it is impossible for any particles to pass through a wrong hole on the back plate if it passes through the correct hole on the second plate. Of course there is no guarantee of this as ions can pass through the front plate at any angle. So now the position of this intermediate plate is fixed and is treated as the back plate in the expression above and the process repeated. This is done until the calculated position is less than the thickness of the shim, in which case the rear face and back face of the same shim have satisfied the conditions for preventing a stray ion. The plate positions, as measured from the image plane, calculated using this method are shown below in Table 3-3. These results assume that the smallest separation equals the distance across a hole.

Plate number	Plate position in microns
1	34000
2	33938
3	33875
4	33750
5	33500
6	33000
7	32000
8	30000
9	26000

Table 3-3. Solution for simple 2D model of plane plate collimator system.

As mentioned this is a simplified model but will hold for a real collimator as long as the axis it is solved for is that which contains the shortest separations. For FONEMA this is in the x direction as defined in Figure 3-6. A more complex expression could be used to account for the modified angular range due to the finite thickness of the shims used, mainly because at angles that are not normal to the shims the finite thickness limits the angular range through the hole. However, microscopic inspection of the finished collimator holes show that due to the production technique the entrance area is greater than the exit area producing angled sides to each hole and not the ideal parallel sides. In this case the simple model will still apply as the exit hole from each shim will be represented by the theoretical zero thickness shim as long as we do not consider angles greater than the flaring angle of the holes. The trajectory with largest theoretical angular separation from the normal through the collimator which will still result in an undeflected particle hitting the detector plane occurs in collimator number 3 parallel to the y axis. This allows for an angle of approximately 30°, which therefore represents the largest angle that needs to be considered overall. When determining the position for the 3rd plate after the 2 outer plates are fixed, the angular ranges being considered are of the order of 7° but by the 5th plate the angle is up to this 30° level. Unfortunately the flaring angle produced on the real holes is variable and difficult to verify making the construction of a theoretical model that accounts for the physical characteristics of the collimator difficult. However, it is clear that the flaring angle is much less than the 30°

trajectory that needs to be considered. Assuming that an accurate theoretical model could be produced, the form of the solution would be similar to that shown in Table 3-3, which possesses the following difficulties:

1. It will be mechanically difficult to mount 2 shims less than 0.5mm apart (see Table 3-3), as in the first 4 shims. At a separation this small there are also considerable problems in insuring the flatness of the frames. This is especially true for the polycarbonate frame that is needed for the pre-acceleration region.
2. This design is very sensitive to a small movement of a single plate. If the conditions fail for one plate i.e. plate no. 2 then there is no guarantee that the others will work. This problem is surmountable to a degree by adding a margin to the hole separation in the calculation.
3. Aligning 9 plates to a high accuracy in a stack will be very difficult.

Although the first is a mechanical problem it highlights other areas of difficulty. Even if accurate mounting could be achieved the small spaces coupled with large comparative unsupported area of shim would mean that the collimator would probably be damaged during vibration testing of the instrument. Also, as described later, there is a need for a pre-acceleration voltage to be applied within the collimator structure, i.e. between 2 plates, and it is preferable for this to occur near the entrance of the collimator where the plate separations are at their smallest. This voltage will reach a maximum of 1753V, so assuming a maximum field to avoid any breakdown problems of 1kVmm^{-1}, this means that this field could only safely be applied between plates 7 & 8 or 8 & 9.

The remaining two problems are essentially concerned with horizontal and vertical alignment of all the plates. A slight misalignment or incorrect spacing of one of the plates, combined with the dependency on the previous plate for the solution to work, would mean that the whole collimator could fail. This problem could be alleviated by adding contingency to the separation of the holes, but increasing the hole diameter term would mean more plates in the final design. Besides, assuming that the positions of the shims would not be exact meant that it was important to show the effects of positioning on overall performance. The only way to discover the effect of such a movement would be to simulate the collimator in a computer model.

As the simulation had to be produced anyway it was logical to go on to design the collimator in this way.

3.3 Computer Modelling

This simulation package was called the FONEMA Instrument Collimator Simulator (FICS) and was written in VAX Fortran running under VMS on a VAX 780 system and later upgraded to work under VAX alpha machines. The principle of the model is as follows: an ion of known energy is given a random start position within a hole in the first plate and a random polar and azimuthal angle within a pre-defined solid angle. Its trajectory through the collimator is calculated and position recorded at the plane of intervening shims, or image plane if it gets all the way through. All information on the ion is recorded including initial position, initial velocity, final position, final velocity and status, i.e. whether it traveled through an incorrect hole to reach the image plane. Also produced is a full contour map of the output spot obtained as it would be recorded by the imaging detector. This model does account for the finite thickness of the shim by having each plate represented by two planes positioned 50μm apart, the thickness of the stainless steel shim used. Different flaring angles of the holes could be accounted for by using different hole sizes in the two planes representing a single plate. However, for much of the early work parallel sided holes were assumed. It also has options for including electrostatic and magnetic fields to simulate the effect of stray fields within the collimator and to predict the effects of the applied pre-acceleration field. Each of the 3 detectors that make up a single Thomson parabola analyser had to be treated separately within the simulator. This meant that any particle which could enter a hole in one detector and pass through holes in the collimator plates of other detectors would not show up in the model. However, the angle of trajectory required to perform this would mean that the ion could not possibly reach the image plane.

Now that a working computer model of the collimator was available it could be used to try to find a solution to the problem that had less individual elements than that of the theoretical solution. All that had to be done was to fix the two end plates and move a third plate within the gap to find a position where the number of stray ions relative to the number that were confined to the correct channel is at a minimum. This process could then be repeated again and again with additional plates until the percentage of strays is reduced to zero. To find the initial solution no stray fields or pre-acceleration voltages were introduced into the model to reduce the CPU time required. The philosophy adopted was to design the collimator using the simplest case and then use the simulator's other abilities to give pointers to the performance of the collimator or as a diagnostic tool. This was to some extent imposed by the time constraints of a flight project and by the amount of CPU time needed to run these simulations. Even with all the field code modules commented out of the simulation a run of 10000 events per hole would take nearly 30 minutes for the 3 plate solution and nearly 5 hours for the 4 plate solution. With an average of only about 3% of rays reaching the detector plane, i.e. 300 events per hole, and the random nature of the simulation the actual standard deviation on the data would be about 6%. The only way to decrease the statistical error is to go for longer and longer runs.

For the simulation runs the front and rear plates were fixed at 34mm and 26mm from the focus plane respectively. In the simulations used to decide on the plate positions the holes were 136μm squares. A third plate was then positioned and the simulator run. Figure 3-14 shows the data obtained for all 3 collimators. Figure 3-14 (a) shows the percentage of particles that went through wrong holes with respect to those that went through correct holes plotted against the position of a third plate moved between the 2 fixed plates at each end of the collimator. The curve for Detector 3 shows the standard deviation on the data as error bars, these would be typical for the other two patterns also. The error is calculated assuming binomial statistics, each particle in the simulator either reaches or does not reach the detector plane with a probability of success, p, determined from the result, i.e. the number of detected particles as a fraction of the number tried. The standard deviation, σ, is then given by equation 1-9 (*Lyons*, 1991).

$$\sigma = \sqrt{Np(1-p)} \qquad (3.9)$$

In this equation N is the number of input events tried by the simulator. For this plot the errors are added in quadrature to provide the error in the percentage. As N becomes very large and provided that the number of detected particles is small in comparison the distribution starts to follow Gaussian statistics and the standard deviation becomes the familiar √N. The minimum percentage occurs at around 31.5mm, this was then chosen as the position for the third plate. The plate pattern at the new position is recalculated so that the same holes in all three plates are co-linear with the focus position.

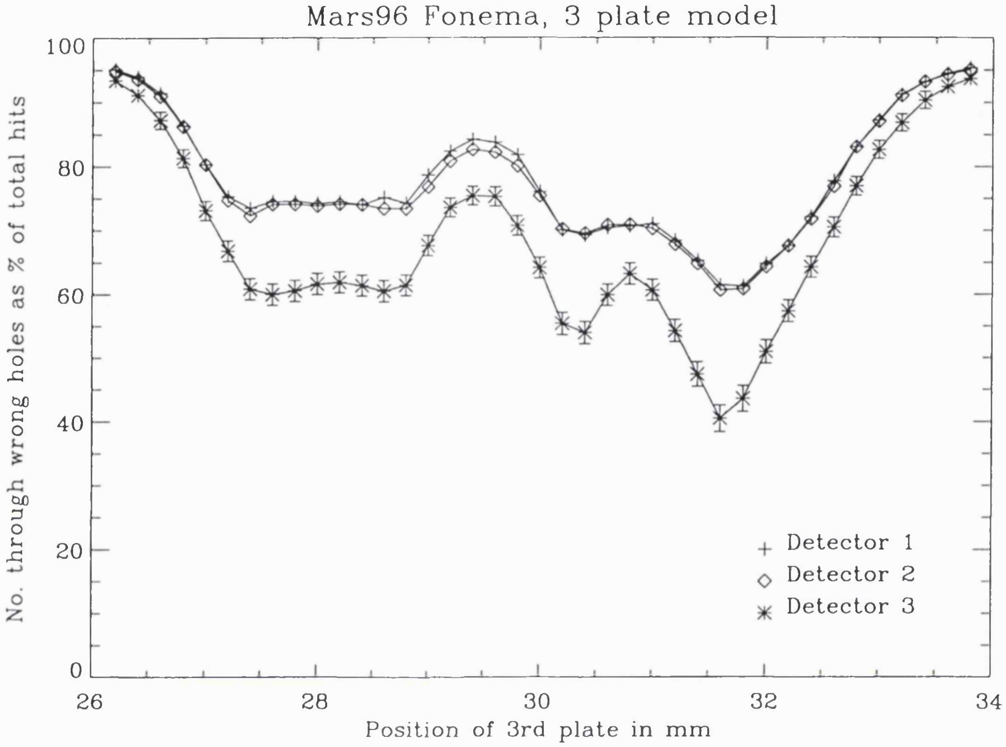

Figure 3-14. Percentage of ions passing through wrong holes to ions striking the image plane for a 3rd plate moving between two fixed plates as a function of position.

It would be possible at this point to then simply add the fixed third plate to the simulation and repeat the process used before for the fourth plate. In fact this method was used many times on early collimator designs. Unfortunately the time required to run the simulation is increased by so much by the addition of a further plate that a simpler method was sought. The output data from the initial simulation runs provided positional and directional data for those rays which had managed to reach the detector plane by traveling through the wrong holes in the three plate solution. Ideally, if enough particles are used in the initial simulation these rays will represent the only population that can pass through wrong holes and reach the detector plane. Therefore it is only necessary now to prevent these rays reaching the detector plane with the fourth plate. This method was implemented in the simulator. A smaller number of rays with a random angular spread about the seed rays became the new input to the simulated collimator. This method allowed many more particles to be tried in the velocity space which was most likely to produce stray events. The output from this method is shown in Figure 3-15 for the same 3 detectors, also shown is the four plate solution simulated with the original method. Also shown on this plot is the fixed third plate at 31.5mm. Note that the y axis for this plot shows a fraction of the very large number of recorded events that have passed through the wrong holes.

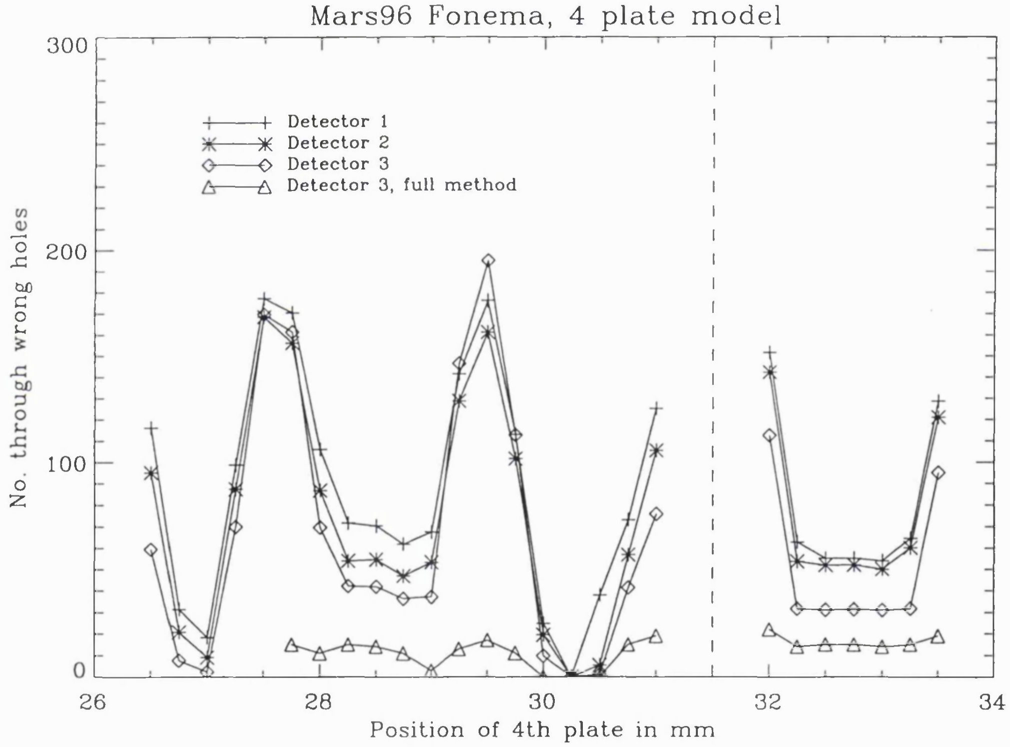

Figure 3-15. Number of ions passing through wrong holes for a 4th plate moving between 3 fixed plates as a function of position. This is shown for the 3 detectors in a single collimator, where the input rays are from the output files of the 3 plate simulation. Also plotted is the number of stray rays as a percentage of correct rays for detector number 3 with a moving 4th plate and random input rays at plate 1 as in the original method.

For the Detector 3 trace, using the original method, the *y* axis is a percentage of stray rays over those that behave in the required way. In this plot it can be seen clearly that the local minima occur at the same position of the fourth plate for all 4 curves with a minimum at approximately 30.25mm.

Figure 3-16 shows the stray particle count versus plate position for the addition of a fifth plate. It can be seen that there is a number of positions for which the count goes to zero. The fifth plate was eventually put at 29mm from the focus position. To confirm these positions as being suitable the three final solutions were simulated again with randomly oriented particles within the input plate holes. This was done for over 5 million particles per hole and resulted in no stray particles getting through. The confirmed plate positions are shown in Table 3-4.

Plate number	Distance from image plane, mm
1 (front plate)	34.0
2	31.5
3	30.5
4	29.0
5 (rear plate)	26.0

Table 3-4. Final plate positions for the FONEMA particle collimators.

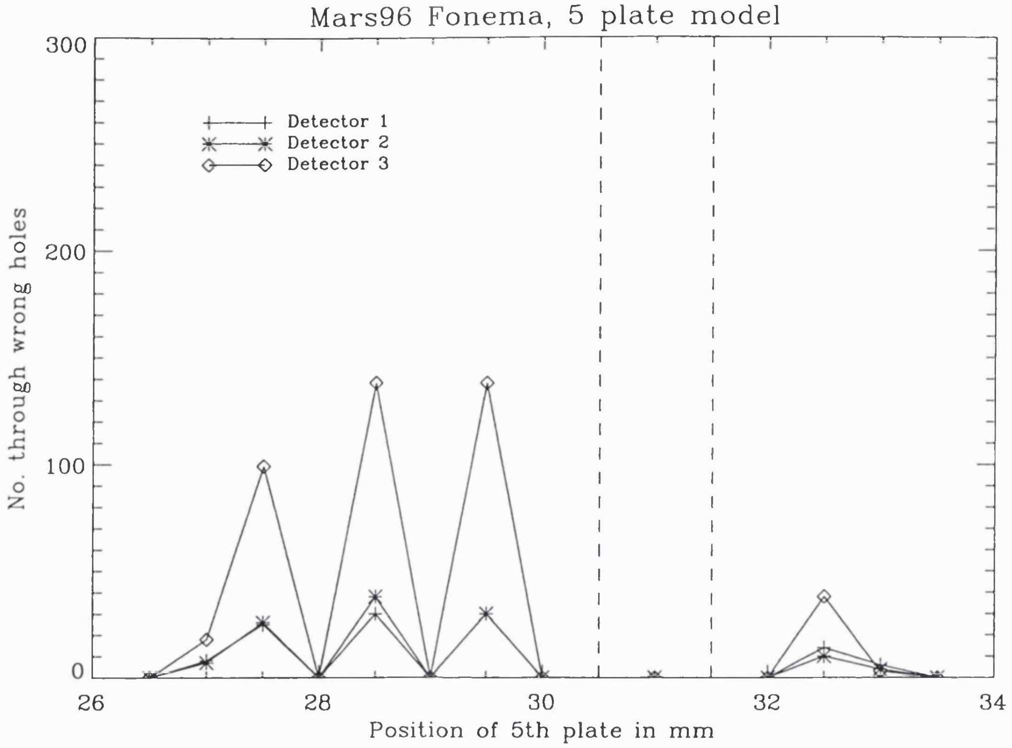

Figure 3-16. Number of ions passing through wrong holes as a function of the position of a 5^{th} plate moving between 4 fixed plates at 26, 30.5, 31.5 and 34mm from the detector plane.

A simple test of the accuracy of the simulation is to use it to confirm certain parameters that are known from theoretical considerations, i.e. the geometric factor variation from hole to hole. Figure 3-17 shows a plot of geometric factor as calculated from equation 3.6 against hole number for detector 3. Plotted on the same graph is the output counts for each hole from the simulator, for a constant input at each hole. The units and scaling are arbitrary on this plot. The general similarity between the two curves suggests that the simulator is producing results that agree with the theory. This is not surprising as the simulator is based on the same assumptions as the theoretical calculation of geometric factor, however it does confirm that the program is operating correctly.

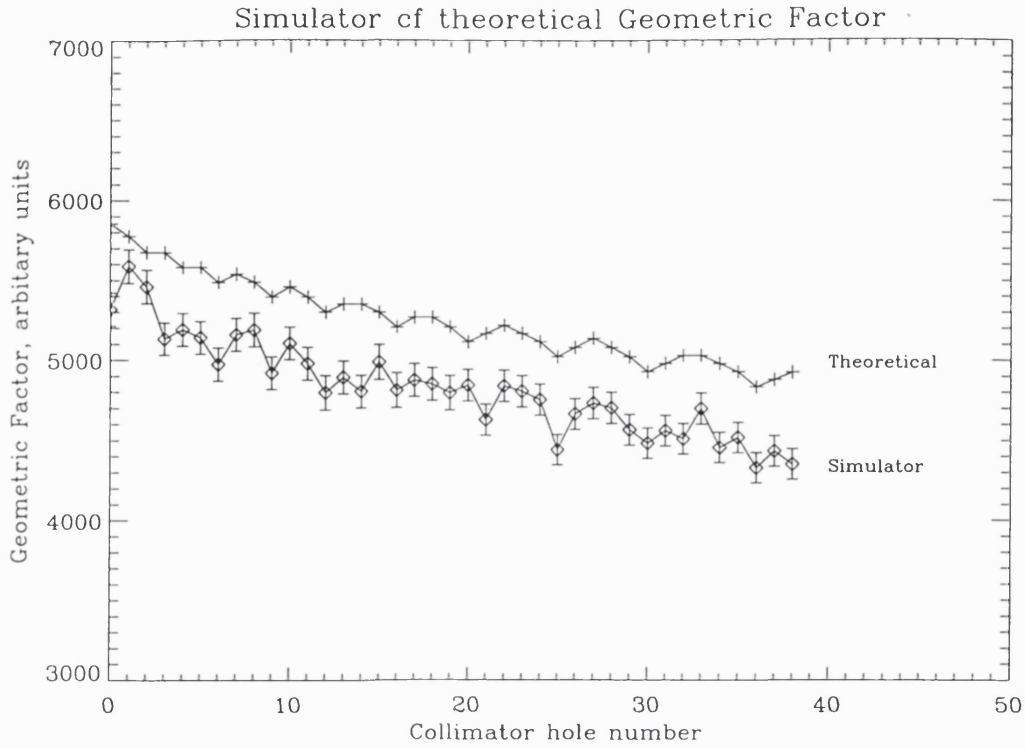

Figure 3-17. Plot of geometric factor, from the simulator and theory, versus hole number for Detector 3.

The conclusion from using the simulation shows that no stray particles get through the collimator if five plates are used in the positions shown in Table 3-4. In practice the collimators are constructed from elements which have a tolerance associated with them and the process of construction will also introduce errors. The simulator, however, can provide a tool to analyse the effect that any variations from the ideal situation may make. Firstly, the question of required tolerance on plate height is addressed. In this analysis the distance of the front plate from the detector plane is varied within the simulator from 32mm to 36mm, its nominal position is at 34mm. Although such large variations are improbable it was interesting to get an idea of how they effected the performance of the collimator. Variation of throughput as a function of plate 1 position is shown in Figure 3-18. The dashed lines in this plot show particles that have reached the image plane by passing through channels other than those intended. It can be seen that this does not occur until the plate height is over 1mm away from the nominal position. At this point though the number of counts getting through is down to ~50% of nominal.

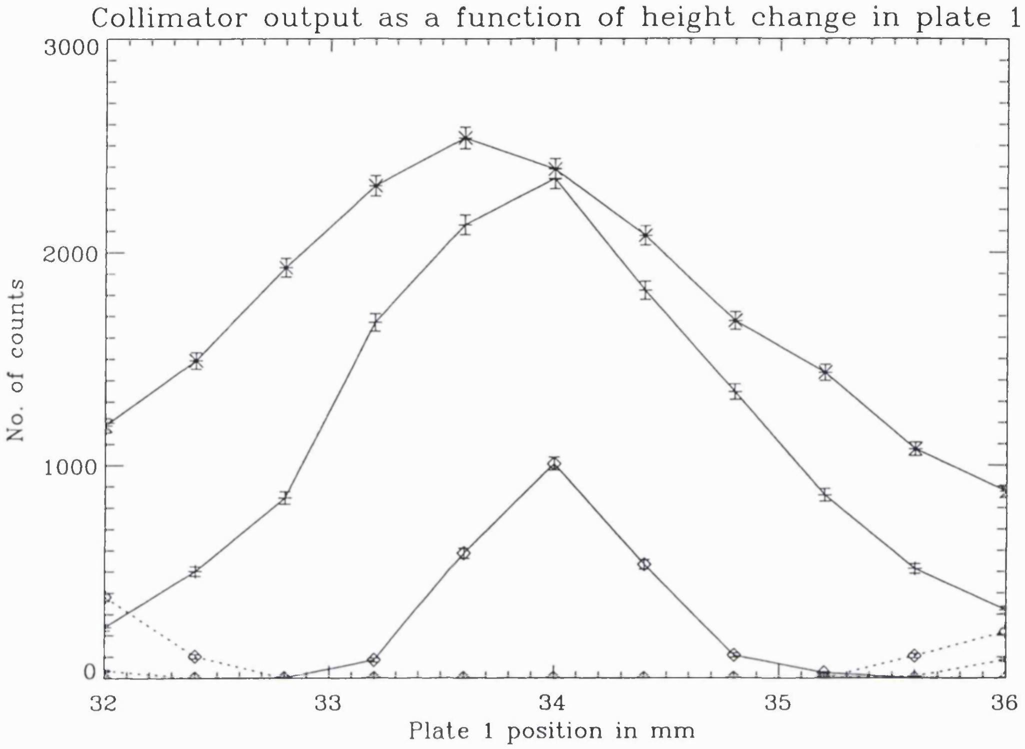

Figure 3-18. Number of particles reaching the image plane as the front plate height is varied for detectors 1 (×), 2 (+) and 3 (diamonds). The dashed lines show the number of particles that reach the image plane after passing through the wrong holes.

In Figure 3-19 more detail is shown for detector 1, covering only a ±1mm movement in the front plate of the collimator. It can be seen that for movements of less than ±200μm the variation in overall output varies by less than three σ of the nominal (error bars on plot). This analysis was repeated for other plates within the collimator with a similar conclusion. This then represents the tolerance that needs to be met in manufacture. The final tolerance on the height of the overall stack was expected to be less than ±100μm for all collimators, so no problems should arise from variation in plate height.

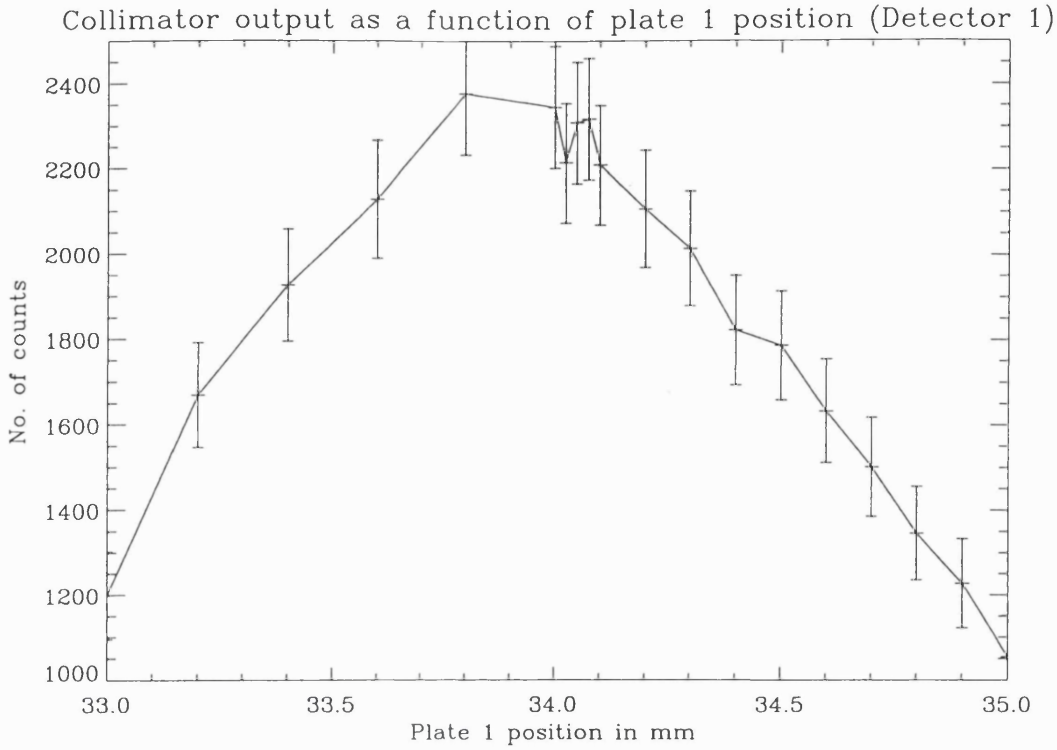

Figure 3-19. Number of events output from the collimator of Detector 1 versus position of plate 1 (nominally at 34.0mm).

Simulations were also made for a shift of plate in the plane of the hole pattern. Figure 3-20 shows the reduction in output counts versus shift in +X, ±Y and X=Y (see Figure 3-10 for explanation of axis). A relative shift in position of just 40μm, in only one of the five plates, can result in a reduction of effective geometric factor of 20%. This meant that the collimator production method had to allow final plate alignment with an accuracy of the order of 10μm.

So far only the total counts output have been discussed. Because both the change in height and the lateral shift in any plate simply represents a reduction in available area through which the particles can go, the relative reduction for single channels is the same. This also explains why the sensitivity to a change in height, and hence tolerance needed, is so much less than for the lateral shift.

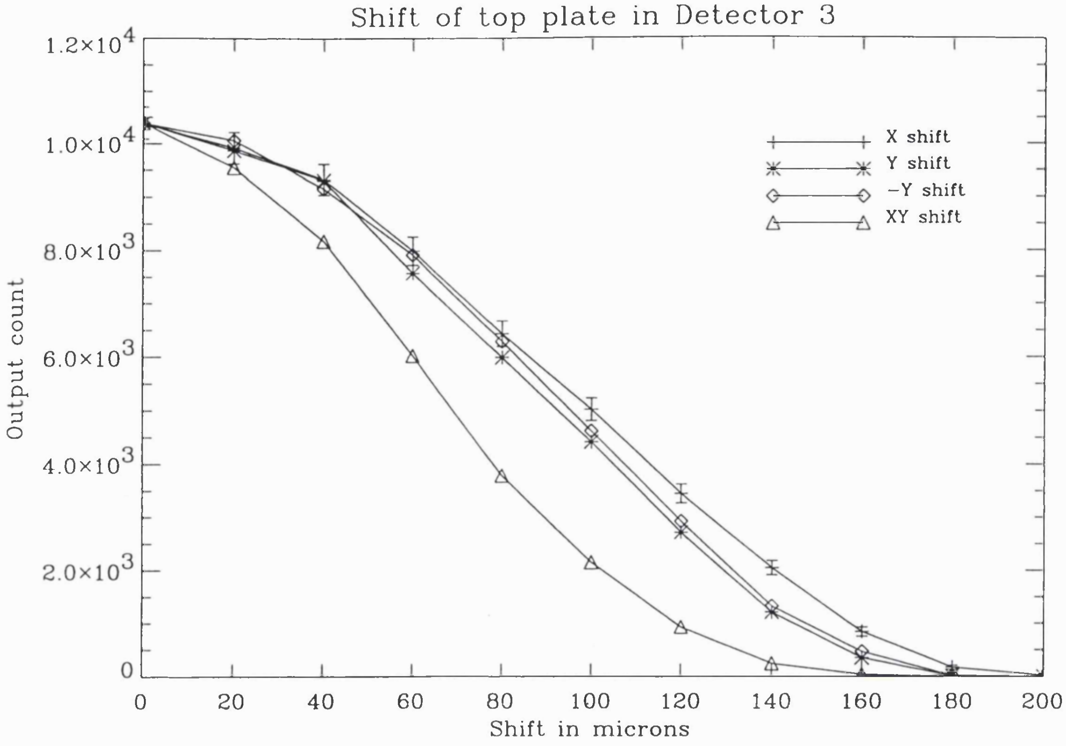

Figure 3-20. Throughput of collimator as a function of a lateral shift in X, +Y, -Y and X=Y.

3.3.1 Pre-acceleration within the collimator

In Chapter 2 it was seen how the energy resolution of the instrument could be made more uniform across the energy range by application of a pre-acceleration to the particles. This acceleration must be applied before the deflection fields are reached i.e. within or before the collimator. The need to test the analysers as individual units and lack of space for other structures meant that the only practical solution was to pre-accelerate within the collimators. Ideally the pre-acceleration field should act along the particle trajectory so as not to introduce a transverse deflection. As the collimator channels are converging the field would have to be maintained between two meshes whose surface is at all times normal to the ion trajectory. This surface is simply a spherical section centred on the collimator focus positions. Space limitations within the collimator, however, meant that separate surfaces could not be considered, and there was also concern about the introduction of two more meshes, reducing transmission and introducing possible scatter. The other option of making two of the collimator shims with the correct surface profile was considered but deemed impractical within the timescale. To laser machine the collimator holes, accounting for the final position, and then form the shims into the correct shape was not believed to be possible to the necessary accuracy. Pre-forming the shims and then machining the holes could not be done without moving the shaped shim underneath the laser keeping the surface to be worked on at the same laser focus and normal to the beam.

A compromise was made and the collimator was designed so that pre-acceleration would occur between the first two parallel plates of the collimator. This had the disadvantage that it opened up the field of view of low energy ions beyond that of the collimator design. These ions, arriving at a large angle that would normally prevent passage through the collimator, on passing through the front plate would be accelerated toward the second plate reducing their angle to the normal and possibly providing passage. The final energy of these ions would also have been increased by the non parallel electric field they had encountered. Whilst these ions pass, other lower energy ions on a valid initial trajectory from the mirror would also be deflected off course and not be detected. Thus, the transmission efficiency for the collimator becomes energy dependent, as does the collimator field of view, making the analysis of the final data more complex. For very low energies, especially in Detector 3, this can result in the effective loss of detector coverage over some input directions.

Placing the pre-acceleration region further back into the collimator, however, has problems more difficult to overcome. If the pre-acceleration region occurs between plates 2 and 3, only plates 3, 4 and 5 will effectively collimate low energy ions to the focus position. As can be seen from Figure 3-14 this could allow for a significant proportion of ions reaching the detector plane through the wrong holes, these will then become noise events on top of the real events. This scenario becomes worse as the pre-acceleration is moved further back through the collimator. Another effect of having the pre-acceleration within the collimator is that the spot size will be enlarged at lower energies.

3.3.2 Effect of stray magnetic field within the collimator

After passing through the collimator the ions are deflected in a magnetic field. Despite shielding it is impractical within the FONEMA design to exclude all of the field from outside the region used for deflection. On the input side of the magnetic deflection region some of this stray field appears in the collimator. As with the pre-acceleration voltage this will produce large enough deflections of the lower energy ions to prevent passage through the collimator. Using the simulator it is possible to introduce a representative magnetic field to produce an estimate of the effect this field has on the collimator transmission. This can then be used to estimate what level of field it is possible to tolerate. Efforts were then made to control the final flight configuration such that the magnetic field configuration was below this level. Measurements of the magnetic field in the final flight configuration are presented in Chapter 4. The maximum field within this region is approximately 3mT parallel to the collimator shims. In mode 2 where the minimum energy is 54eV this magnetic field combined with the pre-acceleration field will produce a deflection of less than 1μm for all ion species. Beyond the two initial plates in the collimator the ions have a minimum energy of 292eV. In travelling the 5.5mm from plate 2 to plate 5 in the collimator a proton will undergo a deflection of 8μm and a O^+ ion a deflection of just 2μm. This means a shift in the predicted position of the proton peak of less than 50μm and a possible 6% reduction in the geometric factor for protons.

3.4 Construction Techniques

As mentioned in section 3.2.1. the multiple plate collimator design depends on spacing the plates appropriately and accurately. It also depends on the hole positions on the plate being determined to a high degree of accuracy, in both a relative and absolute sense. To achieve this the shims would have to be attached to a solid frame, the thickness of which would reflect the separation between the plates. Three of the separating frames were produced from aluminium the fourth had to be constructed from polycarbonate to allow for the pre-acceleration potential to be applied across it.

To each frame a blank collimator shim was glued. These shims were cut out of 50μm thick stainless steel using a high powered infra-red laser (this is described in the next section). Completed plates were then accurately clamped to the laser facility on a specially produced manufacturing jig: basically this consisted of 2 independent spring clamps and 3 accurately aligned dowels for the clamps to work against. Using this method the accuracy of the positioning on the jig was found to be better than 10μm for all 5 plates.

During the simulation of a particular collimator the software automatically produces an array of points which define the position and size of each hole on each plate. Before producing the collimator pattern 2 reference marks, one at each end, are marked on the shim. The pattern of holes is then reproduced on the plates by moving the plate beneath the laser on an XY platform under computer control. After this the computer moves to the 2 reference marks in turn and a set of cross-hairs are moved to re-align to the original marks, a record is then kept of this position shift. Ideally there should be no need to re-align, in practice however there are many factors that can cause a shift, e.g. thermal expansion within the laser facility or mechanical noise causing physical shift of the plate, the jig or optical component, and electrical noise creating an error in the movement commanding interface or laser control electronics. The resolution of the XY table system is less than 0.25μm but the accuracy in determining absolute position is approximately 5μm. The overall error in the screw is less than 10 μm over the full travel of 200mm. Thermal drifts occur as the working volume of the laser heats up over the 70 minutes required to produce the hole array in a single plate. Normal practice was to run the laser for 2 hours each morning on dummy work pieces, this allowed an equilibrium temperature to be reached before the real machining started.

If a mechanical shift greater than 15 μm occurred during a pattern the plate would have to be scrapped and a reserve plate of the same type put in. This, however, meant a longer time was needed to produce the collimator escalating the thermal drift problem. It was only the thermal drift of the optical components that proved difficult to overcome. The problem was that it was important to produce at least one collimator, i.e. five plates, in the same working day which would take on average 5 hours or so. Unfortunately, even allowing a few hours warm up to try to reach thermal equilibrium, shifts of up to 5μm on an individual plate were not uncommon over the time periods needed to produce it. Health and Safety Regulations for the class of laser used combined with the environmental restrictions imposed in a dark clean room and the presence of sensitive optics made adequate cooling difficult to achieve. This meant having to accept a shift of up to 5μm within an individual plate and making use of the alignment marks to account for shifts occurring between plates due to drifting over a longer period. If it was required to remake a plate due to another error or an operator mistake the possibility of larger thermal drifts arose.

Assembling and gluing the stack of plates into a finished collimator was also carried out in the laser facility. This had the advantage that it was possible to make use of the magnifying camera system, used to monitor the laser machining, and the jig, which was also used for final assembly, did not have to be moved. The horizontal shift involved in changing the vertical focus of the camera optics was less than 2μm and predictable over the range of heights used. This allowed the alignment marks to be very accurately positioned as each plate was added to the stack. Plates were glued on one at a time with a 2 hour cure between each one. Essentially the system relied on the dowels for alignment but by applying slight pressure it was possible to move individual plates far enough to compensate for errors due to any shifts that had occurred during manufacture. Shifts during the following 2 hour curing phase were measured as less than 5μm, as were shifts during the following 24 hour period. This, of course, could only be measured on the top plate of the stack.

3.4.1 Laser Machining Facility

The laser machining facility consists of an infrared laser focused onto a moving table arrangement. The system incorporates a neodymium doped, yttrium-aluminium-garnet (Nd:YAG) laser which produces a near infrared, 1064nm wavelength output. This is a Q-switched laser producing a peak power output of 30kW at 1kHz with a minimum pulse width of 100ns in TEM_{00} mode. At the focus of the laser is a X-Y stepper motor driven table which can be moved with a resolution of 0.25μm. Variable table speeds mean that the movement of the workpiece under the laser can be matched with the Q-switch frequency of the laser to produce a smooth machining profile. Although the objective lens at the output of the laser can be changed and the focal length can be varied to alter the footprint of the beam, the most common arrangement is to use the minimum spot size of 25μm

FWHM. This minimum size is defined by the beam divergence component (≅ 20μm) and the diffraction limited resolution (≅ 5μm).

3.5 Optical testing of the finished collimators

The finished collimators were tested by placing a point source at the focus of each collimator detector pattern. Illumination was from a high powered LED, Phillips PLEDH314A, with the plastic lens removed and replaced with a diffuser behind a 1mm pinhole, this being comparable to the spot size produced by the collimator. Light shining through the holes would illuminate a CCD camera placed as close to the front plate as possible. An XY micrometer stage allowed the LED to be moved into the correct focus position. An image could then be taken and analysed to measure the relative throughput of each channel within the collimator. If the geometric factor through a single hole collimator is assumed from theoretical calculations and then measured on the same system an absolute geometric factor can be obtained for all the holes.

To insure that the LED was aligned in the correct focus position it was necessary to make sure that the image on the screen represented the maximum available light through each channel. Unfortunately, to do any data manipulation the image has to be acquired by the computer which is a slow process. To overcome this the video output from the CCD was monitored with a voltmeter measuring AC volts. Because the video output is an analogue signal, when the light level is at a maximum this produced the maximum voltage. This method was confirmed by taking images from the framegrabber at different intensities and comparing them to the output from the voltmeter. To compensate for the warming up of the camera system and any variation in light leakage the images were background subtracted. In addition the LED output showed a temperature coefficient of -0.75%°C^{-1}. Measurements of LED temperature were taken during the experiment using a Comark electronic thermometer, the data was then temperature corrected within the image processing software.

Once an image had been taken, using the CCD camera linked to a frame-grabber card, the data was analysed by computer. The program firstly performs a gamma correction on the image before fitting a gaussian and a constant background to each pinhole. This background is a combination of the CCD dark count and light reflected from within the collimator system. A correction is then made for the angular variation in output of the LED. This effect is greatest for detector 3 and is shown in Figure 3-21. Total transmission is given as the summed area of the gaussians obtained for each pinhole. Multiple experiments and analysis on a single hole collimator showed the repeatability of this method yields a standard deviation on the measured value of approximately ±1%. Table 3-5 shows the total transmissions for the twelve collimators selected for the flight model instrument.

Collimator	Detector 1	Detector 2	Detector 3	Analyser
FSC1	732730	739268	120709	U0l
FSC2	859900	886521	183416	L2l
FSC3	840812	860882	189941	U3r
FSC4	651444	716689	145205	U2l
FSC5	716618	745013	165402	U5r
FSC6	793315	789453	169386	U4l
FSC7	786685	817265	176193	L0l
FSC8	798306	785638	175232	U1r
FSC9	723569	784269	161456	L1r
FSC10	870778	832698	175117	L4l
FSC11	881870	892734	189303	L3r
FSC12	850025	885457	183514	L5r
Mean	792000	811000	169000	
Standard deviation	73000	61000	20000	
Range, %	-18 to +11	-12 to +10	-29 to +12	

Table 3-5. Measurements of total transmission for the 12 flight collimators (units are arbitary).

Collimator production was a very time consuming activity and the accuracy of the method was not as high as expected. It was hoped that the geometric factors as derived from the optical tests would all be greater than about 90% of the theoretical value. In the end it was necessary to except a lower level as the cutoff figure. Even then, the number of collimators produced using the final method was 16. The development work needed to get to the final method accounted for another 29 collimators, including 2 for the Engineering Model instrument and 12 for the Flight Spare.

Although the total throughput is within 10% of the nominal for all the collimators produced, the throughput of individual holes is more variable. Figure 3-21 to Figure 3-22 show the output from all the holes of the three detector patterns in a collimator, with the theoretical geometric factor for comparison. In Figure 3-23 it can be seen that for one hole at least the output is about one third lower than that expected. Any collimator with a single hole displaying less than 50% transmission was rejected. In practice this only happened once and the obstacle in the hole was moved with a high pressure air line. Unfortunately the offending article remained within the volume between the plates and the collimator had to be stripped down and rebonded.

The discrepancy between the experimental and theoretical value for detector 3 shown in Figure 3-21 was typical for all the flight model collimators. Detector 3 is more sensitive to misalignment as all of its channels are between 6.1° and 14.5° from the normal, which may be the cause for the discrepancy. Because it is always the last to be laser machined on each plate, a thermal drift due to the heating of the shim may produce a small shift in the hole positions relative to the alignment marks. This shift would have to be less than 10μm which is the accuracy to which hole positions are measured after they are produced. It is possible that this magnitude of shift between the top and bottom plate could account for the difference.

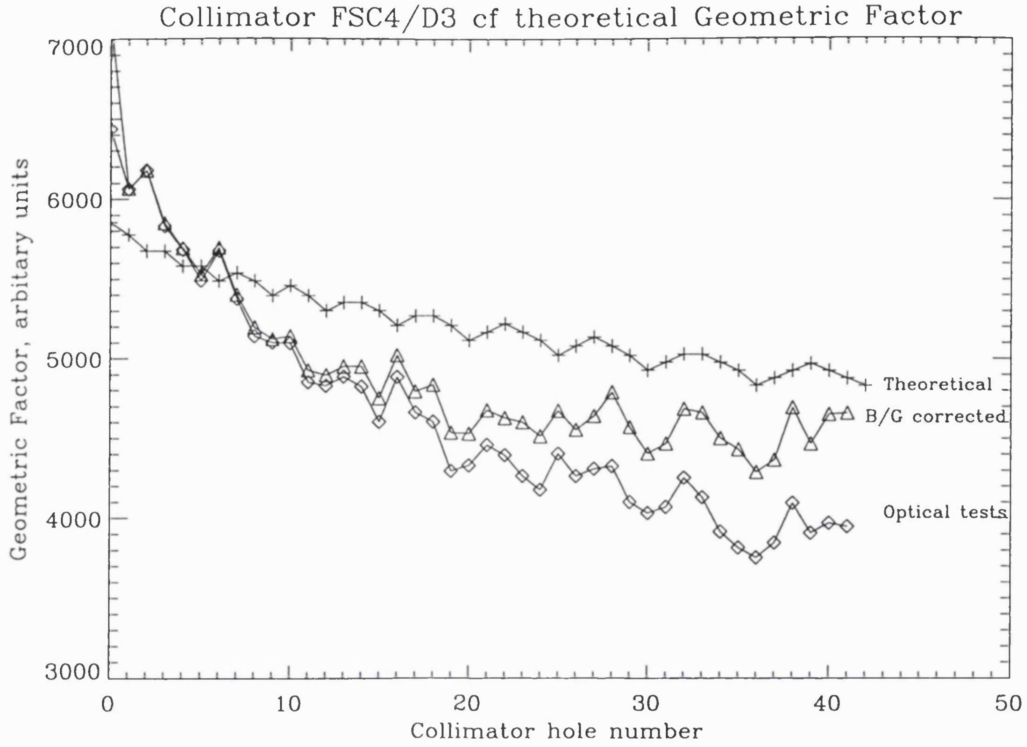

Figure 3-21. A plot of illumination levels through individual holes from the optical testing of collimator FSC4/detector 3 and theoretical values for comparison. The lower curve shows the data before being corrected for the angular dependence of the LED output.

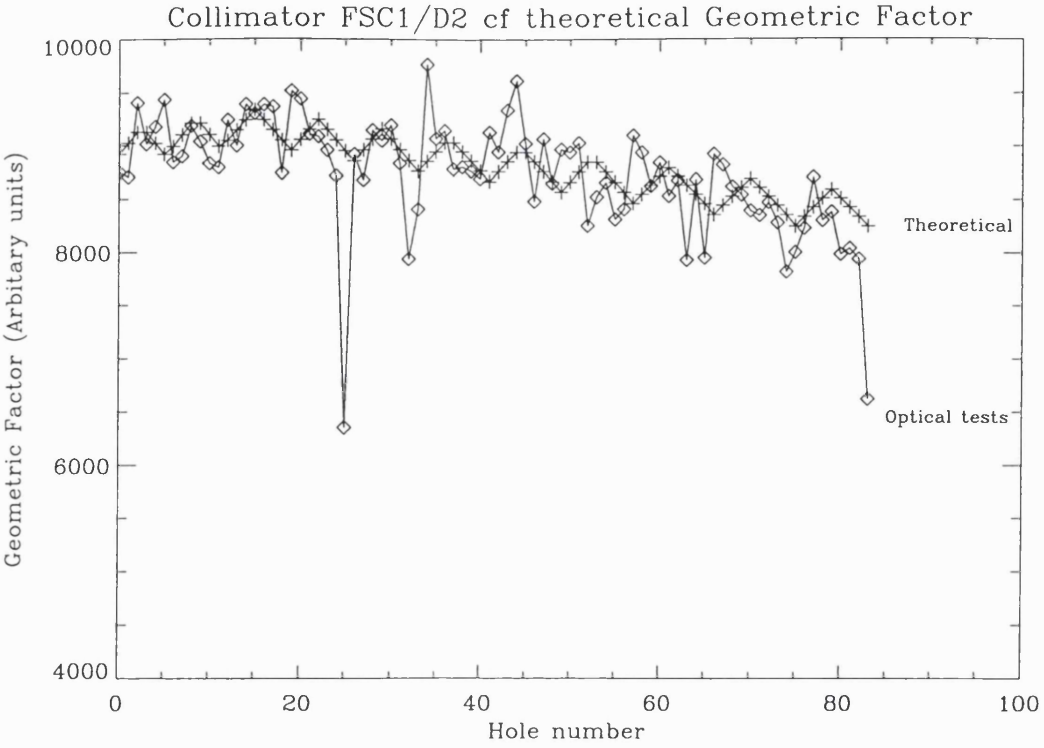

Figure 3-22. A plot of illumination levels through individual holes from the optical testing of collimator FSC1/detector 2 compared to the expected theoretical value.

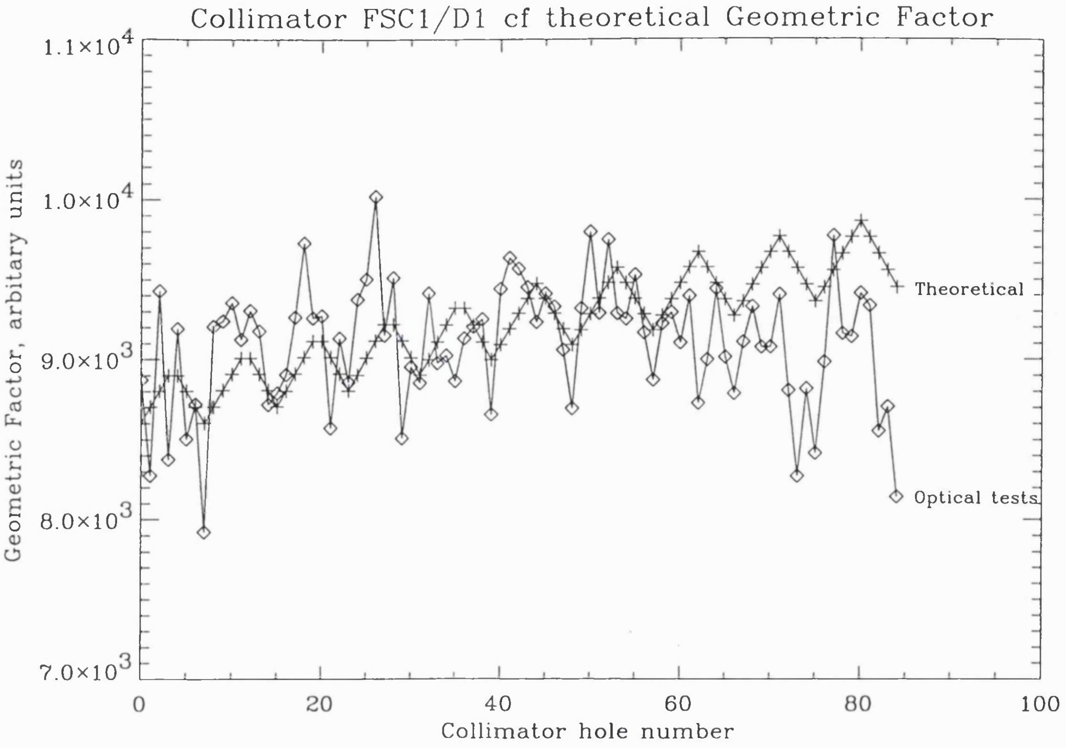

Figure 3-23. A plot of illumination levels through individual holes from the optical testing of collimator FSC1/detector 1 compared to the expected theoretical value.

3.5.1 Reflection of ions within the collimator

It is possible for the ions to reflect off the sides of the holes within the collimator and produce background events. If a single channel of a collimator is considered as a long square section tube the total internal area is $4 \times L_c \times d$, where L_c is the length of the collimator channel (approximately 8.0mm) and d the length of the side of one hole (1.36×10^{-1}mm). This yields an available area of 4.352mm^2. Reflection will only occur at surfaces that ions make glancing angles to, i.e. the sides of the holes within the shim. These present a possible area of only 0.136mm^2, for all five plates. Therefore every ion has a 1/32 chance of hitting one of these surfaces once it has entered the collimator. However, according to *Kaminsky* (1965),an elastic collision of an ion with a metal surface occurs only at glancing angles and when the surface irregularities are smaller than the de Broglie wavelength (this is ~10^{-9} mm for a 100eV hydrogen). A typical cleavage surface of an ionic crystal will exhibit irregularities of the order of 10^{-7}mm. Assuming the cleanest surfaces within the laser machined areas are of this order of flatness no specular reflection of ions is expected within the collimator.

4. Magnetic deflection

4.1 Design considerations

In the ideal Thomson Parabola analyser outlined in Chapter 2 the magnetic field is constrained to a small volume of space far enough from the image plane such that deflection angles are small. This configuration allows for simple interpretation of the final positions and accurate mass determination with high resolution. Initially, it also allows for a simple estimation of the required field strength and hence the magnets needed. However, for FONEMA the electrostatic mirror design defines the analyser focus positions, between 90 and 100mm from the instrument axis, and the overall dimensions of the analyser, i.e. it must fit between the focus plane and the mirror. This reduced space and the relatively large image plane required, determined by the spot size and required geometric factor, means that the analyser geometry needed will possess large deviations from the ideal. Firstly the design confines the magnetic field region to be less than 20mm from the image plane. In order to achieve the required deflection it is then necessary to increase the integrated magnetic field which the particle will experience by increasing the length of the deflection region. Also the solid angle of the reflected particles as determined by the collimator gives a minimum limit to the gap between the magnets. Generally, the smaller this gap the more uniform the field is over the volume covered by the ion beam, and this means less dispersion due to different ions experiencing different field configurations. However, the non-uniformity in the field is worst at the edges of the magnetic volume so it is important that the gap is larger than the distance across the beam.

Stray fields can also represent a problem and should be controlled. EMC (electromagnetic compatibility) requirements of the spacecraft require that no static magnetic field above a certain value exists beyond the bounds of each instrument. This is to prevent contamination of instruments that are measuring the natural magnetic phenomena and to stop deflection of low energy particles that will change the effective field of view of other particle detectors. Within the instrument itself problems due to stray fields can occur in two regions. Firstly, if the magnetic field in the region between the collimator and mirror is too large it can prevent low mass, low energy ions from getting beyond the first plate in the collimator: this has already been discussed in Chapter 3. The other problem area is possible deflection of electrons as they exit the rear of the MCP stack. These electrons will have initial energies ranging from a few eV to a few tens of eV and will be susceptible to even small fields.

4.2 Initial estimation of the required field

In Chapter 2 the idealised equation for deflection due to magnetic field, as formulated by *Sakabe et al.* (1980), was introduced. This relationship assumes a constant value for magnetic field within the deflection region and zero field at all other places, which is valid for small magnet gaps and large area pole pieces. This method is accurate to within 1% if the total angle of deflection is less than approximately 7°. This rises to 10% for a deflection angle of 30°. This is the expected angle of deflection that will be experienced by low energy protons within the FONEMA instrument.

Referring to Figure 4-1 it is simple to derive the formula used by Sakabe. The force experienced by an ion passing perpendicular to the magnetic field, B_z, at velocity, v, is given by:

$$F = qvB_z \tag{4.1}$$

where q is the charge on the ion and the force, F, is directed perpendicular to both B_z and v. This acts as a centripetal force on the ion mass, m:

$$F = \frac{mv^2}{r} \tag{4.2}$$

The ion therefore moves in a circle with the gyroradius, r, given by:

$$r = \frac{mv}{qB_z} \tag{4.3}$$

Now, from the diagram, the deflection y can be derived from the assumption that for small angles both $\sin\theta$ and $\tan\theta$ equal θ. It is also assumed that the tangents to the trajectory at the input and output of the deflection region meet exactly half way through this region.

$$\frac{y}{\frac{l_B}{2}+L_B} = \tan\theta = \theta = \sin\theta = \frac{l_B}{r} \tag{4.4}$$

By rearranging and substituting for *r* from equation 4.3, this gives the deflection as:

$$y = \frac{qB_z d^2}{mv} \tag{4.5}$$

where:

$$d^2 = l_B\left(\frac{l_B}{2}+L_B\right) \tag{4.6}$$

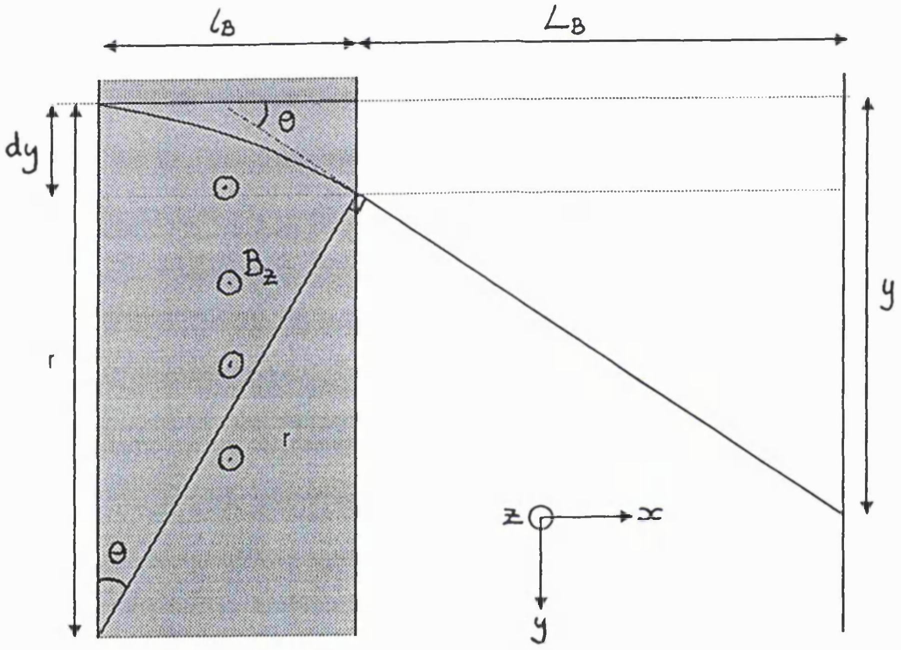

Figure 4-1. Ion trajectory through a constant magnetic field region.

Of course it is possible to solve for θ using *r* and l_B, as in equation 4. Then knowing that:

$$\tan\theta = \frac{y-dy}{L_B} \tag{4.7}$$

and that,

$$dy = r - r\cos\theta \qquad (4.8)$$

it is possible to solve for y without making use of the small angle assumption and without the need for assuming the position of the intersection of the input and output trajectories:

$$y = L_B \tan\theta - r\cos\theta + r \qquad (4.9)$$

This provides true deflection values even when the deflection angle within the magnetic field is going to be greater than a few degrees. By fixing l_B different values of L_B are obtained as a function of the magnetic field B_z. This is done for a value of y that corresponds to the lowest energy proton undergoing full deflection in mode 2, i.e. a 292eV proton with a deflection of 14mm. A plot of this data is shown in Figure 4-2. From the overall geometry the addition of l_B and L_B has to be less than about 30mm: this means, looking at Figure 4-2, that the field needed is likely to be in the range of 1000 to 3000 Gauss.

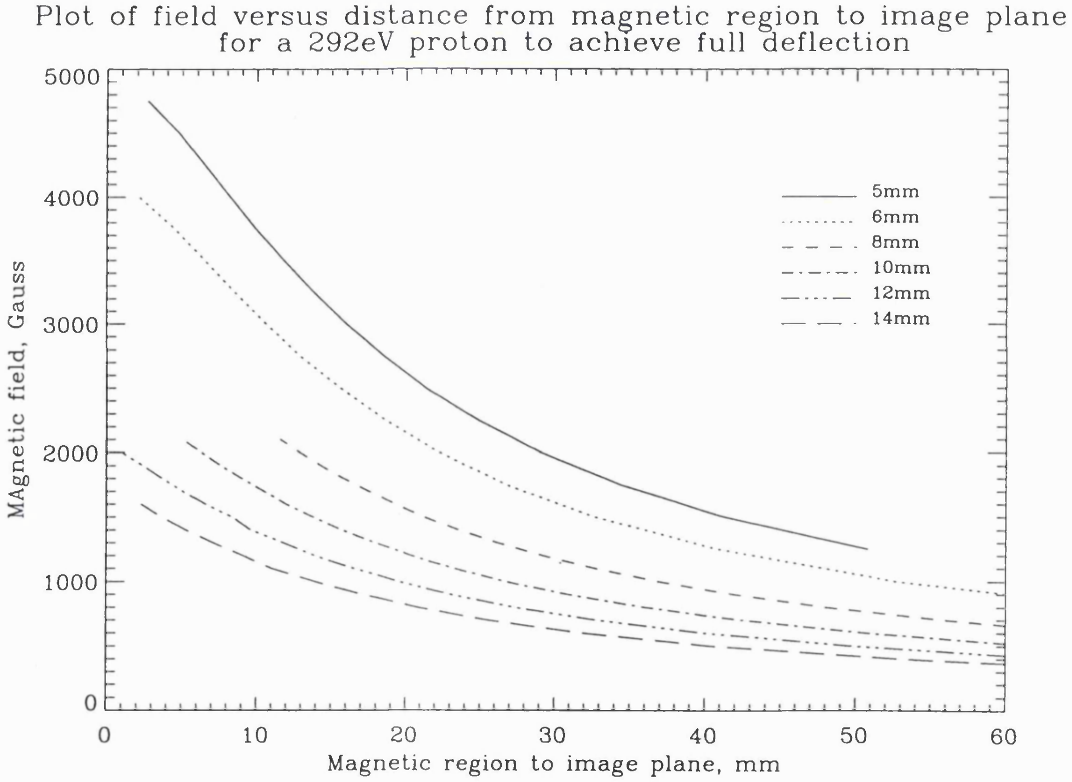

Figure 4-2. Magnetic field required as a function of length of magnetic deflection region from the image plane, L_B. Plots are shown for six different values of length of deflection region, l_B.

4.3 Choice of magnet

As described in Chapter 2 the magnetic field is used to deflect the incoming ion by an amount dependent on the ratio of charge number to momentum. The magnetic field strength required means that a high field permanent magnet would be needed. Currently, the highest energy density magnets available are neodynium-iron-base types (Figure 4-3). VACODYM® magnets use a $Nd_2Fe_{14}B$ matrix phase showing very high saturation and high magnetic anisotropy. The advantage of these over rare-earth cobalt magnets, which possess a similar energy density, are their mechanical properties, which in the harsh environment of a space instrument is an important consideration. Although both are sintered magnets the VACODYM range possess better bending strength, compressive strength, and stress crack resistance, as well as a lower coefficient of thermal expansion (*Vacuumschmelze*, 1988). To prevent selective oxidation of the Nd rich grain boundaries and moisture ingress the final flight magnets were coated with a thin layer of tin. Table 4-1 shows the properties of the VACODYM 370 HR magnets chosen. Also shown for comparison are the properties of the highest energy density rare earth cobalt magnet, VACOMAX. The principle disadvantage of NdFeB magnets is the relatively large change of magnetic properties with temperature (*Parker*, 1990). However, as shown later, the temperature variations experienced by FONEMA during both testing and flight should not cause a problem.

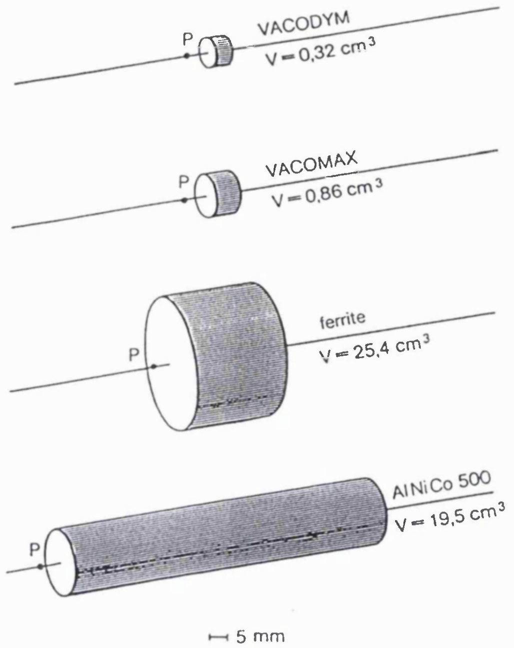

Figure 4-3. Illustration showing the reduction in volume achieved by using VACODYM: The magnets are all designed so that at the reference point P=5mm from the pole surface a field of 100mT is produced. (Vacuumschmelze, 1988)

4.3.1 Working point of magnets

Magnetic field due to 'free magnetic poles' near the ends of a permanent magnet is in the opposing direction to the flux density B within the magnet, and therefore has a demagnetising effect. This demagnetising field, H, then acts in a similar way to an externally applied field in a typical hysteresis loop. Consequently, the operational state of a permanent magnet is always in the range of the demagnetisation curve, i.e. the second quadrant of the hysteresis curve. The working point refers to the pair of values (B, H) relevant to the operational state and is dependent on the geometry of the magnetic circuit. Figure 4-4 shows the B(H) hysteresis curve second quadrant for the FONEMA magnets. The working lines shown on this plot are for sixteen magnets equispaced around the circumference of a circle of radius *R*. The magnets are 1.5 × 10 × 50mm, magnetised parallel to the 1.5mm direction, and *R* is set at 100 and 200mm. The respective values of $B/\mu H$ for these two geometries are 0.05 and 0.032.

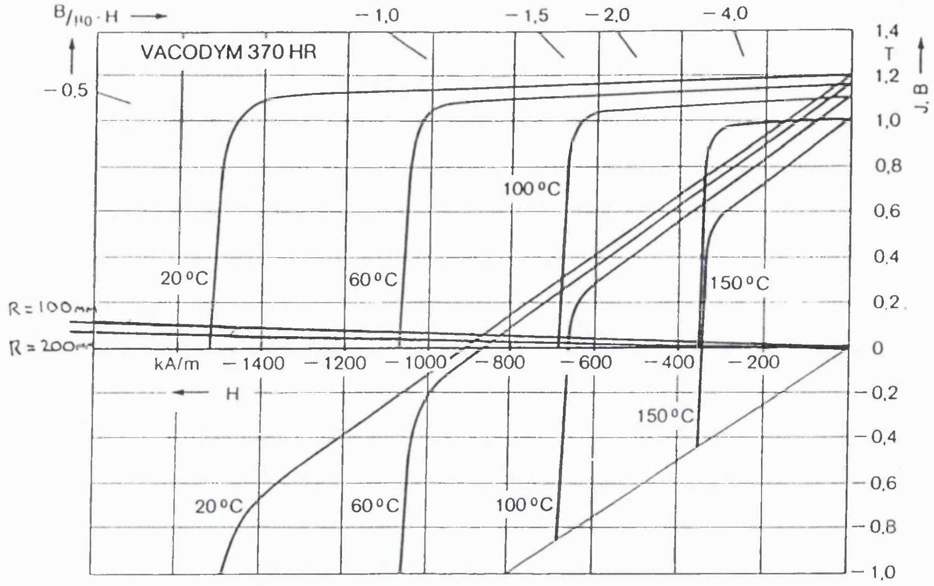

Figure 4-4. B versus H in second quadrant of hysteresis curve (demagnetisation curve) for VACODYM 370 HR showing working lines for various set ups (see text).

Material			VACODYM 370 HR	VACOMAX 225 HR
Composition			$Nd_2Fe_{14}B$	Sm_2Co_{17}
Remanence	B_r	[Tesla]	1.15 - 1.25	1.00 - 1.15
Coercivity	$_BH_c$	[kA/m]	850 - 1000	600 - 900
	$_JH_c$ typical	[kA/m]	1450	1200
	$_JH_c$ min.	[kA/m]	1350	800
Relative permeability	μ_r		1.05	1.05
Energy density	$(BH)_{max}$	[kJ/m^3]	240 - 310	190 - 240
Magnetisation field strength (min.)	H_{mag}	[kA/m]	2500	3500
max. continuous temperature	T_{max}	[°C]	150	300
Curie temperature	T_C	[°C]	~310	~800
Density (typical)		[g/cm^3]	7.4	8.4
Specific electrical resisitivity		[Ωmm^2/m]	1.4 - 1.6	0.75 - 0.85
Specific heat		[J/(kg·K)]	~440	~390
Thermal conductivity		[W(m·K)]	~9	~12
Coefficient of thermal expansion	$\parallel c$	[10^{-6}/K]	5	10
	$\perp c$		-1	12
Young's modulus		[10^{5}N/mm^2]	1.5	1.5

Table 4-1. Characteristic Properties of VACODYM and VACOMAX at room temperature.

4.3.2 Variation of magnetic properties with time

The time dependent variation of magnets at constant temperature is known as magnetic viscosity. Domain regions of magnetisation are in a static self-imposed demagnetising field. Additionally, however, they are also in a superimposed field which fluctuates with time, due to small changes in external or internal temperature or stray fields. An energy input from these fields can initiate a transition for domains in a meta-stable state to a more stable state. These transitions would involve a discontinuous orientation change. *Street et al.* (1949) reported change in magnetisation of the order of 0.5% over 3 years for Alnico 5 magnets and smaller losses for rare earth magnets. Because this is essentially an activation process, it is accelerated at increased temperatures, so that rapid stabilisation can be achieved by raising a magnet's temperature for a short period. Alternatively, as the changes result from magnetisation reversals, subjecting the magnet to a demagnetising field reflecting the expected loss during the period of interest will also achieve stabilisation. In the case of FONEMA the magnets are 'knocked back' anyway to achieve the required field so this should produce the required stabilisation. If it was not necessary to change the magnetisation this conditioning would have to be done at elevated temperatures to avoid subsequent 'aging' during the environmental test program.

4.3.3 Variation of magnetic properties with temperature

The demagnetisation curves of permanent magnets are temperature dependent. A change in temperature causes the working point of the system to shift along the working line (see Figure 4-5). As long as the working point stays within the linear region of the demagnetisation curve, the changes in flux density are reversible, i.e. changes in temperature from T_1 to T_3 producing movements from P1 to P3 will be reversible. Beyond this, i.e. a change in temperature to T_4, the magnet will suffer irreversible losses that can only be remedied by remagnetisation.

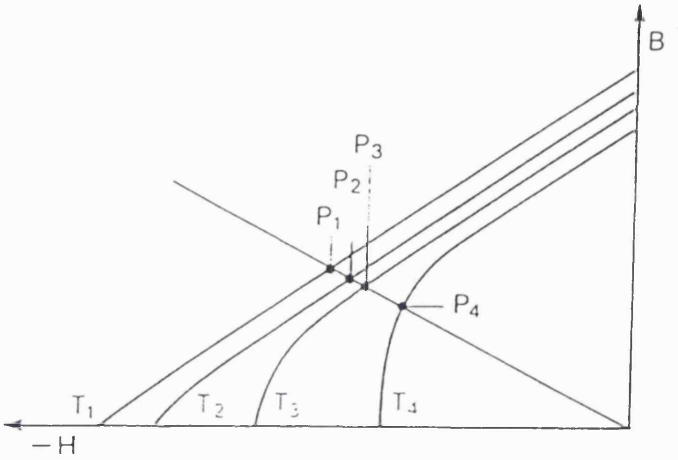

Figure 4-5. B versus H curves at different temperatures showing the working line and various working points.

As an example of the temperature effect Figure 4-6 shows the percentage variation for Alnico magnets as the temperature is cycled between +60 and -60°C. It can be seen that with a B/H value of 35 there is no irreversible loss but as the B/H value decreases the losses become more pronounced. Another way to display this data is to show the irreversible losses plotted against temperature for a range of working lines. This is shown for the FONEMA VACODYM 370 HR magnets in Figure 4-7: the working point for the initial FONEMA design is approximately 0.05 so the maximum operating temperature is about 60°C. This is close to the maximum temperature that FONEMA experiences during the environmental test program and higher than the expected maximum temperature of 30°C in operation. A more temperature resistant magnet would have been desirable but none were available at the time. However, subsequent developments in producing magnets for highly dynamic servo motors has lead to NdFeB magnets showing no temperature dependent losses up to 180°C over all working points (Vacuumschmelze, 1996). The final flight design for the FONEMA magnets with the field return path give a much higher value for $B/\mu H$ (approximately 0.25) so there should be no irreversible losses up to temperatures of the order of 100°C.

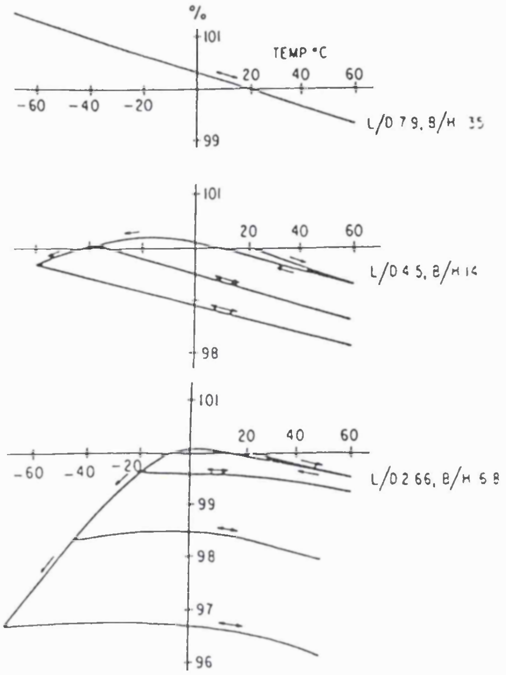

Figure 4-6. Temperature variation of Alnico magnet bars of different *l/d* dimesional ratio and B/H characteristic (from *Clegg*, 1955).

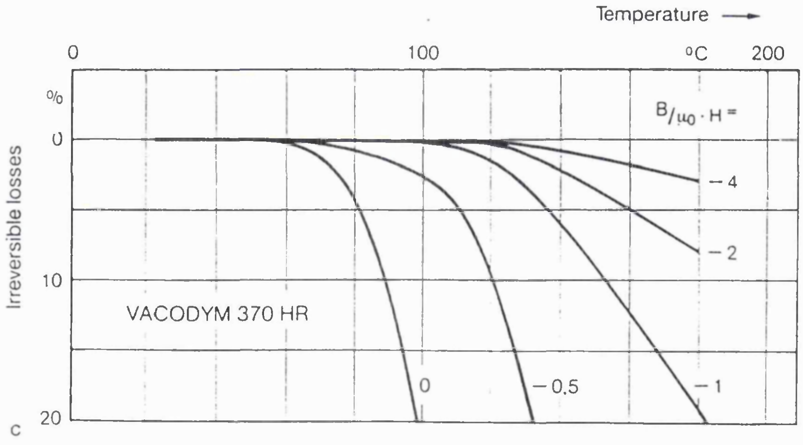

Figure 4-7. Irreversible losses plotted against temperature for the FONEMA VACODYM 370 HR magnets.

4.3.4 Variation in magnetic properties due to radiation damage

During the selection of the magnets there was no data available about the radiation effects on these magnets. Recently though *Pfluger et al.* (1994) reported on tests to measure the radiation damage to NdFeB magnets after 3 years exposure to high energy electrons, neutrons and protons. After a total dose of approximately 10^5 Gray, Pfluger *et al.* report no change in magnetic properties within their experimental error, although some degradation occurs at much higher doses. Although these trials do not distinguish between the sources of radiation the dose is five orders of magnitude higher than that expected during a 2 year mission to Mars (approximately 1 Gray (100 Rads), *Kremnev et al.* (1989)) therefore radiation damage was not considered to be a problem.

4.4 Field Mapping

Some magnets were purchased for evaluation purposes to provide an understanding of the field geometries and field strengths created by different configurations. The initial plan was to experimentally determine the magnetic field of a similar geometry to that which would be used in the final design. A computer model could then calculate the fields for the same geometry and a comparison could be made. If the results from the model could be confirmed at a variety of locations within the instrument by direct experiments, the model could then be added to the complete instrument simulation to provide magnetic field values within the complete instrument volume. In order to map these fields a Walker Scientific MG-3D Hall probe gaussmeter (with calibration fields) was purchased. Due to the small field region that had to be analysed only a one dimensional planar probe could be used. The probe was a 200 × 5 × 1mm rigid stem with the active Hall effect sensor, a 2 × 1 × 0.4mm indium arsenide wafer, placed centrally 2mm from the end. The accuracy of the probe and meter, calibrated as a pair, is better than 0.1%. Although there is a temperature dependency to the electronics all of the experiments were carried out in a cleanroom with the temperature carefully controlled at 20°C and calibration in standard fields, at 0T and 100mT at the start and end of tests showed no noticeable drift. Also, to avoid any variation in probe harness geometry creating noise pickup, and local variations in the ambient magnetic field, the probe was kept stationary and the magnetic assembly was moved around the probe. The magnetic assembly was moved on a XY stage driven by inchworm motors with a resolution of better than 1μm. However, the absolute positional error was that involved in aligning the probe to the magnetic assembly to be tested, this was generally better than 0.1mm.

Initially the plan was to have eight equispaced Thomson Parabola analysers on each half of the instrument. Sixteen equispaced magnets would then produce a ring of field with no reverse field outside the region of deflection. Alternate gaps in the ring structure would be used as the deflection regions for individual analysers. The two opposing field rings in each hemisphere of the instrument would act to diminish the magnetic field outside the volume occupied by FONEMA. Any slight variations in intrinsic field from a magnet would also be compensated by the overall ring structure. Figure 4-8 shows the field, B_y, as the magnets are moved such that the relative motion of the probe, centred between two magnets, is in the $+x$ direction toward the centre of the ring, y is perpendicular to x in the plane of the ring. The magnets used for this test were VACODYM 370HR magnets measuring 1.5 × 10 × 60mm, the easy axis being parallel to the shortest dimension. It can be seen that no opposing field is recorded and the magnitude of the field is still relatively large at some distance from the magnets. This would create problems with low energy particle trajectories within the collimator as already discussed in Chapter 3. There was also some concern about the effect on the output electrons of the microchannel plates within the imaging detector. It was initially envisaged that soft magnetic material could be placed in the gaps between the pairs of magnets not used as part of analysers to constrain the field more and reduce the field outside the inter-magnet gap. This became difficult to achieve if the analysers were to be individually removable for testing and swapping out if problems occurred. It also meant a large volume, and mass, of magnetic material to produce the return paths. However, without some improvement the field from the magnets could not be made large enough. The increase in field needed could only be achieved by sacrificing the equispaced magnets and bringing the deflecting pairs closer together.

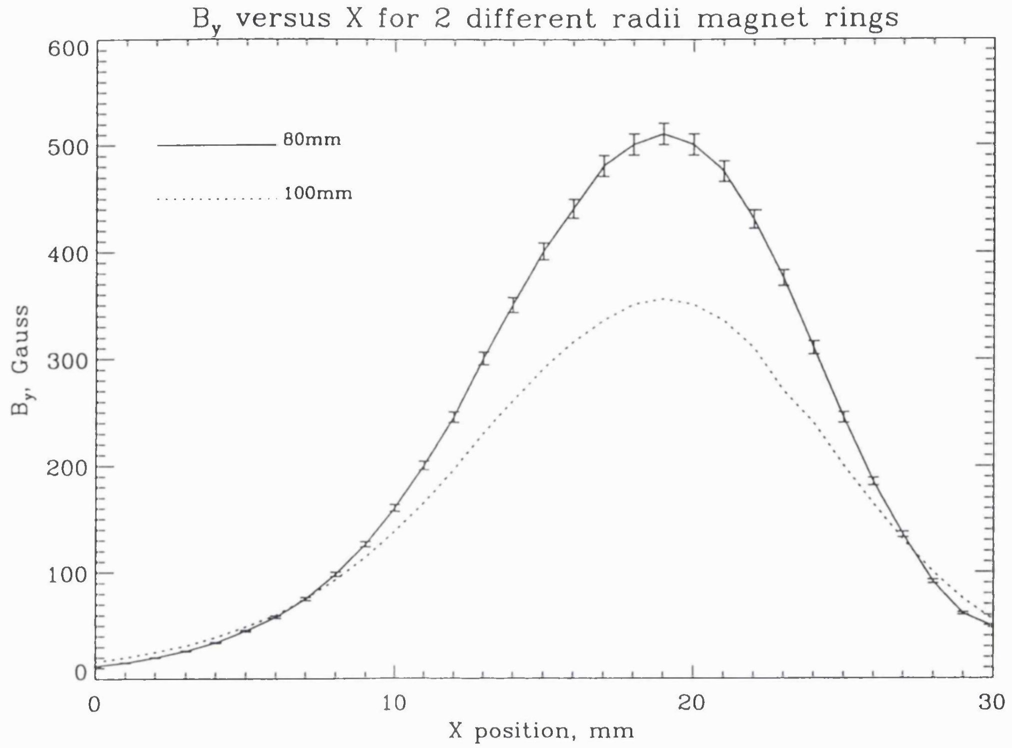

Figure 4-8. Measured field in *y*, B_y, as a function of *x* for 2 different radii of ring, note that *x*=0 is positioned 10mm beyond the outer edge of the magnets for both radii.

Figure 4-9 shows the field values between magnets in a ring of eight pairs where each pair of analyser magnets are radially mounted magnets 11°15′ apart, separated by 33°45′ from the next pair. This deflection field is shown for five different radii of ring of magnets. Typical error bars, from the digitisation of the gaussmeters analogue output, are shown for the 120mm radius plot. Unlike the equi-spaced magnets the flux return path is no longer such that the magnetic circuit is connected around the ring. Instead flux loops around the ends of the volume between the pairs to complete the circuit with the other magnet in the pair. This produces the negative values of field either side of the main deflection field. The main field and the return flux field is largest for the smallest ring radius. Because the magnets are radially mounted in a ring the return path is shortest nearest the centre, hence the higher negative flux on the right hand side of these plots. Looking back to Figure 4-2 this arrangement as it stands is unlikely to produce enough field for the required deflection.

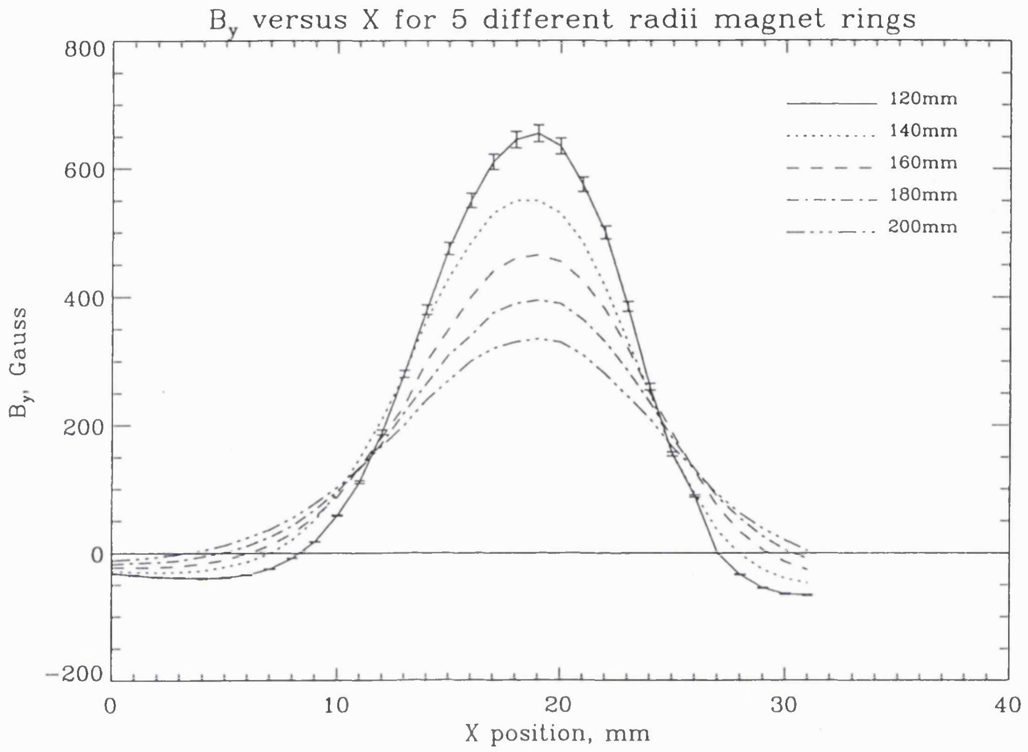

Figure 4-9. B_y as a function of *x* for five different radii of magnet ring. As before *x*=0 is 10 mm beyond the outer edge of the magnets in each ring.

During the development of the Engineering Model the Russian authorities required us to reduce the mass of the instrument. As well as reducing the overall dimensions of the instrument it became necessary to reduce the number of analysers from eight to six on each half of the instrument. Another change to occur at the same time, due to the electrostatic mirror properties, was the need to tilt the image plane and hence the analysers at an angle of 14° to the instrument axis. If a complete ring of magnets is used in this situation the field will be different for the three different polar detectors in each analyser because the radius of the ring will be different. Both these changes meant that to try to give the same performance for each detector the magnets, although shared between the three detectors, would not be part of a larger ring. Instead the magnets would be parallel pairs mounted within the analyser. The problem of the stray fields on the collimator side of the magnetic field is dealt with by using a mild steel shield. This acts as a flux return path between the two magnets, decreasing the amount of stray field around the magnets and enhancing the field within the gap.

The effect of the shield can be seen clearly in Figure 4-11 which shows the field, B_y, as the gaussmeter probe is passed between the pair of magnets with and without the shield, see Figure 4-10. The stray field on either side of the magnets is reduced and the field within the deflection region is increased from about 1800 Gauss to nearer 2850 Gauss. For the unshielded pair the reverse field outside the deflection region is nearly 500 Gauss, for the shielded magnets this reaches a maximum of 170 Gauss at $x = 29.6$mm on the side of where the shield is located. It was clear from these results that this was close to the configuration needed for flight and the next stage was to use a magnetic field model to provide field values over the whole volume of the instrument for the simulator.

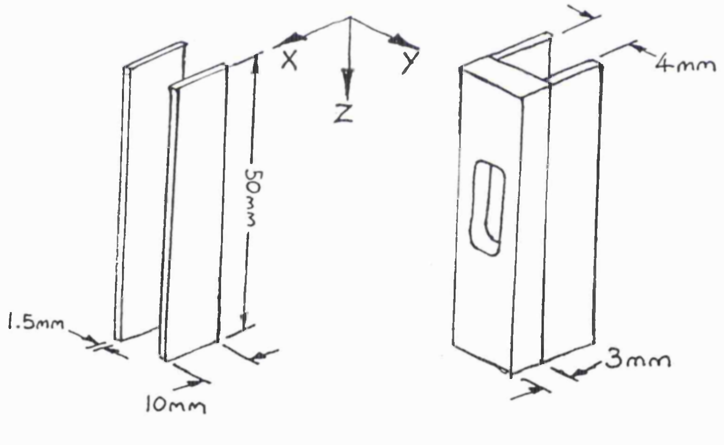

Figure 4-10. Configuration of 3mm thick mild steel shield relative to the pair of magnets. The aperture in the shield through which the Hall probe passes is 3 × 7mm.

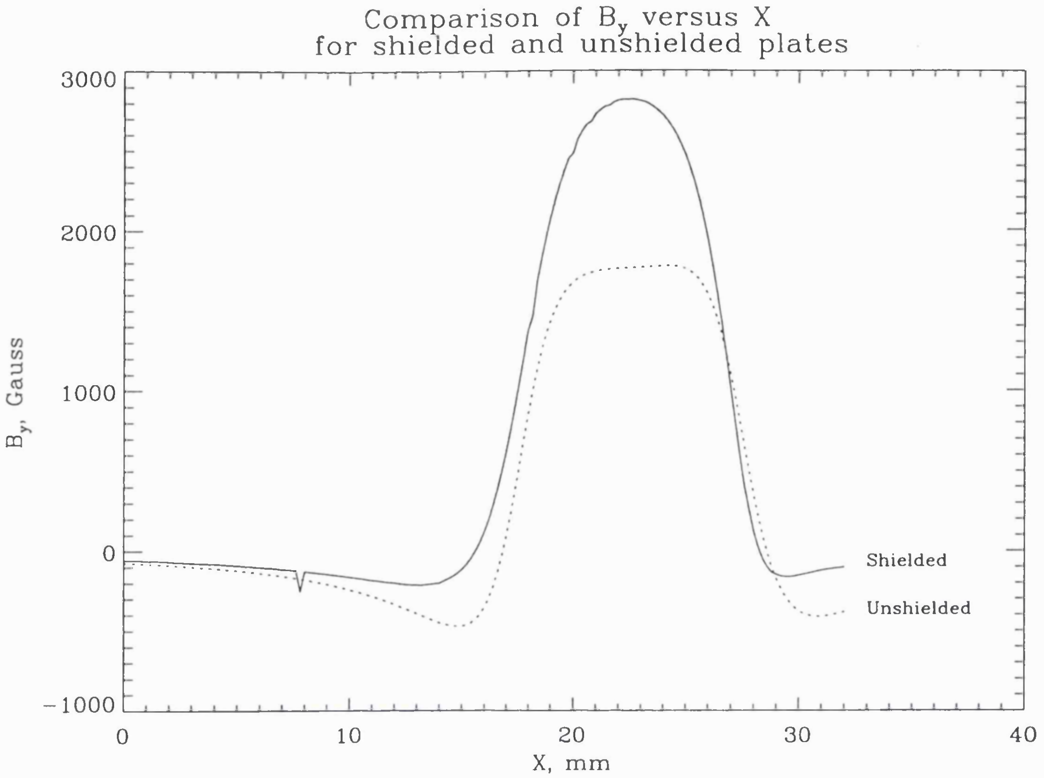

Figure 4-11. Comparison of magnetic field between parallel pair of magnets with and without shield.

4.5 Computer Modelling

A computer model was used to predict the field arrangement and supply data to the full simulation program. For this task the PANDIRA program was used. This was part of the POISSON/SUPERFISH group of codes written by Ronald Holsinger, with theoretical assistance from Klaus Halbach (*Menzel and Stokes*, 1987). The code group was written at the Los Alamos National Laboratory in New Mexico to solve magnetostatic and electrostatic field problems for the Accelerator Theory and Simulation group. These codes work by solving Maxwell's static equations (MSE's) in integral form in two dimensions. When the MSE's are taken together with boundary conditions, they are equivalent to a generalised form of Poisson's equation in two dimensions. The absolute accuracy of the code is reported by the authors to be at least 5% and when evaluating changes on the same magnet to be better than 1% (*LAACG*, 1987). Although only able to solve two dimensional problems this was the only model available that could solve permanent magnet problems. By modelling individual planes it was believed that a reasonable three dimensional model could be obtained.

The experimental setup depicted in Figure 4-10 was programmed into the PANDIRA model. Because it is only a two dimensional model it is necessary to deal with the shield in two ways, one scenario models the field in a plane where there is no gap in the shield, the other where the gap exists. Figure 4-12 shows the field orthogonal to the plane of the magnets at the centre of the gap as in the mapping experiments. For comparison the experimental data from Figure 4-11 is shown with the same field as predicted by PANDIRA. The model which assumes no aperture in the shield matches the mapped data closest over most of x except where the shield is. However, because this model has no aperture all the field within the shield produces a large field, greater than 6000 gauss, in the opposite direction. The maximum field in the gap is underestimated by about 10%, probably due to the missing aperture. Where the model has an appropriate size aperture there is no return path that would normally be provided by the shield away from the aperture. This results in an expansion of the field beyond the shield region and a reduction of flux density within the magnet gap.

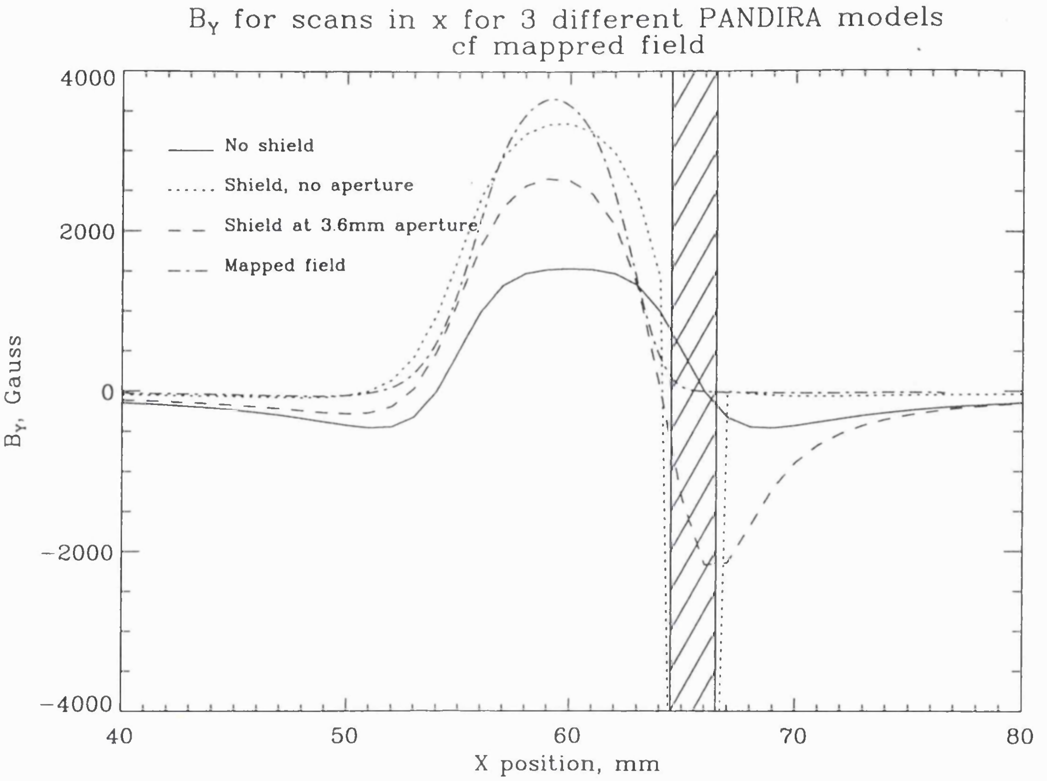

Figure 4-12. Comparison of the output from the PANDIRA program and experimental measurements. The hatched section represents the position of the mild steel shield.

Although PANDIRA could clearly not be used to predict real field values within the instrument it could be used for showing the field topology and highlighting small scale structures not immediately apparent from the mapping. Figure 4-13, Figure 4-14 and Figure 4-15 show the field lines for the three different cases shown in Figure 4-12. In Figure 4-16 the exclusion of field from the apertures within the shield is shown modelled.

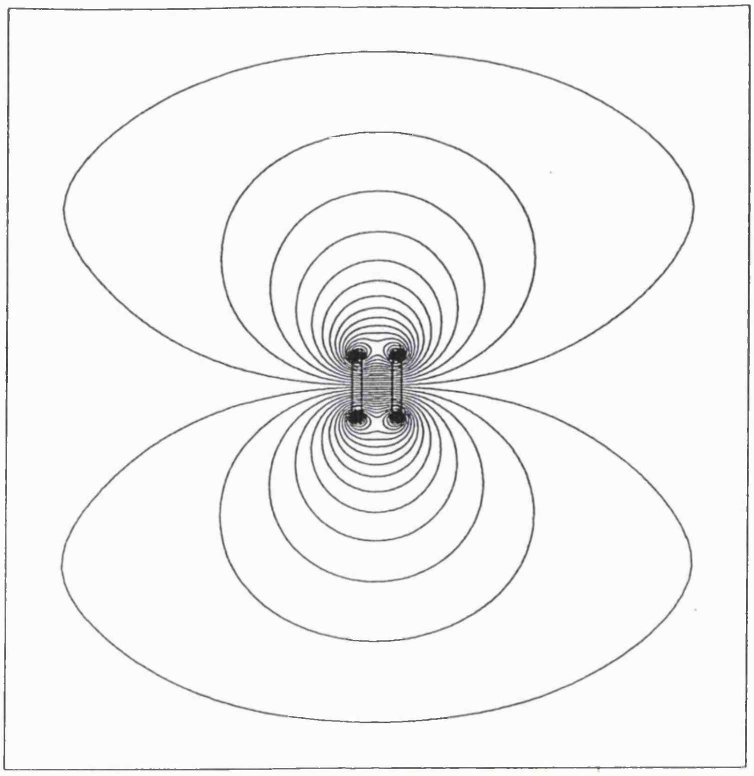

Figure 4-13. Field geometry for unshielded magnets as output from PANDIRA.

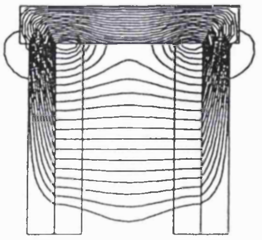

Figure 4-14. PANDIRA output showing field model of magnets after the inclusion of 3mm mild steel shield with no apertures.

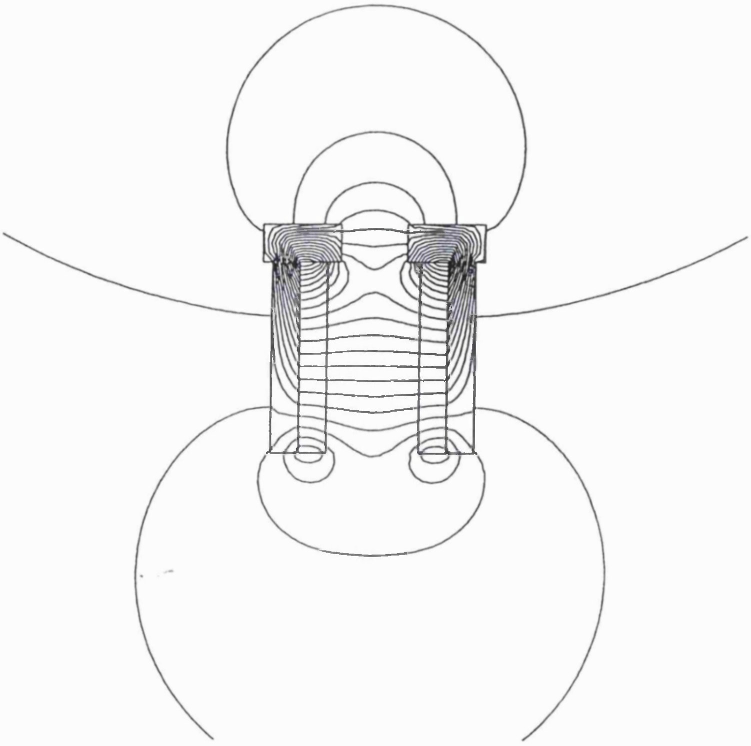

Figure 4-15. PANDIRA output showing field model with a slot placed in the shield.

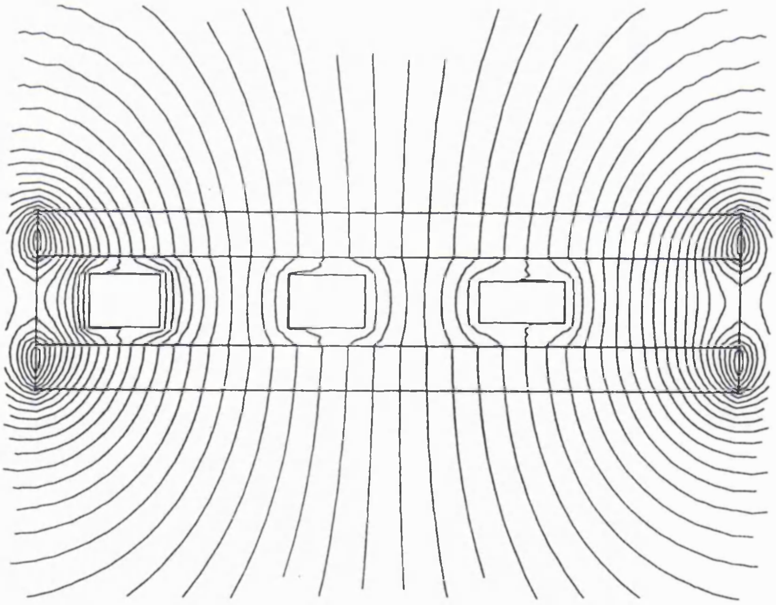

Figure 4-16. Magnetic field model in the plane of mild steel shield showing the almost field free area that exists within the apertures.

4.6 Field Mapping of FONEMA

Due to the limitations of the modelling of the permanent magnets a different approach was investigated. This was to map the fields in enough detail to provide field values for the instrument simulator. A preliminary analysis using the instrument simulation software would determine to a first order the geometry and approximate strength of field required. The magnetic data used for this initial stage was that described in the previous section. A physical model of the instruments with magnets could then be constructed and the actual field mapped. The mapped values would then be fed back into the simulator and the scaling of the local fields needed to achieve the required results would give the factor by which the magnetic field strength would have to be reduced. The remanence of the magnets could be 'knocked back' to a lower value by continuous shocking with a large reverse field within a Helmholtz coil system. This service was provided for us by Magnetic Developments Ltd, Swindon.

The physical model for the magnetic setup of the whole FONEMA instrument was large and weighed in excess of 5kg. This meant that it could not be moved on the XY stage as in the previous mapping experiments. Instead the probe had to be moved about the model, as shown in Figure 4-17. Primarily the aim was to get good data in the deflection region between the magnets but so that a comprehensive data set could be entered into the instrument simulator data was taken in other areas, e.g. the collimator area, the image plane, etc.. Figure 4-18 shows the positions where field values in all 3 axes were taken in relation to a flight analyser. These scans were carried out at eight different heights within the model. In addition to this data was taken at larger distances, to estimate the amount of stray magnetic field that would reach beyond the envelope of FONEMA, and B_y was scanned in x through the apertures in the front magnetic shield.

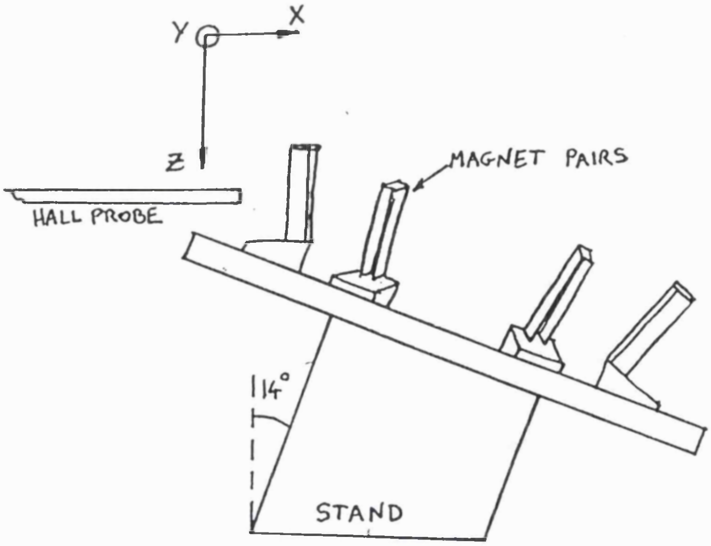

Figure 4-17. Sketch of the physical model of the instrument used to allow accurate magnetic field mapping in the final instrument configuration.

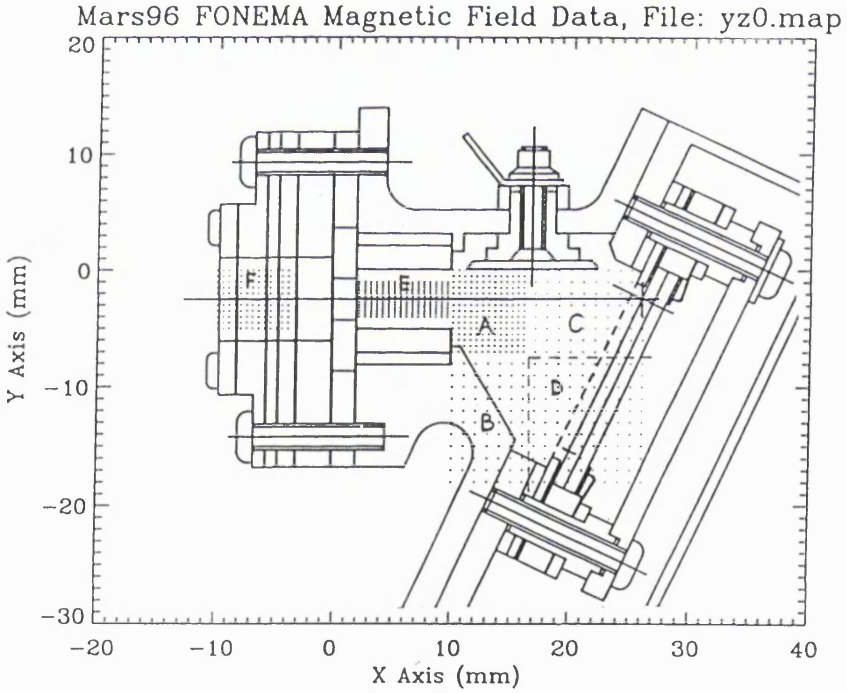

Figure 4-18. A map of positions where B_x, B_y and B_z values were taken. This was done for six different values of z, where z completes the righthanded set of axis. The map is shown with a mechanical drawing of the analyser to show the various areas covered.

The field values taken at each map point in Figure 4-18 were fitted to a surface using a minimum curvature surface interpolation. Six such interpolations are done in the sectors marked A to F in the diagram. Equipotential field lines are shown for each of these sectors in Figure 4-19. For the instrument simulator the raw data values are interpolated by a series of two dimensional splines in the plane of the data. Values obtained from these are then interpolated using two dimensional splines in the plane perpendicular to both the mapping plane and the magnet face.

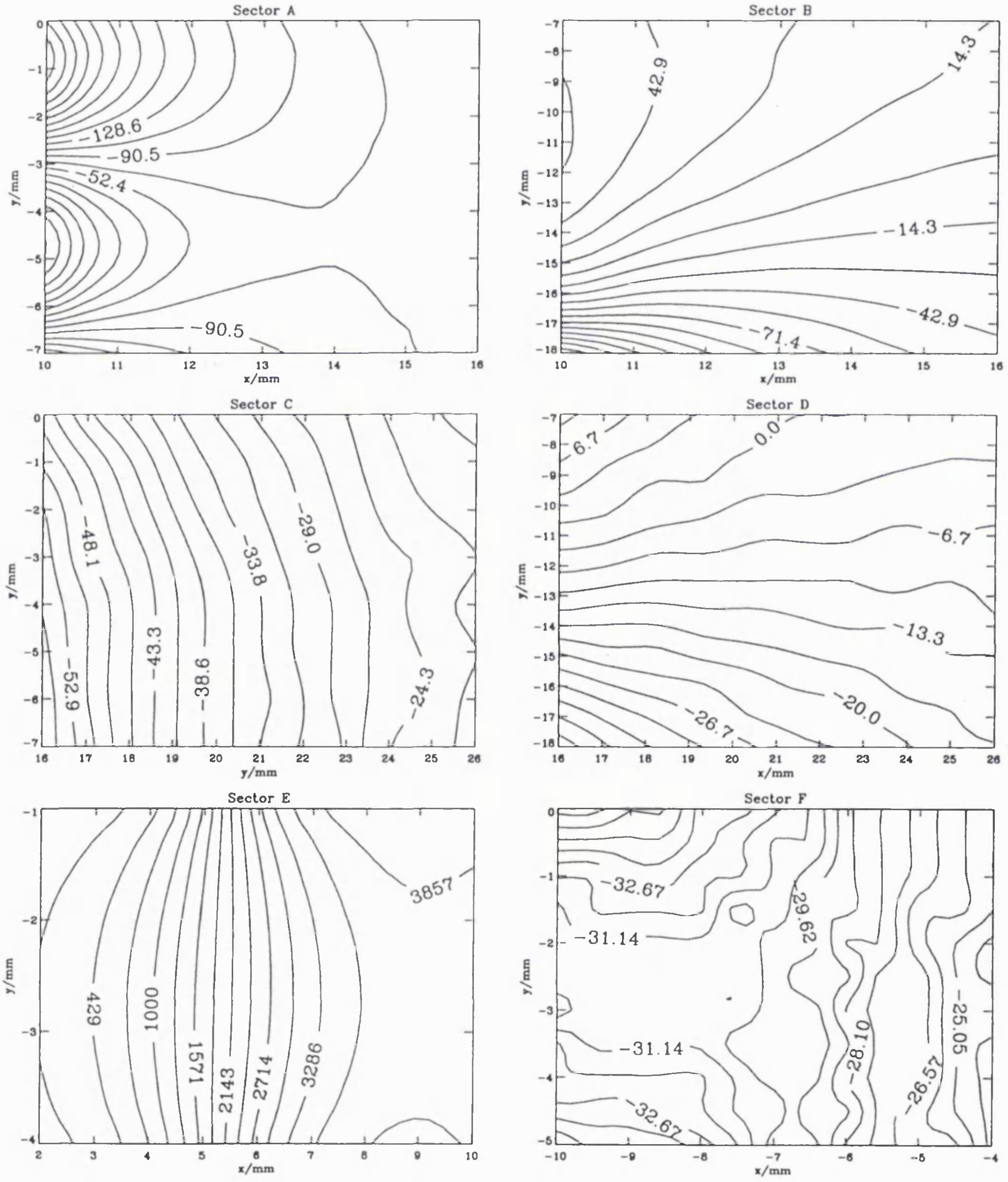

Figure 4-19. Interpolated field data for the six areas identified in Figure 4-18.

4.7 Early deflection results

Magnetic deflection tests using a single analyser were carried out in order to test the instrument simulator code. Initially these were carried out using a collimator with three single channels. The channel axes are perpendicular to the collimator plates and colinear with focus positions of the three detectors. Each collimator is 8mm long with 120μm diameter holes, and the front plate is 34mm from the image plane, giving a spot size of 1.2mm. Only a single hole collimator was used to keep the preliminary investigation of the magnetic deflection properties as simple as possible. For these tests the deflection voltage and pre-acceleration voltage are both set to 0 volts. The ions are produced by a hot filament ion gun which ionises the residual gas within the vacuum chamber. Ions are accelerated out of the gun in a narrow beam by a voltage which then defines their energy. The ions pass through the collimator are deflected by the magnetic field and eventually hit the microchannel plate (MCP). However, the positions have to be shifted to take account of different effects in the imaging. Firstly the recorded positions are remapped to real x and y positions by putting them through a spline interpolation procedure. Basically the pinhole mask image as recorded at the anode is mapped onto the real pinhole positions which are known to within 10μm. The mapping that does this can then be used to turn any anode position into a real position of impact at the front of the MCP. In the case of the magnetic deflection tests there is an added difficulty. The stray magnetic field behind the MCP will deflect the MCP exit electrons producing a shift from the exit position of the MCP (assumed to be the same as the front MCP impact position) to the anode. The magnitude of this shift is difficult to determine exactly as explained in Chapter 7 but is approximately 0.8mm for this experiment. Then the position of the impact on the front of the MCP stack has to be moved to account for the trajectory through the electrostatic field region between the MCP and the mesh. Figure 4-20 shows the recorded image for one such test. Here the ion energy is at 1000eV. The resolution of the imaging system is about 350μm in the strip axis (x) and 200μm in the wedge axis (y).

This image data is summed in the x axis (strip axis in figure) to show the mass peaks. Data for 600eV and 2500eV ions is shown in Figure 4-21 where it can be seen that the protons are easily resolved from the heavier ions for these relatively high energies. However, the ions in the water group are not distinguishable from the N_2^+ and 0_2^+ ions for the 2500eV ions and are only just resolved at the lower energy. The full width half maximum (fwhm) of these peaks is approximately 500μm, the expected fwhm of the spotsize due to the collimator. This should be slightly larger for proton peaks at lower energies, i.e. where the deflection angle is largest, due to the dispersion that occurs within the magnetic deflection region. There are two different aspects to the dispersion if it is assumed that the magnetic field is the same across a plane parallel to the collimator plates. The collimator allows ions with an angular spread of 0.859° into the magnetic deflection region, and it is this angular spread that defines the final spot size on the image. For two ions with this angular spread in the plane *xz* perpendicular to the magnetic field (see Figure 4-18) dispersion is due to the different ions traveling different path lengths within the same field region. This effect will also change the shape of the final spot size as ions that have a small velocity component in the direction opposite to their magnetic deflection will be dispersed less than those with the same transverse velocity component but in the opposite direction. Using a simple two dimensional simulation of the experiment described, the increase in the fwhm due to dispersion in the *xz* plane is 20μm for a deflection of 3mm increasing to 180μm for a full deflection of 16mm. In the final instrument, where the collimator range in detector 3 is approximately 10°, this dispersion will increase the spot size for low energy protons by up to 2mm.

Within the *xy* plane, deviation from the normal trajectory results in a longer trajectory again, but the field that the ion experiences is reduced as it is no longer traveling perpendicular to the field. Dispersion due to angular spread in this plane is negligible for the experiment described resulting in less than 2μm additional spread at the image plane. Because this effect essentially introduces a $cos\theta$ factor into the final deflection value it remains negligible even in the final instrument.

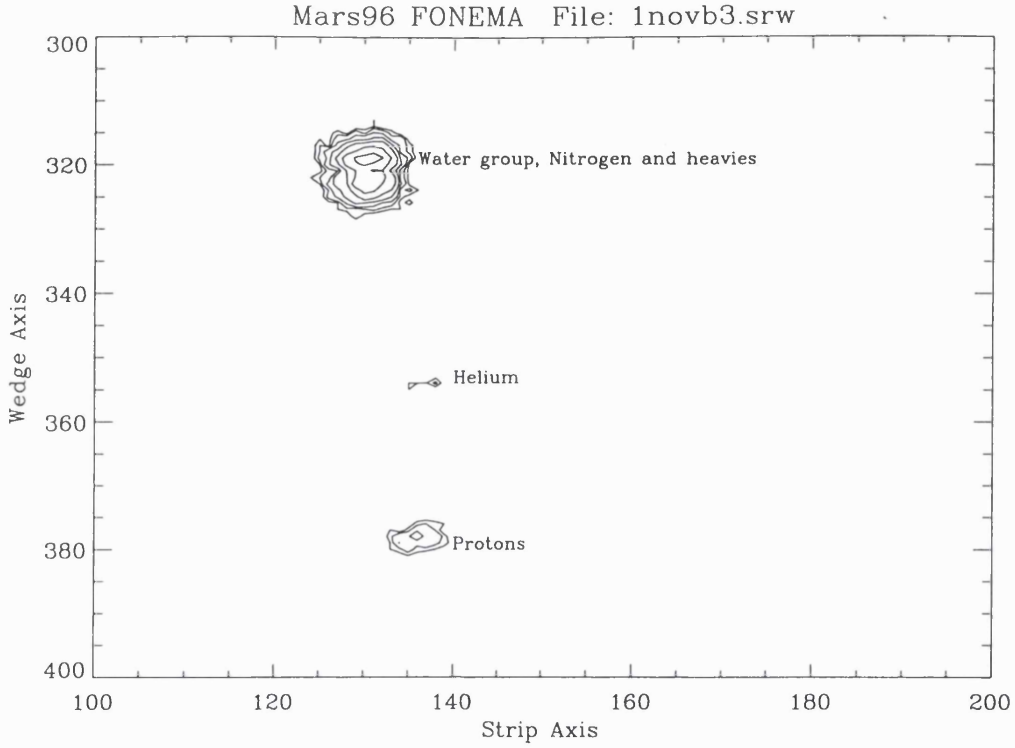

Figure 4-20. Image taken from detector 2 of single FONEMA Thomson Parabola analyser. No deflection voltage is present so only magnetic deflection is occuring in the wedge axis (units are image pixels).

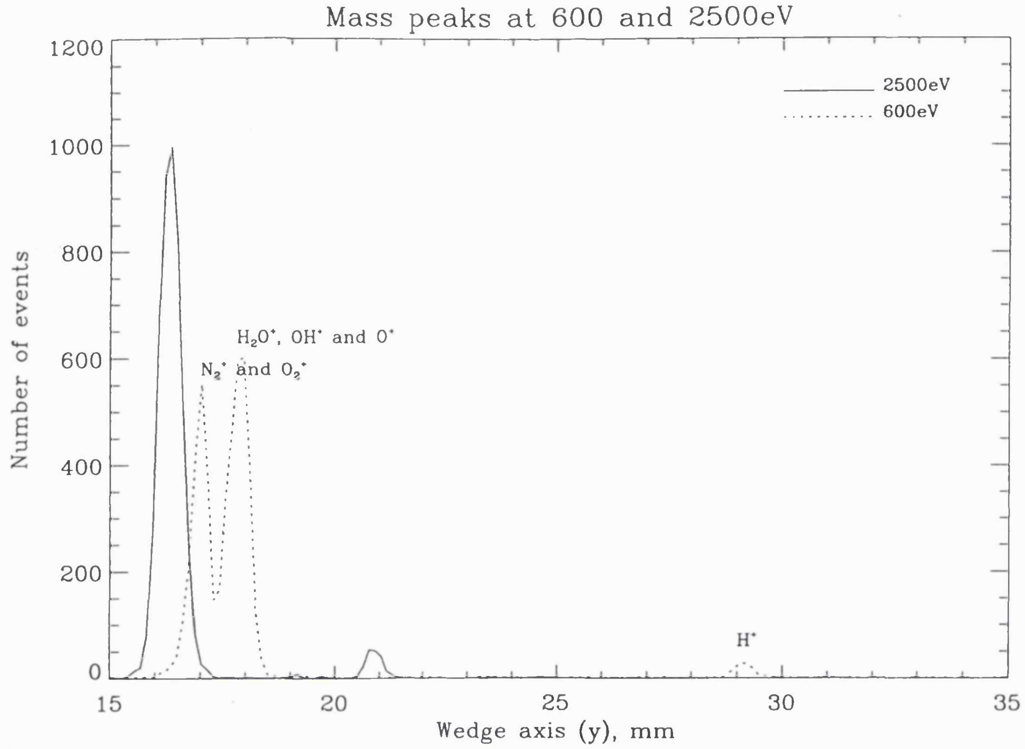

Figure 4-21. Image data summed in the *x* axis (strip axis) to show mass peaks at 2 different energies: 600 and 2500eV. The focus position of the detector is at y = 16mm.

The full data set from these initial deflection tests is plotted alongside simulator results in Figure 4-22. Simulator results are plotted for four masses: H^+, H_2^+, H_2O^+ and N_2^+. One standard deviation error bars are shown on the H^+ experimental results, which is the standard error on the peak position determination for the image and is typical for all the points shown. Although shown as separate points on this graph the nitrogen and water peaks could not be resolved for energies greater than1400eV. These positions are based on the interpolation from the relative peak heights where they can be resolved and the width of the observed peak. As can be seen the fit of the instrument simulator is good for the high mass ions and even for the hydrogen peaks is within 1mm of the experimental data. This error is due, in part, to the errors associated in shifting the event positions as explained earlier. The main error, however, is probably due to the collimator where even a 1° deviation from the normal will create an error of this magnitude. Another possible cause of error is stray electrostatic fields formed around the mesh in front of the MCP. For this early simulator run the field between the front MCP at 2300V and the mesh at ground was assumed to be uniform.

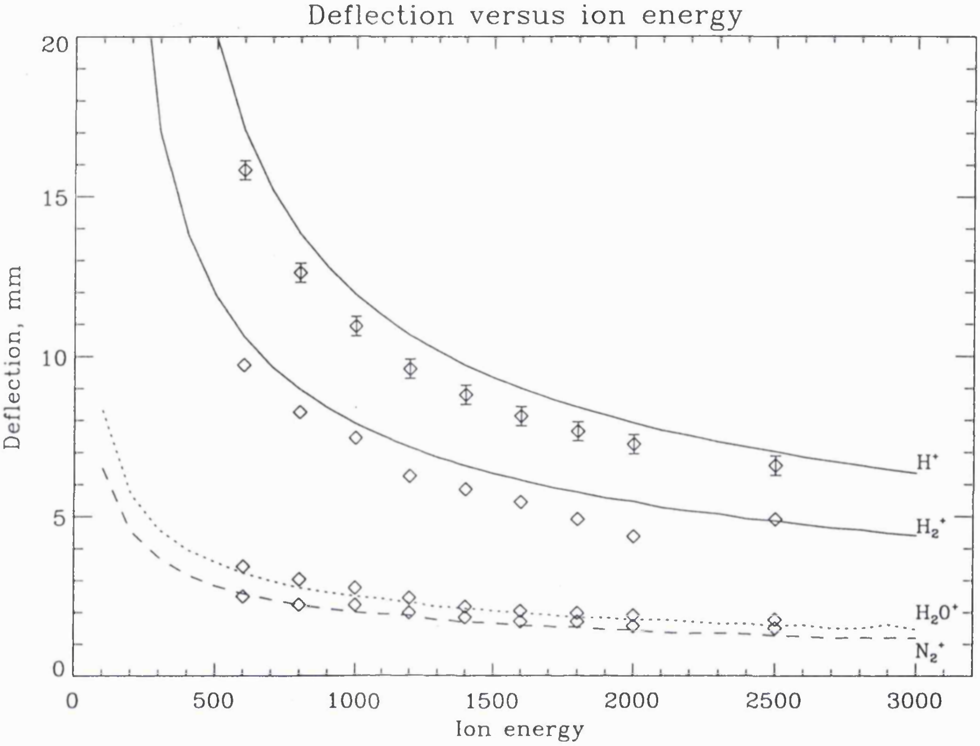

Figure 4-22. Magnetic deflection data plotted alongside simulator data for the same set-up.

5. Electrostatic deflection

5.1 Design considerations

The design considerations for the electrostatic deflection field are basically the same as those outlined for the magnetic field. In order to reduce dispersion and preserve the resolution it is important to have the electrostatic field as uniform as possible over as small a volume as possible. In an ideal Thomson parabola analyser this field should be placed far enough from the image plane such that only small deflections are necessary. Also, unlike the magnetic field, the direction that the particle is deflected is in the same direction as the field. This means that any non-uniformity in field that exists in the direction normal to the plates will have an effect on the ideal operation of the analyser.

Traditionally Thomson parabola analysers used in the laboratory have used the same volume for the magnetic and electrostatic field (*Weber et al.*, 1986, *Rhee*, 1984, *Lu et al.*, 1997). The gap between the magnetic pole pieces then directly determines the lower limit of the measurable velocity for a given length of analyser. To achieve a large dynamic range it would necessary to increase the magnetic gap. Conversely, as previously discussed a smaller gap provides a much more uniform field geometry. *Sakabe et al.* (1980) developed a modified Thomson parabola spectrometer where the two field regions are separated. The magnetic deflection region can then use a narrow gap providing the uniform field required and the electrostatic section can have as large a gap as required to increase the dynamic range.

The requirements for FONEMA are for a dynamic range of 20 in energy which can be achieved using either method described above. However, the need for a magnetic field return path meant that it was impractical to use the magnets as the high voltage plates for the electrostatic field as well. This also allowed electrostatic deflection tests to be carried out independently of the magnetic deflection tests. For FONEMA then the electrostatic deflection takes place after the magnetic deflection as in the high dynamic range Thomson analyser of Sakabe *et al.*. The amount of space that was available made it impractical to use a pair of parallel plates to define the electrostatic deflection region. Instead a single plate made of Beryllium Copper is used for the high voltage plate and the body of the analyser acts as the ground plate.

5.2 Computer modelling

The electrostatic deflection model was produced by Roger Woodliffe at MSSL and acted as the central core for the full instrument simulator. In order that the electrostatic deflection can be calculated at any point along an ion trajectory within the model it is important to be able to determine the electric field at any point. This process is done in two parts and is described in detail by *Woodliffe* (1991). Firstly the region of interest is divided into a mesh and the derivative at each node replaced by a finite difference approximation derived from a Taylor series expansion. These values are then interpolated in two-dimensional planes using a cubic spline routine. Interpolation between planes is then carried out using a second bicubic spline. The data shown in this section are just the field values at discrete mesh points interpolated by the contouring graphics routine.

Figure 5-1 shows a two dimensional equipotential field plot superimposed on a mechanical drawing of the analyser. The plane shown is that which includes the focus point of detector 2. In the figure it is clear that there is some electric field within the magnetic deflection region. The dashed contours show fields of 1% to 9% of the applied deflection potential in each mode. In order to keep the field profile similar for all three analysers the electrostatic plate is extended so that the deflection regions are not effected by the end field. Figure 5-2 shows the field equipotentials in a plane parallel to the electrostatic deflection plate and including the central rays of each collimator.

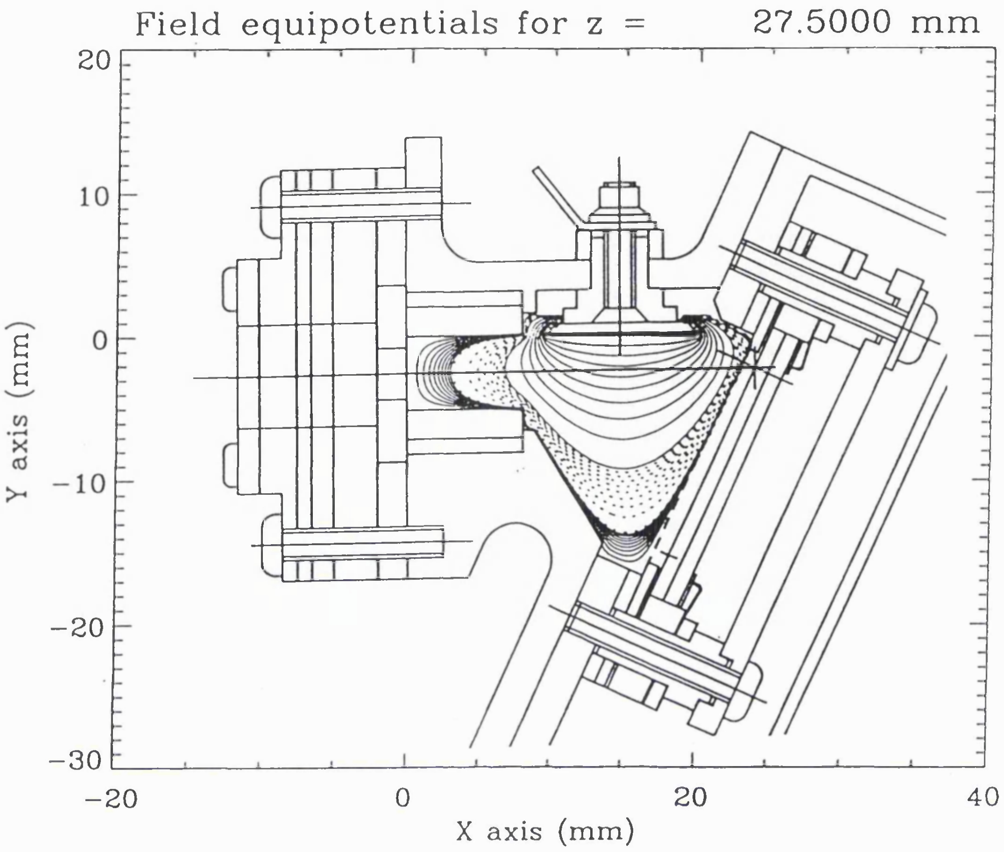

Figure 5-1. Plot of field values from the simulation with the final analyser mechanical design superimposed. Contours show the field potential as a percentage of the applied voltage to the deflection plate. The set closest to the plate vary from 10% to 90% in 10% steps (solid line), the next set (dashed line) vary from 1% to 9%, and the final set 0.1% to 0.9%.

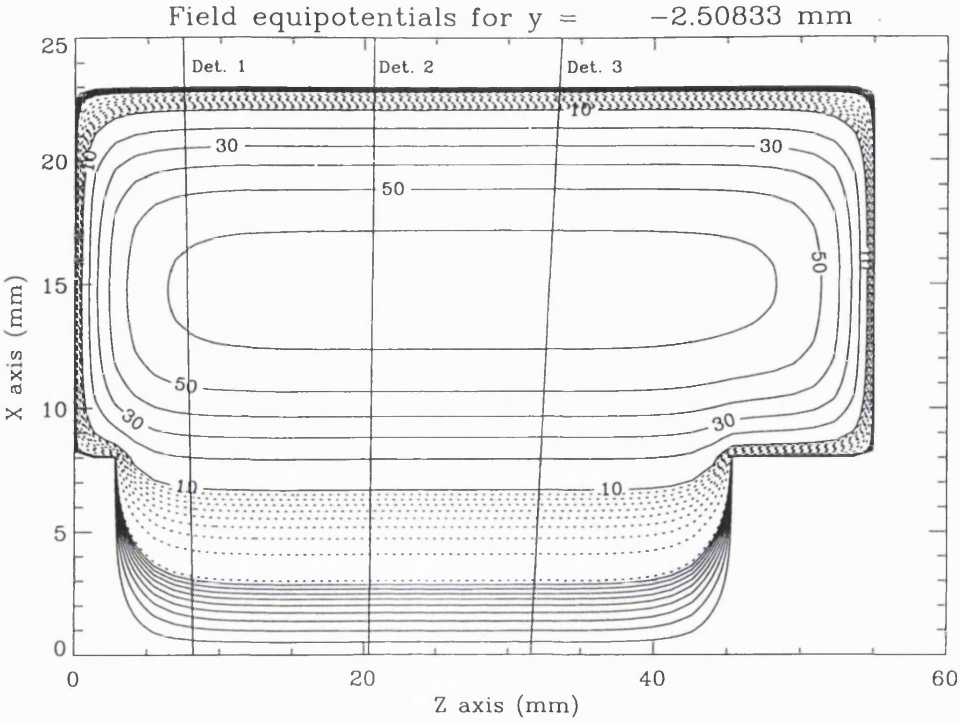

Figure 5-2. Plot of equipotentials in the x-z plane for y = -2.508mm. Contours as in Figure 5-1.

5.3 Initial results

Initial deflection results were carried out using a single hole collimator for each of the three detectors in an analyser unit. Because of uncertainty in the beam properties at different energies the energy was kept constant and the deflection voltage was changed. A typical set of results is shown in Figure 5-3. These results are for detector 2 in a left hand analyser operating in mode 2, i.e. -87.7Volts pre-acceleration voltage and 137.7Volts deflection voltage. As can be seen the results compare favourably over much of the range although at the lower energies the simulator is predicting larger deflections than actually occur. These differences are probably due to differences in the electrostatic field profile. In the experiment the magnets were removed so that the electrostatic deflection could be studied independently. This means that the field profile will be slightly different than that shown in Figure 5-1. Although the magnetic field is set to zero in the simulator the physical outline of the magnets still remains and influences the field structure within the model.

The error bar shown on the experimental points is the resolution of the imaging detector, approximately 140μm. Ideally it should be possible to determine the peak position to a higher accuracy than this but practical uncertainties about the local non-linearity of the MCP/anode system prevent this. These peak positions are measured from a theoretical straight through position for the collimator. Any number of effects could cause a shift in the relative peak position for these experimental results, e.g. non-normal pointing of the collimator channel, positional accuracy of the deflection plate within the analyser body. Essentially though the simulator is showing deflection results similar enough to the experimental results to have confidence in its use as a predictive tool.

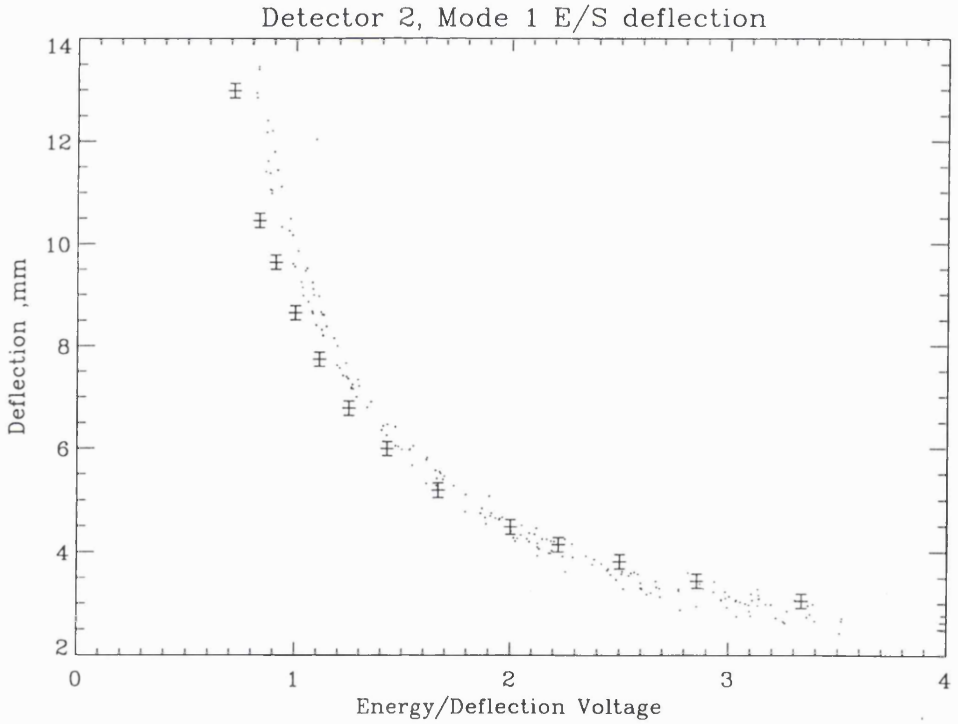

Figure 5-3. Plot of electrostatic deflection versus the ratio of ion energy to deflection voltage for experimental results (crosses) and output from the instrument simulator (dots). The simulator output is for masses 28 and 18 which generally make up over 90% of the ions exiting from the ion gun.

6. Detector

6.1 Introduction

As described in Chapter 2 the principle of the Thomson Parabola requires that a method of imaging in 2 dimensions is available so that both energy and mass information is recorded. The previous 2 chapters have described how this image is produced using magnetic and electrostatic deflections. In this chapter the imaging detectors used in the individual Thomson Parabola analysers on FONEMA are described.

In the original paper by *J. J. Thomson* (1911) describing the parabola experiment the imaging was provided by the use of photographic film. For almost all laboratory uses of the Thomson Parabola design of instrument since then, this has been the preferred method of producing the images (*Slater*, 1978, *Sakabe et al.*, 1980, *Herold et al.*, 1981). A more recent alternative is to use a CR-39 plastic plate to record the ion trace; this is subsequently photographed or analysed under a microscope (*Rhee*, 1984, *Sato*, 1987, *Yoneda et al.*, 1988). Obviously this is not a viable option for a space instrument where data are taken almost continuously and stored in a digital format for eventual telemetry to ground. Also both cellulose nitrate films and CR-39 are sensitive to only relatively high energy ions (>100keV/nucleon).

An alternative imaging detector is available: by using a microchannel plate (MCP) system with a suitable anode mounted behind it, single particles can be counted (*Armentrout et al.*, 1985, *Roquemore et al.*, 1985). Both Armentrout and Roquemore use an array of discrete anodes to capture the charge from the MCP. *Kuswa et al.* (1973) and *Weber et al.* (1986) both use a MCP stack in front of a phosphor screen and then photograph the screen. *Yamamoto et al.* (1990) use a similar method but employ a CCD camera to allow fast data acquisition. Other groups have used single Channel Electron Multipliers (CEMs) as detectors at specified locations in the image plane (*Bartiromo et al.*, 1987). More recently *Funsten et al.* (1997) have used a resistive disc anode behind a MCP stack in their E||B detector.

The imaging detector used on FONEMA consists of a MCP stack with a wedge and strip imaging anode system behind it. Microchannel plates had been used in space borne ion detectors previously flown by MSSL so were proven to be suitable for ion detection e.g. the Johnstone Plasma Analyser on Giotto (*Johnstone et al.*, 1987) and the Low Energy Plasma Analyser on CRRES (*Hardy et al.*, 1992). The combination of the MCP with an imaging anode has not previously been used for plasma instrumentation but has been used, in various forms, for X-ray and UV imaging detectors, most recently in the Coronal Diagnostic Spectrometer flown aboard the SOHO satellite (*Breeveld et al.*, 1992). In a parallel with the FONEMA system within the laboratory a wedge and strip variant was developed for the TIMAS experiment (*Walton et al.* 1996) which was launched in February 1996.

MCP detectors can be divided into two types: light amplification detectors and charge measurement detectors. In the former, the output electron cloud from the MCP is focused onto a phosphor screen producing a large photon pulse which is then optically coupled to the detector. This would generally be a CCD (*Walker et al.*, 1985) or Self-scanned PhotoDiode array (*Fraser*, 1987), but other direct readout systems do exist e.g. the PAPA detector (*Papalioslios et al.*, 1985). Charge measurement detectors will be dealt with in more detail in the next chapter as these are the type generally used in space borne plasma diagnostic instruments. Before that the operation and characteristics of the MCPs themselves will be looked at in more detail.

6.2 Microchannel plates

Since their introduction in the 1960s (*Lecomte et al.*, 1978), MCPs have been used successfully in many imaging and detection systems. Their development, properties and implementation, have been adequately described by many authors (*Wiza*, 1979, *Matsuura et al.*, 1984, *Smith et al.*, 1986, *Fraser*, 1989 and 1992). Much of this literature has dealt with MCPs from western suppliers: Varian, Galileo, Philips and Hamamatsu. In this chapter the operation and typical behaviour will be discussed and compared to that of the Russian MCPs used for FONEMA. These were supplied by Plant Gran, in Vladikavkas, Russian Federation. Some comparative tests of this type of MCP have recently been described by *Pearson et al.* (1993).

6.2.1 General Description

Microchannel plates consist of an array of single channel electron multipliers oriented parallel to one another. These individual channels are typically only 10 to 40μm in diameter separated by a similar amount, thus a typical circular plate of 5cm diameter will have in the region of 10^6 individual pores. To produce a usable gain the channel length to diameter ratio (L/D) is normally between 40 and 80; this leads to a plate thickness of the order of 1 to 2mm. The pores are generally biased at an angle of a few degrees to the normal of the MCP surface. As in single channel electron multipliers the pore walls are made of leaded glass with an optimised secondary electron emission. This also means that the walls are semiconducting so that the charge can be replenished by an external voltage. Each surface of the MCP is coated with a metal contact (usually Nichrome or a similar alloy) and a high voltage applied across these produces a field to accelerate electrons down the channel plate pores. Each pore acts as a continuous dynode structure with its own resistor chain producing a cascade of electrons at the output for a single event at the input. A typical plate will produce an electron gain in excess of 10^4 electrons and will have a time resolution of less than 100 ps (*Wiza*, 1979). Figure 6-1 shows a cross section through a typical MCP. MCPs are sensitive to X-rays, UV, ions and electrons.

The MCPs used for FONEMA were produced in Vladikavkas in the former Soviet Union. The details of these plates are shown in Table 6-1. In reality not all of the ninety plates that were delivered met these specifications. The pore bias angle was found to vary between about 4° and 10°, and the plate resistance was found to vary from as low as 20MΩ up to 11GΩ. The performance of the plates, however, was such that they could be used for the instrument.

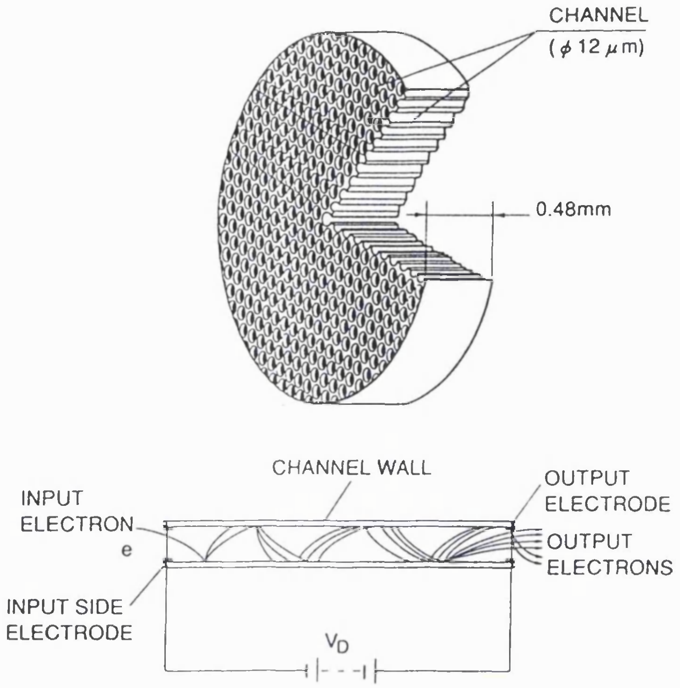

Figure 6-1. Cross section through a typical MCP (taken from *Hamahatsu* (1991))

Resistance, Ohms	2×10^8
Voltage for Gain = 10^4 electrons, Volts	920
Channel diameter, μm	14.9
Channel pitch, μm	17.4
Open Area Ratio	66.5%
Bias angle	7°24'
Plate thickness, mm	0.84
Length to diameter ratio (L/D)	56:1
Maximum Voltage, Volts	1200

Table 6-1. Specification for the Russian MCPs used for the FONEMA instrument.

6.2.2 Pulse Height Distribution

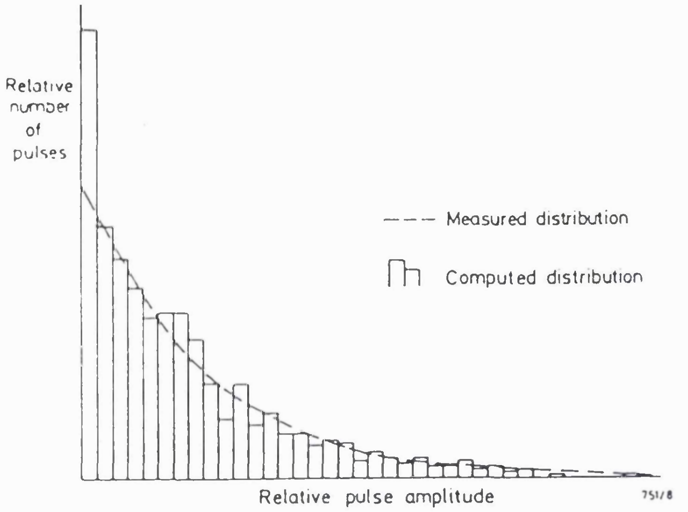

Figure 6-2. Pulse height distribution plot for a single MCP (taken from *Guest*, 1971)

A typical pulse height distribution (PHD) for the output of a single MCP is shown in Figure 6-2. The variation in possible trajectories for secondary electrons within the pore leads to ill defined secondary electron yields and a resulting large spread in gain. This falling exponential profile makes a single MCP difficult to use in real particle counting instruments because a high number of particles produce pulses that are at the low end of the scale and will get confused with noise. Use of a low level discriminator (LLD) in such a system would almost certainly make the determination of true count rates difficult. Another limit to single plate MCP operation is that when gain increases to a certain level self generating noise appears, which is due to ion feedback. Ion feedback occurs when residual gas atoms are ionised by the electron cloud and accelerated back up the channel, and when they eventually strike the wall again they will produce a secondary electron and start a second pulse and the process is repeated. This train of secondary pulses will appear to occur simultaneously with the initial event acting as a source of error. To alleviate these problems MCPs are generally used in a chevron configuration as shown in Figure 6-3 (a). This arrangement, with the bias angles of the stacked plates opposing each other has three benefits. Firstly it will reduce the self generating noise as the ionised residual gas will be absorbed at the junction of the plates. Secondly, the gain is increased by having a longer cascade path and finally, due to gain saturation a chevron pair will produce a peaked pulse height distribution as shown in Figure 6-3 (b).

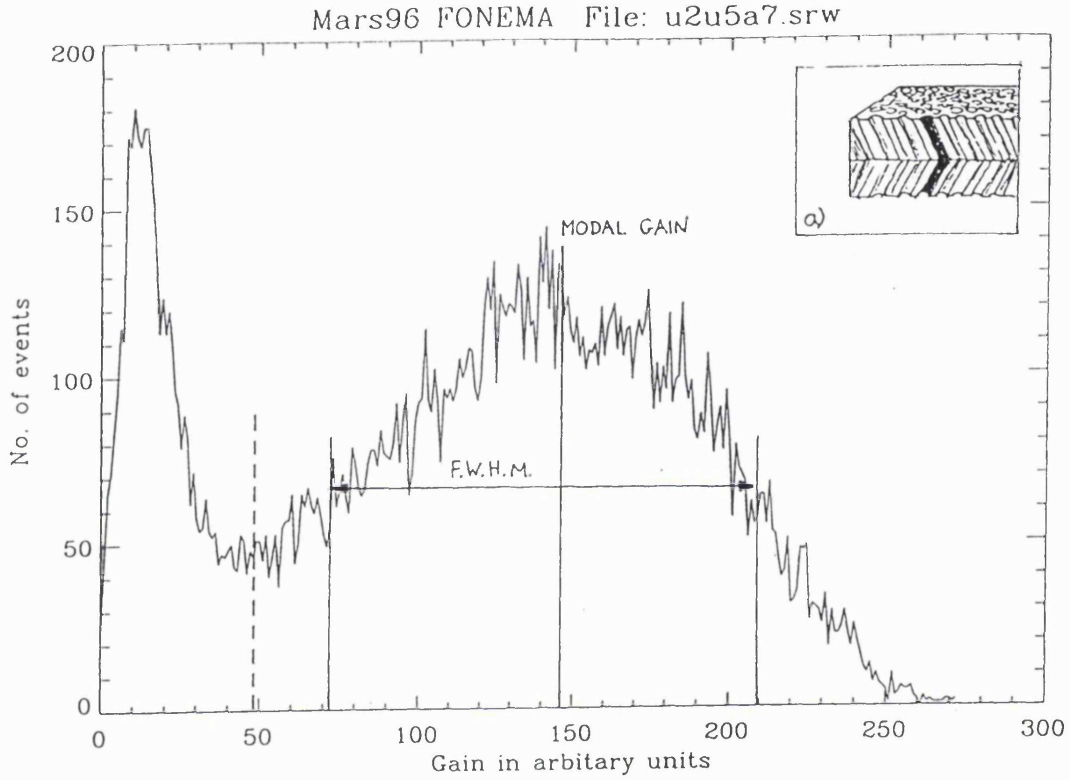

Figure 6-3. a) schematic of a chevron configuration, b) typical pulse height distribution for MCPs used in a chevron configuration. This is for Russian plates with a 30μm gap, operated at 900V per plate

In Figure 6-3 the peaked distribution is shown with the modal gain (G) and full width half maximum (FWHM) marked. The FWHM will often be expressed in terms of a percentage of the modal gain, and in the pulse height distribution shown the FWHM is approximately 100%. This is typical of a chevron made from 80:1 L/D Mullard plates and higher than would be expected for 56:1 plates. *Pearson et al.* (1993), although using a larger interplate gap, report a FWHM of 41% from similar Russian plates. Now a LLD can safely be used to eliminate noise by placing its threshold in the saddle of the distribution: the dashed line in Figure 6-3 shows an ideal location. This also has the advantage that even a large change in gain of the MCP stack, due to a high voltage problem or as occurs naturally over the lifetime of the stack, will not affect the recorded counts by a large amount. The lower the number of counts at the saddle point relative to that at the peak of the distribution, the less effect any gain variations will have on the counting statistics. Ideally the LLD should be variable to allow for readjustment as the gain of the stack varies. The ideal situation for space instrumentation would be to have a variable low level discriminator. As the gain of the MCP stack varied with time it would then be possible to reset the low level discriminator to the saddle point, during operation, to the optimum position. However, as the gain decreases the signal to noise ratio will be reduced and this will, in turn, affect the operation of the imaging anode system: this is discussed later. Also the amount of extra circuitry required often prevents them being used for space flight.

The solution commonly used, and that used for FONEMA, is to provide a fixed lower level discriminator and variable high voltage levels. Because of the uncertainty of actual noise levels on the spacecraft during flight and the need for a signal-to-noise margin, this discriminator is often set higher up the pulse height distribution than the ideal position. As gain decreases with mission lifetime the voltage can be increased to compensate thereby maintaining the optimum gain. However, these will often be fixed voltage steps so before a step up in voltage is made, as the gain decreases, an increasing fraction of the counts will fall below the discriminator resulting in a lower overall detector efficiency. Therefore, the only way to fully deconvolve the real event count from the measured count is to have knowledge of the pulse height distribution as a function of varying voltage and how this changes with time. In some situations this is further compounded by a variation in modal gain with energy of the incident particle. In FONEMA an attempt is made to minimise this effect: this is discussed later. Again, the need to keep mass and power down prevents the use of the extra electronics needed to obtain realtime pulse height distributions during flight, so it is vitally important that a good understanding of the selected MCPs is obtained in pre-flight testing. Some information on the position of the pulse height distribution can be obtained by varying the MCP voltage and recording overall counts in a region of stable particle flux. This is explained in the next section.

6.2.3 Gain

As the voltage across the MCP stack is raised, the intrinsic gain increases, and this continues indefinitely until electrical breakdown occurs in the plates. The pulse height distribution of a chevron stack will begin as a falling exponential function and gradually become increasingly peaked as the pulses saturate. This is generally believed to be due to positive wall charging. As the electron avalanche progresses down the pore, increasing in number, it is continuously depleting the semiconductor wall of more and more charge. This charge cannot be replaced on the same timescale as the pulse transit time, thus a retarding 'wall charge' electric field becomes established. Electron collision energies are therefore reduced until they are sufficient only to produce single secondary electrons on collision with the channel wall (*Fraser*, 1989). This causes the charge cloud magnitude to become saturated and hence the quasi-gaussian curve of the pulse height distribution shown in Figure 6-3(b). The average gain of a single MCP is dependent on the dimensionless ratio L/D (*Adams and Manley*, 1966). In a chevron configuration the gain is also dependent on the overall detector geometry.

Figure 6-4 shows how the shape of the pulse height distribution curve, and hence modal gain, varies as more volts are applied. A summary of these results showing the modal gain and the FWHM of the distribution versus applied voltage is shown in Figure 6-5.

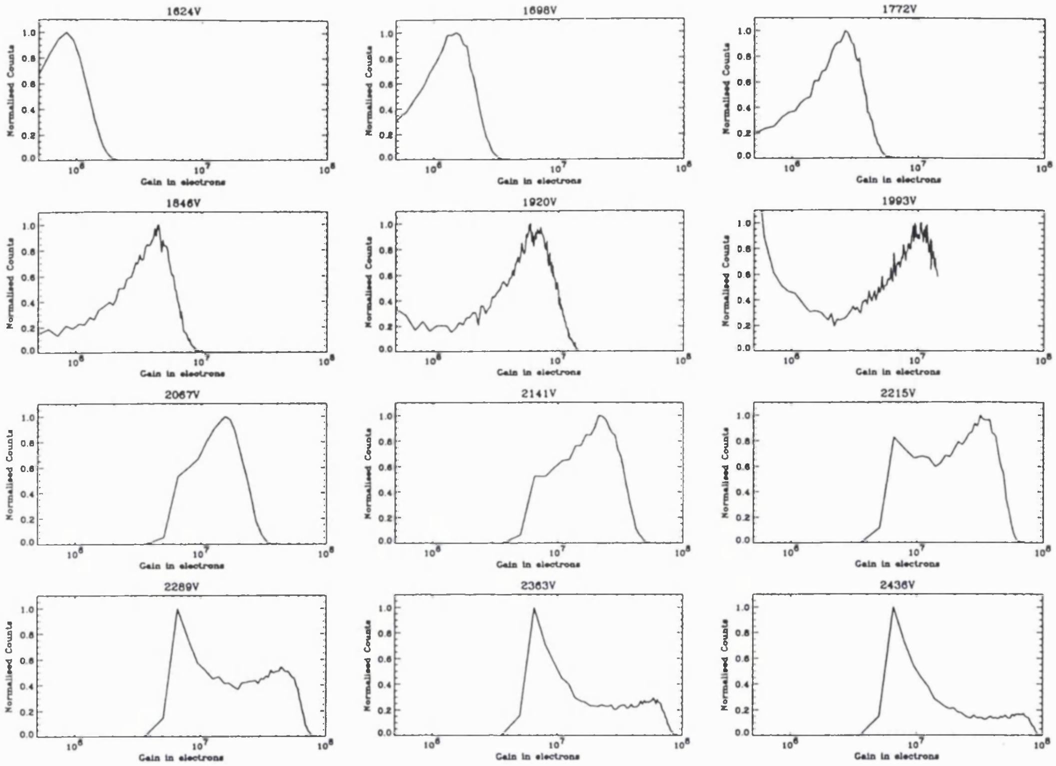

Figure 6-4. Pulse height distributions for 12 different voltage settings for a typical Russian MCP. The lower level discriminator is set at a gain of 5×10^5 electrons for the first six plots and at 5×10^6 electrons for the rest.

In Figure 6-4 the gain can be seen to increase as increasing voltage is applied; the FWHM, where it measurable, increases also but maintains a fractional value of ~100% of modal gain across the voltage range. Between plots 6 and 7 there is a necessary attenuation of signal to allow charge cloud sizes of greater than 10^7 electrons to be measured, which causes the jump in the lower level discriminator. At plot number 9, where the applied voltage is 2215V, the number of events occurring at the valley in the distribution is now more than half the peak number, making determination of the FWHM more difficult. For this reason only the first six values of FWHM are plotted in Figure 6-5.

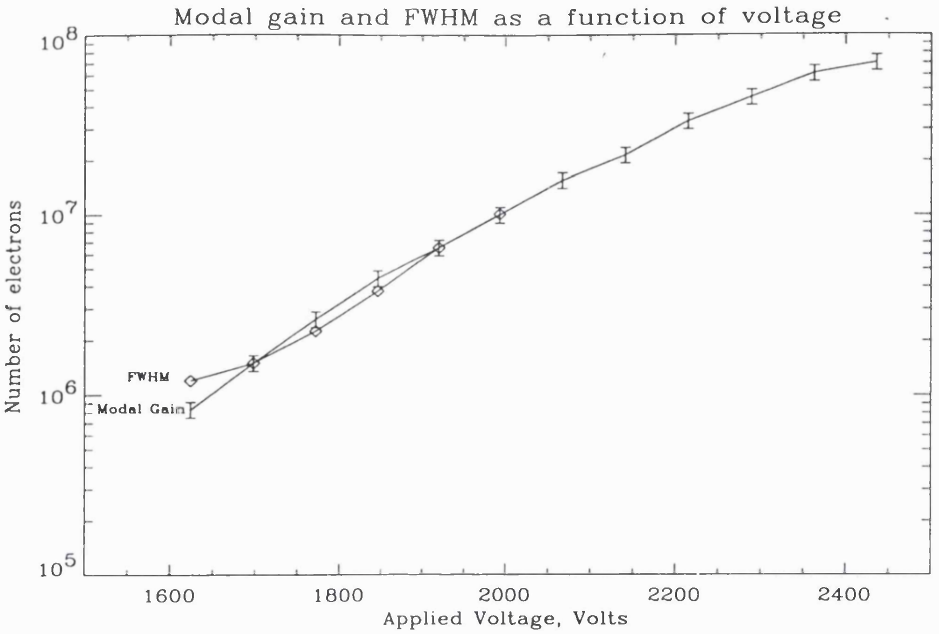

Figure 6-5. Gain and FWHM versus applied voltage for the results in Figure 6-4.

For FONEMA an initial gain of 6×10^6 electrons was chosen, as this showed a good peaked distribution well above the background noise. The lower level discriminator (LLD) was set at an equivalent gain of 3×10^6 electrons. On the FONEMA instrument an upper level discriminator (ULD) is also used, set at 1×10^7 electrons, to reject very large signals which either go out of the analog to digital convertor (ADC) range or into the non-linear region of the ADC operation, both of which would cause incorrect position encoding on an imaging anode system. A secondary effect of this is that if the modal gain is chosen as the average of the 2 discriminator levels, small reductions in MCP gain creating a loss of counts at the low end of the PHD tend to be cancelled by an increase of events recorded at the high end. Hence the overall efficiency of the detector is less sensitive to changes in MCP bias voltage.

This effect is more clearly seen if the number of events counted is plotted as a function of applied voltage for a fixed input count rate, as in Figure 6-6. Where the curve peaks at point B the number of recorded events has reached a maximum. This is generally where the modal gain of the MCPs is half way between the lower and upper level discriminator. At the steepest part of the curve (A) the number of counts as a function of voltage is maximised, and this occurs when the peak of the quasi-gaussian pulse height distribution is at the LLD. Point C represents the point where the background events start to increase and add to the real events which have yet to cross the ULD. If the valley in the initial distribution was at a lower level and the ULD was set lower, the point B would be at the apex of a broad peak. Where a knowledge of the pulse height distribution is not attainable this method allows suitable operating conditions to be found. For FONEMA, at regular intervals during the mission, images will be taken for a range of operating voltages for each MCP thus allowing the detector performance to be monitored.

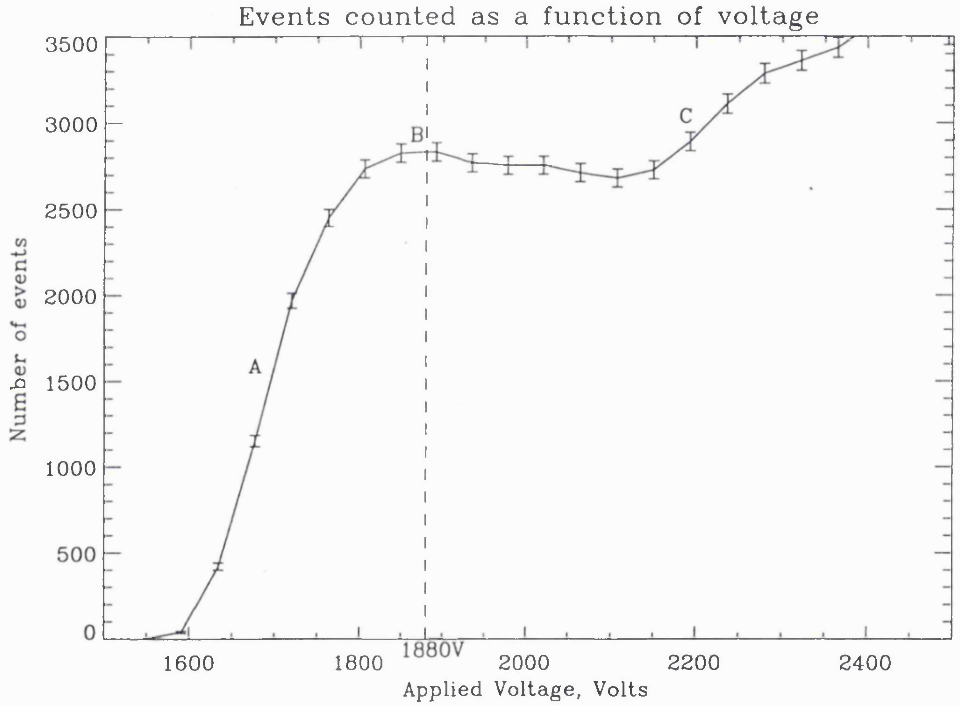

Figure 6-6. Number of events recorded as a function of voltage for a typical MCP setup. In this experiment Russian MCPs are arranged in a chevron stack and illuminated by an ion gun. The LLD was set at 1.6 × 10^5 electrons and the ULD at 6 × 10^7 electrons.

As mentioned previously the Russian MCPs varied substantially in measured resistance values. This did not reflect on the gain versus voltage characteristics for these MCPs as shown in Figure 6-7. Although the spread in voltage values for the same gain is reasonably large there is no correlation between these curves and the

MCP stack resistance. This is clearly demonstrated in Figure 6-8 where the resistance of a selection of MCP stacks is plotted against the applied voltage required to attain a gain of 6 × 10^6 electrons.

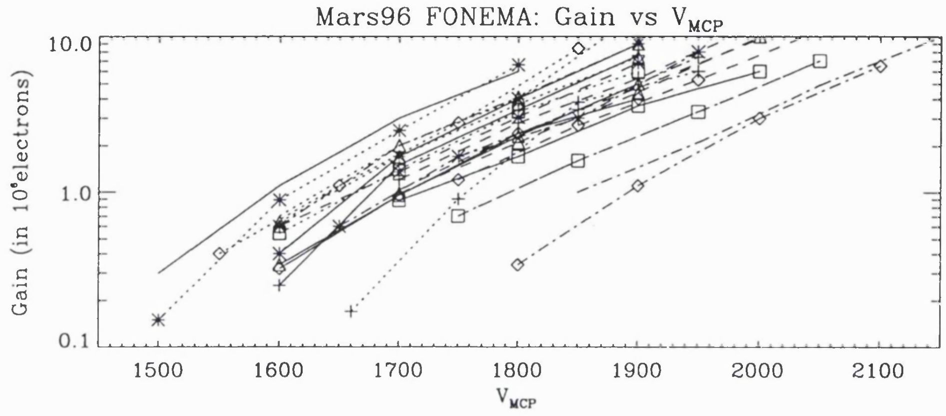

Figure 6-7. Gain versus voltage for 24 pairs of Russian MCPs used for the FONEMA project.

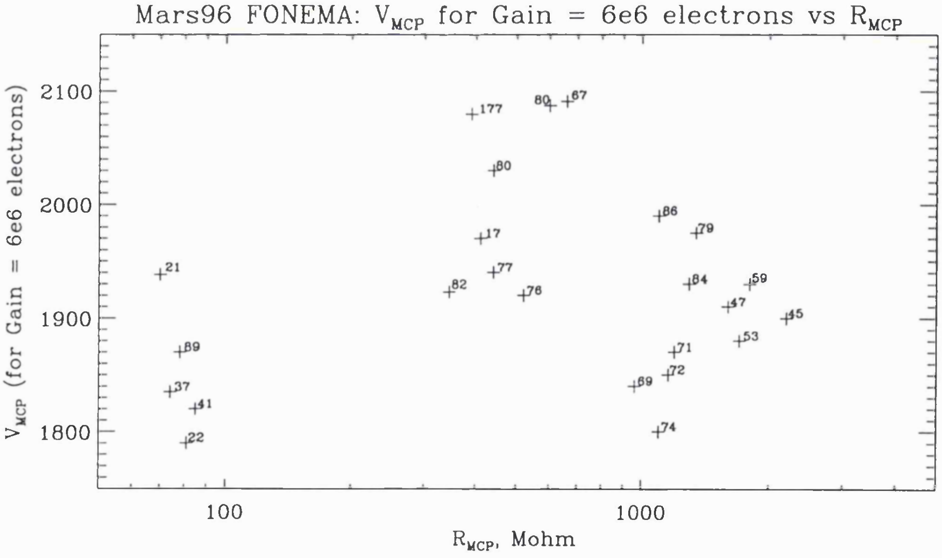

Figure 6-8. Voltage required to achieve a modal gain of 6 × 10^6 electrons versus the resistance for a number of Russian MCP stacks.

6.2.3.1 Gain uniformity

The data presented so far assumes that the gain for an MCP is the same across its whole surface, but in practice this is not the case. Figure 6-9 shows a contour map of gain variations across four of the FONEMA MCP stacks. This was obtained by taking an image of 1keV ions fired through a pinhole mask placed 1mm in front of the MCP stack. The distance between the ion gun and the detector was approximately 0.5m so pore bias angle effects were negligible. These gain uniformity maps were carried out for all the flight model MCP stacks over a range of gain conditions. A value of average gain is obtained for each pinhole imaged and a surface spline is applied to the resulting grid of gain values. The standard error on the individual gain measurements is approximately 4%, whereas the standard deviation about the average gain across the surface is between 8% and 12% for the four plots. This means that these variations are significant and not due to errors in the gain measurements. In the figure itself the contours are marked with the gain as a percentage of the mean gain. These stacks have a 30μm shim between the two MCPs. It is possible that some of the gain non-uniformity is due to differences in the gap size because of variations in the flatness of the shim or the MCP surfaces themselves. This would cause the size of the charge cloud area falling onto the second plate to vary from place to place. The number of illuminated channels in the second plate and number of electrons entering these channels would vary, hence altering the final gain output from the MCP. Variations in gap size due to variations in the shim would be expected to be large scale changes varying smoothly across the MCP area. Variations in gain due to MCP thickness changes are likely to be on a smaller scale. A similar effect may also appear if there is a variation in the depth of electrode material down the channels across the plate, again causing variation in output charge cloud geometry from the first plate. This gain variation may also be due to the manufacturing process of the MCP. The experiments carried out to map the gain uniformity under normal operating conditions did not provide enough evidence to identify which mechanism is dominant. A similar result to that shown in Figure 6-9 would be expected for a chevron stack without an interplate spacer but because a saturated pulse height distribution was not possible with the Russian MCPs in this arrangement the experiments were not done. Data from the PEACE instrument to be flown on the Cluster spacecraft, where larger plates were butted together, did show gain variations across the surface of a similar magnitude (*Reading*, 1997).

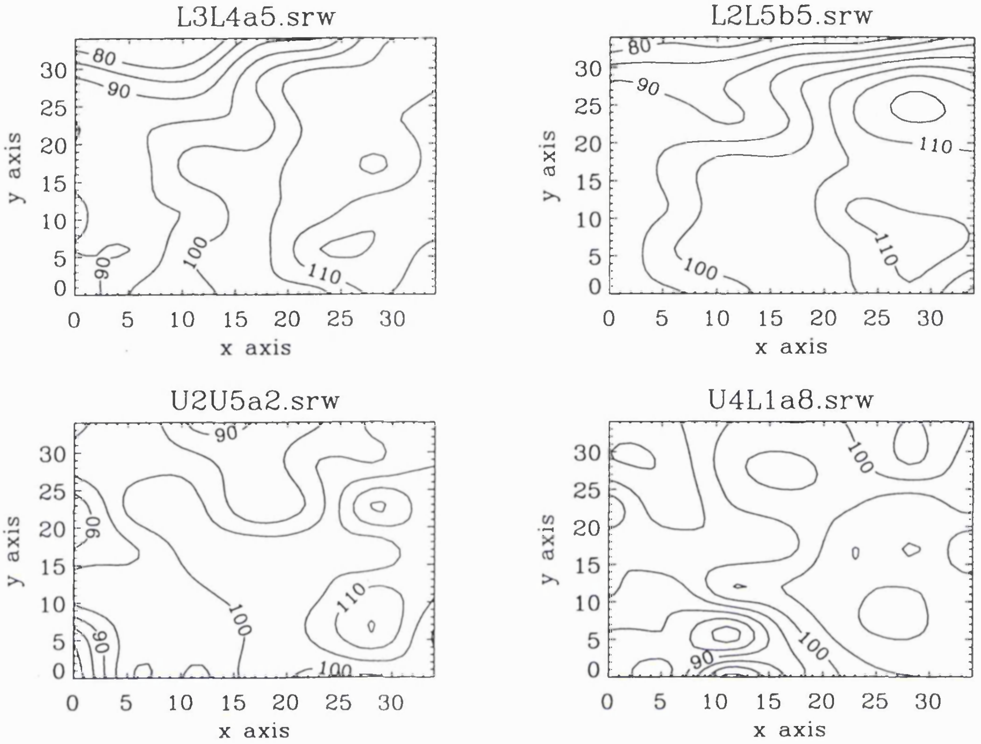

Figure 6-9. Gain variations across the central regions of four of the flight model MCP stacks. The area shown is approximately 14mm^2.

6.2.4 MCP lifetime

With the trend towards longer missions it is important that the MCPs themselves will be able to perform well over the expected lifetime of the instrument. In the case of Mars 96 the provisional operational period was for two years after arrival at Mars, although science operations during the cruise phase would mean almost 30 months of instrument operation. However, the lifetime of the instrument depends on the lifetime of the MCPs, i.e. on how much charge can be extracted from them before the gain becomes too low to allow reliable measurements. It is estimated that the maximum count rate (R_m) for an individual FONEMA analyser is about 2500Hz (see Chapter 3). Assuming an average gain (G_{av}) of 6×10^6 electrons, and an average countrate of half the maximum, with an operational time of only half the total mission time (T), the total accumulated charge per unit area (Q_A) is given by:

$$Q_A = \frac{R_m T G_{av} e}{4A_{mcp}}$$

where e is the charge on an electron and A_{mcp} the MCP area (10cm^2). This gives a value for Q_A of 4.7mC cm^{-2}.

Figure 6-10 shows lifetime tests for 2 different sets of MCPs. The set of solid lines shows the modal gains at different operating voltages plotted against the extracted charge, where the MCPs had a resistance of 475MΩ. Illumination of the detector for this test was with residual gas ions accelerated to 2.4keV and at an estimated count rate of 1.5MHz, calculated from anode current. It can be seen that the gain is halved when 20mC are extracted: these plates have an area of approximately 10cm^2 so the extracted charge per unit area is 2mC cm^{-2}. The glitch that appears at an extracted charge of 125mC was due to a break of vacuum, the re-exposure to atmosphere producing a temporary rise in gain. The dashed line is for a pair of plates with a resistance of 80MΩ, the illumination made with 3keV X-rays at a deadtime corrected rate of 230kHz. Again these plates show a similar initial gain degradation, suggesting that the irreversible loss in gain is dependent on total extracted charge and not the rate at which the charge is extracted. Similar tests by *Sandel et al.* (1977) also suggest that the rate of charge abstraction is unimportant in determining lifetime, hence, the initial operating gain of a particular pair of plates is also unimportant (*Fraser*, 1984).

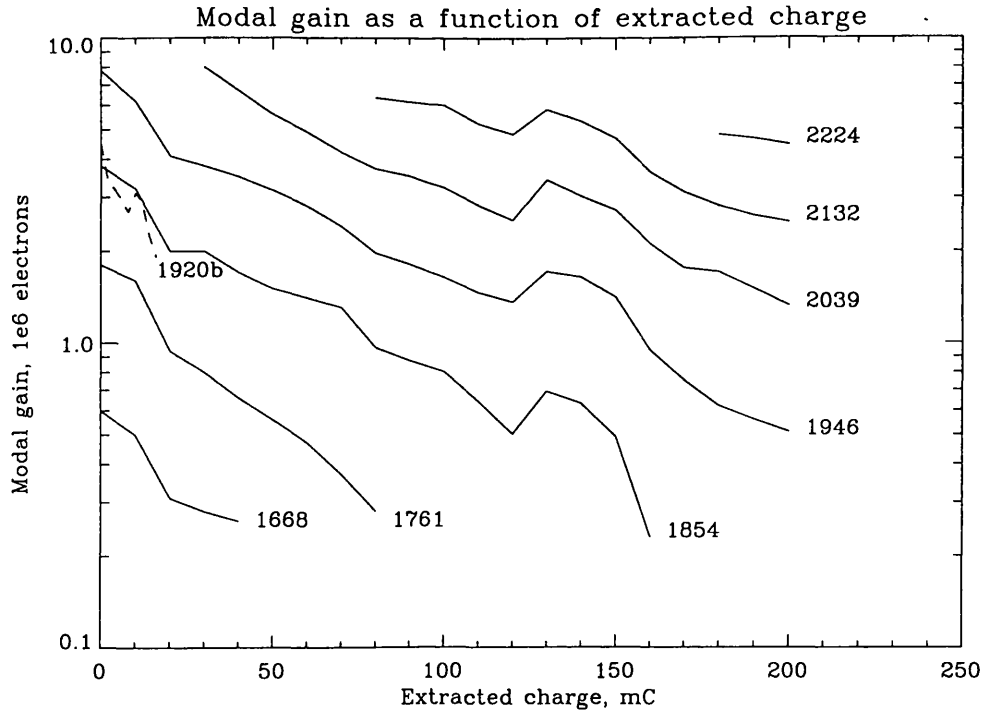

Figure 6-10. Lifetime tests for Russian MCPs. The solid lines show modal gain plotted against total extracted charge for different voltages across the MCPs. The dashed line labelled 1920b shows a similar curve for a second set of MCPs.

The gain degradation measured for the FONEMA MCPs is much worse than that quoted from the manufacturer and that predicted by the models. In fact, *Fraser* (1990) models the gain degradation as a function of the L/D ratio and finds that for 40:1 plates the relative gain falls less rapidly with extracted charge than for 80:1 plates. This is also supported from experimental data taken from *Fraser et al.* (1988) as shown in Table 6-2. With an L/D ratio of 56:1 the model by Fraser would predict an initial halving of gain after 200mC cm^{-2} is extracted from the Russian plates. In experiments carried out on MCPs from the same batch, *Fedorov* (1994) arrived at a figure of 2.5mC cm^{-2}, similar to the FONEMA results. This suggests that the manufacture of the Russian MCPs is not the same as that used for the MCPs upon which Fraser's model is based. Table 6-2 shows values from other experimenters, including typical values from the major manufacturers and Fraser model, of extracted charge as a function of area needed to reduce the modal gain to 50% of the initial figure. It can be seen that the lifetime of the Russian MCPs used for FONEMA is lower than most other quoted figures.

Reference	Configuration	Charge extracted, mC cm^{-2}
Hamamatsu (1991)	Hamamatsu 3-stage, L/D = 50:1, D unspecified	38
Fraser et al. (1988)	Mullard Chevron; L/D = 40:1, D = 12.5μm	7-8
Fraser et al. (1988)	Galileo Chevron; L/D = 40:1, D = 10μm	1-2
Henry et al. (1977)	Mullard front plate 0° bias, rear plate 12°, L/D = 74:1 D=11.7μm	20
Henry et al. (1977)	Mullard front plate 0° bias, rear plate 12°, L/D = 80:1 D=12.5μm	0.7 - 3
Fedorov (1994)	Russian 43x53-15; L/D = 56:1, D = 15μm	2.5
FONEMA plates	Russian 20x53-15; L/D = 56:1, D = 15μm	2

Table 6-2. MCP lifetime results from other authors and manufacturers.

In the tests performed on the Russian MCPs the gain depression as a function of extracted charge is roughly a falling exponential. *Malina and Coburn* (1984) reported a different shape for one set of plates that they tested. They find a plateau region, after an initial gain drop, where gain stays relatively stable over a period when 1mC cm^{-2} is extracted. This plateau is suggested as a property of all MCPs by *Lecomte and Perez-Mendez* (1978) although no experimental evidence is presented to support this.

Despite this lower than expected lifetime the small geometric factor for FONEMA means that the Russian MCPs can be used without compromising the instrument. From Figure 6-10 it can be seen that the initial gain can be recovered by an increase in the potential across the MCPs. In order to recover from the expected abstraction of 4.7mC cm^{-2} the voltage would need to be stepped up by 200V to 300V during the mission. To allow for this compensation the MCP high voltage units in FONEMA were controllable from 1700V to 3100V in 100V steps. The wide range and number of steps of the high voltage unit were to allow for any later changes in specification of the MCPs, including changing supplier, yet allowing design and construction of the units to continue for early models of the instrument. Too many voltage changes throughout the operational lifetime can cause problems to arise within the detectors. Firstly it is only possible to maintain relative efficiencies of detectors if the MCP properties vary in the same way with time and extracted charge. As shown above, the lifetime properties vary between plates from the same manufacturer and are difficult to predict, especially in light of the large range of MCP resistance values that were present in FONEMA. It also assumes that the initial gain to voltage characteristics are the same for each MCP, otherwise the gains will vary in an unpredictable way. From the results of the lifetime test above it can be shown that the gain versus voltage characteristics of an MCP change as charge is extracted (see Figure 6-11). It is possible that this rate of change will vary between plates. Unfortunately there was no provision in FONEMA to record pulse height distributions in flight, which would have allowed measurement of MCP parameters over a mission lifetime for a large number of plates. A further problem, discussed in detail in a later section, is that the MCP bias controls the MCP/anode gap voltage, which is important to the imaging and needs to be predictable. The two halves on FONEMA are supplied from separate high voltage supplies so it is possible to do some first order matching of MCPs so that those with similar properties can be housed in analysers on the same half, thereby minimizing the effects of the voltage change. As long as the voltage increases needed are small these effects should be minimal and result in no significant relative changes in detector efficiency.

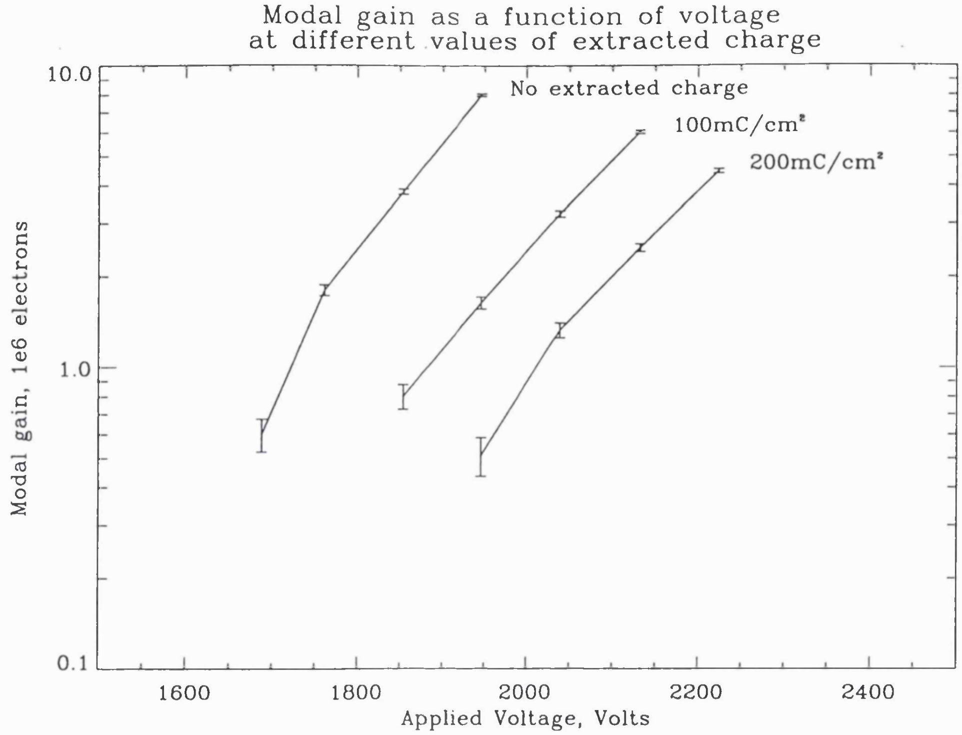

Figure 6-11. Plot of modal gain as a function of applied voltage for 3 different values of extracted charge. The plot shows that a fixed voltage increase produces a changing rise in gain as charge is extracted.

6.2.5 Count rate dependent gain depression

As well as that occurring in the long term due to charge extraction, it is possible to witness gain reduction in MCPs at any time due to count rate dependent gain depression. To some extent the reason for this is an extension of the explanation proposed for saturation. Saturation is caused by the charge depletion in the walls not being replenished quickly enough by the applied voltage to prevent a collapse of the internal electric field. If the count rate is very high over a region of the MCP the total extracted charge rate over that area can be so high that there is no time to replenish the charge before the next event arrives. In that case the available charge for the second pulse is much less and the modal gain is lowered. This effect is reversible, i.e. on returning to a lower count rate the gain will again reach nominal levels. In Figure 6-12 the pulse height distributions are shown for a FONEMA detector operating at nine different count rates. The area of MCP illuminated in this case is a 2 × 3mm rectangle near the centre of the field of view, which simulates the typical area illuminated in a single analyser.

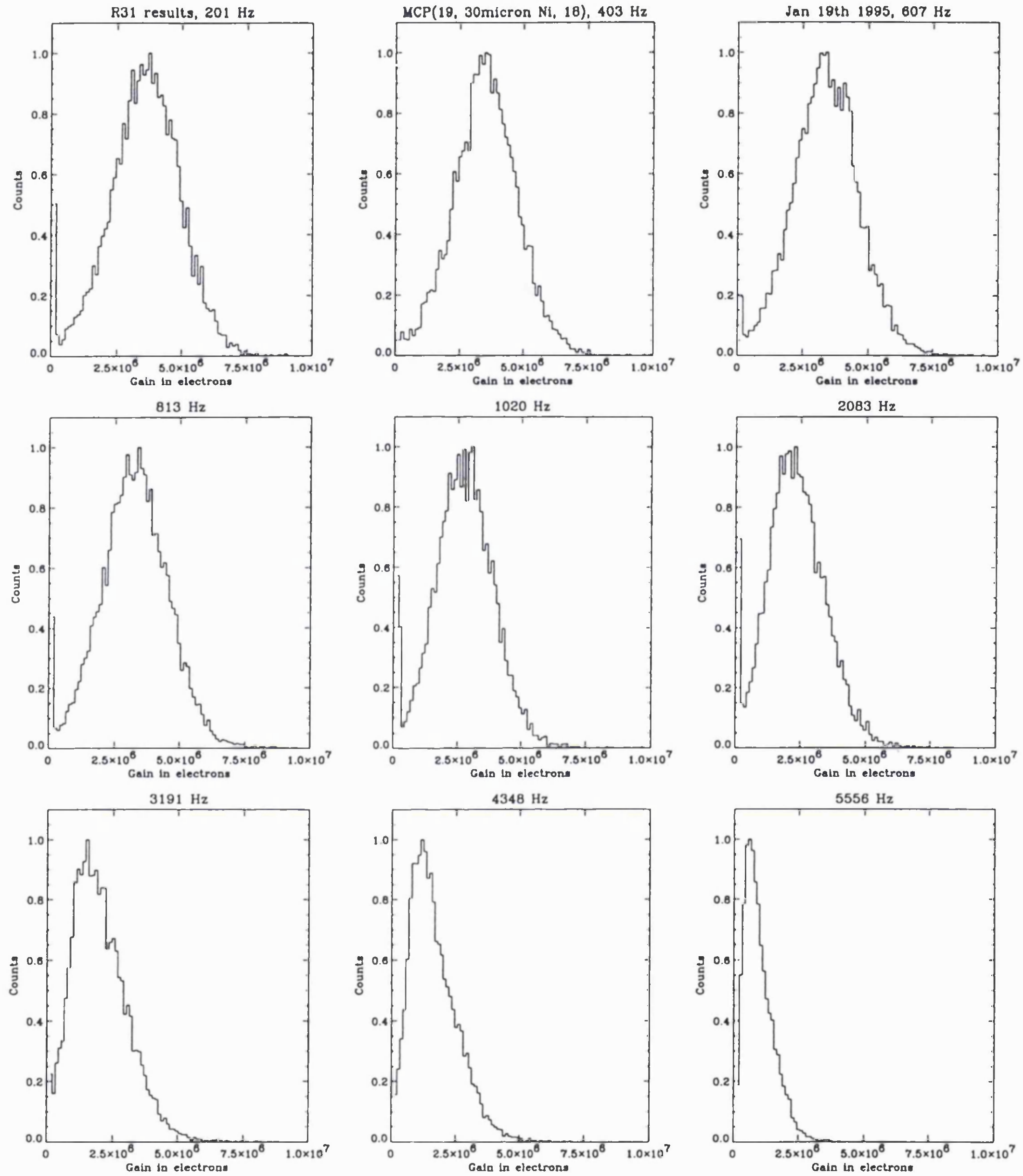

Figure 6-12. Pulse height distribution as a function of count rate. The number of events recorded for each gain value has been normalised to the peak value in each plot.

Accepted wisdom is that MCPs will start going into count dependent gain depression as 10% of the strip current is drawn (*Mullard*, 1976). More recently, *Hamamatsu* (1991) suggest that gain depression starts when the signal current is just 5-6% of the strip current. The strip current is the ambient current running through the MCP and is simply given by applied voltage divided by the MCP stack resistance. In Figure 6-12 the gain depression starts at an input event rate of about 800 counts per second, which corresponds to an electron current of only 2.8% of the strip current, less than specified by the MCP suppliers. Figure 6-13 shows the relative gain versus count rate per pore for the same experimental set-up as that used to obtain Figure 6-12. It can be seen that the relative gain is reduced by half when the count rate is approximately 1 count per second per pore. Although the absolute figures are different due to slightly different set-ups, the form of this relationship is the same as that reported by *Zombeck and Fraser* (1991) and for other authors by *Fraser et al.* (1991). Because with a fixed low level discriminator the number of events recorded must go down as gain is depressed the effect can be modelled as a local MCP deadtime (*Zombeck and Fraser,* 1991). In their model they assume that during an event the charge is instantaneously removed from a channel and then replenished with an RC time constant τ. The time constant τ is related to the single channel time constant τ_{ch} by:

$$\tau = k\tau_{ch} = kR_{ch}C_{ch} \tag{6.1}$$

where R_{ch} and C_{ch} are the resistance and capacitance of a single microchannel in the rear plate and k is a factor that represents the properties of an unknown channel recharge circuit. *Fraser et al.* (1991) state that on the basis of previous experimental evidence the parameter k should be an increasing function of illuminated area in any multi-stage detector. If the MCP is simply an assemblage of lumped parameter RC circuits, then:

$$R_{ch} = nR_{mcp} \tag{6.2}$$

and

$$C_{ch} = (1/n)C_{mcp} \tag{6.3}$$

where n is the number of channels in the MCP (about 4×10^6 for these plates) and R_{mcp} and C_{mcp} are the measurable plate strip resistance and capacitance, respectively. Thus,

$$\tau_{ch} = R_{mcp}C_{mcp} = \tau_{mcp} \qquad (6.4)$$

Assuming that immediately after an event has passed the gain is zero and it recovers exponentially with the time constant τ, then the gain as a function of time is given by

$$G(t) = G(0)(1-\exp(-t/\tau)) \qquad (6.5)$$

where $G(0)$ is the low count rate gain.

It is then straightforward to show that the average MCP gain at the higher count rate N counts s^{-1} per active rear channel is given by the expression:

$$G_m(N\tau) = G(0)(1+N\tau)^{-1} \qquad (6.6)$$

The average pulse current per channel is then

$$I_p = G_m N \qquad (6.7)$$

and the strip current in the rear plate is given by

$$I_s = V/R_{ch} = V/(nR_{mcp}) \qquad (6.8)$$

where V is the voltage across the rear plate.

By dividing equation 6.7 by equation 6.8 and substituting in from the other relations the following ratio of signal current over channel current can be obtained:

$$I_p/I_s = G(0)(nR_{mcp}/V)(1/N + kR_{mcp}C_{mcp})^{-1} \qquad (6.9)$$

By fitting the above equation to the experimentally obtained variation of pulse current to strip current ratio with count rate per channel, a value for k and hence τ can be obtained. If this model is fitted to the experimental data from the FONEMA plates the value obtained for k is 300, which corresponds to a dead-time τ of 4.8 seconds. Because k is obtained from a fit to the data, the value of dead-time per channel is related to the operating conditions and primarily the area of MCP illuminated.

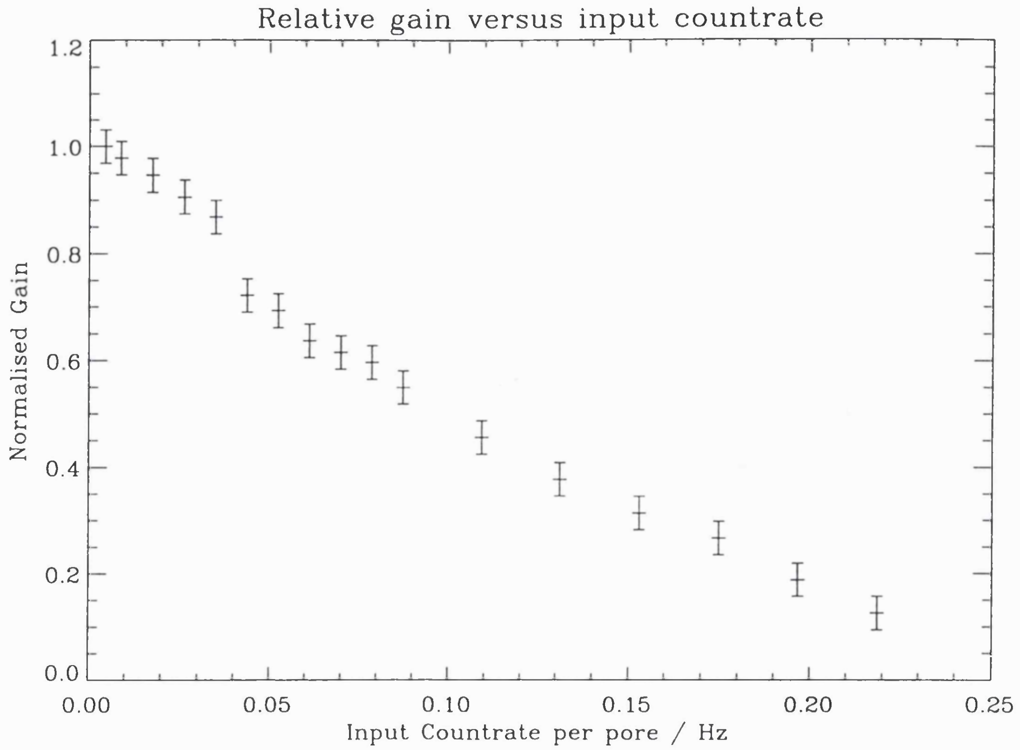

Figure 6-13. Relative gain as a function of count rate per pore. These results are for a narrow beam covering only 0.0057 of the MCP area.

Edgar et al. (1992) demonstrated that count rate dependent gain depression is a relatively long range phenomenon in that active pores can significantly depress the gain in the surrounding quiescent pores at distances of a few millimetres. In an instrument such as FONEMA where different mass groups may be close together on the detector this could be a significant effect. Of course the point at which this gain depression becomes significant depends on the operating conditions of the detector and should be determined for each set-up. *Pearson et al.* (1988) and *Fraser et al.* (1991) have both shown that the gain depression is proportional to the number of illuminated pores in the second plate of the chevron stack. *Tremsin et al.* (1996) have shown how the effect of count dependent gain depression can be reduced by using metal electrodes of gold as opposed to the typical nichrome; presumably lower resistance decreases the charging time of individual pores.

6.2.6 Preferential ageing

Another problem that can occur is non-uniform aging of the MCP due to different areas of the image plane receiving more events than others e.g. the position relating to solar wind protons. This means that the gain in these regions will decrease more quickly than the rest of the MCP reducing the overall detector efficiency for that particular species. Hence the relative densities of species will appear to vary during the mission lifetime. Eventually it will be necessary to increase the voltage so that the pulses of the largest population appear above the lower level discriminator. In doing this, it is possible that regions which represent minor populations, that may not have suffered from the gain reduction, will experience a gain increase that will take the event levels over the upper level discriminator, and hence, artificially reduce the population still further. Figure 6-14 is a contour plot showing the gain of an MCP stack as a percentage of the maximum gain.

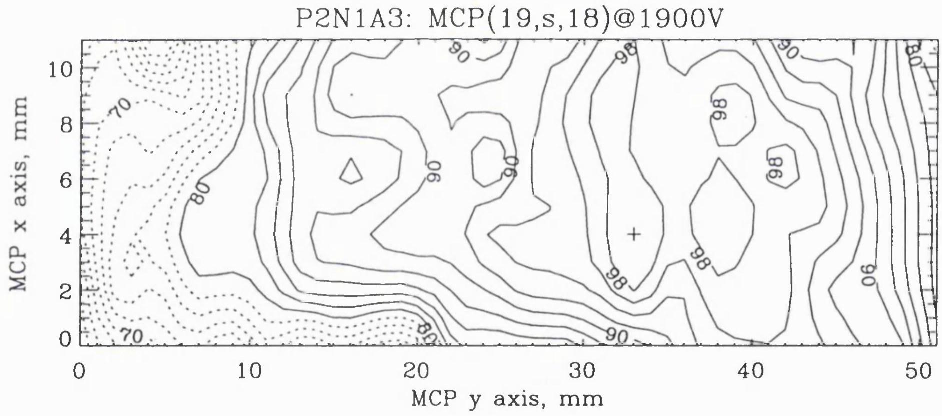

Figure 6-14. Contour map showing the MCP gain across a 11 × 51mm area of a Russian MCP chevron stack. The contours show the local gain as a percentage of the maximum gain, 4.56×10^6 electrons, which is marked by the cross. The standard error in gain is 1.5% whilst the standard deviation on the mean gain across the image is 12%. Again the setup is such that pore bias angle effects are negligible.

Degradation due to preferential use in certain areas of the MCP, resulting in loss of gain, can be clearly seen in the image. These plates have been used for numerous experiments over a period of 2 or 3 years, and the low gain shown at the left of this plot is a consequence of that testing. However, much of the MCP, where y>20mm, has had very little use.

On the strength of the evidence from the lifetime tests, these effects will not occur at a significant level until well into the mission. The problem is that it may be difficult to interpret exactly when they are significant. The only way to account for this variation is to measure, regularly, from conditions of known relative density or to cross calibrate with other instruments on board. Of course this problem could be alleviated fully with real-time knowledge of the pulse height distribution on an event by event basis. It is also possible that variations in the operation of the imaging system with gain may allow some estimation of the relative gains across the detector, i.e. from fixed patterning, which is discussed in a later section. Unlike the quantum efficiency, discussed in the next section, this effect varies from plate to plate so the necessary data cannot be obtained from post flight calibration of similar MCPs in the laboratory.

6.2.7 Quantum efficiency and energy dependent gain

The areal detection efficiency is of prime importance when using an MCP for single ion counting, particularly where counting statistics are limited or counting rates of different ions have to be related to each other. Although MCP detectors have good quantum efficiency, one feature of their construction inherently limits their efficiency: the walls of the individual channels which make up the plates are of finite thickness and thus form an interchannel web. One would expect that the open area ratio of the MCP would then form the upper limit to the areal efficiency for incident particles. However, *Panitz and Foesch* (1976) demonstrated that ions impacting the metallic surface of the interchannel web will produce secondary electrons. *Taylor et al.* (1983) reported on a method of increasing the overall quantum efficiency by placing a grid in front of the MCP and applying a small electric field to return these secondary electrons to the MCP surface. By careful choice of voltage, spacing and mesh it is possible to increase the areal efficiency from the open area ratio of 58% to almost 80% without other detrimental effects. However, these tests were done using not ions, but UV radiation, where the gains from the electrons will be very similar.

With the Russian MCPs it was impossible to produce a saturated MCP pulse, even with ions unless a spacer was used. Even with a spacer no saturation pulses could be produced for X-rays. It is suspected then that the gain from web electrons would be less than that produced with the ions and therefore the same population would be represented by two different PHDs making true event rates difficult to determine. *Gao et al.* (1984) point out that using this method there is also the possibility of loss of spatial resolution as secondary electrons may return to the surface some distance from the initial impact unless fields > 1000V cm^{-1} are used.

For FONEMA, in order that the electrostatic deflection field could be well understood and the field topology not upset by changes in MCP voltage a grid was placed 1mm in front of the MCP surface. This grid was fixed at the pre-acceleration potential which varied from -88V to -1753V. As the anode was kept at ground this meant that the front MCP potential was at approximately -2.2kV in normal operation. The field between the mesh and the MCP would therefore be accelerating secondary electrons away from the MCP back to the grid whilst simultaneously accelerating the ions toward the MCP. This meant that the problem of two different sources of event at the front MCP was avoided while limiting the areal efficiency to that of the open area ratio, 66.5% for the Russian MCPs. Another advantage of this arrangement is that the final ion impact energy is enhanced and the impact angle to the MCP normal for low energy events lessened. This is explained later in this section.

Unfortunately, at the time when the MCP performance was being investigated, the equipment necessary for absolute measurement of detector efficiency was unavailable. As well as a calibrated detector to measure absolute rates from the ion source it is necessary to have an ion gun that can provide some mass differentiation. With the present experimental setup there is no knowledge of the relative ionisation of species within the ion gun, so even having a calibrated residual gas analyser does not allow a comparsion of even relative efficiencies. It was hoped that after launch the necessary funds and time needed to complete these tests would be available. Obviously, representative MCPs would have to be used, but the evidence suggests that the absolute detection efficiency of plates would not vary within the same batch and according to the limited literature available is similar between plates from different manufacturers. It was also planned to do some calibration in flight, i.e. with other ion instruments and from density measurements made in the solar wind.

Data on the absolute quantum efficiency of MCPs for ions is available from other authors. Figure 6-15 is taken from a study by *Gao et al.* (1984) and shows the absolute efficiencies for H^+, He^+, and O^+ ions at normal incidence. In these results the dependence is purely on the energy of the ion. Results from *Oberheide et al.* (1977) , Figure 6-16, covering a larger mass range show a mass dependence of the absolute detection efficiency, with lower mass ions having a higher efficiency at similar energies. Both these results show the detection efficiency reaching a maximum when the energy of all ions reaches between 3 and 5keV. In contrast *Schecker et al.* (1992) show absolute quantum efficiency leveling out at 60% for hydrogen ions at energies above 1keV. Similarly, *Tobita et al.* (1987) obtained a constant detection efficiency of about 50 ± 10% in the impact energy range 1-10keV.

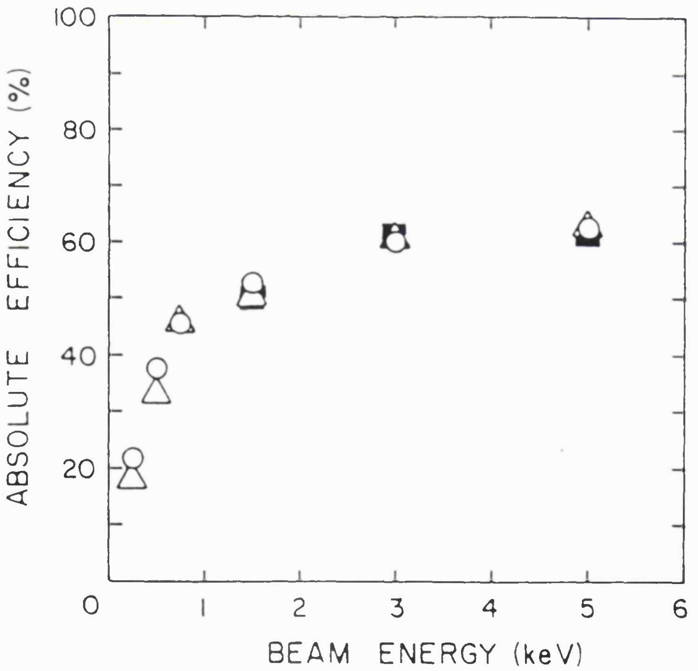

Figure 6-15. Absolute detection efficiencies for H^+ (circle), He^+ (triangle), and O^+ (square) particles at normal incidence to the detector surface (*Gao et al.*, 1984).

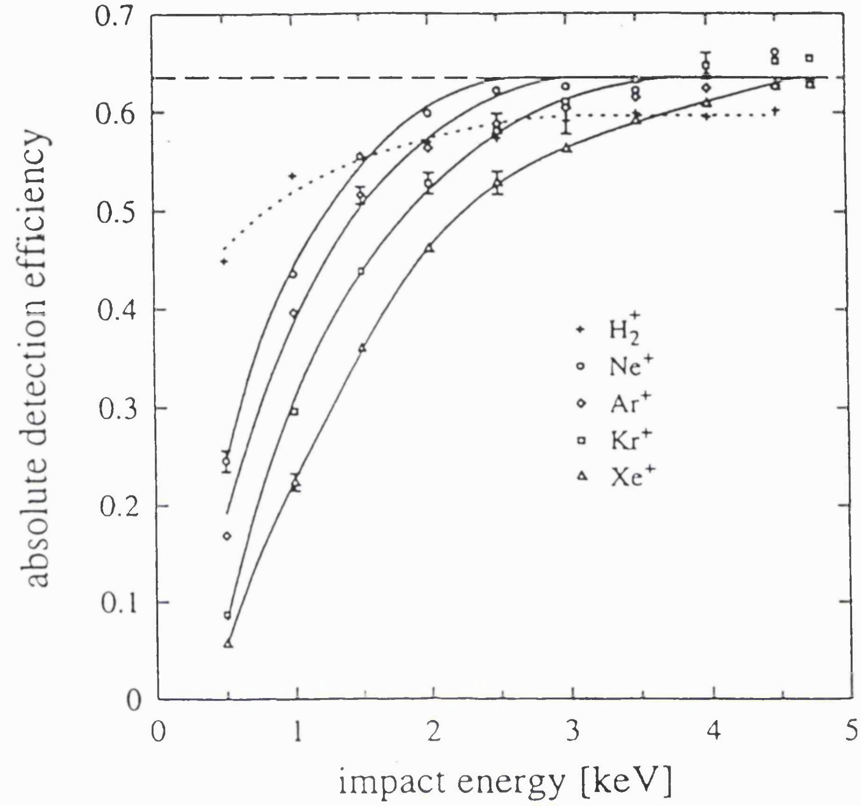

Figure 6-16. Absolute detection efficiencies of an MCP as a function of ion impact energy. The broken line shows the saturation of absolute detection efficiencies at 63.5% (*Oberheide et al.*, 1997).

The QE of MCPs also varies with the angle of incidence of the radiation or particle, although very little data is published on this variation for ions. *Gao et al.* (1984) have found that this is independent of particle species and energy. Figure 6-17 shows this angular dependence which is for H^+, He^+, and Ne^+ in the energy range from 750eV to 3000eV. These measurements are only taken in a plane, the plane perpendicular to the plate that contains the MCP pore. For full characterisation a scan in both angles is necessary. However, the MCP pores in the FONEMA analyser are arranged so that in going from the front face to the back face of the front MCP the pores point upwards away from the direction of the ions deflected in the magnetic field. This means that the smallest angle to the MCP pores, approximately 8°, is for high mass, high energy ions which have an intrinsically larger quantum efficiency anyway. For lower energy ions the field between the grounded mesh and the MCP deflects the ions to a more normal direction. From simulations the maximum angle to the MCP is about 30° which should produce a quantum efficiency at least as high as that shown by *Gao et al.*, i.e. in excess of 80%.

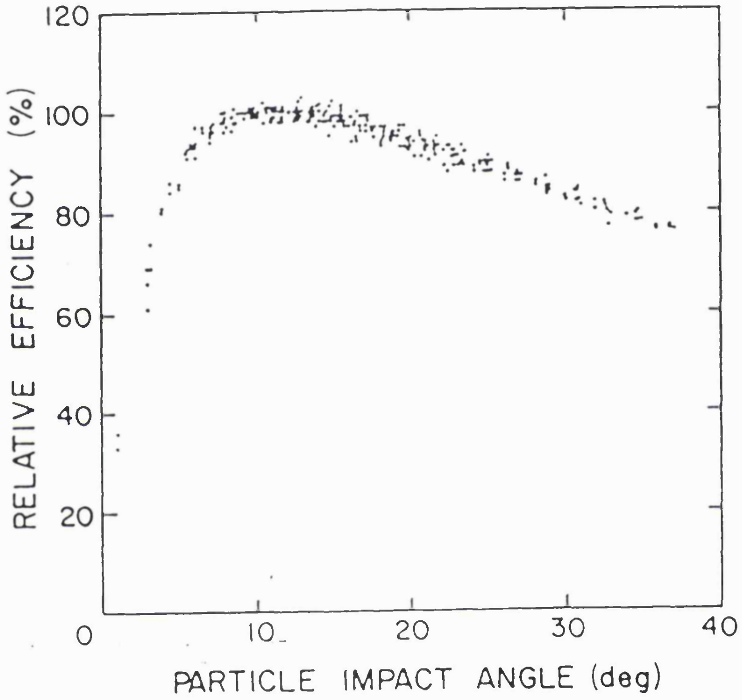

Figure 6-17. Relative detection efficiency as a function of the angle between the particle trajectory and the channel axis direction (from *Gao et al.*, 1984)

It was suggested above that the impact energy and type of radiation or particle hitting the MCP would have an effect on the gain of the output MCP pulses. This is despite the fact that a saturated pulse height distribution is considered. This is because the peaking occurs as a saturation effect in a number of channels in the second and not the first plate. These channels are centred at the excited, unsaturated channel in the first plate. The number of saturated channels depends on the number of electrons which exit the first plate, the applied voltage and the interplate separation. Because the first plate is operating in an unsaturated mode the number of electrons leaving the end of an excited channel is directly proportional to the number of secondary electrons ejected in the ion collision with the channel wall at the input (*Hellsing et al.*, 1985).

Oberheide et al. (1997) indicate that the secondary electron emission from the nichrome is much less than 1 for 50eV electrons, but from the MCP material is 1.5. For 3keV ions they give a secondary electron yield of 2.3 for collision with the electrode material and 5 for the insulating MCP material. Assuming a simple Poisson distribution of the number of secondary electrons, then the probabilities for the emission of electrons are close to unity whether the ion strikes the penetrating electrode material or the glass. Hence the assertion earlier that the pulse height distribution from ions impacting the channel wall directly would be different from that produced by the lower energy secondary electrons. It is clear from this that if a grid is used to collect the secondary electrons from the interchannel web, the depth to which the electrode material is deposited down the pore, the flaring, will have an influence on the overall quantum efficiency. Ion detection, where the secondary electrons are repelled, is relatively immune to this effect.

From the preceding argument it is clear that the gain of MCPs will vary with the input energy of the incident ions. Any gain differences will result in changes to the overall detector efficiency at that energy so should be kept to a minimum. *Oberheide et al.* (1997) have recently investigated the energy dependent gain of MCPs for ions and their results are shown in Figure 6-18. Similar results are reported *by Hellsing et al.* (1985). Results for a limited range of energies from the FONEMA analysers are shown in Figure 6-19. The error bars show the one standard deviation level on the gain measurement. Within the experimental error the gain for the three higher mass groups is reasonably constant. For protons the gain is decreased across the whole range and at the lower energies drops to about 60% of nominal gain in mode 1.

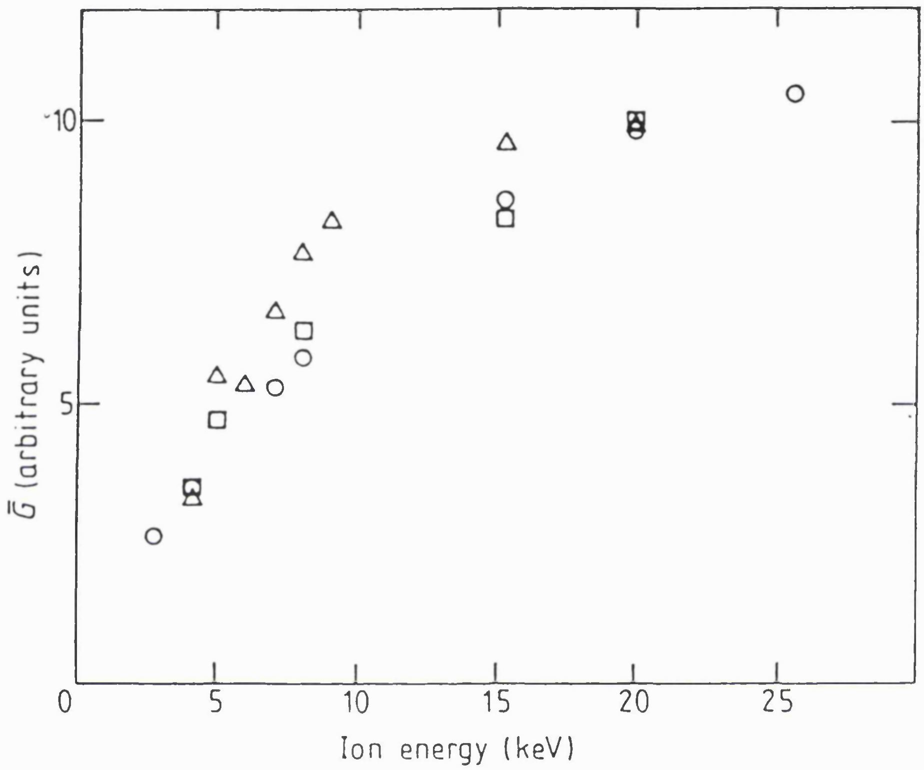

Figure 6-18. The mean gain of the MCP stack for ions as a function of the ion impact energy.

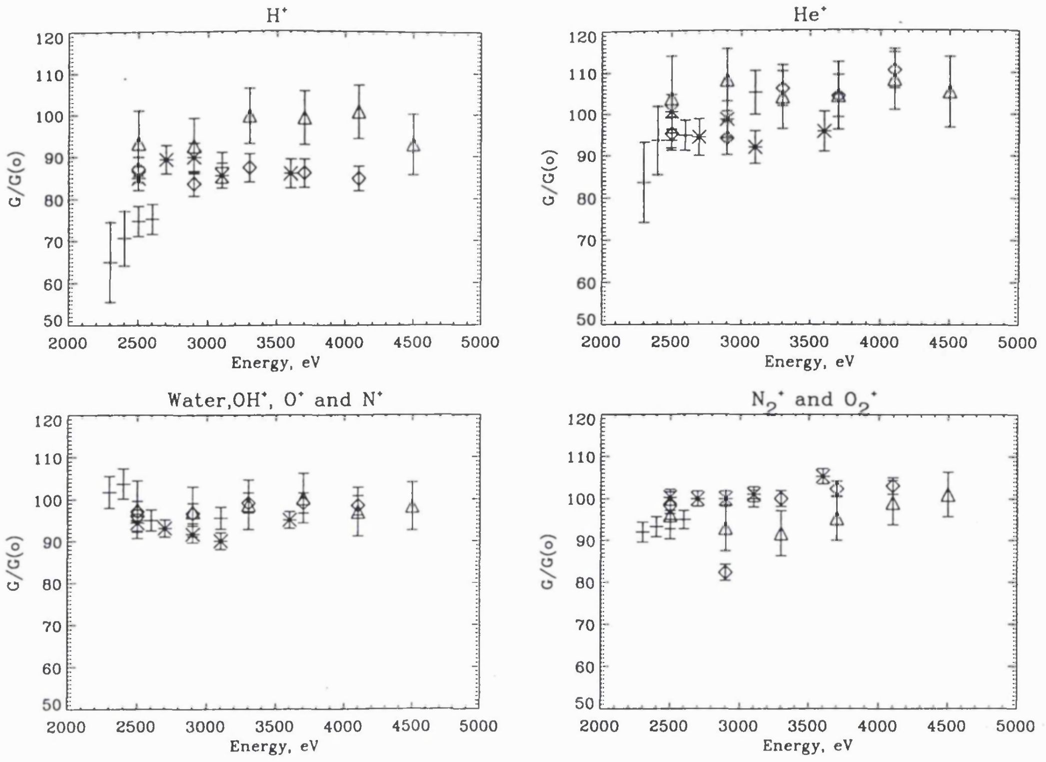

Figure 6-19. Mean gain versus ion impact energy for 4 mass groups. The different symbols represent the four different instrument modes (mode 1 - crosses, mode 2 - asterisks, mode 3 - diamonds, mode 4 - triangles).

The grid placed in front of the MCP stack in FONEMA means that all ions will undergo a pre-acceleration before hitting the MCP. This acceleration will be added to the ion energy which has already been pre-accelerated at the front of the analyser. Because the MCP acceleration voltage is simply the analyser pre-acceleration voltage subtracted from the MCP operating voltage the total energy gained by the ions on impacting the MCP is the operational voltage. Assuming the initial operating voltage of 2200V and an instrument energy range from 20-8000eV, the impact energies at the MCP will be from 2220eV to 10200eV. In addition to this some of the lower energy ions in each mode will have additional energy supplied by the deflection field, although this is at most a few tens of eV. Assuming from the published data that QE will even out at above 3keV, for most of the energy range of the FONEMA instrument there will be no relative difference in QE due to energy and for normal incidence the QE will be the open area ratio of the plates, i.e. 66.5%. By increasing the energy of the impacting ions this arrangement also means that any gain variations due to energy differences are effectively reduced. The reduction in gain for protons is not, however, explained by these arguments and suggests some other dependence which will need to be investigated further.

6.2.8 Noise sources associated with the MCPs

6.2.8.1 UV radiation

MCPs have been used in the past for UV imaging detectors (*Siegmund et al.*, 1986, *Breeveld, 1995*). It is therefore not surprising that one of the problems with particle instruments based on MCP imaging detectors is the rejection of the solar UV component. UV radiation that does impinge on the surface of the MCPs will either produce spurious events or add noise to legitimate particle events, depending on the energy and final angle of incidence. The question is at what rate these UV events will occur?

On FONEMA all the analysers are designed so that the only passage to the MCP surface is through the particle collimator. The arrangement of the aperture and the electrostatic mirror means that during normal orbital operation, when the +*X* axis of the instrument points to the sun, no solar photons can hit the front of an analyser. All surfaces within the outer cover of the instrument are blackened with low reflectivity paint (Electrodag 501+) to increase absorption and reduce the number of reflected photons. The reflectivity at ultraviolet wavelengths of Electrodag 501+ is of the order of 4%. Each channel in the collimator if extended outward from the analyser would hit the blackened surface of the inner electrode on the electrostatic mirror. Single UV specular reflections which do occur at the electrode in these areas do not go down any channels at an angle that allows them to pass through the collimator. There is the chance of reflection from the edges of the holes in the collimator shims but this number is two orders of magnitude lower than the number of similar photons reflected from the wire mesh used as the grounded surface of the electrostatic mirror.

This mesh is made of 80 μm diameter Tungsten-Rhenium wire with two crossed sets of 720 wires around the circumference. This has a reflectivity of about 27% at a wavelength of 121.6nm at normal incidence depending on the surface properties (*Lynch and Hunter*, 1985). This increases to about 35% at angles between 45° and 55° (*Hunter*, 1985). It is possible that specular reflection from the surface of these wires could result in trajectories passing down the collimator channels where these channels are radial to the mirror. Most of these will then be lost in internal reflections between the collimator plates or will hit the light stop which is a part of the mesh support in front of the MCP. The UV that reaches the MCP surface will be those rays that reflect off the edges of the collimator holes causing them to miss the light stop or those reflected off the light stop and reflected again within the analyser. The UV flux at Mars over all wavelengths from 0.1nm to 140nm (upper limit of MCP sensitivity) is 1.36×10^{11} photons cm^{-2} s^{-1} (*Heroux et al.*, 1985). During normal orbital operations one half of the instrument faces anti-sunward. The number of photons that reach the front collimator plate at a position occupied by a hole is estimated by looking at the solar presented area on a circular cross sectional wire where specularly reflected photons will hit the hole. This is calculated as $2.16 \times 10^{3}cm^{-2}$ per analyser. Therefore 2.9×10^{8} photons s^{-1} reach the wire and with the given reflectivity approximately 1×10^{8} photon s^{-1} enter a front hole of the collimator. Just over 1% of these will hit the light trap at the focus directly. Reflection of the light trap directs the photons away from the image plane to behind the electrostatic deflection plate. After multiple reflections the number of photons reaching the image plane is expected to be less than 1000 per second per analyser. Of those that do not get through the collimator it is expected that on average 15000 of them will undergo a reflection that will take them beyond the collimator, however, accurate estimation of this is difficult given the inherent variability in the profile of these holes. Of those photons that do pass through the rear plate of the collimator, only a quarter of them would hit the quadrant containing the analyser imaging plane in detector 1. In detector 2 and 3 half would hit the image plane. The light traps are 1.6×2.5mm within the image plane and just over half will hit these. Of those that remain approximately 19% of these would be reflected by the mesh in front of the MCP leaving about 2500 photons hitting the image plane. A further method by which a UV photon could reach the MCP is by passing through any hole in the front plate and then undergoing multiple reflections between the two collimator plates resulting finally in the photon going through a hole in the second plate, etc.. Due to the tight tolerances needed during construction and the danger of blocking holes the collimator itself is not blackened. Background events from this effect are believed to be negligible. This gives a total count of approximately 3500 photons per second reaching the image plane. The open area ratio for the MCPs is 66.5% and quantum efficiency of the MCP at these wavelengths is about 10%. For the lyman alpha wavelength of 121.6nm, which makes up just over 80% of the solar UV flux, the MCP quantum efficiency is between 0.5 and 2% (*Hamahatsu*, 1991). With an MCP quantum efficiency this low the expected background photon rate from this source is estimated at less than 50 per second per analyser. Because the gain of the Russian MCPs for UV radiation is lower than that for particles the number of recorded events from solar photons is expected to be less than 30 events per second per analyser. These events will occur around the focus position of the image plane for each detector. Because of the electrostatic deflection voltage and the accelerating grid in front of the MCPs no secondary electrons produced by the UV photons within the analyser will be detected. The limited time available for the final test and calibration programme meant that UV susceptibilty tests were not carried out for the FONEMA instrument before flight.

6.2.8.2 Dark noise

The pulse height distribution of noise within an MCP is of an exponential form suggesting that the source is uniformly distributed within the MCP volume. This dark noise occurs at a typical rate of ~0.2 counts cm^{-2} s^{-1} for well scrubbed MCPs operated at pressures of less than 10^{-6}mbar. There are three main non-thermal sources of noise: field emission from channel defects, cosmic background radiation and internal radioactivity. *Fraser et al.* (1987) have identified the major source of noise, >90%, as due to the internal radioactivity. Potassium and Rubidium isotopes, used in the manufacture of the MCPs themselves, will sporadically decay giving rise to spurious events. Most of the events come from beta particles emitted by ^{40}K which makes up approximately 0.0118% of naturally occurring potassium, ^{39}K (*Tennent*, 1978). MCP glass is made up of 5% potassium by weight. Background event rates for FONEMA plates were found to be between 1 and 5 events per second over the whole area of 10cm^2 which is consistent with that quoted in the literature.

6.2.9 Magnetic immunity of MCPs

Two separate effects of magnetic field exist within the detector system which need to be considered. Firstly there is the effect of the magnetic field on the electron trajectories within the MCP pores and secondly is the effect on the electron trajectories in the MCP to anode gap. The latter will be discussed in the next chapter which deals with the imaging anode. Within the MCP there are two extreme conditions to consider: where the magnetic field is parallel to the pores and where it is transverse. When perpendicular the MCP gain simply decreases with increasing magnetic field. As the field increases the gyroradius of the electrons decreases, so trajectories within the pore and hence impact energies are lowered reducing the secondary electron yield. In the case of a parallel field the trajectories of electrons may be extended when the gyroradius is comparable to the channel radius resulting in an increase in gain as magnetic field is applied. However, as the field becomes stronger and the gyroradius decreases the situation is the same as the transverse case and the gain decreases (*Hamamatsu*, 1991). Detailed analyses of the effect of magnetic fields on MCP operation can be found in *Coleman* (1982).

Referring back to Chapter 4, figures 4-18 and 4-19, the magnetic field within the MCP volume is expected to be at most 5mT. The direction of this field varies across the MCP surface so the effect will change from position to position. However, assuming a 3eV secondary electron in an MCP pore and ignoring its gain in energy due to the electric field, its gyroradius in a perpendicular magnetic field of 5mT is 1.1mm. This makes the effect of the magnetic field negligible on the MCP operation within the FONEMA analysers. Studies *by Morenzi et al.* (1988), *Fraser* (1990) and *Schecker et al.* (1992) all show insignificant effects for fields less than about 1Tesla oriented parallel to the pores.

7. Charge measurement detectors

As mentioned previously MCP detectors are of two general types, those used for light amplification and those where charge measurement is employed. This section will discuss the various types of the latter and the advantages that each type possesses. Charge measurement detectors can be further split into two categories, discrete anode and continuous anode readout detectors. The former relies on simply detecting a charge pulse whereas the latter relies on some division and measurement of the charge pulse. In all the following systems, except the Hybrid system by *Liptak et al.* (1984), the number of electronic channels required refers to those needed by the anode system itself. Generally, a separate processing channel is needed for the pulse generated in the rear MCP by the charge depletion, which is then used as a gating system for the anode electronics.

7.1.1 Discrete Anode Readout

Discrete anode readouts use many anode electrodes, each anode being either a pad or a wire. The simple act of determining whether a charge pulse is present or not on a particular anode gives information about the position of the primary event.

7.1.1.1 One Dimensional Coincidence anode

The one dimensional coincidence anode consists of interlocking fingers of coarse zones and fine zones (see Figure 7-1). The charge cloud would be required to fall on at least two but no more than four electrodes, so the MCP to anode gap must be of the order of 100μm and the electrode spacing must be of a similar value.

7.1.1.2 MAMA (Multi-Anode Microchannel array)

Multi-Anode Microchannel arrays (MAMA's) are the most commonly used form of discrete anode readout, combining high sensitivity and photometric stability with a high resolution imaging capability (*Timothy et al.*, 1981). They exist in two basic forms, the discrete anode array and the coincidence anode array, examples of which are shown in Figure 7-2.

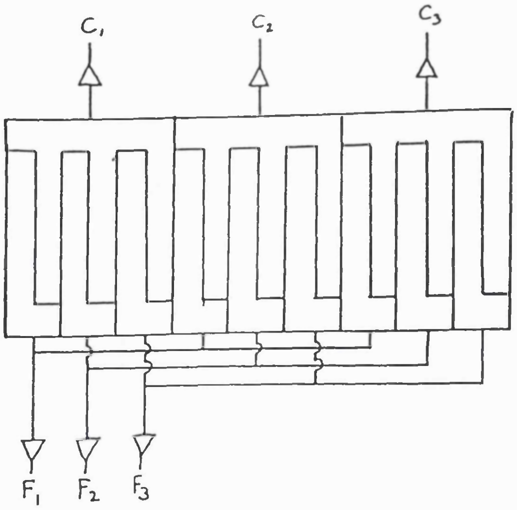

Figure 7-1. A simple one dimensional coincidence anode showing 3 coarse zones and 3 fine zones to produce a nine pixel output.

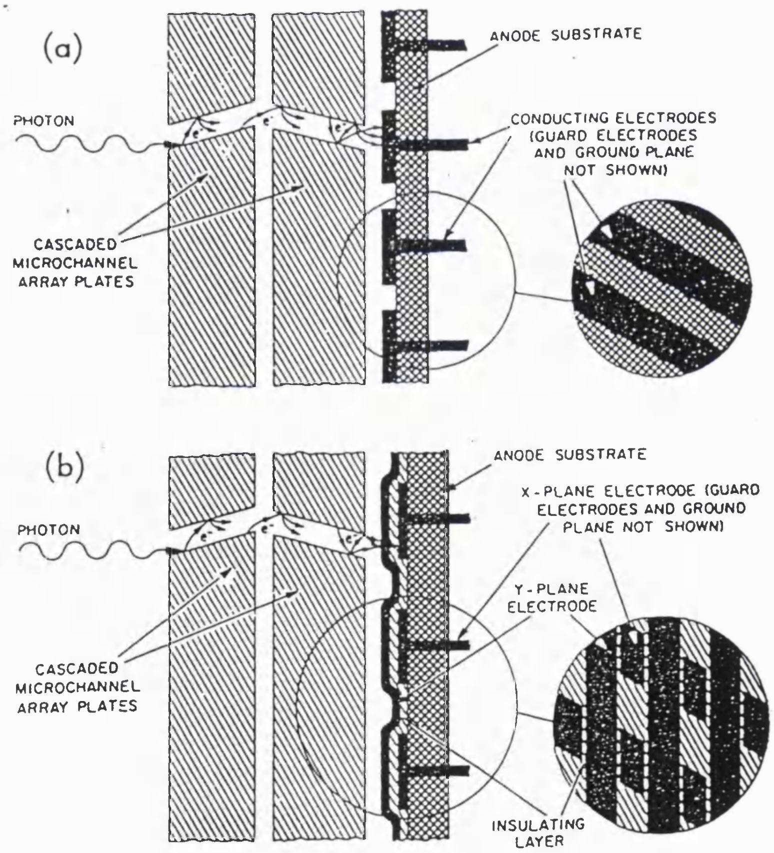

Figure 7-2. a) a simple discrete anode array, for which connection is made through the back of each electrode. b) a coincidence anode.

The Discrete Anode Array

The discrete anode array consists of a pattern of discrete anodes on a single substrate. Each anode represents a single pixel within the image, the spatial resolution being defined solely by the anode geometry. The disadvantage of these types of detectors is that each anode requires its own amplifier, discriminator and counting electronics. So for an $m \times n$ array, $m \times n$ separate electronic channels are required.

The Coincidence Anode Array

In the coincidence anode array two orthogonal sets of linear anodes, insulated from each other, are exposed to the charge cloud from the MCP. Coincident arrival of a pulse from each set of anodes is taken as a valid event and where the two individual anodes intersect defines the position. Using this method position resolutions down to 50μm have been reported by *Timothy and Bybee* (1975). For coincidence anode arrays only $m + n$ channels are needed to provide $m \times n$ pixels. The coincidence technique can be extended to each of the 2 sets individually as in the 1-dimensional coincidence anode but this then requires more complex electronics to reject multiple anode events, or strict control of electron cloud size.

The signal to noise ratio (SNR) requirement is not high for MAMA's as they rely only on discrimination to determine position. This means that MCP gains as low as 10^6 electrons are sufficient.

7.1.1.3 CODACON (Coded Anode Converter)

This one dimensional detector, the most complex of the discrete anode systems, was produced at the University of Colorado by *McClintlock et al.* (1982). Basically a three layer anode is produced with 1024 individual 15μm metal strips, called charge spreaders, on a 25.4μm spacing as the top layer. The second layer is made of 10μm thick dielectric. The third layer consists of 10 pairs of binary code tracks and a discriminator track, all running orthogonal to the charge spreaders. These are used to determine which of the charge spreaders the charge cloud hits. Each pair of code tracks consists of two strips of metallisation which alternate between wide and narrow, upon which charge is induced from the charge spreaders.

The total charge induced is proportional to the width of the strip underneath that charge spreader. A differential amplifier then determines which of the two tracks produces the largest signal. The unique address generated is coded using reverse binary or Gray code. Figure 7-3 shows an energised charge spreader in position 4 and how the unique address 110 is arrived at. The dielectric material has a low resistance so that charge leaks away between pulses with a 1ms time constant.

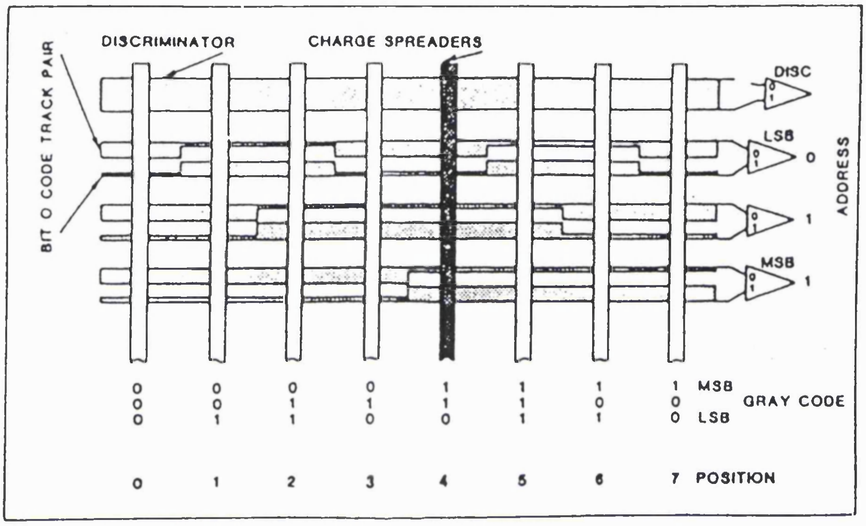

Figure 7-3. Simplified example of an eight channel CODACON. From *McClintlock et al.* (1982).

7.1.1.4 Hybrid MCP/Anode system

This system from *Liptak et al.* (1984) is a hybrid in the sense that it consists of a 38 pixel discrete one-dimensional anode yet coincidences the signal from this with a second orthogonal anode which is etched onto the rear-face of the MCP itself (see Figure 7-4). This means that the signal from this anode will be positive, not negative, as the charge is extracted from the MCP. The advantage to this system is that it acts as a 2-dimensional coincidencing anode but can be made without having the specialist skills needed in producing a multilayer anode. The obvious disadvantages are the need to produce a pattern on the output face of an MCP and the increased complexity of the electronics.

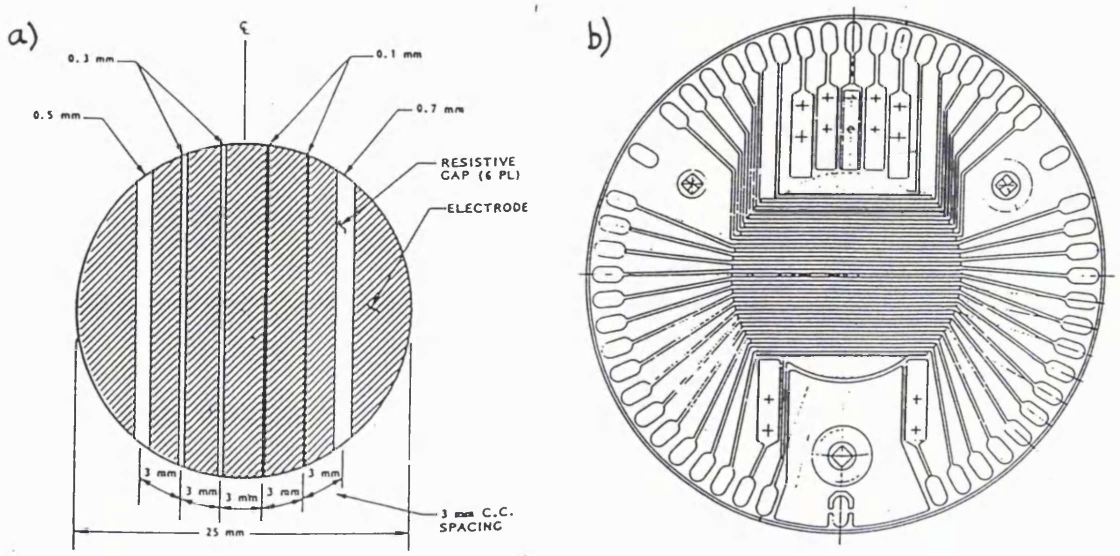

Figure 7-4. a) MCP output electrode pattern. b) Prototype Anode Electrode.

7.1.2 Continuous Anode Readout

In continuous anode readout systems the output charge cloud from the MCP is generally divided between a number of different electronic channels. The different ratios, rise-times or arrival times of the signals produced give information about the position of the charge cloud. Capacitative charge dissection and resistive charge division are analogous and will both be treated together in this section.

7.1.2.1 Resistive anode

Probably the most commonly used of all the anode systems, the resistive anode was first described by *Stumpel et al.* (1973), initially for use in a proportional counter. Often called the resistive disc anode (RDA), various one-dimensional and two-dimensional designs have been used for both ground based (*Firmani et al.*, 1982, *Paresce et al.*, 1987, *Chauvet et al.*, 1987, *Clampin et al.*, 1988, *Clampin et al.*, 1989^{a,b}, *Floryan et al.*, 1989, *Courtney et al.*, 1991) and space borne detectors (*Allington-Smith and Schwarz*, 1984, *Mason et al.*, 1984). The anode itself is a sheet of uniform resistive material on an insulating substrate, and signals are taken off from 3 or 4 points around the circumference. The event position can then be determined by either timing or pulse height methods, although both have their limitations. With the timing method the zero crossing point of the signal in the amplifiers is measured. This signal becomes small near the edge of the disc resulting in ill determined positions. Experiments by *Allington-Smith and Schwarz* (1984) show a threefold degradation in position resolution from the centre to the edges of the disc. Other drawbacks for the RDA are that the resolution is limited by Johnson noise and the image can be distorted by geometry and poor termination.

7.1.2.2 Delay line

The delay line is similar to the RDA working in the timing mode, basically the incident charge pulse divides into two pulses that progress down the delay line in opposite directions. Each travels to its end of the line where it is amplified, discriminated and fed into the time interval measuring circuit. The STOP leg has a fixed additional delay so that it never precedes the START signal. The time interval registered will then be given by:

$$t = t_0 + 2X / V \qquad (7.1)$$

where X is the event centroid position, V is the propagation velocity of the delay line and t_0 is a constant. By inverting the above equation the event position is decoded as:

$$X = X_0 + \tfrac{1}{2} V t \qquad (7.2)$$

and the error in the derived position, δx, can then be expressed in terms of the error in the timing circuitry, δt, by differentiating equation (7.2):

$$\delta X \;=\; \tfrac{1}{2} V \, \delta t \qquad (7.3)$$

So, to achieve high resolution it is important to keep both the propagation velocity and the timing error as small as possible (*Lampton et al.*, 1987). Ignoring the solid state delay line (*Keller et al.*, 1987), where the distortion limits the resolution to 0.25mm, there are 2 main types in common use.

1. Planar Delay Lines

In this type of device the delay line pattern, all in the same plane, is a zigzag conductor running between 2 multiple wedge combs (Figure 7-5). The normal delay line signal processing of the deposited charge on the wedge is used to determine the event position in the *X* axis. Information about position in the *Y* axis is obtained from analysing the signals from the multiwedge. A disadvantage of this system is that it is necessary to employ 2 different techniques to get the 2D information, delay line timing for *X* and signal amplitude comparison for *Y*. A resolution of 50μm FWHM is reported by *Lampton et al.* (1987) using this system, a more complex version by *Siegmund et al.* (1989) suggests a possible resolution of 20μm FWHM over a distance of 58mm.

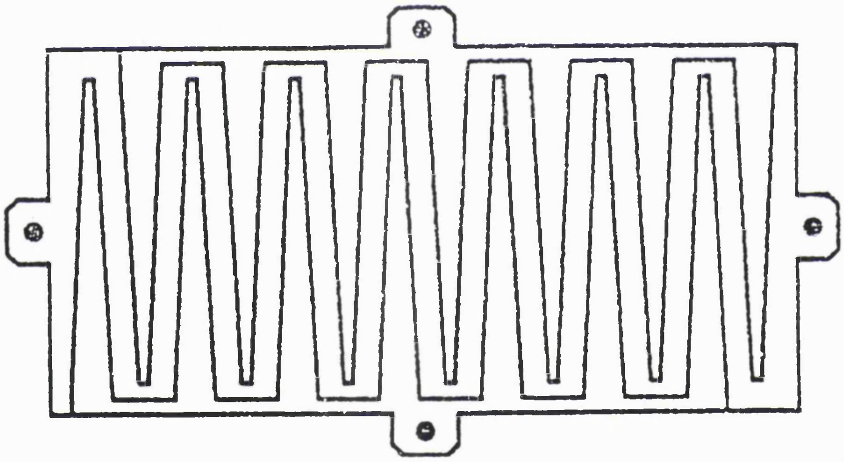

Figure 7-5. Layout of planar zigzag delay line, *y* axis information is available from the upper and lower multiwedges.

2. Transmission Line Delay Lines

Figure 7-6 shows the transmission line delay line as demonstrated by *Williams et al.* (1989). Two flattened helical delay lines are wound on a square frame. The wires are insulated from the copper core by four ceramic strips, one pair smaller than the other so that one delay line is wound inside the other. Each delay line is composed of two interleaved windings of 200μm diameter bare copper wire.

The d.c. voltage levels are adjusted so that only one winding on each delay line collects the charge. *Williams et al.* report a resolution of approximately 18μm using a 140mm × 140mm anode of this design.

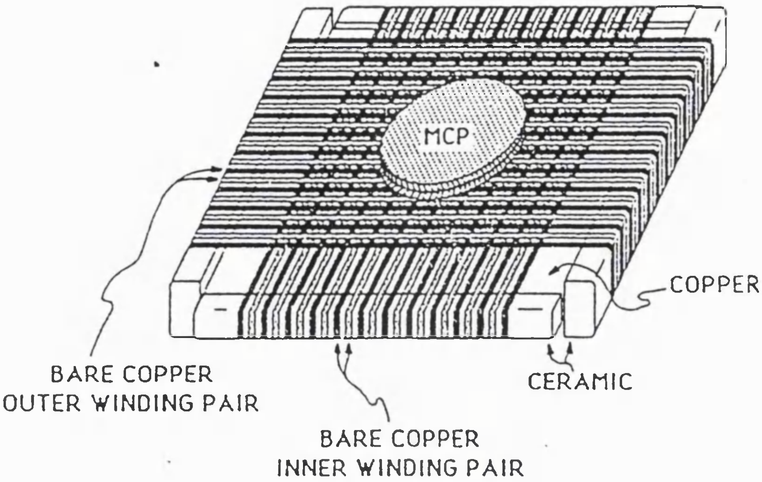

Figure 7-6. Schematic of MCP and delay line readout (*Williams et al.*, 1989).

7.1.2.3 Crossed wire grid

Sharing similarities with both the delay line and resistive anode, the crossed wire grid consists of a series of wires or electrodes connected in series by either a resistive (*Chappell et al.*, 1989) or capacitive (*Richter et al.*, 1986) network. The final position of the event is determined by either charge measurement or pulse timing at both ends of the network. Two dimensional imaging is possible by arranging two isolated, orthogonal sets of wires as in the X-ray detector for the HEAO-B X-ray observatory (*Henry et al.*, 1977). In this system the wire planes consist of 125, 100μm wires on 200μm centres, with every eighth wire connected to an amplifier, the seven intermediate wires coupled to an amplifier wire by resistors. Coarse position is then determined by which amplifier was triggered, and fine position from centroiding this signal with neighbouring amplifiers. Although a resolution of 20μm has been reported by *Chappell et al.* (1989), this was for a relatively low event rate of a few 10^4 counts per second. The large number of amplifiers and associated electronics needed make this method unsuitable for smaller instruments, although more recently it has been used for the ROSAT High Resolution Imager (HRI) (*Fraser*, 1989).

7.1.2.4 Backgammon

Initially developed to derive position information from multiwire proportional counters, the 'backgammon' electrode can be used behind a MCP as a one dimensional position sensitive detector (*Allemund and Thomas*, 1976). The anode is 2 sets of interleaved wedges, the position information coming from the relative size of the charge cloud falling on each wedge. This system only requires two processing channels.

7.1.2.5 MBWC

The 'modified backgammon method with weighted coupling capacitors' (MBWC) consists of a backgammon anode combined with capacitive charge dividers (*Mizogawa et al.*, 1997). A charge cloud from the MCP, with a footprint larger than the pattern pitch, falls on the anode and divides with a ratio dependent on the position, as in the standard backgammon anode. Then each of the fractions is transferred to charge dividers where, through capacitive coupling, they induce charges into the single wedge/wedge electrode situated at the base of the main wedge system. Thus four charge signals are extracted producing two dimensional position information. Figure 7-7. shows the layout of the MBWC anode for which resolutions of 30 to 40μm have been claimed.

7.1.2.6 Graded-Density Electrode

Again, originally developed as the cathode in a multiwire proportional counter, the graded-density system was first described by *Mathieson et al.* (1980). Later, *Smith et al.* (1982), showed its applicability to MCP based detector systems. The electrode comprises a planar array of wires, with uniform pitch, connected electrically into two groups A and B such that the linear density of group A decreases approximately linearly across the electrode. Conversely, the linear density of B will increase by an equal amount. A schematic of the anode is shown below in Figure 7-8, from Smith *et al.*. Two such electrodes can be placed orthogonally to produce a two dimensional imaging system. With such a system Smith *et al.* have demonstrated a resolution of ~40μm and an integral non-linearity of better than 1%.

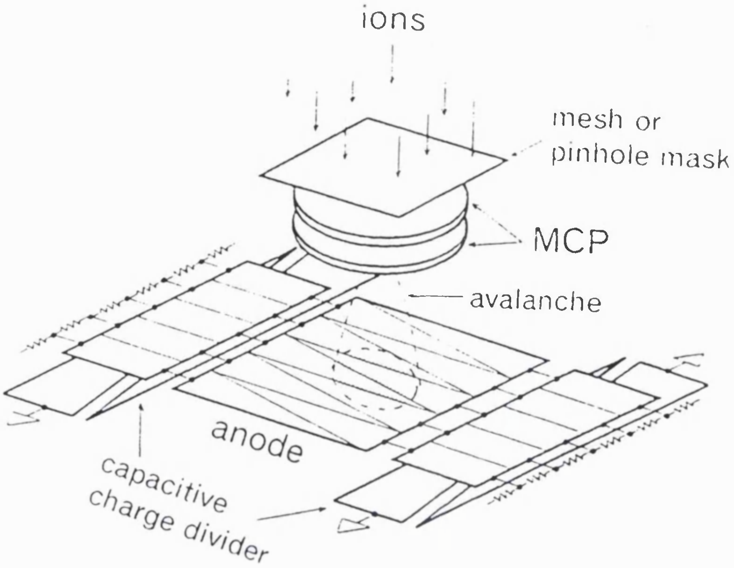

Figure 7-7. MBWC anode arrangement.

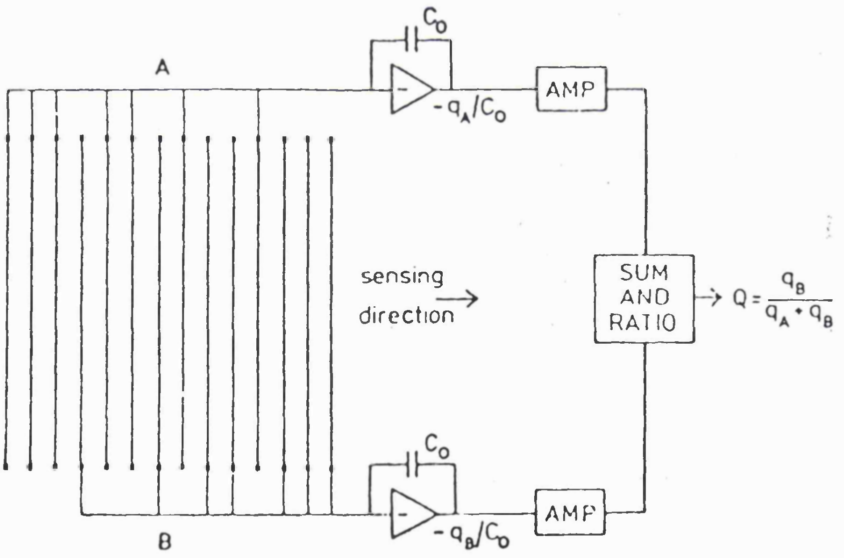

Figure 7-8. Schematic representation of one dimensional graded density electrode encoding system.

7.1.2.7 Quadrant anode

Originally described by *Lampton and Malina* (1976) the Quadrant anode aims to provide high spatial resolution with good image uniformity for smaller detector areas. A circular disc is split into four quadrants, as shown in Figure 7-9, each connected to a low noise charge sensitive amplifier. The simplicity of this system means that the timing accuracy is limited only by the variations in the avalanche arrival times, which can be less than 1ns. With discrete and continuous resistive anodes this time is dependent on the charge diffusion time within the anode. Another advantage over resistive anodes is that it does not suffer from thermal noise. A later version of this system by *Purschke et al.* (1987) claims a resolution of 12μm, although this is only achieved at the expense of image uniformity.

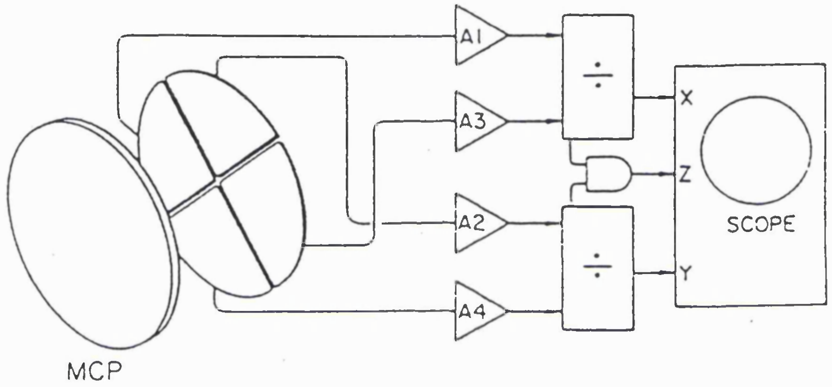

Figure 7-9. Schematic of the Quadrant anode image system. Event position is determined by the relative charge on each anode and is viewed with the ratio circuit and oscilloscope shown (*Lampton and Malina*, 1976).

7.1.2.8 Cyclic Continuous Electrode Readouts (SPAN and Vernier)

In other charge measuring readouts, e.g. delay lines, WSA described above, the ADC dynamic range can be used once only across the whole area of the pattern. In a cyclic continuous electrode readout (CCER) the full range of the ADC is used in the determination of fine position within a single cycle which is repeated many times across the pattern (*Lapington et al.*, 1991, *Edgar*, 1993). An idealised diagram of a CCER is shown in Figure 7-10, it consists of three electrodes, the sum of whose widths, *w*, is constant. The fine position is determined by the phase angle within a cycle and the coarse position is found by determining in which cycle an event occurs.

Resolution of the order of the MCP pore size is possible with this anode. The disadvantage with this system is that it requires six channels of processing electronics. The Coronal Diagnostic Spectrometer flown aboard the SOHO spacecraft used an anode of this type (*Breeveld et al.*, 1992).

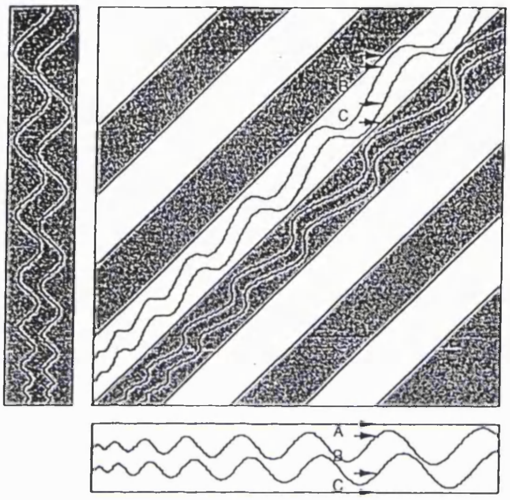

Figure 7-10. A schematic of the SPAN readout design showing the x axis electrode structure (white) and the y axis (grey).

7.2 Wedge Strip Anode

7.2.1.1 Wedge and Strip

First described by Anger (1966) the most highly developed and widely used of the large format continuous anode systems is the Wedge and Strip Anode (WSA) (*Martin et al.*, 1981). Basically the output charge cloud from a microchannel plate is collected on a three anode system as shown in Figure 7-11. Here it can be seen that the wedge anode dimension in the x axis, and hence the area, increases as y increases. The strip anode increases in area as x increases. The remaining anode that separates these two regions is called the Z anode and provides a normalisation factor used by the position decoding algorithms shown below. A typical MCP output charge cloud will have a circular imprint when landing on the anode and the charge collected by each anode will, to first order, be proportional to the area covered by the cloud. In reality the output charge cloud shape from a chevron pair is best described as the sum of two exponential components (*Edgar et al.*, 1989). The centroid of the electron charge cloud can be determined using the relationships:

$$X = \frac{S}{W + S + Z} \tag{7.4}$$

and

$$Y = \frac{W}{W + S + Z} \tag{7.5}$$

where W, S and Z are the charges recorded on each of the 3 anodes respectively and $W + S + Z$ is the sum signal, representing the total charge in the event.

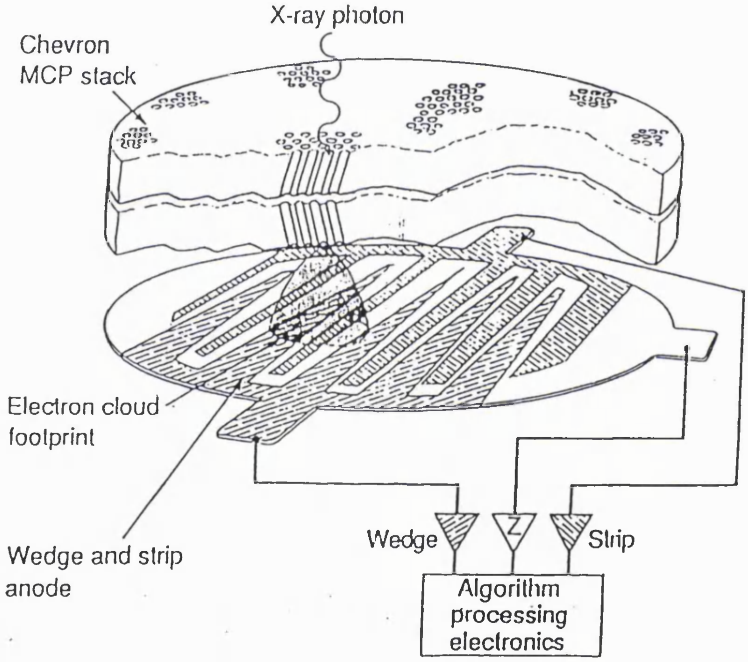

Figure 7-11. Schematic showing operation of a wedge and strip anode behind a MCP stack.

The normalisation by the sum signal is required because of the variation in charge cloud size from event to event, as described by the pulse height distribution (see Chapter 6). Ideally the maximum wedge and strip areas will be half the available area, therefore X and Y from the above expressions would be in the range 0 to 0.5. Normally a factor of 2 will be introduced in both these equations so that for an anode where the dynamic ranges in the two axes are similar, the final X and Y positions will be normalised between 0 and 1. In reality the maximum achievable range of positions will be from about 0.1 to 0.9 depending on the geometry of the particular anode and the manufacturing processes used. The minimum ratio is defined by the smallest possible electrode width in the wedge and strip anodes and the maximum ratio by the minimum width that the *Z* electrode can have. The resolution of a WSA is defined by the noise of the *W*, *S* and sum signals. This noise is a combination of electronic noise and the statistical fluctuation in the charge division process, termed partition noise.

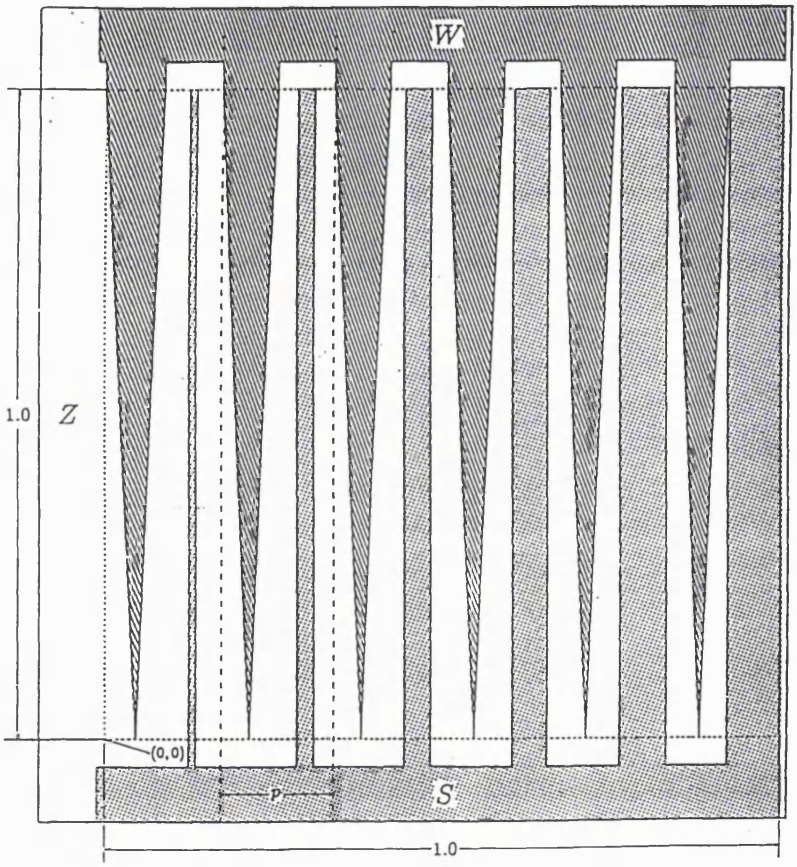

Figure 7-12. Schematic diagram of a WSA (from *Smith et al.*, 1989).

The main advantage of the wedge and strip system is that it only requires 3 electronic processing channels making it ideal for a space borne detector system. Also because it has a simple co-planar geometry the WSA can be manufactured by simple photographic etching processes or micro-machining processes. This arrangement also eliminates the need for any sub-plane interconnections and the consequent need for through plated holes. The simplicity of the design with easy reproducibility and the small number of electronic processing channels made the WSA the ideal choice for the FONEMA instrument.

Wedge and strip anodes have been used in space before, primarily in UV detectors (*Siegmund et al.*, 1986). Variations on the WSA have been discussed by *Burton* (1982) including an anode with a position dependent resolution, the resolution increasing near the centre of the circular image plane. Another novel WSA is described by *Rasmussen and Martin* (1989) which involves a mosaic of smaller WSA systems. One of the first WSA based detectors to be used for a plasma instrument in space is the TIMAS instrument on the POLAR spacecraft. *Walton et al.* (1996) produced a circle/sickle anode for the TIMAS based on an idea by *Knibbeler et al.* (1987).

7.2.2 The Anode design

In order to save on power and mass, only one set of shaping amplifiers and analogue to digital converters (ADCs) are used for the whole FONEMA instrument. A further reduction in both mass and power is achieved by combining the anodes of adjacent analysers so that they can make use of the same set of charge to voltage preamplifiers. A pair of such anodes is shown in Figure 7-13. The wedges are the same on both anodes; the strips, however, increase from left to right on the left-hand anode and continue to increase further in the opposite sense on the right hand anode. The six analysers in an instrument are composed of three left and right pairs. These analysers are exact mirror images of each other except for the orientation of the magnetic field and the anode pattern. The parabolic patterns on the image are therefore mirrored also. By having the strip anode of the form shown in Figure 7-13 the right-hand images are reversed in the final image plane. This allows the mass and energy look up tables in the final design to have the same orientation. In the ideal case where all analysers had the same performance this would mean only one mass and energy look up table instead of two.

Substrate:	Material	Deranox 975
	Relative Permittivity, ε_r	9.55
Coating:	Adhesion layer	Chrome, <10 nm
	Main layer	Copper, 50 nm
Pattern:	Pitch	690 μm
	Number of pitches	32
	Pattern width	22080 μm
	Wedge length	55150 μm
	Wedge width minimum	60 μm
	Wedge width maximum	360 μm
	Strip length (over both anodes)	55150 μm
	Strip width minimum (left-hand anode)	60 μm
	Strip width maximum (left-hand anode)	137.5 μm
	Strip width minimum (right-hand anode)	132.5 μm
	Strip width maximum (right-hand anode)	210 μm
	Z width minimum	60 μm
	Wedge to Strip ratio	2:1

Table 7-1. A list of parameters for the FONEMA anode.

In the previous section it was noted that the anode signal ratios would vary from 0 to 0.5 in an ideal case. This is only true if the maximum anode dimension is the same in both wedge and strip. For FONEMA the resolution needed in the strip direction is less than that needed in the wedge direction because of the shorter distance. As explained previously, one attractive feature of WSAs is the ability to produce patterns with novel resolution variations. For FONEMA, the wedge and strip areas have been adjusted to trade off reduced resolution in the strip axis for increased resolution in the wedge axis. Therefore the strip axis is only digitised to 7 bits rather then the full 8 bits used for the wedge. The actual sizes for the FONEMA anode are shown in Table 7-1 and the anode ranges in Figure 7-13.

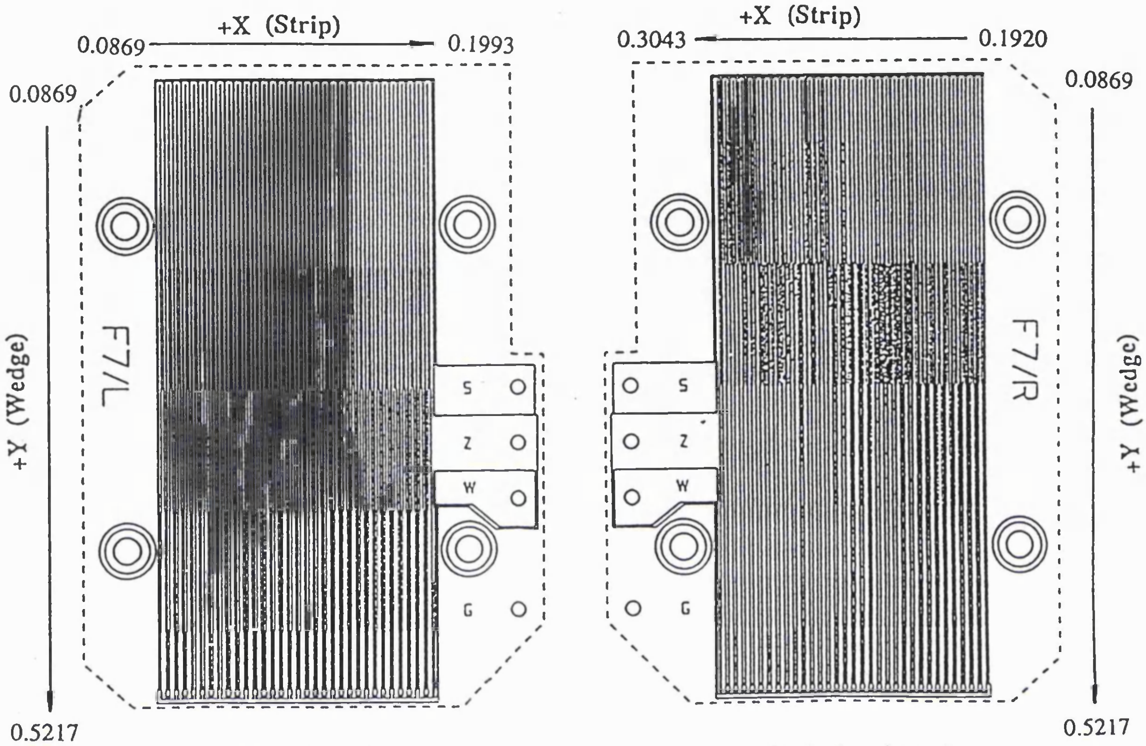

Left-hand anode Right-hand anode

Figure 7-13. Patterns for the right-hand and left-hand FONEMA anodes. The dotted lines show the outer edge of the substrate and the mounting holes. The figures show the range of fractional areas occupied by the axes, which are calculated from the figures in Table 7-1.

7.2.3 Laboratory Electronics

Signals from the three electrodes, Wedge, Strip and Z, pass through the chamber wall on high voltage BNC connectors and are connected to EG&G Ortec 142B charge to voltage preamplifiers. Generally the gain of the MCPs is kept at 6×10^6 electrons, so assuming that it is shared equally between all three anodes that means that each charge pulse is approximately 0.32pC. The output from each preamplifier is fed into an EG&G Ortec model 572 shaping amplifier. Bipolar outputs in the range 0 to 10V are then fed into Canberra fast Analog-to-Digital converters, model 8077. Digitised signals are finally read into a computer and a program computes the position algorithms. An image of the recorded events is then displayed on the screen. At the same time another output from one of the three shaping amplifiers is fed into a single channel analyser, the output of which is fed into a counter. This allows an independent determination of the count rate and allows any dead-time during computer read sessions to be calculated. This same shaped output pulse is also displayed on an oscilloscope. The digitisation resolution of the output signals is variable with the laboratory electronics but is usually kept high so that the limiting noise is that due to the amplifier. This also helps to avoid any fixed noise patterning when the MCP gains are low.

In this system the gains of the W, S and Z signals must be kept the same. If not, the sum term in the algorithm will become position dependent and the image will no longer be rectangular. This means that the ranges defined by the anode areas, as shown in Figure 7-13, will be directly translated into the image, i.e. assuming the ADCs are both in 9 bit mode (512 by 512 pixel image) the image in X will go from 89 to 312 and that in Y from 89 to 534. This theoretical anode area is shown as a dotted line in Figure 7-14.

7.2.4 Flight Electronics

A slightly different approach is used in the flight design to cut down on power and mass in the front end electronics. The same algorithm applies but the division is performed by summing the three analogue signals W, S and Z to produce a sum signal. This signal is then used as the reference signal for two ratiometric ADCs. The W and S signals are fed separately into the signal inputs of the ADCs. Using this approach the ADC is not encoding a pulse amplitude as in the laboratory set-up but a ratio of two pulses, the sum and either the W or S signal. Of course the reference pulse has to be less than the 5V limit on the power rail. This arrangement allows the gain of both the W and S signals to be increased after the sum signal is produced so that the maximum ratio is approximately 1 in both axes. More of the image space is then being used by the system. For the strip signal the required amplification will be greater so the noise will also be amplified more and the signal to noise ratio will not be improved.

To achieve a large dynamic range in count rate the processing time per event must be kept as short as possible and precautions must be taken to avoid a second pulse occurring during the processing of a previous pulse which may result in a false position. Shaping times are minimised by using a 6 pole critically damped LCR network which gives a baseline return within 1.5μs. This approach is limited by a degrading signal to noise ratio which is manifested in a reduced position resolution and increased power consumption. Also the pulse from the back face of the MCP is shaped using a 4 pole RC network with a pulse pair resolution of 125ns. This shaped pulse goes to a LLD which produces a logic pulse. This provides a high speed stream of pulses which can provide total count rates even if position information is unavailable. These pulses are used with delays to provide the strobe signals for the position encoding ADCs. Pulse pile-up rejection circuitry also uses these pulses to deal with high count rates by rejecting any pulses where the position information may be degraded. This combination of a fast pulse counting stream and a slower position encoding stream allows accurate measurement of both count rate, after deadtime correction, and image information at total count rates in excess of $10^6 s^{-1}$.

7.2.5 Resolution of wedge and strip anodes

The spatial resolution and uniformity of wedge and strip anodes has been discussed by various authors: *Martin et al.* (1981), *Siegmund et al.* (1983), *Schwarz and Lapington* (1985), *Lapington and Schwarz* (1986), *Siegmund et al.* (1986) and *Thornton* (1987). There are two main components of noise associated with wedge and strip anodes which define the resolution limit. Firstly there is the electronic noise, N_e, which is controlled by the pre-amplifiers and the input capacitance. Secondly there is partition noise, N_p, which is a quantum effect produced by statistical fluctuations in the distribution of electrons among discrete electrodes. In the following discussion the theoretical noise limits are applied to the FONEMA anodes in order to anticipate the final resolution.

7.2.5.1 Partition noise

From *Lapington and Schwarz* (1986) the resolution component R_p in X (strip axis) for any given position is given as:

$$R_P = \frac{2.355L}{(f_{\max} - f_{\min})}\left[\frac{f(1-f)}{Q}\right]^{\frac{1}{2}} \tag{7.6}$$

where:-

f is the fractional charge collected by an electrode,

f_{max} and f_{min} are the limits on f,

Q is the number of electrons per event,

L is the length of the anode in the axis being considered.

7.2.5.2 Electronic noise

Again from *Lapington and Schwarz* (1986) the resolution component in X due to the electronic noise is:

$$R_E = \frac{2.355L}{(f_{\max} - f_{\min})Q}\left[N_S^2(1-2f+f^2)+(N_W^2+N_Z^2)f^2\right]^{\frac{1}{2}} \tag{7.7}$$

where N_S, N_W and N_Z are the respective rms noise levels, in number of electrons, on the S, W and Z electrodes. All other symbols have their previous meaning. A similar expression exists for the resolution in the Y axis. It can be seen from equations 7.6 and 7.7 that both partition noise and electronic noise will decrease as the gain, quantified by Q, is increased. This decrease is faster for the electronic noise, being dependent on $1/Q$ than for the partition noise, proportional to $1/Q^{0.5}$. For the FONEMA anode and electronics, however, the electronic noise will stay larger than the partition noise up to a gain of in excess of 10^7 electrons. Equation 7.7 takes no account of the correlation of the noise which tends to make any noise present on the sum signal negligible. For most practical applications the noise can be anticipated to within 10% by simply equating the fractional noise in each axis to the fractional noise of the associated anode electronics:

$$\frac{\delta X}{X} = \frac{\delta S}{S} \tag{7.8}$$

With the partition noise being negligible for most applications the electronic noise dominates. This noise is dominated by the associated electronic noise of the particular axis which is dependent on the input capacitance to the preamplifier and the shaping time. The resolution of a WSA is therefore primarily dependent on the anode capacitance and hence the dielectric constant of the substrate.

7.2.5.3 Other noise sources and non-linearities

In the laboratory the anodes themselves are sensitive to pickup noise and microphonics within the system which will add to the overall noise. Considering the image in Figure 7-14 of two flight anodes the resolution in X and Y for a spot in the centre of the image is 382μm and 233μm respectively. Using the equations 7.6 and 7.7 the resolution associated with this position on the anode was calculated to be 305μm in X and 164μm in Y. The spot is larger than expected by 82μm in the strip axis and 69μm in the wedge axis due to excess noise in the system. Another source of distortion is cross talk due to capacitive coupling between the anodes. This was measured by applying a stimulation pulse to the Z anode only and measuring the resultant signal on both wedge and strip. Using this method cross-talk to the strip was measured at between 2.5 and 3% and to the wedge between 1.75 and 2.5%. Cross-talk between the wedge and strip anode was found to be negligible, less than 0.2%. The effect of cross-talk is to produce a reduction in the size of the image and a slight rotation. Less important sources of error come from intrinsic non-linearities in the electronics and from the finite size of the MCP pores.

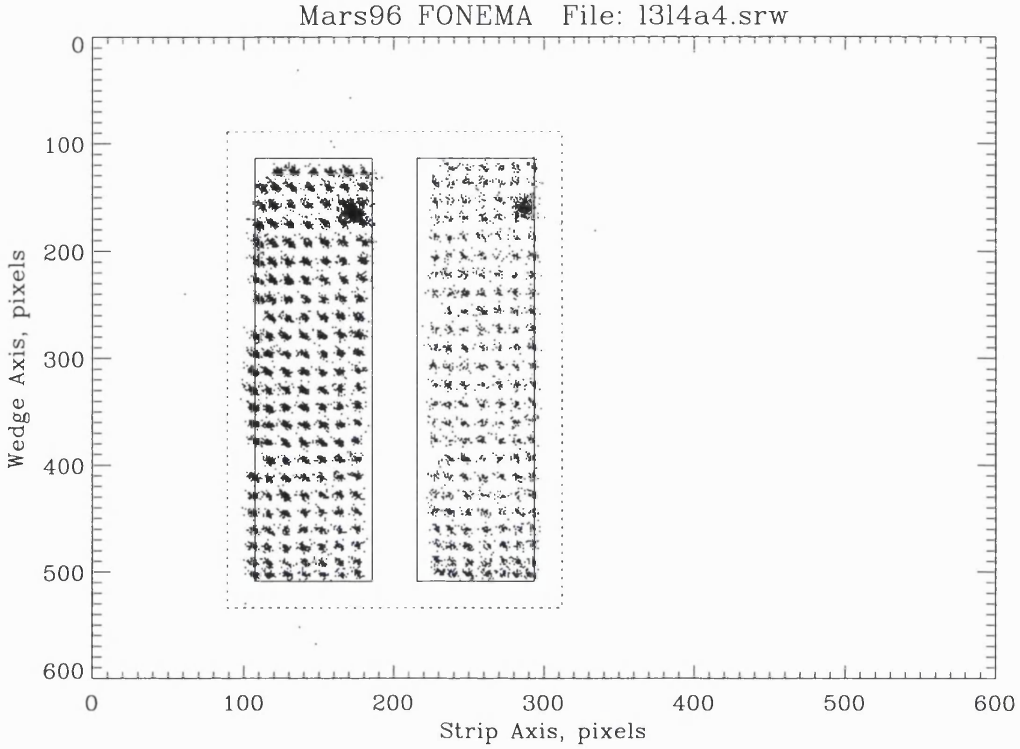

Figure 7-14. Images from two of the flight analysers. A pinhole mask is placed in front of the MCPs and is illuminated from an ion gun 0.5m away. The dotted line shows the theoretical anode area and the two solid boxes show the theoretical extent of the imaging area defined by the rear MCP clamp plate. The denser spot in the top right corner of each anode is where a cross is cut into the pinhole mask for identification purposes.

7.2.5.4 Resolution with flight electronics

Assuming a gain of 6×10^6 electrons an expected maximum signal from the wedge electrode would be 3.12×10^6 electrons. The gains are adjusted so that this corresponds to about 2.4V at the ADC input. The maximum ADC signal is 4V and this is equivalent to the full 8 bits in the wedge axis, i.e. a single resolution element has an associated signal of 2.4V/255 = 9.4mV. This is then equivalent to approximately 12200 electrons per resolution element. The flight pre-amplifiers (Amptek A250) were measured as having an rms noise level of 26000 electrons. This noise level is the same for the strip axis. Applying this to the expressions for partition noise and electronic noise the resolution for the flight anode comes to approximately 1.1mm in the wedge axis and 1.8mm in the strip axis. As explained previously the noise present in the *Z* signal is anticorrelated so that the actual resolution turns out to be better than that given by equation 7.7, 0.57mm in wedge and 0.93mm in strip. This is more in line with equation 7.8 rather than equation 7.7. This combined with the spot size from the collimator makes the actual resolution approximately 1.6mm in wedge and 2mm in strip. Figure 7-15 shows the same pinhole images as in Figure 7-14 but with the flight electronics.

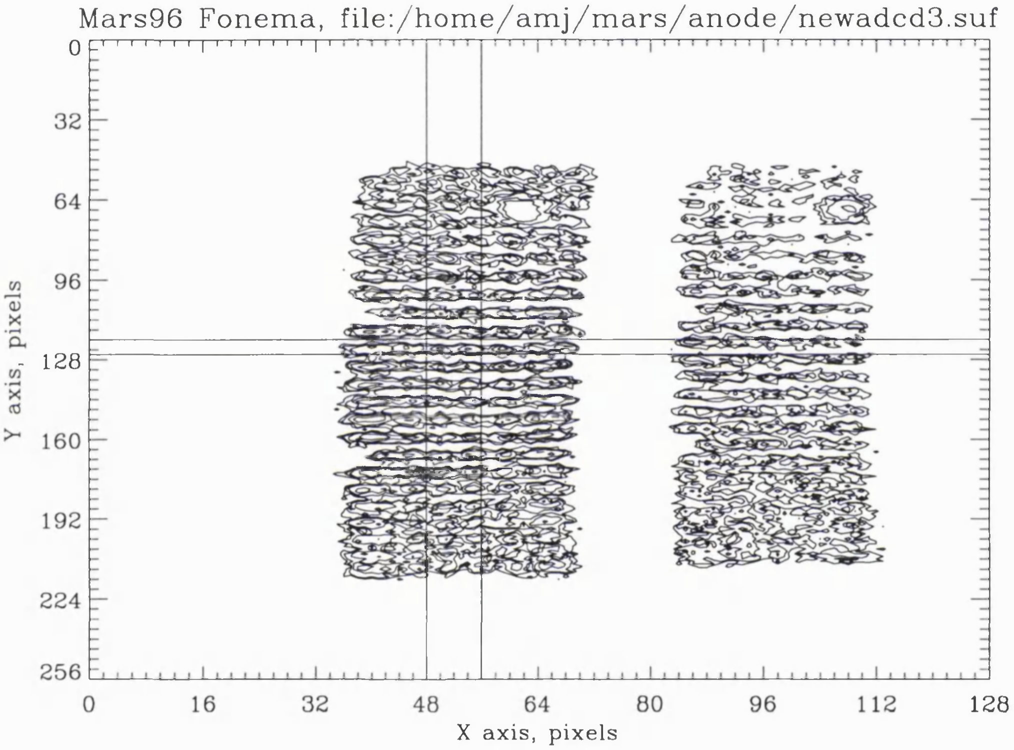

Figure 7-15. Image of pinhole mask with flight electronics. The bars in the image show the regions which were used in the resolution plots (Figure 7-16 and Figure 7-17).

In this image scans are taken in the areas indicated and summed in one axis to produce the plots in Figure 7-16 and Figure 7-17. The summed data in Figure 7-16 shows the peaks of the pinhole mask image summed in the strip axis so that resolution in the wedge axis can be estimated. Only a central section of the full scan is shown in this plot. The individual pinholes, which are 2mm apart, are clearly resolved in this image. From this plot, after deconvolution of the spot diameter, the resolution is calculated to be approximately 570μm. Figure 7-17 shows a scan in the other axis and here the pinholes are not so easily resolved, the resolution in this case being approximately 926μm for the left-hand anode. This is due to the previously explained trade-off in resolution between the two axes. In the right hand anode the strip resolution is worse than this, at almost 1.8mm. These two MCPs were not perfectly matched and the gain is slightly lower in the right-hand anode producing the reduced resolution.

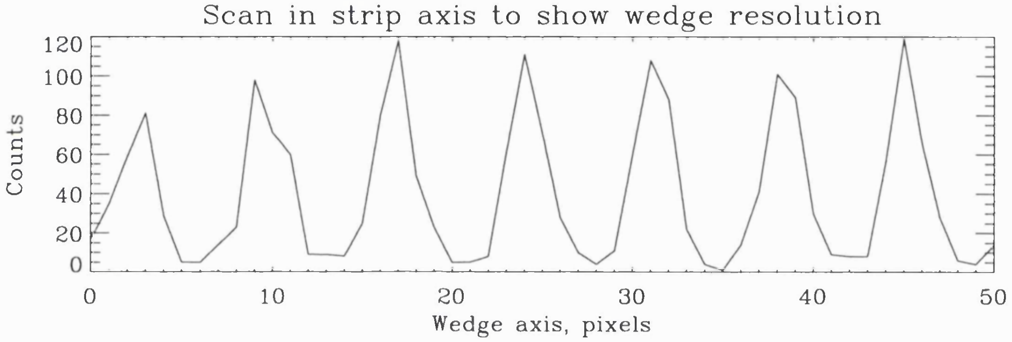

Figure 7-16. Sum in the strip axis of the vertical slice shown in Figure 7-15. This image shows the resolution in the wedge axis to be approximately 0.6mm.

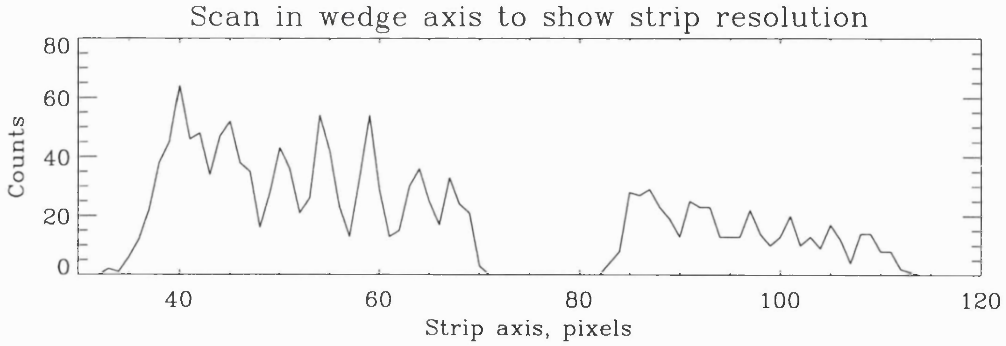

Figure 7-17. Sum in the wedge axis of the horizontal slice shown in Figure 7-15. This image shows the resolution in the strip axis to be approximately 0.9mm for the lefthand anode and 1.8mm for the righthand anode.

7.3 Construction techniques

The anodes for FONEMA were made in-house on polished ceramic substrates supplied by Morgan and Matroc Limited. A chrome layer of 0.01µm is deposited on the anode in a sputter coating facility. This layer provides adhesion for the copper layer which is deposited next. The copper layer is approximately 0.04µm thick. The substrate is then moved on an X-Y table under computer control beneath a focused spot from a Nd:YAG infra-red laser which removes the metallic coating to produce the pattern shown in Figure 7-13. After this laser machining, the anode is cleaned to remove the surface layer of oxidised material and any debris produced. Ultrasonic bonding is then used to connect adjacent Z electrodes together with 25µm aluminium wire. This is to reduce the resistance in the Z electrode that can lead to differential charging of the anode. Finally the three electrodes and the grounded area around the pattern are connected to solder tag contacts using 12BA bolts and silver loaded epoxy resin. During final analyser assembly these wires are passed through holes in the analyser body and PTFE grommets are used to seal the holes. The four wires are then soldered into miniature MJS connectors. This technique allows the analyser to be almost airtight, the only open aperture being the holes in the collimator. Purge connectors in the side of each analyser then can be used to bleed argon into the analyser bodies during spacecraft testing and pre-launch activities to minimise contamination of the MCPs by moisture, dust or hydrocarbons, which can degrade MCP performance.

7.4 Testing the finished detectors

7.4.1 Test Facility

All the tests of the detectors, individual analysers and completed instruments were carried out in a 0.8m diameter × 1.2m long cylindrical vacuum chamber. This chamber is a three stage pumped system consisting of a single stage rotary pump, sorption pumps and a cryogenic pump.

7.4.2 Sintimid anode

Initial experiments were carried out using an anode made from SINTIMID®, which is a sintered polyimide material with good mechanical strength and a dielectric constant of only 3.5. The lower dielectric constant meant that the interelectrode capacitance was lower and hence the noise from the preamplifiers, therefore giving a better intrinsic resolution. Unfortunately trials failed to produce good images, possibly due to a high secondary electron emission within the insulator gaps. Although other plastic materials exist with a dielectric constant this low they all tend to suffer from a high out-gassing rate making them unsuitable for spaceflight especially in the vicinity of MCPs which are known to be sensitive to contamination. Tests on SINTIMID for outgassing determined the total mass loss (TML) to be 3%, mainly due to water. After baking at 150°C for 24hours this reduced to less than 1%, the recommended upper limit for space qualified material. A sample tested by ESA, however, gave the TML as 3.03% and they could not recommend it. Consequently trials on SINTIMID were stopped and a ceramic anode was developed.

7.4.3 Modulation effects in wedge and strip anodes

Modulation occurs when the charge cloud size is comparable to the pitch of the pattern. When this happens the charge cloud splitting proportional to anode area becomes invalid as the charge cloud no longer spans a full pitch. The resulting image will show stripes of high and low intensity parallel to the wedges. This occurs because it is the strip anode that varies discretely across the anode, changing width once per pitch. The wedge anode is continuous so will not suffer from this effect. Examples and a full explanation of this effect can be found in the paper by *Smith et al.* (1989). The charge cloud size is controlled by two factors, the MCP to anode gap distance and the MCP to anode gap voltage. For FONEMA the distance is fixed at 4mm and the gap voltage varies from approximately 189V to a possible 408V over the lifetime of the instrument. Over this range of parameters no modulation effects are seen. The 4mm gap between the anode and the rear face of the MCP was set at this level to prevent modulation with the pattern used. A difficulty with increasing the gap too much is that the charge cloud can land on an area off the pattern producing severe edge distortions. To combat this it is necessary to extend the pattern beyond the edge of the active area. This then reduces the resolution of the system as the active area of the pattern is now a smaller proportion of the full anode. For FONEMA the anode is extended 3.5mm beyond the edge of the active pattern in all directions. In the strip axis this means that 22mm of anode is needed for only 15mm of active area.

7.4.4 Variation of image with gap voltage

As mentioned in the previous chapter the MCP voltages will have to be stepped up a number of times to compensate for gain reduction with lifetime. Because the voltage between the MCP and the anode is controlled by a resistor, as the MCP operating voltage is increased the MCP to anode gap voltage is also increased. For each analyser this gap voltage is likely to increase from about 250V at the beginning of the mission to approximately 400V after two years operation. To test the effect of this a pinhole mask was illuminated with 1keV ions and the image recorded for different values of gap voltage, but with the same voltage across the MCPs to maintain a constant gain. Each pinhole is 0.2mm in diameter and the separation is 2mm. Figure 7-18 shows the centroided positions of the pinhole images for an area in the centre of one of the FONEMA detectors for six different gap voltages. The statistical error associated with the centroiding is 0.2mm in both axes, this compares to the '+' symbol used for the highest gap voltage measurement which is approximately 0.28mm across in the strip axis and 0.5mm across in the wedge axis. It can be seen that as the gap voltage is changed the image shifts. This shift is however dependent on the position in the image plane. These measurements were done for all the flight detectors using laboratory electronics before final integration so that corrections could be made to flight data as MCP voltages were changed.

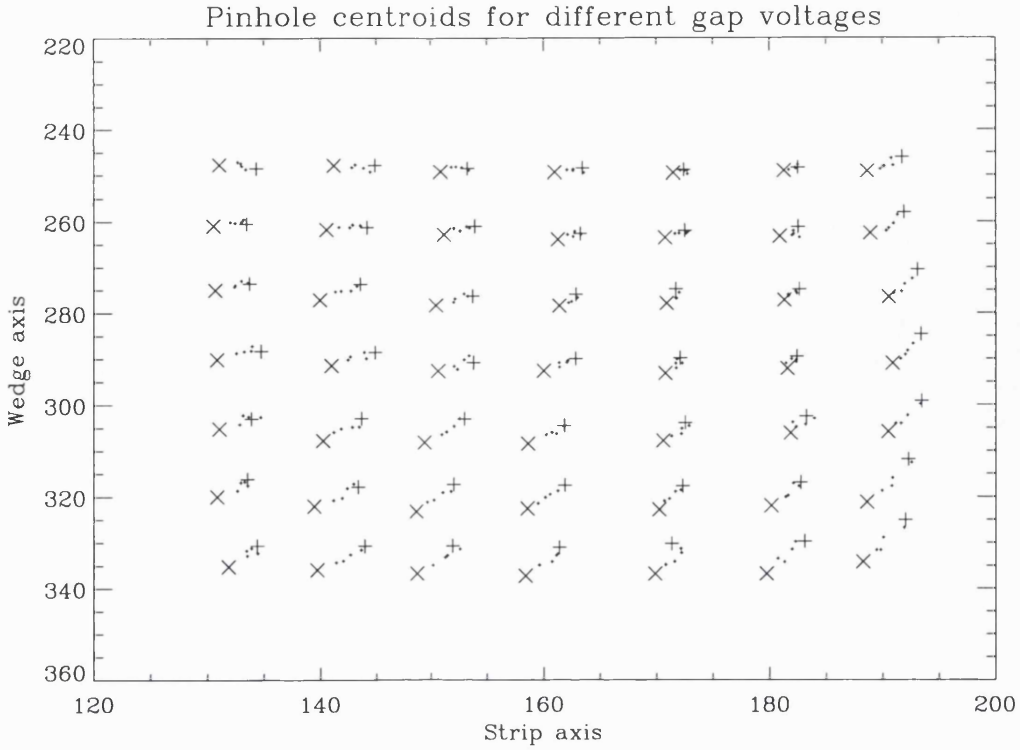

Figure 7-18. The centroid position of pinhole images for six MCP to anode gap voltages: 189V (×), 236V, 263V, 311V, 359V and 408V (+).

Although the example shown in Figure 7-18 is for a prototype anode and one of the most severe examples found, the effect was observable in all detectors. The largest shift between the two extreme gap voltages in Figure 7-18 is approximately 1.3mm, near the bottom left corner. Typically though the shifts were of the order of 0.5mm, over double the standard error of the centroid position which shows that the result is statistically significant. To increase the gap voltage the resistor value used to define the voltage is changed and the voltage applied to the front of the MCP stack increased. This means that the voltage between the mesh which is held at ground in this experiment and the MCP voltage is increased. However, the deflection that this would cause in the 1keV ions is less than 2μm. A shift due to this effect would also show the shifts in individual pinholes point to the normal beam focus, this is not the case in Figure 7-18 or the other experiments, so it is concluded that this effect is negligible.

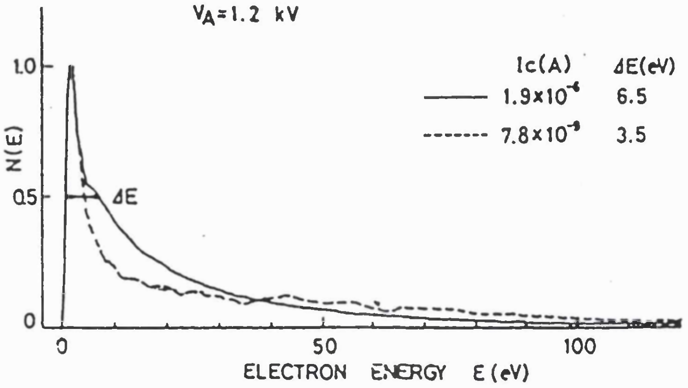

Figure 7-19. Output energy distribution curves in unsaturated (broken line) and saturated (solid line) operation modes (from *Koshida and Hosobuchi*, 1985).

Obviously, as it is the gap voltage that is changing this is where the shift is likely to occur. Figure 7-19 shows the output energy distribution from a single thickness MCP with an L/D ratio of 40 and a 12° bias angle (*Koshida and Hosobuchi*, 1985). The energies range from about 5eV up to over 100eV in the saturated mode. Assuming that the electric field is uniform within the 4mm gap between the rear MCP and the anode in the FONEMA detector and that a stray magnetic field of 5mT exists parallel to the MCP surface the shift in charge cloud center can be estimated to first order by looking at the trajectory of a single electron. The difference in position of an electron leaving the plate at 10eV is approximately 400μm between the 189V and the 408V gap voltage. For 100eV electrons this difference is reduced to nearer 200μm (Figure 7-21). This is a crude estimation but suggests that the processes causing the image shift are not entirely due to the shift in the primary output electrons. A possible explanation is that the imaging is influenced more by the secondary electrons produced at the anode by the impact of the higher energy primaries. Although the secondary electron yield and energy distribution will be similar for all the gap voltages used, the influence of the field in the gap on these secondaries will be different. At higher gap voltages the secondary electrons will be unable to travel as far as they can with the lower gap voltage. The effect of secondary electrons will very much depend on the number and distribution of these electrons. This in turn depends on the surface finish of the anode and may account for the differences between different detectors. This difference in surface finish, especially localised oxidation of the copper will affect the trajectories of these secondaries also. Another factor that will affect the secondary electrons is the finite difference in resistances of the three anodes which can cause differential charging on the timescale associated with the acquisition of the charge pulse. The wire bonding across the *Z* anode is an attempt to reduce this effect. Figure 7-20 shows an image where the anode had not had its *Z* electrodes wire bonded and the surface had suffered slight oxidation. The final image shows large distortions over much of the area.

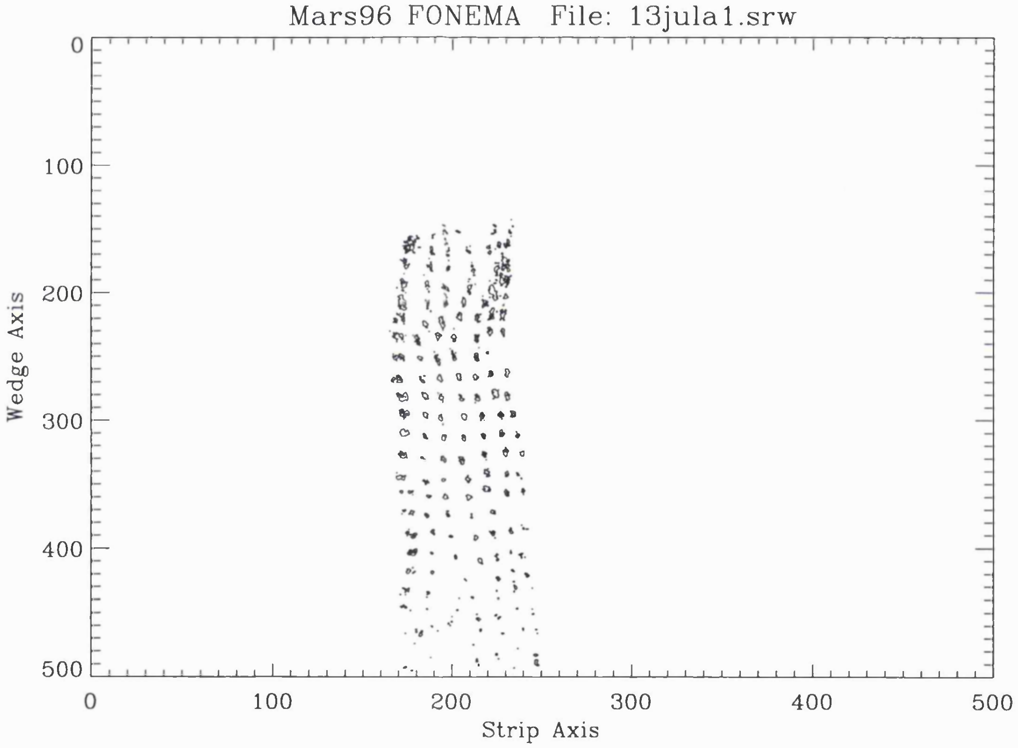

Figure 7-20. Image of a pinhole mask where the anode had no *Z* wire bonds.

The study of the influence of secondary electron emission on the imaging properties of this type of anode is beyond the scope of this project and will be a major part of research efforts at MSSL in the near future (*Lapington*, 1997). Because the ability to download full images exists as a diagnostic on FONEMA, it was enough to record the variations in image position and uniformity as a function of gap voltage during pre-flight testing. Any variations from these results, possibly due to cleaning up of the anode during operation, should be noticeable in the diagnostic images.

7.4.5 Magnetic immunity of imaging system

In Chapter 6 the effect of the magnetic field on the MCP performance was discussed. Another effect that can occur with imaging systems is that the electrons exiting the MCP can be deflected if a significant magnetic field is present. This produces two effects, a reduction in gain as exit electrons are returned to the MCP close to the exit of the pores, and a shift in the expected position of the output charge cloud. Single electron simulations of the situation for FONEMA show that no electrons with an energy greater than 1eV will be turned around by a 5mT field at the lowest gap voltage of 189V. This is confirmed by the fact that no gain reduction is observed between experiments before and after magnets are placed in a FONEMA analyser. Again the shift can be estimated based on the trajectory of single electrons but time did not allow for any more complex simulations to be produced. Figure 7-21 shows the electron deflection within the gap due to the magnetic field and the anode gap voltage. For this simulation the field is assumed to be 5mT parallel to the MCP face and the electrons are ejected perpendicular to the MCP surface.

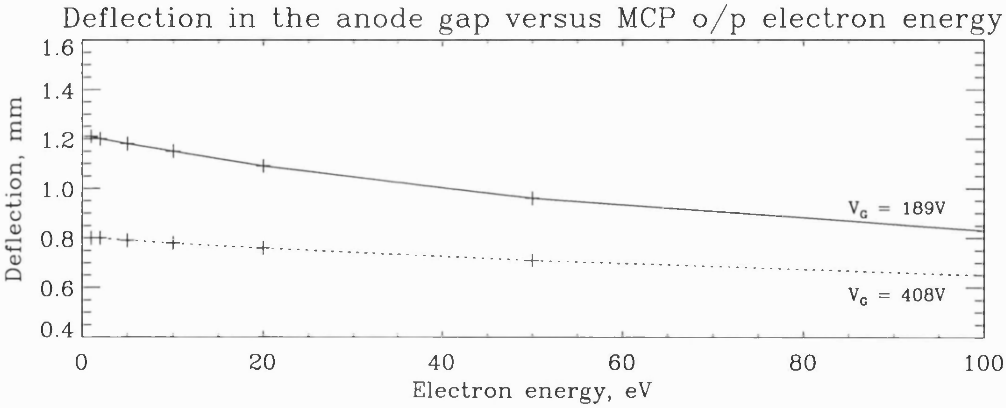

Figure 7-21. Electron deflection in the MCP/anode gap due to stray magnetic fields plotted as a function of electron energy for two anode gap voltages.

Another magnetic effect is reported by *Roquemore and Medley* (1986) when using a 180° magnetic deflection system. In this system the secondary electrons from the interchannel web on the front surface of the MCP are accelerated back to increase overall detector efficiency. In the presence of a strong magnetic field these particles are returned to the surface under the influence of $\mathbf{E} \times \mathbf{B}$ fields. This produces ghost images up to several centimetres away from the original events. In FONEMA the secondary electrons formed in the interchannel web are pulled away from the front surface by the field between the MCP and the mesh. Therefore this effect is not seen in FONEMA images.

8. Flight model calibration

8.1 Calibration

Probably the most important part of the development of a space plasma instrument is the pre-launch calibration. Unfortunately it is often the most difficult part of the programme to get funding for and because it takes place at the end of the project after environmental testing there is not usually adequate time to do this job as fully as is desirable. The enormity of the calibration job is often underestimated especially for an instrument such as FONEMA. The response function that must be measured for FONEMA is a four dimensional one: energy, mass, polar angle and azimuthal angle. Assuming the response function was measured with an angular resolution of just 5° in both polar and azimuth, for a hundred energies and the 4 mass groups, this still comes to over 2 million independent response function measurements. If a computer controlled calibration system could be set up to perform this task at a rate of one measurement per second it would take nearly a month.

In some instruments, including FONEMA, it is possible to take advantage of symmetries within the instrument design to reduce the size of the parameter space. Another reduction method, again used in FONEMA, is to use a computer simulation to predict the response function after confirming the simulator with experimental results at a smaller number of positions within the parameter space.

Funding difficulties meant that the planned calibration within an ion thruster at the UKAE facility at Culham was not possible. The fall back plan on calibration was to do as much as possible within the remaining time at MSSL and then to cross-calibrate with other tested instruments that shared energy and mass coverage on board. To some extent the instrument is self calibrating in flight by making use of the diagnostic images. Unfortunately, the chance to cross-calibrate never came so a true operational characterisation of the FONEMA instrument was not undertaken. The tests that were carried out at MSSL do, however, give us an insight into the operation of the detector in mono-energetic, narrow beams. The results from these tests help to define the limits of the instrument in terms of resolution of angle, energy and mass of incoming particles.

8.2 Prototype analyser

A single FONEMA analyser was constructed to test the overall performance and to verify the model. Again, initial tests were performed with a single hole collimator with the three channels normal to the plate surface and focused on the real detector foci. This means that the initial trajectories into the analyser are not the same as in the final design, resulting in different deflections in both the electrostatic and magnetic fields. As discussed in Chapter 4 and Chapter 5 this also means that dispersion, due to the finite area covered by the collimator, is not present. In addition to this deviation from the final design two more differences are present in the prototype. Firstly, because only one anode is present in the prototype the capacitance between anodes is halved. Therefore noise is doubled and position resolution is halved. Secondly the magnets are no longer part of a ring system and the field is slightly reduced. This effect is negligible as the difference in field is less than 2%.

Figure 8-1 shows a section of an image, covering the detector 2 area, taken from the prototype analyser. The ion source is again a hot filament gun ionising residual gas molecules. Ten thousand events were recorded at four different energies. The masses present in each spot are labelled on the diagram. Clearly the protons (H^+), H_2^+ and the heavier ions are resolvable over this reduced energy range. The actual energy range for mode 2 operations is 54eV to 1090eV so the highest energy is represented in the plot. Intrinsic resolution in both mass and energy gets progressively better as the energy is decreased. In the final flight configuration, however, dispersion will increase the spot size and hence reduce resolution as the deflections get larger. Although H_2^+ may not be present at Mars or in the solar wind its mass/charge ratio is the same as that for alphas (He^{2+}) which will be.

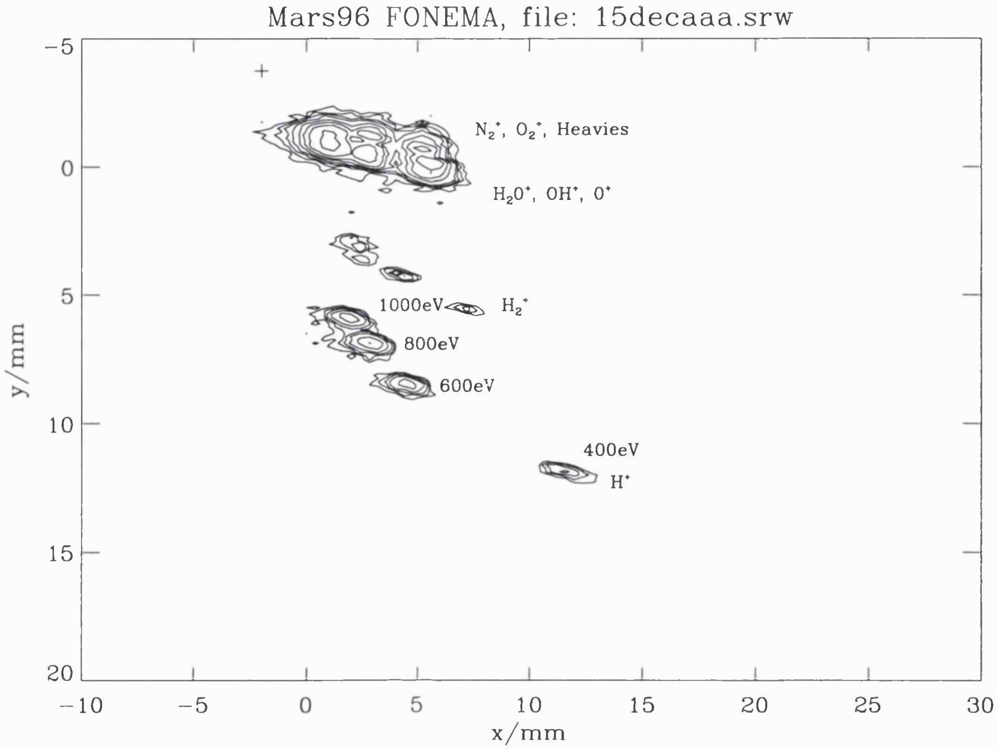

Figure 8-1. Image from the prototype analyser, detector 3, operating in mode 2 with a pre-acceleration voltage of -238V. Final positions for four energies are shown and the ions in each spot identified.

Although He^{2+} cannot be produced in the vacuum chamber at MSSL it is possible to bleed helium into the ionisation chamber of the ion gun and produce He^{+}. This gives a second peak, along with H^{+}, which is clearly identifiable over the whole energy range and contains a unique mass/charge ratio. Generally the H_2^{+} peak contains too few counts to provide statistical accuracy and the higher mass peaks cannot be resolved from other nearby masses. Having two clearly identified peaks makes the comparison between the experimental data and the simulator easier. Because the helium peak is not present normally in the residual gas, its controlled introduction provides an easily identifiable peak that can be used to quickly determine the other peaks. The disadvantage of having helium in the system is that the cryogenic pumps used to produce the vacuum cannot remove it from the system. This means only very small amounts can be used and the partial pressure of helium needs to be monitored closely. The 600eV results from Figure 8-1 are summed in the *x* direction to show the mass resolution of the analyser in Figure 8-2a). In Figure 8-2(b) the same experiment is repeated but this time after helium has been let into the vacuum system. The enhancement in the water group ions is probably due to the inadvertent introduction of moisture into the system. This is probably present in the gas piping used to transfer the helium from the gas bottle to the vacuum chamber.

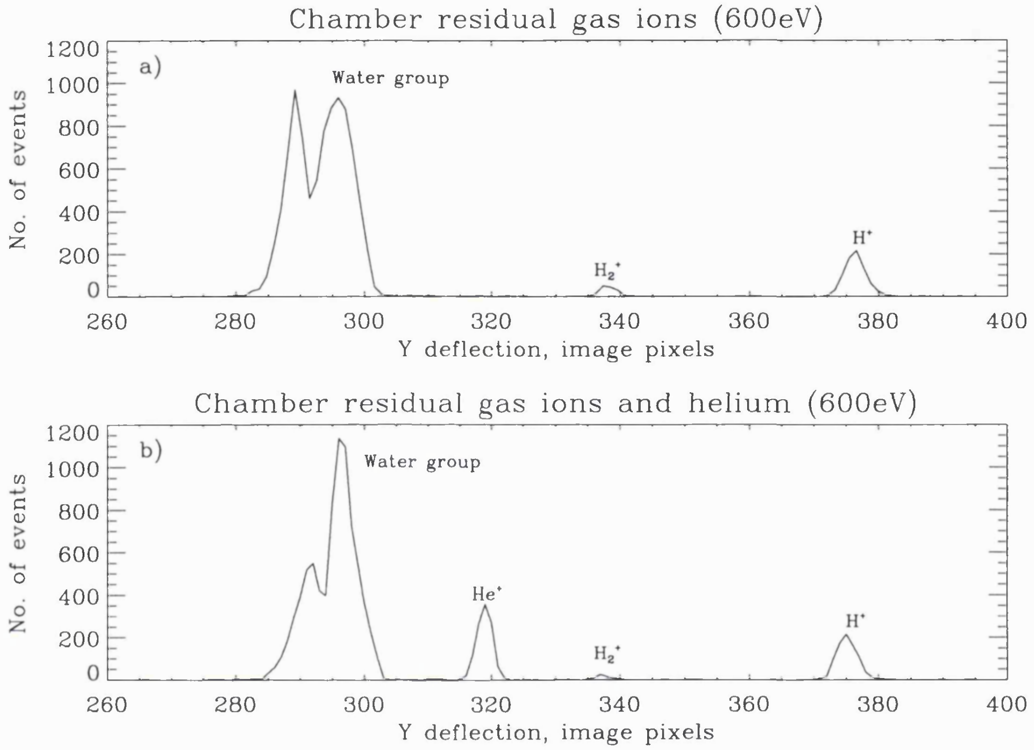

Figure 8-2. a) 600eV residual gas ions recorded in the FONEMA prototype analyser and summed in the *x* direction to show the mass resolution. b) as (a) but after the introduction of helium gas into the vacuum system

During all of the testing a quadrupole residual gas analyser is used to monitor the gas content within the vacuum chamber. These mass spectra can then be compared to those recorded by the FONEMA prototype. The match of these spectra will not be exact due to the different geometry of the two analysers, the different filament material used and the variation in operational levels. All of these factors will change the relative ionisation sensitivity for different ions within the system and hence the detection efficiency for these ions. Different type filaments operating under different conditions will also produce varying amounts of carbon monoxide which will show up in the mass 28 peak. This peak will also contain N_2^+. The relative amount of each should be calculable by looking at the carbon (mass 12) and nitrogen (mass 14) peaks which should contain about 5% of the number of C0 and N_2 ions in the mass 28 peak respectively. A typical mass spectrum for the vacuum chamber used is shown in Figure 8-3.

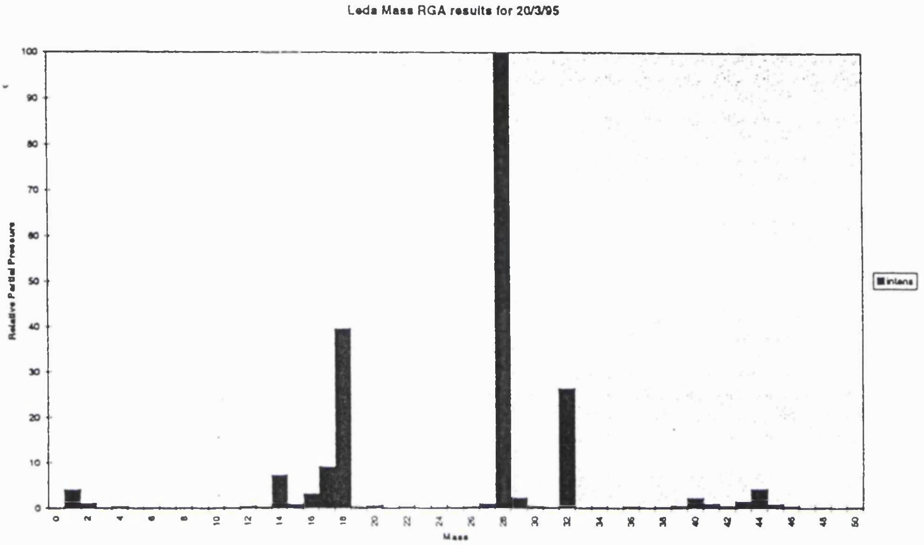

Figure 8-3. Typical residual gas analyser (RGA) mass spectrum for the Edwards Vacuum system used for all the FONEMA testing.

8.3 Simulator

Delays in the production of a working prototype analyser and the shortage of time meant that very few simulations of a prototype analyser were carried out. Those that did occur were mainly for electrostatic or magnetic deflection only, as previously presented in Chapters 4 and 5. These tests confirmed that the field data and the simulator modeled the real situation to the required accuracy. Once this had been achieved the simulator was used to model the final configuration. Figure 8-4 and Figure 8-5 show simulator data for a left hand analyser operating in modes 1 and 2 and modes 3 and 4 respectively. In these plots protons, alphas, O^+ and N_2^+ are present with energies ranging from the minimum to the maximum energy for the respective mode (see Table 8-1).

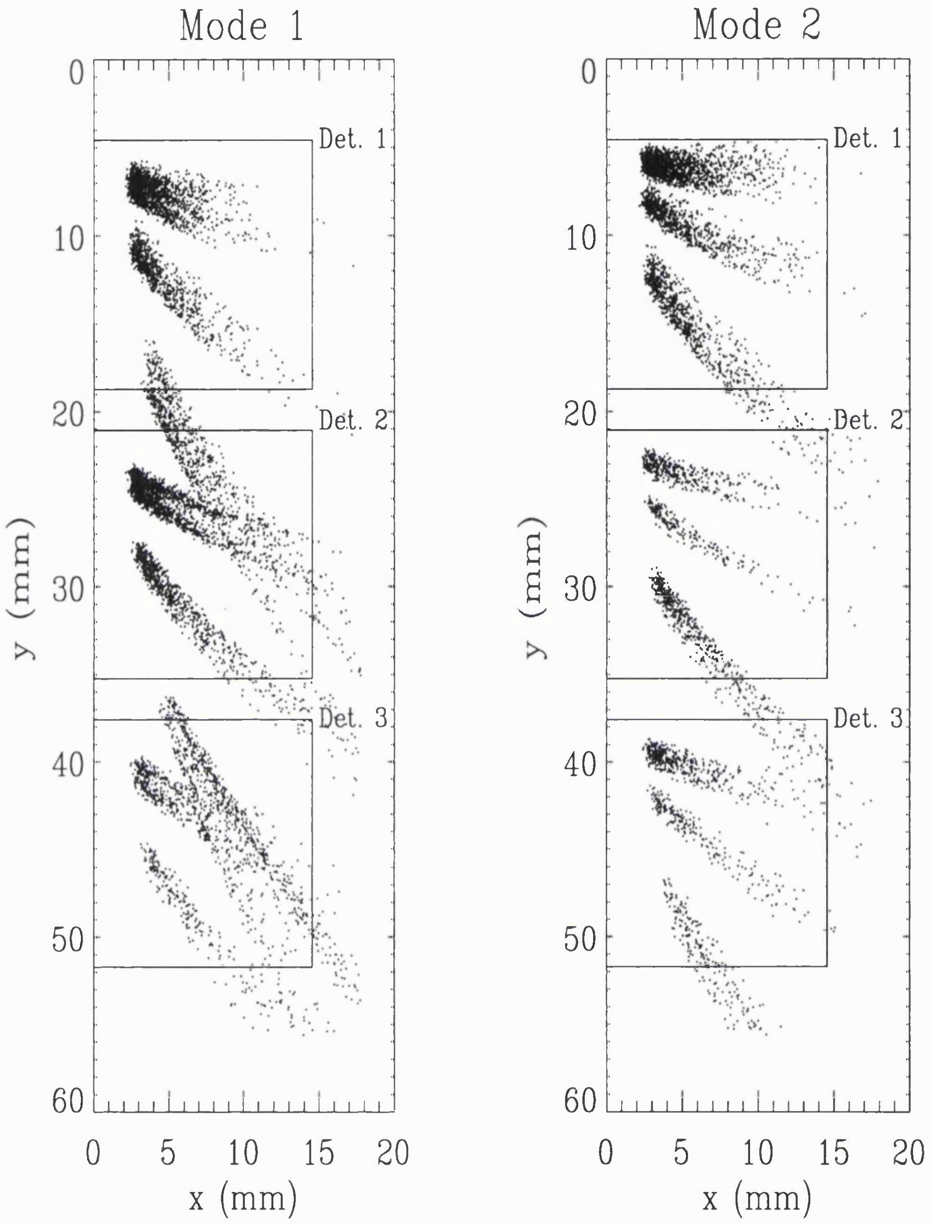

Figure 8-4. Simulator data for the final configuration, modes 1 and 2. The box represents the limits of the mass and energy look up tables.

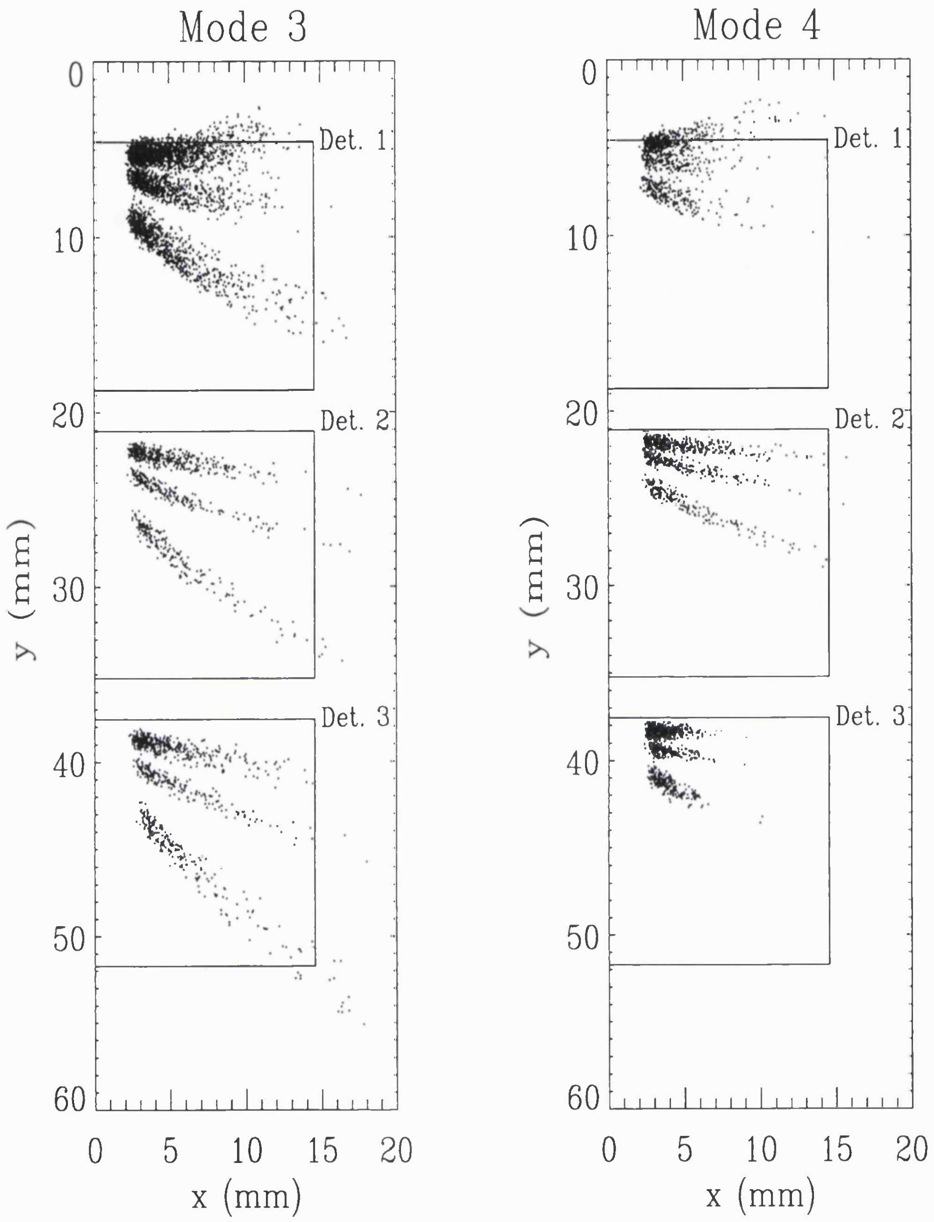

Figure 8-5. Simulator data for the final configuration, modes 3 and 4.

8.4 Flight Operation

In flight there are three main modes of operation: picture mode, spectra mode and quick-and-dirty spectra mode. In picture mode the full images covering a right/left pair of analysers, as shown in Chapter 7, are telemetered down, after data compression, in their entirety. To increase the amount of science return within the limited allocation of telemetry some on board processing is carried out. In spectra mode, rather than return full images which requires 1024bytes of data each, the image resolution is halved and the pixels assigned a mass and energy value. Any event that is recorded in a pixel then simply adds to a counter representing that mass energy bin. Energy spectra are then downloaded in the telemetry for each mass and for each of the 36 individual energy bins. Full spectra data, after compression, only requires 72bytes. The tables that assign an energy and mass number to an event position are collectively called the mass energy look-up table (MELT). In quick-and-dirty spectra mode the instrument keeps track of the analyser which is producing the most counts. In this case, only data from that bin and the four closest neighbouring bins is converted into spectra for transmission to ground. In both spectra and quick-and-dirty spectra modes a choice can be made to the combination of mass bins that are included in the telemetry.

8.5 Production of MELT

Using the simulator results the MELT for FONEMA was constructed. In reality there are separate mass look-up tables and energy look-up tables for each angular bin and for each mode. This totals to 288 separate look-up tables. Earlier in the project it was envisaged that memory could be saved by uploading only MELT parameters which could then be used to construct the final table. Although a table could be constructed in less than four seconds it was found that with a suitable compression scheme the complete MELT could be stored in almost the same amount of memory as that required by the parameters. Update of a new MELT, as required between mode changes could then be performed in much less time than that needed to change the voltage levels. Construction of MELTs on the ground is carried out based on information obtained from the simulator of the full instrument. It was envisaged that after post launch testing of the flight spare detector these could be modified with more realistic tables where necessary. The data processing unit possessed an upload capability so that memory tables, parameter tables and code could all be uploaded during flight.

Mass table construction

The construction of the mass array is based on the use of cubic polynomials which are fitted to the simulation data to separate the mass groups. Mass boundaries are calculated by finding the midway point in y between the mean position of the two main masses in adjoining groups, e.g. H^+ and He^{++}, for several discrete values in x. Having identified these discrete points on the mass boundary a cubic spline fitting routine is used to calculate the cubic polynomial that will represent the boundary. These mass boundaries occur at values of mass/charge of 1.5, 10 and 20. A series of mass coefficients representing the variables for the cubic polynomials for each of the 36 individual analysers are then stored on board to allow mass tables to be derived when needed. Finally, each pixel is assigned a 2 bit number depending on which mass group it lies within. Those on the boundary are assigned the value of the mass group in which the largest fraction of their area lies.

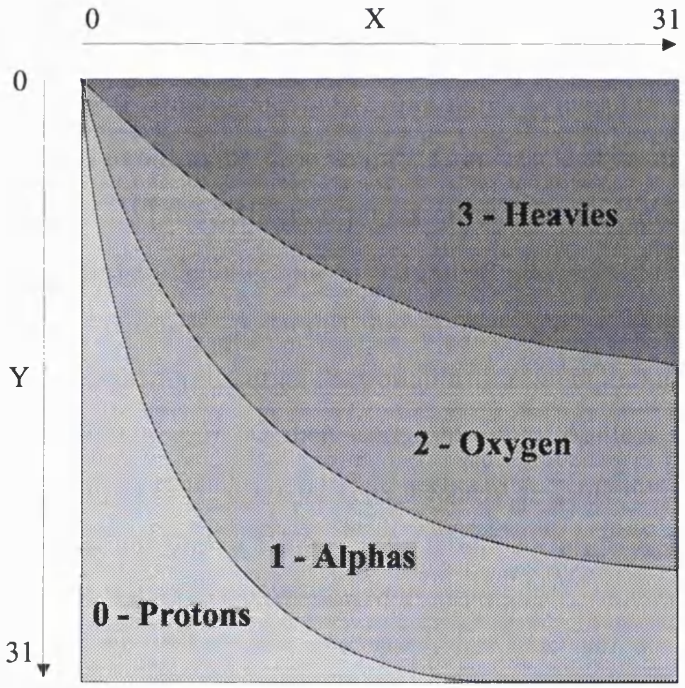

Figure 8-6. General form of the mass look up table.

The mass boundaries will be used to construct the final mass table as depicted in Figure 8-6. Each of the 1024 (32 × 32) pixels forming the image will be assigned a value, representing its mass range, in the range 0-3 (2 bits). In Chapter 7 it was shown that the final image plane is digitised to 7 bits in *X* and 8 bits in *Y*. For the spectra mode this resolution is reduced by dropping the least significant bit in each axis producing a full image plane of 128 × 64 pixels. In practice the images do not fill the full 128 × 64 pixels of the theoretical image plane. Pixels outside the area of the analyser images are assigned the value 0, although this is the same assignment as for protons i.e. the lowest mass group, these pixels will be ignored for the construction of spectra. This also means that only the three higher mass groups have to be specified if a new table is uploaded during flight thus reducing the number of spacecraft commands needed. Actual image sizes are 16 × 25 pixels so only 29% of the available digital image space is used. A typical mass look-up table derived from the simulator is shown in Figure 8-7 with data from the simulator superimposed.

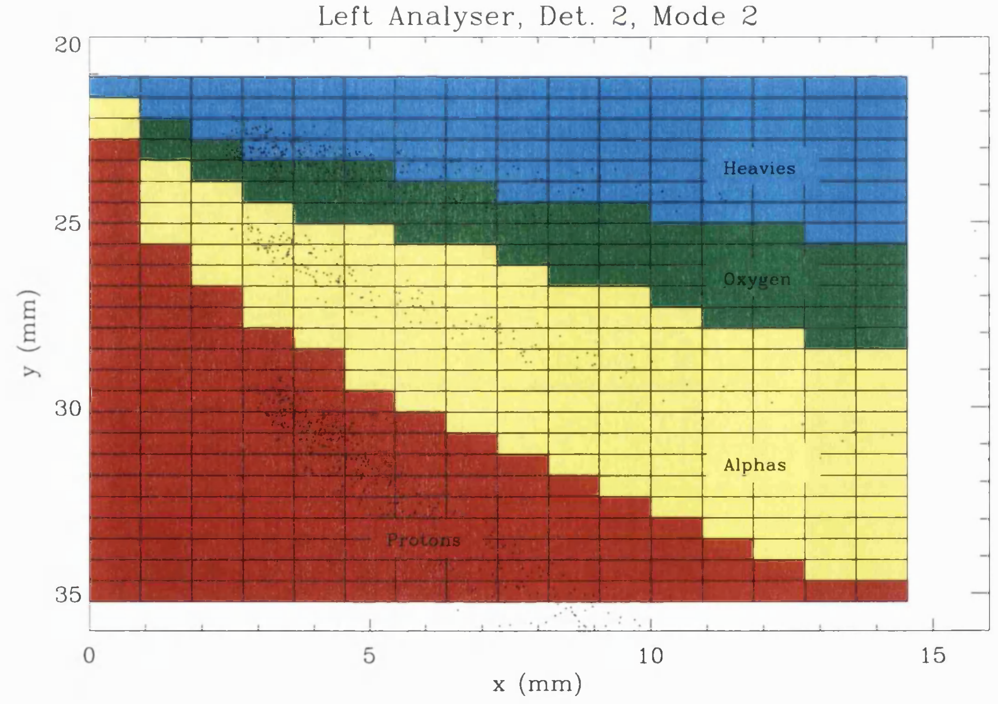

Figure 8-7. Mass look-up table with the simulator data from detector 2, mode 2 superimposed

Energy table construction

In a similar method to the mass look up table the energy boundaries were initially controlled by a set of fifteen linear equations. The variation in the energy distribution along the parabolas of different masses meant that these could not be used to separate the energies efficiently. Going to higher order polynomials would require too much memory for storing the parameters. Instead the full tables were loaded into memory. As previously mentioned facilities were available to load up new tables or revise individual pixel designations as needed during flight. Again the energy look-up table will cover 16 × 25 pixels. The simulator data for detector 2 operating in mode 1 is shown in Figure 8-8 with the energy table that was created using it. The energy ranges are shown in the colour bar to the right of the figure. Similar energy tables were constructed using the simulator data for all 36 individual analysers operating in all modes.

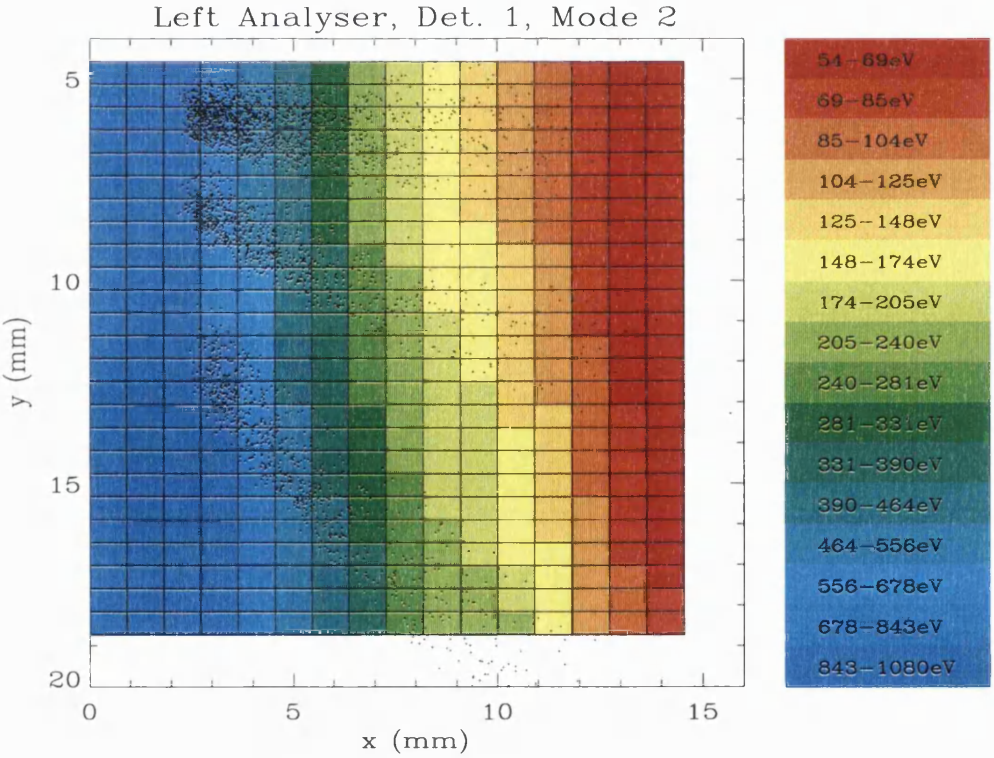

Figure 8-8. Energy look-up table with the simulator data from detector 1, mode 2 superimposed.

8.6 Instrument resolution

During final integration of the flight instrument it was found that magnetic field coupling from the high voltage power convertor to the harnessing and conducted mode noise from the high voltage power convertor, reduced the resolution of the final images. The conducted noise was suppressed by introducing an LC network. Inductors were placed in series on the power lines followed by capacitors to ground. The radiative noise was reduced by surrounding the high voltage box with a thin μ-metal shield connected to chassis ground. Although these measures were successful in reducing the noise the final resolution was not as good as expected.

8.7 Testing of completed instrument

Time and money constraints within the programme meant that the full instrument calibration that was planned to take place at the Culham laboratory did not happen. This test was to have placed the completed FONEMA instrument onto a two axis rotation system within the output stream of a 30cm diameter ion thruster. Although the countrates would be higher than expected at any time during the mission it would allow full characterisation of the instrument. The backup plan was to rely on a combination of in-flight calibration and the calibration of a refurbished flight spare instrument. Loss of the spacecraft meant that no further funding to support this effort was available. The data presented in this section is from the small amount of testing within the laboratory facilities which was done in the few days before and after thermal vacuum testing.

As mentioned in Chapter 4 angular dispersion will occur in the magnetic field region. Unlike the ideal Thomson Parabola, where electrostatic deflection and magnetic deflection can be treated as independent processes, this will effect the amount of deflection the ions undergoes in the electrostatic region. The larger the initial angle from the normal, defined by the collimator channel, the greater the deflection in the magnetic field region. This then means that the path length through the electrostatic field, and the consequent deflection, is also increased. Because a larger magnetic deflection translates into a larger electrostatic deflection, the outcome is a stretching of the final spot on the image plane. This effect is not seen in the flight model results because only a narrow ion beam was available, which meant only a small number of collimator channels were used at any one time.

Figure 8-9 shows the normalised counts versus position taken from a diagnostic image of the flight model instrument during final testing. The electrostatic mirror was illuminated from a narrow beam ion gun positioned such that the beam was pointing along a polar angle of approximately 60° to the instrument axis at 270° azimuth. This places the ions almost centrally in the field of view of detector number 1 in the upper lefthand analyser U4L. The instrument was in mode 2 with a pre-acceleration voltage of 238.5Volts, a deflection voltage of 150Volts and an approximate energy range of 54 to 1090eV. Peaks are shown for six energies from 200eV to 1200eV. The 200eV peak can only just be resolved from the 600eV peak. Experiments described in Chapter 7 show that the limiting spatial resolution from the electronics should be a little under 1mm in the strip axis (*x* axis). The resolution in this image, however, is approximately 9 pixels or 3.9mm. Subtracting the image spot size of just over 1mm leaves a spatial resolution element due to the electronics of nearly 3mm, nearly three times that expected. Dispersion effects can be ignored in this calculation as the narrow beam ion source means that only a small area of mirror is illuminated and hence only a narrow beam enters the analyser. The energy resolution, *dE/E*, calculated from this plot is 1.25 at 200eV and 1.4 at 1200eV. The minimum resolution occurs at 600eV where *dE/E* = 1.12. The same plot is shown for mode 3 of the instrument in Figure 8-10. Again the energy resolution is very similar to the value for mode 2. In both these plots the rough appearance of the lowest energy peaks is due to a lower intrinsic countrate at these energies.

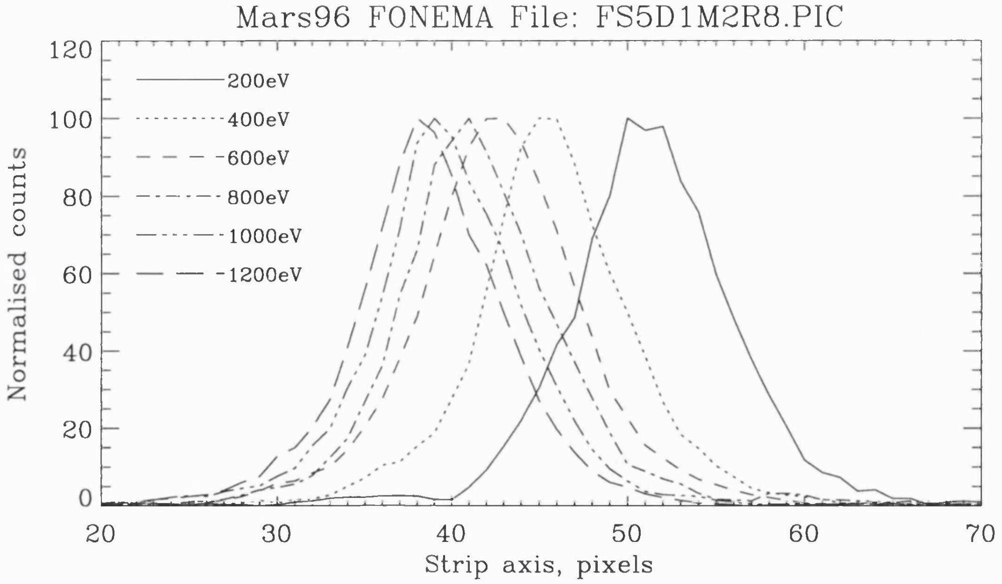

Figure 8-9. Counts versus position for six energy peaks in detector 1 of one of the upper lefthand analysers operating in mode 2.

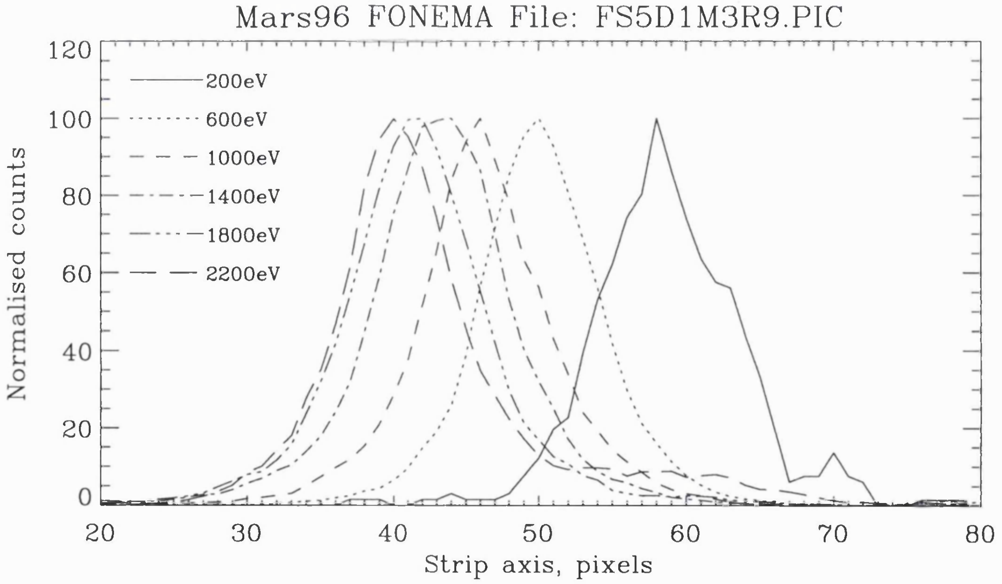

Figure 8-10. Counts versus position for six energy peaks in detector 1 of one of the upper lefthand analysers operating in mode 3.

The peak positions from Figure 8-9 and Figure 8-10 are plotted against energy in Figure 8-11 and Figure 8-12 respectively. Error bars on the peak position are a combination of the standard error on determining the peak position from the image and the uncertainty in determining the focus position of the analyser from earlier experiments. In both plots the flight model results (crosses) are plotted with results from the simulator (dots) for comparison. The three branches in the simulator results are an artifact of only using nine holes in the collimator for this simulator run. Referring back to Chapter 3 the hole numbers resulting in the lower branch in both plots are 8, 49 and 85 which are all positioned on the righthand side of the collimator when looking from the instrument axis. The central branch results from ions starting from holes 4, 45 and 81 at the front of the collimator, all central holes. The upper branch is from holes 1, 41 and 77 on the lefthand side of the collimator. In both plots the experimental results coincide with the central branch as expected from the alignment of the ion beam. The simulation results in these two plots show the problem of angular dispersion within the Thomson Parabola clearly, with a much larger spread in deflection at the lower energies and hence a reduce mass resolution. As shown earlier, however, the mass bins in FONEMA get progressively wider at lower energies so the effect of the dispersion is not seen as clearly in the spectral data.

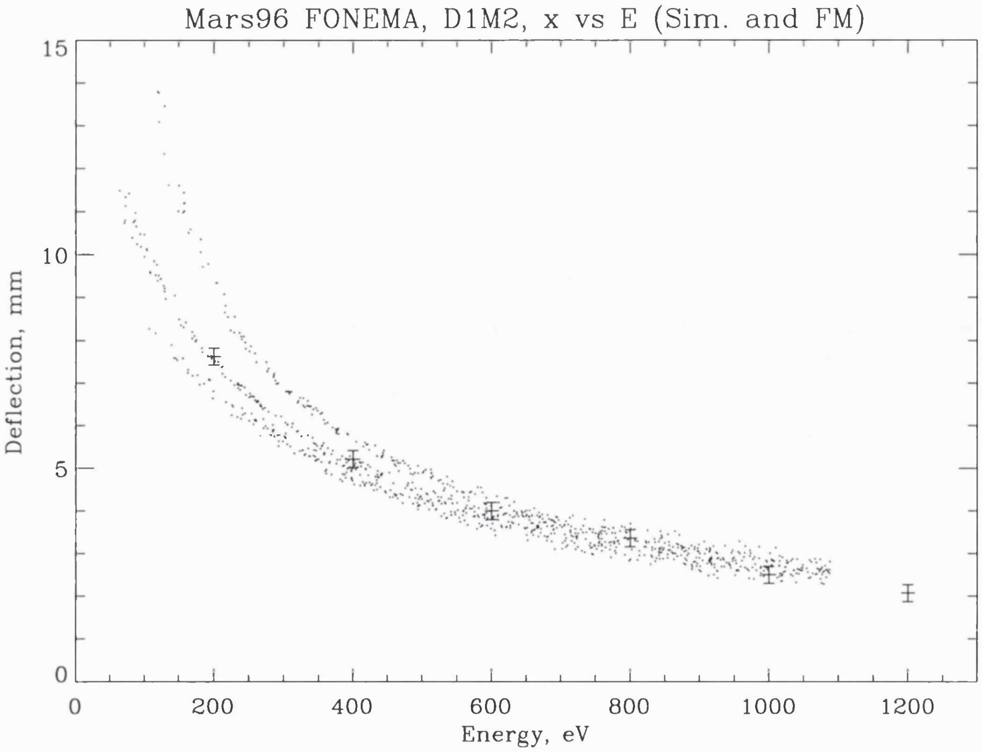

Figure 8-11. Peak positions from Figure 8-9 plotted against energy. These are compared with results from the simulator.

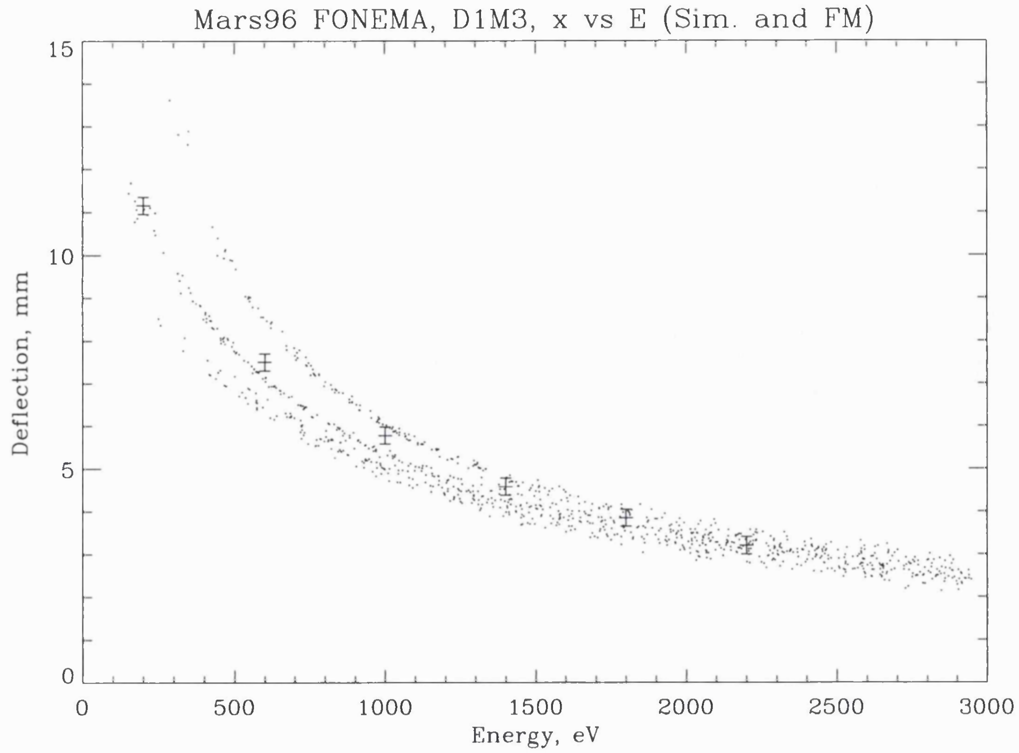

Figure 8-12. Peak positions from Figure 8-10 plotted against energy. These are compared with results from the simulator.

8.8 Response function

The response function (or transmission function) is defined as the fraction of a beam of particles (of a given energy and direction, incident uniformly upon the entrance aperture) that is detected by the instrument (*Vasyliunas*, 1971). With the imaging system of FONEMA each pixel has its own unique response function, R(E, θ, ϕ, mass). Due to the energy and mass resolution of the instrument, response functions from neighbouring pixels will overlap. However, in the spectra mode of FONEMA, energy spectra are transmitted for each of the four mass groups for all 36 angular bins. Therefore the response function of any particular bin in the energy spectra is necessarily an integration of the combined response functions of the individual pixels which make up that bin. In all the FONEMA modes it is possible to download full images which will have a resolution of double that of the pixel size used in the mass energy lookup tables. These diagnostic images can then be used to check the validity of the integrated response functions used to analyse the spectra data on the ground.

The response function for any individual pixel in the image plane is dependent upon two separate factors, the energy dependent geometric factor of the combined mirror/collimator system (see Chapter 3) and the detector efficiency (see Chapter 6).

8.8.1 Energy dependent geometric factor

Each of the 36 individual detectors that make up FONEMA represents a single angular bin of approximately 60° in azimuth and 20°, 30° and 40° in polar for detector 1, 2 and 3 respectively. This range is defined by the combination of the particle collimator and the electrostatic mirror. The angular transmission of the mirror varies with the energy of ions. Because the collimator selects specific angles this produces an effective energy dependent transmission of the combined system. Examples of the angular transmission plots for the mirror were shown in Chapter 3. Another factor is the transmission in the collimator, and as explained in Chapter 3, this varies from channel to channel simply dependent on geometry. Combined with this is an energy dependent factor due to the pre-acceleration voltage and a small mass dependent factor due to the stray magnetic field in the collimator. In practice therefore there is a separate angular response function for each energy/mass couplet within each detector. Because the final position of the event on the image plane gives the unique energy and mass values, this response function is applied to each pixel. In practice, a spectral bin will cover a few pixels so the response function for a bin will be some form of weighted integration of the constituent pixel response functions. The final spectra from a particular detector cannot be assumed to all come from one direction. The direction is defined by the centre of influence of the combined mirror/collimator system for a particular energy. The response function then gives an angular width to this particular direction.

8.8.2 Detector efficiency

For each individual pixel the average MCP gain within the area of that pixel may differ from the gain in the neighbouring pixel. This is due to the inherent gain variations that exist within MCPs (see Chapter 6). If the pulse height distribution is at a lower gain then the number of events above the lower level discriminator that are counted will be less. Of course the position of the pixel on the MCP will be related to the mass and energy of the incident particle so values for the modal gain and the quantum efficiency of the MCPs at that energy and mass should be available. An energy bin in spectral mode will be made up of a number of these pixels so the detector efficiency for the bin will have to be taken as the average of the efficiencies for the individual pixels. As the mission progresses it is possible that the pulse height distribution will vary from pixel to pixel. It is here that the diagnostic images can in useful in showing any possible dark spots that may be affecting the detector efficiency in a particular bin. Initially, however, the detector efficiency as a function of energy, *D(E)*, can be estimated from the following equation:

$$D(E) = QE(E,m) \times CAT(E) \times MT \qquad (8.1)$$

where *QE(E,m)* is the quantum efficiency of the MCP, *CAT(E)* is the 'counts above threshold' factor and *MT* is the transmission of the mesh in front of the MCPs (81%). For nearly all but the lowest energy protons *QE(E,m)* is the open area ratio of the MCPs (66.5%) and at normal operating conditions *CAT(E)* is approximately 83%, although this varies from analyser to analyser due to changes in the fwhm of the pulse height distribution. This gives a total detector efficiency of 0.447.

As mentioned full calibration of the final instrument was not carried out. These response functions were to have been derived from what little data was available and by extensive simulations. After the loss of Mars 96 funding and manpower were not available to finish this task.

8.9 Spacecraft charging

Build up of charge on the outer skin of spacecraft can often produce large fields which can deflect particles near the entrance apertures to instruments. FONEMA is positioned such that only charging of its own surface is likely to have a major effect on performance. One of the last ground tests performed on FONEMA was to verify the resistance to spacecraft ground of the thermal insulation blanket. This resistance was measured at twelve positions and found to be less than 0.6Ω everywhere.

8.10 Instrument Specification

Table 8-1 shows the final specification for the FONEMA instrument. The dimensions include the thermal blanket for the sensor unit but not for the DPU which is included within the spacecraft thermal blanket. Because of the location of FONEMA on the spacecraft over 7m of cable was needed to attach the sensor unit to the DPU. The weight of this cable is not included in the table as it was supplied by the spacecraft contractor. Power estimates are for a fully operational instrument operating in spectra mode with 8 second accumulations at 25°C.

Sensor Unit weight (kg)		8.1
Sensor Unit power (W)		6.65
Sensor Unit dimensions (mm)		260 × 320 × 381
DPU weight (kg)		1.54
DPU power (W)		2.16
DPU dimensions (mm)		100 × 150 × 180
Energy ranges (eV):	Mode 1	20 - 400
	Mode 2	54 - 1090
	Mode 3	150 - 2950
	Mode 4	400 - 8000
Energy resolution ($\Delta E/E$)		$\cong 1.1$
Mass ranges (amu):		0 to 1.5
		1.5 to 10
		10 to 20
		Over 20
Time resolution (max.)		125ms
Angular coverage (steradians)		4π
Geometric factor ($cm^2 sr$)		$1.23\ 10^{-4}$

Table 8-1. Instrument specification for FONEMA.

9. Conclusion

This thesis has shown the design and implementation of a novel high speed plasma analyser and through limited laboratory testing demonstrated the capabilities and shortcomings of this instrument. Despite the low overall geometric factor and energy dependent variation in total quantum efficiency, this work has demonstrated that a detector of this design has a place in space plasma diagnostics and would be a valuable addition in one form or other to any spacecraft. FONEMA is the only ion mass spectrometer with true 4π coverage to have been included as part of a spacecraft payload. This full sky coverage allows full particle distributions to be measured at the unprecedented rate of 8 per second with sufficient sensitivity to enable differentiation of protons, alphas and heavier ions.

It is clear from the complexity of the design of this instrument and the calibration difficulties outlined in this thesis, that in order to ascertain precise knowledge of this device, without relying on in-flight cross calibration with other instruments, it is important to have access to a versatile calibration facility. Such a facility should possess a wide ion beam with a large dynamic range and a narrow ion beam mounted on a four axis stage; two linear and two rotational. The facility should also allow for rotation of the instrument about two axes. Because of the full 4π coverage of the instrument, providing test ions over the full angular range is a difficult problem, especially near the mounting bracket.

So that the intrinsic symmetry of the instrument can be utilised in reducing the number of calibration measurements needed, it is important that the Thomson Parabola analysers are very closely matched. For the magnetic and electric field geometry of FONEMA this was achieved. The collimators and imaging detectors, however, are sufficiently different to make testing of each analyser necessary.

Uniform collimator performance is achievable using the method described in Chapter 3 if enough time is available to select from a large number of builds. A more complex procedure can be envisaged where the plates are mounted to the collimator stack in the laser facility. To avoid damage to the plate below during laser machining a small beam stop is inserted behind the plate. This would involve leaving one end of the collimator open to allow entry of the beam stop. The total positional error obtained with the method used amounts to about 20μm, the improvement outlined above will hopefully irradicate the re-alignment error estimated at about 5μm. Positional errors due to thermal effects could be reduced by choosing a different laser system that uses laser ablation with UV light rather than infrared. Again the variability in the anodes is a consequence of differences in the conducting layer and non uniformity in the laser machined tracks. The use of a more stable conductor, e.g. gold, and more accurate machining methods should enable anodes to be produced in a repeatable manner.

Future applications of the FONEMA design should also pay close attention to the MCP selection and the way in which they are used. For FONEMA the need to save on mass and keep the overall volume down required that the anodes of two adjacent analysers were shared. As only one back face MCP signal was needed to trigger the event electronics for the two analysers they shared the same back face MCP connection. This meant that they shared the same rear face bias resistor meaning that MCPs not only needed matching in chevron pairs but also between pairs of analysers. Due to the non-uniform performance of the MCPs this was not achievable for FONEMA. Instead the different characteristics of the MCPs meant that for a long duration mission the performance of each MCP stack would be changing at different rates. This is not a problem if the state of each MCP stack is verifiable by means of in flight pulse height distribution information, and can be controlled if the MCP high voltage levels can be varied independently. Without at least one of these two design features it can be very difficult to deconvolve absolute counting efficiencies within the individual analysers unless the MCPs are matched across the whole instrument. At present the manufacturing techniques used by the MCP suppliers are such that this is unrealistic. Therefore it is recommended that for all MCP based detector systems on space borne instruments should have the ability to record pulse height distributions on an event by event basis. The discussion on variation in MCP performance with energy, countrate and time has shown that this type of information should not be viewed as diagnostic information to be obtained in an engineering mode. In flight, knowledge of pulse height distributions should instead be viewed as an essential in-flight calibration mode.

From the results of the simulator and final flight assembly it was shown that the resolution was much worse than anticipated due to noise in the electronics system. Even without this noise the mass and energy resolution at higher energies was shown to be relatively poor. It should be remembered though that in the Martian environment the number of different masses present will be reduced. Much of the time the analyser will be detecting mainly protons and alphas. The performance of FONEMA for these masses is very good allowing the design requirement of full 4π coverage at a rate of 8 accumulations per second. The detection of heavier ions will also be greatly improved as the number of mass groups will be reduced. Generally the major heavy ion will be oxygen. Other groups which flood the image plane during laboratory testing like the water group ions and nitrogen should not be present in the Martian environment.

9.1 Future improvements to FONEMA

The development of solid-state detectors and new ultra thin CCDs may allow the measurement of ions with energies as low as a couple of hundred eV in the very near future. *Murphy et al.* (1993) and *Hoenk et al.* (1993) have both suggested that CCDs may be useful as energetic particle detectors. CCDs can be regarded as arrays of very small *pn* junctions, sizes ranging from 100μm down to 7.5μm. At present the upper energy limit is determined by the thickness of the sensitive layer. For current devices this is of the order of a few Mev/nucleon for ions and about 50keV for electrons. The lower threshold is determined by the thickness of the ‘dead layer’ where liberated electrons are not collected. The amount of energy lost in this dead zone is indeterminate so it is important to make them as thin as possible. *Hoenk et al.* (1993) have developed a new delta-doped CCD that they claim, in a cooled mode, will be sensitive to 100eV electrons at the 3 electrons/pixel noise limit. If successful this will bring solid state detectors into the energy range of FONEMA and many other instruments that presently use MCPs or CEMs as the final detection device. Introduction of high spatial resolution CCDs, with pixel sizes down to 7.5μm, will also mean that for deflection devices the required deflections will become smaller and hence the magnetic and electric fields needed will be lower. This means that the overall mass of the instruments can be reduced for the same dynamic range, or the range can be increased significantly for the same mass. Using CCDs for imaging in

FONEMA would mean that no high voltages would be needed for the detector reducing mass and power. CCDs would also mean that the electronics design becomes easier without the need for numerous amplifier chains.

Alternatively, developments in new chip technologies are working toward producing large numbers of the more traditional amplifier chains on single devices (*Cook*, 1993a, *Cook et al.*, 1993b, *Voss et al.*, 1993, *Grande et al.*, 1993). These VLSI devices would reduce the weight and power needed in the original FONEMA design. *Detwiller* (1993) discusses the possibility of reducing the weight of power conversion units for space instrumentation and *Cushing and Lindelef* (1993) describe the use of Application Specific Integrated Circuits (ASICs) in reducing the power and weight requirements of an instrument electronic package. This miniaturisation of spacecraft electronics, although highly desirable in terms of reduced spacecraft resources, may increase the risk of radiation damage and reduce reliability (*Barnes et al.*, 1993). With all these new technologies it is important not to lose sight of the final goal which is to produce a reliable, well calibrated, scientifically useful instrument. With smaller budgets and faster turnaround times for modern missions it is important not be using time and money trying to incorporate cutting edge technology at the expense of a well calibrated, well understood sensor. A more realisable improvement to FONEMA can be achieved with a very small reduction in the power requirements and mass of the electronic signal processing chains. By having one set of electronics per anode the noise levels should be greatly improved. This also allows the anode size to be halved reducing the capacitance into the preamplifiers and hence the noise. This noise could also be reduced by finding an alternative anode material with a lower relative permittivity than alumina. As a first step the design could be changed to enable the implementation of a quartz anode reducing the capacitance by a factor of approximately 3. Although SINTIMID was rejected for use in FONEMA other polymers may become available that will prove useful as an anode substrate.

Improved MCP performance and increased understanding of the charge transfer mechanisms within an MCP/WSA system may lead to improvements within the conventional system. At present the variability of the MCP gain across the surface and the variation in specification from plate to plate make the characterisation of the MCPs a time consuming process within a project development. If manufacturing of these plates improves to the extent that the customer need not undertake a characterisation process then using large numbers of MCPs in a multi-sensor instrument like FONEMA becomes easier. One of the problems with the FONEMA Thomson Parabola is the angular dispersion due to the field of view of each analyser resulting in a reduced resolution in both energy and mass. This can be reduced by using a larger number of individual analysers with a smaller FOV. One of the arguments against this approach is the larger number of MCPs that would have to be used. The FONEMA design compromised uniform polar bin sizes so that co-linear focus positions would result in less individual analysers.

At the front end of FONEMA there is still some concern about UV rejection. This could be improved by reducing the reflectivity of the wires used in the grounded mesh of the electrostatic mirror by application of a suitable coating. A technique used in cylindrical electrostatic detectors of scalloping surfaces could be used on the inner electrode of the mirror. The use of a less reflective paint, such as Ebanol C would also reduce UV photons from these surfaces entering the analyser (*Alsop et al.*, 1996). Within the collimator, using modern coating techniques, it may be possible to apply a low reflectivity coating to the individual plates without blocking up the holes. Alternatively, laser machining the holes in pre-coated shims may help reduce some UV background caused by multiple reflections within the collimator. Finally, the UV photon traps at the focus of the collimators could be improved in design and be coated with a low reflectivity surface.

Another area of improvement within the collimator is the pre-acceleration region. With the present design many low energy ions are prevented from reaching the Thomson parabola due to the linear pre-acceleration within the collimator. As discussed in Chapter 3 this can be alleviated by having a field region which is at all times normal to the ion trajectories. In the present FONEMA design this was almost impossible to achieve within the available space although a re-design of the instrument should try to incorporate this. On a similar topic, if the azimuthal angular bin size could be reduced substantially by introducing more analysers, the magnetic and electrostatic fields could be tailored to match the incoming trajectories from the collimator. This would reduce the size of the spot which at present is limited by the dispersion within the deflecting fields. Dispersion is also reduced by keeping the deflection angles down which can only be achieved by having a large distance between the deflection fields and the image plane so that the resolution can be maintained. Increasing this distance, however, increases the spot-size unless the collimator holes are reduced which will reduce the geometric factor. The distance to the focus position is of course controlled by the mirror geometry so any attempts to change it will require a new mirror design.

Another advantage of reducing the deflection angles is the associated reduction in field strengths required. Smaller deflections also mean that a less open geometry is needed in the field design. Both the tighter field geometry and reduced fields would result in a reduction in the magnitude of stray fields. This is especially important in the magnetic field where stray fields can cause image distortions in the imaging detector. Uniform field regions would also allow solution of the trajectories without the need for a full instrument simulator.

9.2 Future Prospects

Despite the loss of the Mars 96 spacecraft in November 1996 the concept of the Thomson Parabola analyser as a spaceborne mass spectrometer has been validated by the work carried out on FONEMA. In view of this, a triplet of FONEMA analysers have been proposed for a spacecraft environment monitoring package to be used on the International Space Station. In addition it is hoped that a FONEMA based instrument will be selected for the ESA Mars Express mission in the near future.

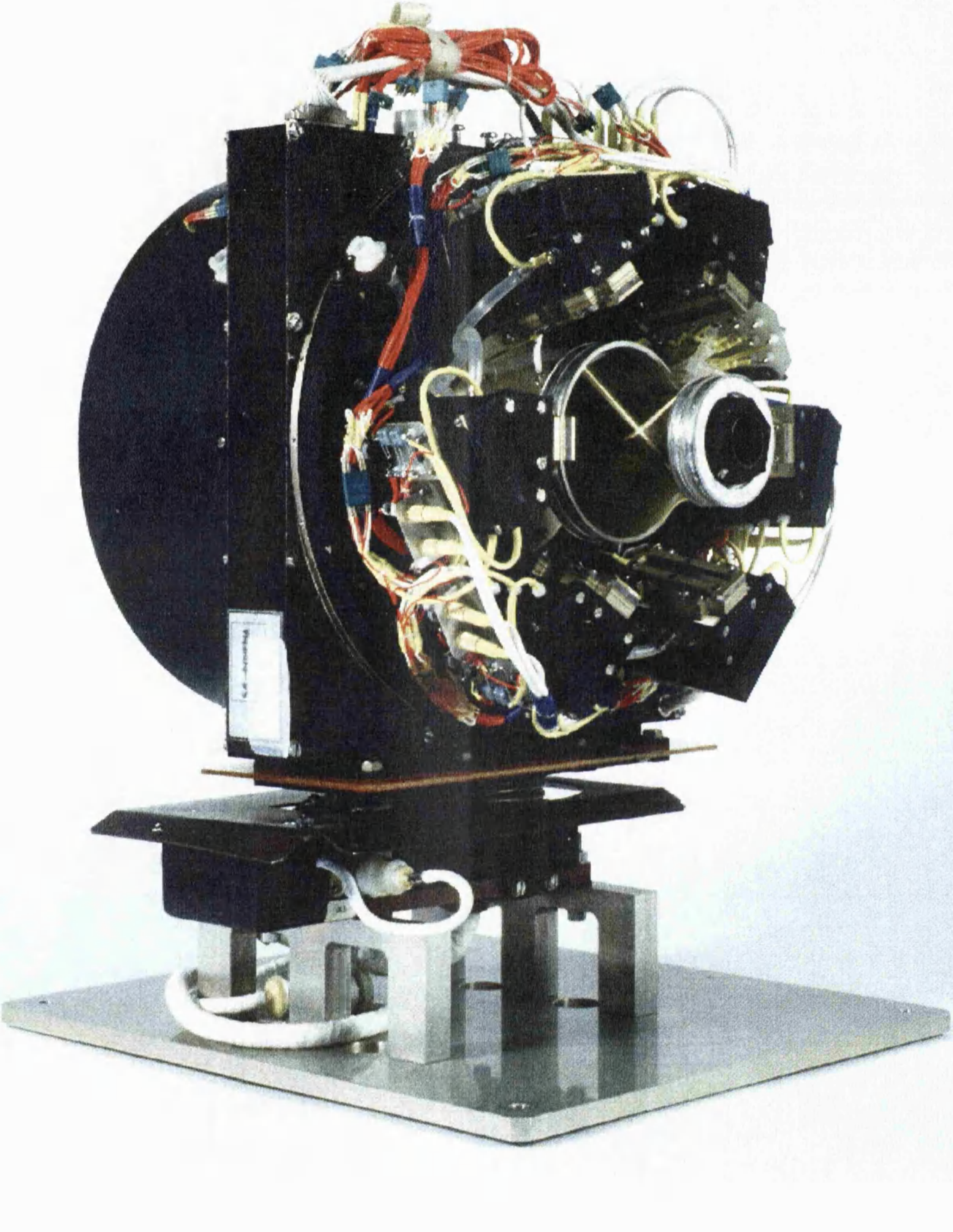

Figure 9-1. Photograph of the FONEMA flight spare instrument.

10. Acknowledgements

Firstly I wish to thank Professor Johnstone for his guidance and for giving me the opportunity to do this PhD and to work on such an interesting project. Secondly I would like to thank the FONEMA team at MSSL, Tom Kennedy, Matthew Whillock, Jim Bowles, Mark Birdseye, Cedric Dela Nougerade, Frank Thurlow and other members of staff at MSSL who played their part in producing the FONEMA instrument. Special thanks to John Raymont for help in the test programme and for his advice and encouragement. Thanks must also go to the other members of the project from the other Co-I groups, especially Andrey Fedorov and Oleg Vaisberg at the Institute of Space Research in Moscow. Special thanks also go to Dave Walton, Jon Lapington and Liam Worth for their help throughout the final stages of the project.

I wish to thank Dave Walton, Jon Lapington, Matt Whyndham, Alice Breeveld, Dave Linder, George Papathodorou, Mick Edgar and Chris Alsop for useful discussions on detector physics throughout the years. I would like to thank Sarah Szita, Alan Johnstone and Andrew Coates for explaining plasma physics to me. Thanks to Sarah Szita, Alan Johnstone, Dave Walton and Andrew Coates for proof reading the chapters for me and giving many useful suggestions. Finally a special thankyou to Sarah for her practical help and encouragement.

I acknowledge the support of a SERC grant during my studentship at MSSL. Finally I wish to thank the director of MSSL, Professor Len Culhane, for giving me the chance to finish this thesis.

11. Bibliography

Acuna, M. H., *NASA Press Release, 97-204*, 1997.

Adams, J., B. W. Manley, Mechanism of Channel Electron Multiplication, *IEEE Trans. Nucl. Sci., NS 13*, 88, 1966.

Afonin, V., S. McKenna-Lawlor, K. Gringauz, K. Kecskemety, E. Keppler, E. Kirsch, A. Richter, D. O'Sullivan, A. Somogyi, A. Thompson, A. Varga, M. Witte, Energetic ions in the close environment of Mars and particle shadowing by the planet, *Nature, 341*, 616, 1989.

Allemund, R., G. Thomas, Nouveau Détecteur De Localisation, *Nucl. Instr. Meth. 137*, 141, 1976.

Allington-Smith, J. R., H. E. Schwarz, Imaging Photon Detectors for Optical Astronomy, *Q. Jour. R. Astr. Soc. 25*, 267, 1984.

Alsop, C., L. Free, S. Scott, Optimisation of the Cluster PEACE 'top hat' electrostatic analyser design to reduce Solar photon background, submitted to *Proc. AGU Chapman Conference on Measurement Techniques in Space Plasmas*, 1996.

Anderson, H. R., Mariner IV Measurements near Mars: Initial Results, *Science, Vol. 149*, 1226, 1965.

Anger, H. O., *Instr. Soc. Am. Trans. Vol. 5*, 311, 1966

Armentrout, C. J., G. Bramson, R. Evanko, E parallel B canted detector neutral-particle spectrometer, *Rev. Sci. Instrum., vol. 56,* 2101, 1985.

Armentout, C. J., Design study for a compact E parallel B particle spectrometer, *Rev. Sci. Instrum., vol. 61,* 3098, 1990.

Bader, M., Preliminary Explorer 12 data on Protons below 20 keV, *J. Geophys. Res., 67,* 5007, 1962.

Bagenal, F., Planetary Magnetospheres, from *Solar System Magnetic Fields, Ed. by E. R. Priest, Geeophysics and Astrophysics Monographs, D. Reidel Publishing Co.*, 224, 1985.

Balsiger, H., P. Eberhardt, J. Geiss, A. Ghielmetti, H. P. Walker, D. T. Young, H. Loidl, H. Rosenbauer, A Satellite-Borne Ion Mass Spectrometer for the Energy Range 0 to 16 keV, *Space Sci. Instrum., 2,* 499, 1976.

Balsiger, H., Recent Developments in Ion Mass Spectrometers in the Energy range below 100 keV, *Adv. Space Res., 2,* 3, 1982.

Balsiger, H., K. Altwegg, F. Buhler, J. Fischer, J. Geiss, A. Meier, U. Rettenmund, H. Rosenbauer, R. Schwenn, J. Benson, P. Hemmerich, K. Sager, G. Kulzer, M. Neugebauer, B. E. Goldstein, E. G. Shelley, T. Sanders, D. Simpson, A. J. Lazarus, D. T. Young, The GIOTTO Ion Mass Spectrometer, The Giotto mission - Its Scientific Investigations, edited by R. Reinhard and B. Battrick, *European Space Agency, ESA SP-1077,* p. 129, 1986.

Bame, S. J., D. J. McComas, D. T. Young, R. D. Belian, Diagnostics of space plasmas (invited), *Rev. Sci. Instrum., 57,* 1711, 1986.

Barabash, S., O. Norberg, Indirect detection of the Martian Helium corona, *Geophys. Res. Lett., 21,* 1547, 1994.

Barabash, S., E. Kallio, R. Lundin, H. Koskinen, Measurements of the nonthermal helium escape from Mars, *J. Geophys. Res., 100,* 21307, 1995.

Barnes, C., A. Johnston, J. Coss, The effects of Miniaturisation on the Reliability and Radiation Response of Microelectronics, *Proceedings of the Small Instrument Workshop held in Pasadena, California, 29-31 March, edited by B. T. Tsurutani*, p.7-35, 1993.

Bartiromo, R. , G. Bracco, M. Brusati, G. Grosso, S. Mantovani, B. Tilia, V. Zanza, Design and calibration of the JET neutral particle analyser, , *Rev. Sci. Instrum., vol. 58,* 788, 1987.

Breeveld, A. A., M. L. Edgar, A. Smith, J. S. Lapington, P. D. Thomas, A SPAN MCP detector for the SOHO Coronal Diagnostic Spectrometer, *Rev. Sci. Instrum., vol. 63,* 673, 1992.

Bridge, H. S.,C. Dilworth, B. Rossi, F. Scherb, An Instrument for the Investigation of Interplanetary Plasma, *J. Geophys. Res., 65*, 3053, 1960.

Bridge, H. S., A. J. Lazurus, S. W. Snyder, E. J. Smith, L. Davis, P. J. Coleman, D. E. Jones, Mariner 5: Plasma and magnetic fields observed near Venus, *Science, 158*, 1669, 1967.

Burrous, C. N. B., A. J. Lieber, V. T. Zaviantseff, Detection efficiency of a continuous channel electron multiplier for positive ions, *Rev. Sci. Instrum., 38, 1477*, 1967.

Burton, W. M., RALICON anodes for image photon counting fabricated by electron beam lithography, *Rutherford Appleton Laboratory Report, RL-82-003*, 1982.

Chapman, S., V. C. A. Ferraro, A New Theory of Magnetic Storms, *Terr. Magn. Atmos. Elec., 36*, 171, 1931.

Chappell, J.H., S. S. Murray, Position Modeling for the AXAF High Resolution Camera (HRC), *SPIE Vol. 1159 EUV, X-Ray, and Gamma-Ray Instrumentation for Astronomy and Atomic Physics*, 460, 1989.

Chauvet, G., A. Brenac, Simple electronic device for position-sensitive detectors in VUV spectrometry, *Rev. Sci. Instrum., vol. 58,* 197, 1987.

Clampin, M. F., J. Crocker, F. Paresce, M. Rafal, Optical Ranicon detectors for photon counting imaging, *Rev. Sci. Instrum., vol. 59,* 1269, 1988.

Clampin, M., F. Paresce, Spatial resolution characteristics of a GaAs-photocathode RANICON, *Rev. Sci. Instrum., vol. 60,* 1092, 1989[a].

Clampin, M., F. Paresce, Photon-counting imaging with a GaAs photocathode: evaluation of the Red-RANICON for astronomical imaging, *Astron. Astrophys. 225,* 578, 1989[b].

Clegg, A., *Br. J. Appl. Phys. 6*, 120, 1955.

Clouthier, P. A., M. B. McElroy, F. C. Michel, Modification of the Martian Ionosphere by the Solar Wind, *J. Geophys. Res., 74*, 6215, 1969.

Coleman, C. I., Effects of perturbing magnetic fields on the performance of photoelectric sensors, *Rev. Sci. Instrum., 53*, 735, 1982.

Cook, W., Introduction to Electronic section, *Proceedings of the Small Instrument Workshop held in Pasadena, California, 29-31 March, edited by B. T. Tsurutani*, p.7-1, 1993a.

Cook, W. R., A. Cummings, B. Kecman, R. A. Medwaldt, D. Aalami, S. A. Kleinfelder, J. H. Marshal, Custom Analog VLSI for the Advanced Composition Explorer (ACE), *Proceedings of the Small Instrument Workshop held in Pasadena, California, 29-31 March, edited by B. T. Tsurutani*, p.7-19, 1993b.

Coplan, M. A.,J. H. Moore, R. A. Hoffmann, Double focusing ion mass spectrometer of cylindrical symmetry, *Rev. Sci. Instrum., vol. 55,* 537, 1984.

Courtney, S. H., W. L. Wilson, Multichannel time-correlated single photon counting: Spectroscopy and time-gated imaging using a resistive anode photomultiplier tube, *Rev. Sci. Instrum., vol. 62,* 2100, 1991.

Cushing, T. E., E. E. Lindelef, Miniature Electronics packaging for Spacecraft Instruments, *Proceedings of the Small Instrument Workshop held in Pasadena, California, 29-31 March, edited by B. T. Tsurutani,* p.7-27, 1993.

Dessler, A. J., Ionizing plasma flux in the Martian atmosphere, in *The Atmosphere of Venus and Mars,* edited by J. C. Brandt and M. B. McElroy, p. 241, Gordon and Breach, New York, 1968.

Dolginov, Sh. Sh., Ye. G. Yeroshenko, L. N. Zhuzgov, Magnetic field investigation by Venera-4 spacecraft, *Cosmic Res., 6(4),* 561, 1968.

Dolginov, Sh. Sh., Ye. G. Yeroshenko, L. N. Zhuzgov, Magnetic Field in the Very Close Neighbourhood of Mars According to Data from the Mars 2 and Mars 3 Spacecraft, *J. Geophys. Res., 78,* 4779, 1973.

Dolginov, Sh. Sh., Ye. G. Yeroshenko, L. N. Zhuzgov, The Magnetic Field of Mars According to Data from the Mars 3 and Mars 5 , *J. Geophys. Res., 81,* 3353, 1976a.

Dolginov, Sh. Sh., Ye. G. Yeroshenko, L. N. Zhuzgov, V. A. Sharova, K. I. Gringauz, V. V. Bezrukikh, T. K. Breus, M. I. Verigin, A. P. Remizov, Magnetic Field and Plasma inside and outside of the Martian Magnetosphere, in *Solar-Wind Interaction with the Planets Mercury, Venus, and Mars, Ed. by N. F. Ness, NASA-SP394,* 1, 1976b.

Dolginov, Sh. Sh., L. N. Zhuzgov, The magnetic field and the magnetosphere of the planet Mars, *Planet. Space Sci, Vol. 39, No. 11*, 1493, 1991.

Dryer, M., G. R. Heckman, Application of the Hypersonic Analog to the Standing Shock of Mars, *Solar Physics 2, D. Reidel Publishing Company,* p112 - 124, 1967.

Dubinin, E. M., K. Sauer, R. Lundin, K. Baumgartel, A. Bogdanov, Structuring of the transition region (plasma mantle) of the Martian magnetosphere, *Geophys. Res. Lett., Vol. 23, No. 7,* 785, 1996.

Dubinin, E. M., K. Sauer, K. Baumgartel, R. Lundin, The Martian Magnetosheath: PHOBOS-2 Observations, *Adv. Space Res., Vol. 20, No. 2*, 149, 1997.

Edgar, M. L., R. Kessel, J. S. Lapington, D. M. Walton, Spatial charge cloud distribution of microchannel plates, *Rev. Sci. Instrum., 60*, 3673, 1989.

Edgar, M. L., A. Smith, J. S. Lapington, Long range effects of gain depression in microchannel plates, *Proc. SPIE, 1743*, 283, 1992.

Edgar. M. E., A High Performance, Microchannel Based, Photon Counting Detector For Space Use, *Ph.D. Thesis*, University of London, 1993.

Fedorov, A. O., *Private Communication*, 1994.

Fedorov, A. O., O. L. Vaisberg, A. D. Johnstone, A. M. James, A. Kogjukhovsky, R. Woodliffe, Rapid Non-scanning Ion Distribution Measurements using Electrostatic Mirror and Multichannel Collimator for the INTERBALL and MARS-96 Missions, submitted to *Proc. AGU Chapman Conference on Measurement Techniques in Space Plasmas*, 1996.

Firmani C., E. Ruiz, C. W. Carlson, M. Lampton, F. Paresce, High-resolution imaging with a two-dimensional resistive anode photon counter, *Rev. Sci. Instrum., vol. 53,* 570, 1982.

Floryan, R. F., C. B. Johnson, Resistive-anode position sensing photomultiplier tube operational modeling, *SPIE Vol. 1072 Image Intensification*, 30, 1989

Foote , J. H., G. W. Coutts, L. R. Pedrotti, L. Schlander, B. E. Wood, E||B end-loss-ion analyser for Tandem-Mirror Experiment-Upgrade, *Rev. Sci. Instrum., vol. 56,* 1117, 1985.

Foote , B. E. Wood, M. D. Brown, G. M. Curnow, Plasma measurements with the TMX-U E||B end-loss ion spectrometers, *Rev. Sci. Instrum., vol. 57,* 1786, 1986.

Fraser, G. W., X- and gamma-Ray Imaging using Microchannel Plates, *Nucl. Instr. Meth., 221*, 115, 1984.

Fraser, G. W., J. F. Pearson, J. E. Lees, Dark Noise in Microchannel Plate X-Ray Detectors, *Nucl. Instr. Meth., A254*, 447, 1987.

Fraser, G. W., J. F. Pearson, J. E. Lees, Evaluation of Long Life (L^2) Microchannel Plates, *IEEE Trans. Nucl. Sci., NS-35*, 529, 1988.

Fraser, G. W., 1989, X-Ray Detectors in Astronomy, *Cambridge University Press, Cambridge*, p. 169, 1989.

Fraser, G. W., The Gain, Temporal Resolution and Magnetic-Field Immunity of Microchannel Plates, *Nucl. Instr. Meth., A291*, 595, 1990.

Fraser, G. W., M. T. Pain, J. E. Lees, J. F. Pearson, The operation of microchannel plates at high count rates, *Nucl. Instr. Meth., A306*, 247, 1991.

Fraser, G. W., Microchannel Plate Detectors for Space Astronomy, *Proceedings of an ESA symposium on Photon Detectors for Space Instrumentation, ESA, SP-356,* 97, 1992.

Funsten, H. O., D. J. McComas, E. E. Scime, E||B energy-mass spectrograph for measurement of ions and neutral atoms, *Rev. Sci. Instrum., vol. 68,* 292, 1997.

Gao, R. S., P. S. Gibner, J. H. Newman, K. A. Smith, R. F. Stebbings, Absolute and angular efficiencies of a microchannel-plate position-sensitive detector, *Rev. Sci. Instrum., 55,* 1756, 1984.

Ghielmetti, A. G., D. T. Young, A double focusing toroidal mass spectrograph for energetic plasmas: I. First order theory, *Nucl. Instrum. Meth., A258,* 297, 1987.

Gloeckler, G., Ion composition measurement techniques for space plasmas[a)], *Rev. Sci. Instrum., 61,* 3613, 1990.

Grande, M., S. L. Thomas, P. Seller, VLSI Charge Amplifiers as used on POLAR and Cluster, *Proceedings of the Small Instrument Workshop held in Pasadena, California, 29-31 March, edited by B. T. Tsurutani,* p.7-11, 1993a.

Grard, R., A. Pedersen, S. Klimov, S. Savin, A. Skalsky, J. G. Trotignon, C. Kennel, First measurements of plasma waves near Mars, *Nature, 341,* 607, 1989.

Green, T. S., A Spectrograph for the Simultaneous Measurement of Velocity Spectra and Charge-to-Mass Ratios of Ions, *Rev. Sci. Instrum., vol. 41,* 1533, 1970.

Gringauz, K. I., V. V. Bezrukuhk, G. I. Volkov, T. K. Breus, I. S. Musatov, L. P. Havkin, G. F. Sloutchenkov, Results of Solar Plasma Electron Observations on Mars-2 and Mars-3 Spacecraft, *J. Geophys. Res., 78,* 5808, 1973.

Gringauz, K. I., V. V. Bezrukuhk, M. I. Verigin, A. P. Remizov, On Electron and Ion Components of Plasma in the Antisolar Part of Near-Martian Space, *J. Geophys. Res., 81,* 3349, 1976.

Guest, A. J., A computer model of channel multiplier plate performance, *Acta Electronica, 14,* 79, 1971.

Hamamatsu, MCP Assembly (Technical Information), *Hamamatsu Photonics K. K., Electron Tube Center, TMCP9001 E01*, 1991.

Hanson, W. B., S. Sanatani, D. R. Zuccaro, The Martian ionosphere as observed by the Viking retarding potential analyzer, *J. Geophys. Res., 82,* 4351, 1977.

Hardy, D. A., D. M. Walton, A. D. Johnstone, M. F. Smith, M. P. Gough, A. Huber, J. Pantazis, R. Burkhardt, The Low Energy Plasma Analyzer, *IEEE Trans. Nucl. Sci., 40,* 246, 1992.

Hays, P. B., W. E. Sharp, Twilight Airglow 1. Photoelectrons and [OI] 5577-Angstrom Radiation, *J. Geophys. Res., 78,* 1153, 1973.

Hellsing, M., L. Karlsson, H-O. Andren, H. Norden, Performance of a microchannel plate ion detector in the energy range 3-25keV, *J. Phys. E: Sci. Instrum., 18*, 920, 1985.

Henry, J. P., E. M. Kellogg, U. G. Briel, S. S. Murray, L. P. Van Speybroeck, P. J. Bjorkholm, High Resolution Imaging X-Ray Detector for Astronomical Measurements, *SPIE Vol. 106 X-Ray Imaging*, 196, 1977.

Herold, H., A. Mozer, M. Sadowski, H. Schmidt, Design and calibration of a Thomson ion analyser for plasma focus studies, *Rev. Sci. Instrum., vol. 52,* 24, 1981.

Heroux, L. J., H. F. Hinteregger, Handbook of Geophysics and the Space Environment, *edited by A. S. Jursa, Air Force Geophysics Laboratory, Air Force Systems Command, United States Air Force*, chapter 2, 1985.

Hirahara, M., T. Mukai, Satellite borne energetic ion mass spectrometer for three-dimensional measurement of velocity distribution, *Rev. Sci. Instrum., vol. 64,* 406, 1993.

Hoenk, M. E., P. J. Grunthaner, F. J. Grunthaner, R. W. Terhune, S. Nikzad, Delat-doped CCDs - Potential New Low Energy Particle Detectors, *Proceedings of the Small Instrument Workshop held in Pasadena, California, 29-31 March, edited by B. T. Tsurutani,* p.4-29, 1993

Hunten, D. M., J. A. Slavin, L. H. Brace, D. Deming, L. A. Frank, J. M. Grebowsky, R. M. Haberle, W. B. Hanson, D. S. Intriligator, T. L. Killeen, A. J. Kliore, W. S. Kurth, A. F. Nagy, C. T. Russell, B. R. Sandel, J. T. Schofield, E. J. Smith, Y. L. Yung, U. von Zahn, R. W. Zurek, Mars Aeronomy Observer: report of the Science Working Team, *NASA Tech. Memo., TM-89202,* 73, 1986.

Hunter, W. R., Measurement of Optical Constants in the Vacuum Ultraviolet Spectral Region, *Handbook of Optical Constants of Solids, edited by E. D. Palik, Naval Research Laboratory, Academic Press,* p. 72, 1985

Intriligator, D. S., E. J. Smith, Mars in the Solar Wind, *J. Geophys. Res., 84,* 8427, 1979.

Ip, W. H., On a Hot Oxygen Corona of Mars, *Icarus, 76,* 135, 1988.

James, A. M., A. D. Johnstone, D. M. Walton, O. Vaisberg, A. Fedorov, A fast omni-directional ion detector for the study of space plasmas, submitted to *Proc. AGU Chapman Conference on Measurement Techniques in Space Plasmas,* 1996.

Johnson, F. S., J. E. Midgley, Induced magnetosphere of Venus, *Space Res., 9,* 760, 1969.

Johnson, F. S., W. B. Hanson, Viking 2 Electron Observations at Mars, *J. Geophys. Res., 97,* 6523, 1992.

Johnstone, A. D., J. A. Bowles, A. J. Coates, A. J. Coker, S. J. Kelllock, J. Raymont, B. Wilken, W. Studemann, W. Weiss, R. Cerulli Irelli,, V. Formisano, E. de Giorgi, P. Perani, M de Bernadi, H. Borg, S. Olsen, J. D. Winningham, D. A. Bryant, The Giotto mission - Its Scientific Investigations, edited by R. Reinhard and B. Battrick, *European Space Agency, ESA SP-1077*, p. 15, 1986.

Johnstone, A. D., A. J. Coates, B. Wilken, W. Studemann, W. Weiss, R. Cerulli Irelli, V. Formisano, H. Borg, S. Olsen, J. D. Winningham, D. A. Bryant and S. J. Kellock, The Giotto three-dimensional positive ion analyser, *J. Phys. E: Sci. Instrum., 20*, 795, 1987.

Johnstone, A. D., A. J. Coates, D. Walton, R. Kessel, O. L. Vaisberg, A. O. Fedorov, L. M. Zeleny, V. N. Smirnov, V. K. Lichtenstein, S. Fisher, V. Formisano, J. Safrankova, Z. Nemecek, *Proposal to the Institute of Space Physics, Moscow, for the FONEMA-FND instrument*, 1988.

Kaminsky, M, Atomic and Ionic Impact Phenomena on Metal Surfaces, *Springer-Verlac, Berlin-Heidelberg*, p.95, 1965.

Kaye, G. W. C., T. H. Labey, Tables of Physical and Chemical Constants, *16th edition, Longman Group Limited*, 1995.

Keller, H., G. Klingelhofer, E. Kankeleit, A Position Sensitive Microchannelplate Detector using a Delay Line Readout Anode. *Nucl. Instr. Meth. A258*, 221, 1987..

Kivelson, M. G., C. T. Russell, Introduction to Space Physics, *Cambridge University Press*, p.108, 1995.

Kliore, A., D. L. Cain, G. S. Levy, V. R. Eshelman, G. Fjeldbo, F. D. Drake, Occultation Experiment: Results of the First Direct Measurement of Mars's Atmosphere and Ionosphere, *Science, Vol. 149*, 1243, 1965.

Kliore, A., Radio Occultation Observations of the Ionospheres of Mars and Venus, *Venus and Mars: Atmospheres, Ionospheres, and Solar Wind Interactions, Geophysical Monograph 66*, pp 265, 1992.

Knibbeler, C. L. C. M., G. J. A. Hellings, H. J. Maaskamp, H. Ottevanger, H. H. Brongersma, Novel two-dimensional position-sensitive detection system, *Rev. Sci. Instrum., 58*, 125, 1987.

Knudsen, W. C., Evaluation and Demonstration of the Use of Retarding Potential Analyzers for Measuring Several Ionospheric Quantities, *J. Geophys. Res., 71*, 4669, 1966.

Koshida, N., M. Hosobuchi, Energy distribution of output electrons from a microchannel plate, *Rev. Sci. Instrum., 56*, 1329, 1985.

Kremnev, R. S., G. N. Rogovsky, K. M. Pitckhadze, Mars-94 Spacecraft Scientific Equipment Operational Requirements, *Babakin Engineering and Research Centre, Moscow*, p.19, 1989.

Kusama, Y., M. Nemoto, K. Tobita, H. Takeuchi, Compact and wide-range charge exchange neutral particle analyser with an acceleration tube, *Rev. Sci. Instrum., vol. 61,* 3107, 1990.

Kuswa, G. W., L. P. Bradley, G. Yonas, Ion acceleration in electron beams, *I.E.E.E. Trans. Nucl. Sci., NS-20,* 305, 1973.

LAACG, Reference Manual for the POISSON/SUPERFISH Group of Codes, *Los Alamos National Laboratory, Accelerator Theory and Simulation Group, LA-UR-87-126*, 1987.

Lampton, M., R. F. Malina, Quadrant anode image sensor, *Rev. Sci. Instrum., vol. 47,* 1360, 1976.

Lampton, M., F. Paresce, The RANICON: A resistive anode image converter, *Rev. Sci. Instrum., vol. 45,* 1098, 1974.

Lampton, M., O. Siegmund, R. Raffanti, Delay line anodes for microchannel-plate spectrometers, *Rev. Sci. Instrum., vol. 58,* 2298, 1987.

Lapington, J. S., A. A. Breeveld, M. L. Edgar, M. W. Trow, A Novel Imaging Readout With Improved Speed And Resolution, *Nucl. Instr. Meth., Vol.310,* 299, 1991.

Lapington, J. S., The effects of secondary electron emission on the operation of position sensitive anodes, *Nucl. Instr. Meth., Vol.392,* 336, 1997.

Lazurus, A. J., H. S. Bridge, J. M. Davis, C. W. Snyder, Initial results from the Mariner 4 solar plasma experiment, *Space Research VII, North Holland, Amsterdam,* pp. 1296-1305, 1967.

Lecomte, P., V. Perez-Mendez, Channel Electron Multipliers: Properties, Development and Applications, *I.E.E.E. Trans. Nucl. Sci., NS-25,* 964, 1978.

Levine, J. S., G. M. Keating, E. J. Prior, Helium in the Martian atmosphere thermal loss considerations, *Planet. Space Sci., 22,* 500, 1974.

Liptak, M., H. Rosenbauer, W. G. Sandie, E. G. Shelley, D. A. Simpson, Microchannel Plate Electron Multiplier for Mass Spectrometer Applications, *IEEE Trans. Nucl. Sci. NS-31,* 780, 1984.

Lu, M. F., C. Z. Liu, S. Z. Yang, Modified Thomson spectrometer for the detection of low energy (<1 keV) high power ion beams, *Rev. Sci. Instrum., vol. 68,* 3738, 1997.

Luhmann, J. G., L. H. Brace, Near-Mars Space, *Reviews of Geophysics, 29*, 121, 1991.

Luhmann, J. G., S. J. Bauer, Solar Wind Effects on Atmosphere Evolution At Venus and Mars, *Venus and Mars: Atmospheres, Ionospheres, and Solar Wind Interactions, Geophysical Monograph 66, Ed. by J. G. Luhmann, M. Tatrallyay, and R. O. Pepin, AGU, Washington D. C.*, 417, 1992

Lundin, R., B. Hultqvist, S. Olsen, R. Pellinin, I. Liede, A. Zakharov, E. Dubinin, N. Pissarenko, The ASPERA Experiment on the Soviet PHOBOS Spacecraft, *AGU Monograph 54, Solar System Plasma Physics, edited by J. H. Waite Jr., J. L. Burch, R. L. Moore*, 417, 1989.

Lundin, R., A. Zakharov, R. Pellinen, H. Borg, B. Hultqvist, N. Pissarenko, E. M. Dubinin, S. W. Barabash, I. Liede, H. Koskinen, First measurements of the ionospheric plasma escape from Mars, *Nature, 341*, 609, 1989.

Lundin, R., A. Zakharov, R. Pellinen, S. W. Barabash, H. Borg, E. M. Dubinin, B. Hultqvist, H. Koskinen, I. Liede, N. Pissarenko, ASPERA/PHOBOS measurements of the ion outflow from the Martian Ionosphere, *Geophys. Res. Lett., Vol. 17, No. 6*, 873, 1990a.

Lundin, R., A. Zakharov, R. Pellinen, H. Borg, B. Hultqvist, N. Pissarenko, E. M. Dubinin, S. W. Barabash, I. Liede, H. Koskinen, Plasma Composition measurements of the Martian Magnetosphere Morphology, *Geophys. Res. Lett., Vol. 17, No. 6*, 877, 1990b.

Lundin, R., A. Zakharov, R. Pellinen, S. W. Barabash, H. Borg, E. M. Dubinin, B. Hultqvist, H. Koskinen, I. Liede, N. Pissarenko, On the Momentum Transfer of the Solar Wind to the Martian Topside Ionosphere, *Geophys. Res. Lett., Vol. 18, No. 6*, 1059, 1991.

Lynch, D. W., W. R. Hunter, Comments on the Optical Constants of Metals and an introduction to the Data for Several Metals, *Handbook of Optical Constants of Solids, edited by E. D. Palik, Naval Research Laboratory, Academic Press*, p. 364, 1985.

Lyons, L., A Practical Guide to Data Analysis for Physical Science Students, *Cambridge University Press, Cambridge*, p. 79, 1991.

Malina, R. F., K. R. Coburn, Comparative Lifetesting Results for Microchannel Plates in Windowless EUV Photon Detectors, *IEEE Trans. Nucl. Sci. NS-31,* 404, 1984.

Martin, C., M. Lampton, R. F. Malina and H. O. Anger, Wedge and Strip Anodes for Centroid-Finding Position-Sensitive Photon and Particle Detectors, *Rev. Sci. Instrum., vol. 52,* 1067, 1981.

Mason, I. M., G. Branduardi-Raymont, J. L. Culhane, R. H. D. Corbet, J. C. Ives, P. W. Sanford, The EXOSAT imaging X-ray detectors, *IEEE Trans. Nucl. Sci. NS-31,* 795, 1984.

Mathieson, E., G. C. Smith, P. J. Gilvin, The Graded-Density Cathode, *Nucl. Instr. Meth. A174*, 221, 1980.

Matsuura, S., S. Umebayashi, C. Okoyama, K. Oba, Current Status of the Micro Channel Plate, *IEEE Trans. Nucl. Sci., NS 31*, 399, 1984.

McClintlock, W. E., C. A. Barth, R. E. Steele, G. M. Lawrence, J. G. Timothy, *Applied Optics, Vol. 21, No. 17*, 3071, 1982

McComas, D. J., J. E. Nordholt, New approach to 3-D, high sensitivity, high mass resolution space plasma composition measurements, *Rev. Sci. Instrum., 61*, 3095, 1990.

Medley, S. S., Energetic ion mass analysis using a radio-frequency quadrupole filter, Rev. Sci. Instrum., 49, 698, 1978.

Menzel, M. T., H. K. Stokes, User's Guide for the POISSON/SUPERFISH Group of Codes, *Los Alamos National Laboratory, Accelerator Theory and Simulation Group, LA-UR-87-115*, 1987.

Mizogawa, T., M. Sato, M. Yoshino, Y. Itoh, Y. Awaya, *Nucl. Instr. Meth. A387*, 395, 1997

Mohlmann, D., W. Riedler, J. Rustenbach, K. Schwingenschuh, J. Kurths, U. Motschmann, T. Roatsch, K. Sauer, H. T. M. Lichtenegger, The Question of an Internal Martian Magnetic Field, *Planet. Space Sci., 39*, 83, 1991.

Moore, T. E., Spectrograph suitable for the mass and energy analysis of space plasmas over the energy range 0.1 - 10keV, *Rev. Sci. Instrum., 48*, 221, 1977.

Morenzoni, E., K. Oba, E. Pedroni, D. Taqqu, Performance of microchannel plates in high magnetic fields, *Nucl. Instrum. Meth., A263*, 397, 1988.

Mullard Limited, *Technical Information 31 Microchannel plates, TP1561*, p. 7, 1976.

Murphy, G. B., D. R. Croley, M. Hoenk, S. Nikzad, R. W. Terhune, P. Grunthaner, F. Grunthaner, CCDs as particle detectors- Possibilities, Problems and Advances, *Proceedings of the Small Instrument Workshop held in Pasadena, California, 29-31 March, edited by B. T. Tsurutani*, p.4-16, 1993.

Ness, N. F., K. W. Behannon, R. P. Lepping, Y. C. Whang, K. H. Schatten, Magnetic field observations nea Venus: Preliminary results from Mariner 10, *Science, 183*, 1301, 1974.

Neugebauer, M., C. W. Snyder, Mariner 2 Observations of the Solar Wind, *J. Geophys. Res., 71*, 4469, 1966.

Oberheide, J., P. Wilhelms, M. Zimmer, New results on the absolute ion detection efficiencies of a microchannel plate, *Meas. Sci. Tech., 8*, 351, 1997.

O'Gallagher, J. J., J. A. Simpson, Search for Trapped Electrons and a Magnetic Moment at Mars by Mariner IV, *Science, Vol. 149*, 1233, 1965.

Panitz, J. A., J. A. Foesch, Areal detction efficiency of channel electron multiplier arrays, *Rev. Sci. Instrum., 47*, 44, 1976.

Papalioslios, C., P. Nisenson, S. Ebstein, Speckle imaging with the PAPA detector, *Applied optics, Vol. 24, No.* 2, 287, 1985

Papatheodorou, G., A. D. Johnstone, R. D. Woodliffe, D. J. Rodgers, D. M. Walton, A. J. Sims, A miniature plasma analyser with a differential energy response, submitted to *Proc. AGU Chapman Conference on Measurement Techniques in Space Plasmas*, 1996.

Paresce, F., M. Clampin, C. Cox, J. Crocker, M. Rafal, A. Sen, W. A. Hiltner, The RANICON for Ground-Based Optical Astronomy, *Santa Cruz Summer Workshop on Instrumentation for ground-based optical astronomy; Present and Future*, 1987

Parker, R., Advances in Permanent Magnetism, *John Wiley and Sons*, pp 86-87, 1990.

Parks, G. K., Physics of Space Plasmas, *Addison-Wesley Publishing Company*, p501, 1991.

Paschmann, G., H. Loidl, P. Obermayer, M. Ertl, R. Laborenz, N. Sckopke, W. Baumjohann, C. W. Carlson, D. W. Curtis, The Plasma Instrument for AMPTE IRM, *IEEE Trans. Geosci. Remote Sensing, GE-23*, 262, 1985.

Pearson, J. F., J. E. Lees, G. W. Fraser, Operating characteristics of sandwich microchannel plates, *IEEE Trans. Nucl. Sci., NS-35*, 520, 1988.

Pearson, J. F., J. E. Lees, G. W. Fraser, K. Gringauz, N. Schutte, Y. Roze, Comparative tests of Russian microchannel plates, *Nucl. Instr. Meth. A325*, 578, 1993.

D. T. Pelz et al., Radio Sci. v.8, p.4, 277, 1973 (Abstract).

Perez-De-Tejada, H., Solar Wind Erosion of the Mars Early Atmosphere, *J. Geophys. Res., 97*, 3159, 1992.

Purshke, M., W. Nuxoll, G. Gaul, R. Santo, An Improved Quadrant Anode Image Sensor with Microchannel Plates, *Nucl. Instr. Meth. A261*, 537, 1987

Rasmussen, A., C. Martin, Development and testing of a prototype mosaic wedge-and-strip anode detector, *SPIE 1159*, 538, 1989.

Reading, D. H., Cluster 1 and Cassini MCP Uniformities, *Rutherford Appleton Laboratory, PEACE/RAPID internal report, SC-PR-RAL-TN-97-0004*, 1997.

Rhee, M. J., Compact Thomson Spectrometer, *Rev. Sci. Instrum., vol. 55,* 1229, 1984.

Richter, L. J., W. Ho, Position-sensitive detector performance and relevance to time resolved electron energy loss spectroscopy, *Rev. Sci. Instrum., vol. 57,* 1469, 1986.

Riedler, W. D. Mohlmann, V. N. Oraevsky, K. Schwingenschuh, Ye. Yeroshenko, J. Rustenbach, Oe. Aydogar, G. Berghofer, H. Lichtenegger, M. Delva, G. Schelch, K.

Pirsch, G. Fremuth, M. Steller, H. Arnold, T. Raditsch, U. Auster, K.-H. Fornacon, H. J. Schenk, H. Michaellis, U. Motschmann, T. Roatsch, K. Sauer, R. Schroter, J. Kurths, D. Lenners, J. Linthe, V. Kobzev, V. Styashkin, J. Achache, J. Slavin, J. G. Luhmann, C. T. Russell, Magnetic fields near Mars: first results, *Nature, 341*, 604, 1989.

Riedler, W., K. Schwingenschuh, H. Lichtenegger, D. Mohlmann, J. Rustenbach, Ye. Yeroshenko, J. Achache, J. Slavin, J. G. Luhmann, C. T. Russell, Interaction of the Solar Wind with the Planet Mars: PHOBOS 2 Magnetic Field Observations, *Planet. Space Sci, 39*, 75, 1991.

Roquemore, A. L., G. Gammel, G. W. Hammett, R. Kaita, S. S. Medley, Application of an E||B spectrometer to PLT charge-exchange diagnostics, *Rev. Sci. Instrum., vol. 56,* 1120, 1985.

Roquemore, A. L., S. S. Medley, Design concepts for compact mass/energy charge exchange analysers, *Rev. Sci. Instrum., vol. 57,* 1797, 1986.

Roquemore, A. L., S. S. Medley, Gyro-electron ghost images due to microchannel-plate operation in transverse magnetic fields, *Rev. Sci. Instrum., vol. 57,* 2966, 1986.

Rosenbauer, H., R. Schwenn, E. Marsch, B. Mayer, H. Miggenrieder, M. D. Montgomery, K-H. Mulhauser, W. Phillip, W. Voges, S. M. Zink, *J. Geophys. Res., 42*, 561, 1977.

Rosenbauer, H., N. Shutte, I. Apathy, A. Galeev, K. Gringauz, H. Grunwaldt, P. Hemmerich, K. Jockers, P. Kiraly, G. Kotova, S. Livi, E. Marsch, A. Richter, W. Riedler, T. Remizov, R. Schwenn, K. Schwingenschuh, M. Steller, K. Szego, M. Verigin, M. Witte, Ions of martian origin and plasma sheet in the martian magnetosphere: initial results of the TAUS experiment, *Nature, 341*, 612, 1989.

Rosenthal. A., Satellite Handbook, A Record of NASA Space Missions 1958-1980, *NASA Goddard Space Flight Center*, p.148, 1981.

Russell, C. T., Planetary Magnetism, *Rev. Geophys. Space Phys., 18*, 77, 1980.

Russell, C. T., J. G. Luhmann, J. R. Spreiter, S. S. Stahara, The Magnetic Field of Mars: Implications from Gas Dynamic Modeling, *J. Geophys. Res., 89*, 2997, 1984.

Russell, C. T., J. G. Luhmann, K. Schwingenschuh, Limitations of Spectral Analysis of the PHOBOS Magnetometer Data in the search for an Intrinsic Martian Magnetic Field, *Planet. Space Sci., 40*, 707, 1992.

Sagdeev, R. Z., A. V. Zakharov, Brief history of the Phobos mission, *Nature, 341*, 581, 1989.

Sakabe, S., T. Mochizuki, T. Yamanaka, C. Yamanaka, Modified Thomson parabola ion spectrometer of wide dynamic range, *Rev. Sci. Instrum., vol. 51,* 1314, 1980.

Sato, M., Intense Ion Beam Flux of Adsorbed Gases and Metallic Anode Materials in the "Point Pinch Diode" Measured with Thomson-Parabola Ion Spectrometer, *Japanese Journal of Applied Physics, Vol. 26, No. 6,* 927, 1987.

Schecker, J. A., M. M. Schauer, K. Holzscheiter, M. H. Holzscheiter, The performance of a microchannel plate at cryogenic temperatures and in high magnetic fields, and the detection efficiency for low energy positive hydrogen ions, *Nucl. Instr. Meth. A320*, 556, 1992.

Schunk, R. W., A. F. Nagy, Ionospheres of the Terrestrial Planets, *Rev. Geophys. Space Phys., 18*, 813, 1980.

Schwarz, H. E., J. S. Lapington, Optimization Of Wedge And Strip Anodes, *IEEE Trans. Nucl. Sci., Vol.32, No.1*, 433, 1985

Shelley, E. G., A. Ghielmetti, E. Hertzburg, S. J. Battel, K. Altwegg-von Burg, H. Balsiger, The AMPTE/CCE Hot Plasma Composition Experiment (HPCE*), IEEE Trans. Geosci. Remote Sensing, GE-23*, 241, 1985.

Shelley, E. G., A. G. Ghielmetti, H. Balsiger, R. K. Black, J. A. Bowles, R. P. Bowman, O. Bratschi, J. L. Burch, C. W. Carlson, A. J. Coker, J. F. Drake, J. Fischer, J. Geiss, A. Johnstone, D. L. Kloza, O. W. Lennartsson, A. L. Magoncelli, G. Paschmann. W. K. Peterson, H. Rosenbauer, T. C. Sanders, M. Steinacher, D. M. Walton, B. A. Whalen, D. T. Young, The Toroidal Imaging Mass-Angle Spectrograph (TIMAS) for the POLAR Mission, *Space Science Reviews, 71*, 497, 1995.

Shinagawa, H., T. E. Cravens, A One-Dimensional Multispecies Magnetohydrodynamic Model of the Dayside Ionosphere of Mars, *J. Geophys. Res., 94*, 6506, 1989.

Shutte, N. M., P. Kiraly, T. E. Cravens, A. V. Dyachkov, T. I. Gombosi, K. I. Gringauz, A. F. Nagy, W. E. Sharp, S. M. Sheronova, K. Szego, T. Szemerey, I. T. Szucs, M. Tatrallyay, A. Toth, M. Verigin, Observations of electron and ion fluxes in the vicinity of Mars with the HARP spectrometer, *Nature, 341*, 614, 1989.

Shutte, N., G. Kotova, S. Livi, A. F. Nagy, H. Rosenbauer, K. Szego, M. Verigin, Low Energy (E<400eV) Ions in the Magnetosphere of Mars as measured by the HARP instrument on PHOBOS 2, *Adv. Space Res., Vol. 20, No. 2*, 169, 1997.

Shyn, T. W., W. E. Sharp, P. B. Hays, Gridless retarding potential analyser for use in very-low-energy charged particle detection, *Rev. Sci. Instrum., 47*, 1005, 1976.

Siegmund, O. H. W., M. Lampton, S. Chakabarti, J. Vallerga, S. Bowyer, R. F. Malina, Application of wedge and strip image readout systems to detectors for astronomy, *SPIE 1159*, 476, 1986.

Siegmund, O. H. W., M. L. Lampton, R. Raffanti, A high resolution delay line readout for microchannel plates, *SPIE Vol. 1159 EUV, X-Ray, and Gamma-Ray Instrumentation for Astronomy and Atomic Physics*, 476, 1989.

Slater, D. C., Thomson parabola ion analyser for laser plasma studies, *Rev. Sci. Instrum., 49,* 1493, 1978.

Slavin, J. A., R. E. Holzer, Solar Wind Flow About the Terrestrial Planets 1. Modeling Bow Shock Position and Shape, *J. Geophys. Res., 86,* 11401, 1981.

Slavin, J. A., R. E. Holzer, J. R. Spreiter, S. S. Stahara, D. S. Chaussee, Solar Wind Flow About the Terrestrial Planets 2. Comparison with Gas Dynamic Theory and Implications for Solar-Planetary Interactions, *J. Geophys. Res., 88,* 19, 1983.

Slavin, J. A., R. E. Holzer, J. R. Spreiter, S. S. Stahara, Planetary Mach Cones: Theory and Observation, *J. Geophys. Res., 89,* 2708, 1984.

Slavin, J. A., K. Schwingenschuh, W. Riedler, Ye. Yeroshenko, The Solar Wind Interaction With Mars: Mariner 4, Mars 2, Mars 3, Mars 5, and Phobos 2 Observations of Bow Shock Position and Shape, *J. Geophys. Res., 96,* 11235, 1991.

Smith, A. D., J. R. Allington-Smith, A Study of Microchannel Plate Intensifiers, *IEEE Trans. Nucl. Sci., 33,* 295, 1986.

Smith, A., R. Kessel, J. S. Lapington, D. M. Walton, Modulation effects in wedge and strip anodes, *Rev. Sci. Instrum., 60,* 3509, 1989.

Smith, E. J., L. Davis Jr., P. J. Coleman, D. E. Jones, Magnetic Field Measurements near Mars, *Science, 149,* 1241, 1965.

Smith, G. C., J. F. Pearson, E. Mathieson, Microchannel Plate Read-out using Graded-Density Electrodes, *Nucl. Instr. Meth. A192,* 383, 1982.

Spreiter, J. R., A. W. Rizzi, The Martian Bow Wave - Theory and Observation, *Planet. Space Sci., 20,* 205, 1972.

Spreiter, J. R., A. L. Summers, A. W. Rizzi, Solar Wind Flow Past Nonmagnetic Planets - Venus and Mars, *Planet. Space Sci., 18*, 1281, 1970.

Stalder, R. E., T. van Zandt, T. W. Kenny, M. H. Hecht, F. E. Grunthaner, Micromachined Bessel Box Array, *Proceedings of the Small Instrument Workshop held in Pasadena, California, 29-31 March, edited by B. T. Tsurutani*, p.3-47, 1993.

Steckelmacher, W., Energy analysers for charged particle beams, *Jour. Phys. E: Scientific Instruments, 6*, 1061, 1973.

Street, R., J. Wooley, *Proc. Phys. Soc. London, A62*, 562, 1949.

Stumpel, J. W., P. W. Sandford, H. F. Goddard, A position sensitive proportional counter with high spatial resolution, *J. Phys. E, No. 6,* 397, 1973.

Szego, K., S. Klimov, G. Kotova, S. Livi, K. Quest, W. Riedler, H. Rosenbauer, V. D. Shapiro, A. Skalsky, N. Shutte, K. Schwingenschuh, M. Verigin, T. L. Zhang, The interaction of the shocked solar wind and the planetary ions at Mars, *Adv. Space Res., Vol. 20, No. 2*, 159, 1997.

Szucs I. T., T. Szemerey, P. Kiraly, W. E. Sharp, N. M. Shutte, T. E. Cravens, T. I. Gombosi, K. I. Gringauz, A. F. Nagy, S. M. Sheronova, S. Szendro, M. Tatrallyay, A. Toth, M. I. Verigin, The Harp Electron And Ion Sensor On The Phobos Mission, *Nucl. Instr. Meth., 290, No. 1*, 228, 1990.

Taylor, R. C., M. C. Hettrick, R. F. Malina, Maximising the quantum efficiency of microchannel plate detectors: The collection of photoelectrons from the interchannel web using an electric field, *Rev. Sci. Instrum., 54*, 171, 1983.

Tennent, R. M., Science Data Book, *Oliver and Boyd Publishers, Edinburgh*, 90, 1978.

Thomson, J. J., Rays of Positive Electricity, *Phil. Mag. S. G. Vol. 21, 122,* 225, 1911.

Timothy, J. G., R. L. Bybee, Two-dimensional photon-counting detector arrays based on microchannel array plates, *Rev. Sci. Instrum., vol. 46,* 1615, 1975.

Timothy, J. G., G. H. Mount, R. L. Bybee, Multi-anode Microchannel Arrays, *IEEE Trans. Nucl. Sci. NS-28,* 689, 1981

Tobita, K., H. Takeuchi, H. Kimura, Y. Kusama, M. Nemoto, Absolute detection efficiency of a microchannel-plate detector for ions and neutrals, *Japan J. Appl. Phys., 26,* 509, 1987.

Tremsin, A. S., J. F. Pearson, G. W. Fraser, W. B. Feller, P. White, Microchannel plate operation at high count rates: new results, *Nucl. Instr. Meth. A162,* 139, 1996.

Trotignon, J. G., R. Grard, S. Barabash, R. Lundin, E. Dubinin, Solar wind measurements near Mars and their implication in the Red Planet environment, *Planet. Space Sci., 44,* 117, 1996.

Vacuumschmelze, Rare-Earth Permanent Magnet Materials, M 054, 1988.

Vacuumschmelze, Rare-Earth Permanent Magnets, PD-002, 1996.

Vaisberg, O. L., A. V. Bogdanov, V. N. Smirnov, S. A. Romanov, On the Nature of the Solar-Wind-Mars Interaction, in *Solar-Wind Interaction with the Planets Mercury, Venus, and Mars, Ed. by N. F. Ness, NASA-SP394,* 21, 1976.

Vaisberg, O., V. Smirnov, The Martian Magnetotail, *Adv. Space Res., 6,* 301, 1986.

Vaisberg, O. L., A. O. Fedorov, A. D. Johnstone, E. I. Kolesnikova, A. I. Kozhukhovsky, V. M. Balebanov, The possibility of making fast measurement of ion distribution functions, *Proc. Int. Workshop on Space Plasma Physics Investigation by Cluster and Regatta, ESA SP-306,* 143, 1990.

Vaisberg, O. L., The Solar Wind Interaction with Mars: A Review of Results from previous Soviet Missions to Mars, *Adv. Space Res., Vol. 12, No. 9*, 137, 1992a.

Vaisberg, O. L., The Solar Wind Interaction with Mars: A Review of Results from Early Soviet Missions to Mars, *Venus and Mars: Atmospheres, Ionospheres, and Solar Wind Interactions, Geophysical Monograph 66, Ed. by J. G. Luhmann, M. Tatrallyay, and R. O. Pepin, AGU, Washington D. C.*, 311, 1992b.

Van Allen, J. A., L. A. Frank, S. M. Krimigis, H. K. Hills, Absence of Martian Radiation Belts and Implications Thereof, *Science, Vol. 149*, 1228, 1965.

Vasyliunas, V. M., Deep space plasma measurements, *in Methods of Experimental Physics, 9B, edited by R. H. Lovberg and H. R. Griem, Academic Press, New York*, 49, 1971.

Verigin, M. I., N. M. Shutte, A. A. Galeev, K. I. Gringauz, G. A. Kotova, A. P. Remizov, H. Rosenbauer, P. Hemmerich, S. Livi, A. K. Richter, I. Apathy, K. Szego, W. Riedler, K. Schwingenschuh, M. Steller, Ye. G. Yeroshenko, Ions of Planetary origin in the Martian Magnetosphere (PHOBOS 2/TAUS Experiment), *Planet. Space Sci., 39*, 131, 1991.

Voss, H. D., J. R. Kilner, R. A. Baraze, J. Mobilia, R. B. Kash, A. J. Goodwater, E. Kwok, Analog/Digital Microcircuits for Space Flight Applications, *Proceedings of the Small Instrument Workshop held in Pasadena, California, 29-31 March, edited by B. T. Tsurutani*, p.7-3, 1993a.

Walker, D., P. Sandford, A. Lyons, J. Fordham, D. Bone, A. Walker, A. Boksenberg, The UCL charge-coupled device camera at the South-African Astronomical Observatory, *Advances in Electronics and Electron Physics, vol.64*, 185, 1985.

Wallis, M. K., Does Mars have a Magnetosphere?, *Geophys. J. R. astr. Soc., 41*, 349, 1975.

Walton, D. M., Thomson Parabola Properties, *MSSL internal document*, 1987.

Walton, D. M., A. M. James, J. A. Bowles, A. D. Johnstone, High- speed 2-D Imaging for Plasma Analysers using Wedge-and-Strip Anodes, submitted to *Proc. AGU Chapman Conference on Measurement Techniques in Space Plasmas*, 1996.

Weber, R., J. E. Balmer, P. Ladrach, Thomson parabola time-of- flight ion spectrometer, *Rev. Sci. Instrum., vol. 57,* 1251, 1986.

Wilken, B., Identification Techniques for Nuclear Particles in Space Plasma Research and Selected Experimental Results, *Reports on Progress in Physics, Vol.47, No.7,* 767, 1984.

Wiza, J. L., Microchannel Plate Detectors, *Nucl. Instr. Meth. 162,* 587, 1979.

Woodliffe, R. D., Design of space borne plasma analysers by computer simulation, *Ph.D. Thesis*, University of London, 1991.

Yamamoto, T., K. Ishii, K. Hirano, Thomson Parabola Ion Analyser with Quick Data Acquisition, *Japanese Journal of Applied Physics, Vol. 29, No. 9,* 1841, 1990.

Yeroshenko, Ye. W. Riedler, K. Schwingenschuh, J. G. Luhmann, M. Ong, C. T. Russell, The magnetotail of Mars: PHOBOS observations, *Geophys. Res. Lett., 17*, 885, 1990.

Yoneda, H., K. Horioka, Y. Kim, K. Kasuya, Thomson parabola ion energy analyser with a coincident and jitter-free applied electric field ramp, *Rev. Sci. Instrum., vol. 59,* 457, 1988.

Young, D. T., Space Plasma Mass Spectrometry Below 60keV, *AGU Monograph 54, Solar System Plasma Physics, edited by J. H. Waite Jr., J. L. Burch, R. L. Moore*, 143, 1989.

Zakharov, A.V., The Mars-94 and Mars-96 missions, *Phil. Trans. R. Soc. Lond. A, 349,* 295, 1994.

Zhang, T. L., K. Schwingenschuh, H. Lichtenegger, W. Riedler, C. T. Russell, J. G. Luhmann, Interplanetary Magnetic Field control of the Mars Bow Shock: Evidence for Venuslike Interaction, *J. Geophys. Res., 96*, 11265, 1991.

Zhang, T. L., K. Schwingenschuh, W. Riedler, G. Kotova, M. Verigin, M. Tatrallyay, C. T. Russell, Solar Wind Deceleration at Mars and Earth: A comparison, *Adv. Space Res., Vol. 20, No. 2*, 133, 1997.

Zombeck, M. V., G. W. Fraser, Dead-time effects in microchannel-plate imaging detectors, *SPIE, 1549*, 90, 1991.